STRUCTURAL HEALTH MONITORING OF BRIDGE STRUCTURES USING FIBER BRAGG GRATING SENSORS

A THESIS

SUBMITTED TO THE

NATIONAL INSTITUTE OF TECHNOLOGY WARANGAL

FOR THE AWARD OF THE DEGREE OF

DOCTOR OF PHILOSOPHY

IN

PHYSICS

BY

SRAVANTHI ALAMANDALA

Roll No. 716051

Supervisor (s):

Prof. R.L.N. SAI PRASAD (Dept. of Physics)

Prof. P. RATHISH KUMAR (Dept. of Civil Engineering)

DEPARTMENT OF PHYSICS

NATIONAL INSTITUTE OF TECHNOLOGY

WARANGAL-506004, INDIA

SEPTEMBER – 2021

NATIONAL INSTITUTE OF TECHNOLOGY

Warangal – 506 004, Telangana (India)

DEPARTMENT OF PHYSICS

CERTIFICATE

This is to certify that the thesis entitled **"Structural Health Monitoring of Bridge Structures Using Fiber Bragg Grating Sensors"** being submitted by **Ms SRAVANTHI ALAMANDALA** to the Department of Physics, National Institute of Technology, Warangal, India is a record of bonafide research work carried out by her under our supervision and it has not been submitted elsewhere for award of any degree.

(Dr. P. Rathish Kumar)
Professor and Head
Department of Civil Engineering
Thesis Co-Supervisor

(Dr. R.L.N Sai Prasad)
Professor
Department of Physics
Thesis Supervisor

DECLARATION

This is to certify that the work presented in the thesis entitled **"STRUCTURAL HEALTH MONITORING OF BRIDGE STRUCTURES USING FIBER BRAGG GRATING SENSORS**" is a Bonafide work done by me under the supervision of **Prof. R.L.N. Sai Prasad**, Department of Physics, and **Prof. P. Rathish Kumar**, Department of Civil Engineering, National Institute of Technology, Warangal, and was not submitted elsewhere for the award of any degree.

I declare that this written submission represents my ideas in my own words and where others' ideas or words have been included, I have adequately cited and referenced the original sources. I also declare that I have adhered to all principles of academic honesty and integrity and have not miss represented or fabricated or falsified any idea/ data/ fact/ source in my submission. I understand that any violation of the above will be a cause for disciplinary action by the institute and can also evoke penal action from the sources which have thus not been properly cited or from whom proper permission has not been taken when needed.

A. Sravanthi

(Sravanthi Alamandala)

सरस्वति नमस्तुभ्यं वरदे कामरूपिणि ।

विद्यारम्भं करिष्यामि सिद्धिर्भवतु मे सदा ॥

Dedicated to

My

Beloved Parents

ACKNOWLEDGEMENTS

I take this opportunity to thank the people who have been involved in my efforts directly or indirectly, to complete this dissertation. The words mentioned here may not be sufficient to express my gratitude towards them.

Foremost, I sincerely thank my supervisor(s), **Prof. R.L.N. Sai Prasad** from department of Physics and **Prof. P. Rathish Kumar** from department of Civil engineering, for their valuable guidance, motivation and encouragement throughout my work. It has been great pleasure for me to work under their guidance. I am thankful to my supervisor(s) for believing in me, and also patiently bearing me. This thesis wouldn't have been possible without their immense support, academically and personally.

I am thankful to my Doctoral Scrutiny Committee members, **Prof. D. Dinakar** (Head of the department), **Prof. M. Sai Shankar** (Retd)., **Dr. Sourabh Roy**, and **Prof. T. Kishore Kumar (**department of Electronics and communication engineering) for constantly reviewing my progress and providing valuable suggestions in a constructive way that helped me to carry forward my work successfully. I would like to extend my sincere thanks to all the faculty members, office staff and students of Physics department for their support, whenever necessary.

I am deeply indebted to senior colleagues Dr. P. Kishore, Dr. P.V.N. Kishore, Dr. C. Hari Krishna for their valuable suggestions and advice on many occasions. I sincerely thank my co-scholars Mr.V.D.R. Pavan , Mr. P. Srinath, Mr. Koustav Dey, and Mr. Rajesh, Dr. B. Surekha, Mr. Gnyaneshwar, for their moral support during my stay. I am extremely thankful to Mr. Debamalya Dutta, Mr. Guruprathap Reddy, Mr. Amith Yadhav and Mr. Sai Asrith, and had wonderful time working with them.

I thank OSA (Optical Society of America), and SPIE (International Society for optics and photonics technology) for travel grants to attend international conference.

Many thanks to my elder sisters **Swapnalatha** and **Srujana** for their encouragement and support all the way from my childhood. I wish to thank my entire extended family and friends for all their support.

Finally I would like to thank my parents **A. Laxminarayana** and **A. Padma** for everything. Without their prayers, sacrifice and never ending support, I wouldn't be writing these lines of my thesis.

I gratefully acknowledge one and all once again.

A. Sravanthi

Date: 28-09-2021 (Sravanthi Alamandala)

CONTENTS

CHAPTER 2

LITERATURE REVIEW

CHAPTER 3

BRIDGE WEIGH-IN-MOTION (BWIM) SYSTEM FOR MEASURING THE VEHICLE PARAMETERS

CHAPTER 4

COST-EFFECTIVE LOAD MEASUREMENT SYSTEM FOR HEALTH MONITORING

CHAPTER 5

COMPARATIVE STUDY BETWEEN DIGITAL IMAGE CORRELATION AND FIBER BRAGG GRATING SENSORS

CHAPTER 6

STUDY ON CHANGES IN THE DYNAMIC CHARACTERISTICS OF VIBRATED AND SELF-COMPACTING BEAMS BEFORE DAMAGE AND AFTER REPAIR

CHAPTER 7

CONCLUSIONS AND FUTURE SCOPE OF WORK

NOTATIONS

mm, cm, nm	milli meter, Centi meter, Nano meter
l, w, h	Length, Width, Thickness
λ_B	Bragg Wavelength
$\Delta \lambda_B$	Shift in Bragg Wavelength
ε	Strain
P_e	Strain Optic coefficient
$\mu\varepsilon$	Micro strain
Δt	Time difference
V	Velocity of the Vehicle
d	Distance between two FBGs
P_1, P_2	Two peaks (position of the vehicle front and rear wheels)
D	Dip shape (position of FBG in between vehicle wheels)
E	Modulus of Elasticity
I	Moment of Inertia
Δy_{max}	Maximum deflection
μw	microwatt
V/A	Voltage/Ampere
Tx	Transmitter
Rx	Receiver
Bd	Baud rate
V	Voltage
N	Newton

F(x,y)	Grey scale intensity function of reference image
G(x',y')	Grey scale intensity function of deformed image
C	Correlation
(u,v)	Displacement fields along (x,y) direction
s	Seconds
$\varepsilon_{xx}, \varepsilon_{xy}, \varepsilon_{yy}$	Strain along xx, xy, yy direction
$\varepsilon_{1,2}$	Maximum, minimum Principal strains
r	Radius of the APT
ϕ	Angle of Orientation of FBG
ω, ω_n	Circular frequency, Natural frequency
a_0	Initial amplitude
n	number of rotations
(a_n,b_n)	different amplitudes at 'n' no.of rotations
Hz	Hertz

ABBREVIATIONS

SHM	Structural Health Monitoring
NDT	Non Destructive Testing
BWIM	Bridge Weigh In Motion
ECT	Eddy Current Technique
AE	Acoustic Emission
VBDI	Vibration-Based Damage Identification
VBDD	Vibration-Based Damage Detection
ARMA	Auto Regressive Moving Average
DIC	Digital Image Correlation
DSLR	Digital Single-Lens Reflex Camera
FOS	Fiber Optic Sensors
FBG	Fiber Bragg Grating
LPG	Long Period Grating
LPFG	Long Period Fiber Grating
TMB	Tsing Ma Bridge
ADC	Analog to Digital Converter
MQTT	Message Queuing Telemetry Transport
IoT	Internet of Things
FAS	Fast and Simple
ESSDA	Enhanced Sequential Similarity Detection Algorithm
NVC	Normal Vibrated Concrete
SCC	Self Compact Concrete
GFRSCC	Glass Fiber Reinforced Self Compact Concrete
SP	SuperPlasticizer
PF	Packing Factor
W/B	Water/ Binder Ratio

HSC	High Strength Concrete
MPa	Mega Pascal
SF	Steel Fiber
GF	Glass Fiber
GFRPC	Glass Fiber Reinforced Polymer Concrete
PSD	Power Spectral Density
FEM	Finite Element Method
DLV	Damage Locating Vector
PFM	Proportional Flexibility Matrix
DOF	Degrees of Freedom
FRF	Frequency Response Function
APT	Accelerated Pavement Testing Track
PPD	Pigtailed Photo Diode
TIA	Trans Impedence Amplifier
SNR	Signal to Noise Ratio

List of Figures

List of Tables

ABSTRACT

Structural Health Monitoring (SHM) is a thrust area these days which includes assessing a structure's overall function through continuous monitoring. SHM aids in identifying the present condition of the structure or if structural damage exists, and then evaluating the type of maintenance required. Proper monitoring can help to minimize the number of catastrophic occurrences and, as a result, the economic and human psychology of the country. In structural health monitoring, data normalization is the process of separating variations in sensor readings caused by deterioration from those produced by changing operating and ambient circumstances. When selecting excitation techniques, sensor kinds, sensor number, and sensor position, as well as data acquisition storage or transmittal hardware, cost considerations are essential. Also, monitoring the conditions that affect each sensor or structure in a unique way.

The economy of every country relies on transportation infrastructure such as bridges, trains, and roadways. Failure of these facilities may have an impact on the nation's GDP. As a result, in order to enhance the architectural design, it is necessary to continually monitor these bridges using suitable health monitoring technologies. If damage is identified prior to the failure of the structure, suitable actions can be taken to prevent the structure from extensive damage or collapse.

The evaluation of bridge loads and its effects may be used to monitor the health of large bridges. Keeping an eye on the wind, weather, and traffic is typical. Every bridge structure has a limit to the amount of strain that may be applied to it. If this strain variation exceeds the limitations of the structure owing to factors such as increased loading, ageing of the structure, repeated traffic loads, changes in environmental conditions, and increased fatigue, the structure may be damaged. So it is important to accurately assess the strains developed in the bridges.

Conventional electro-mechanical sensors have been in use for many years for bridge monitoring, but they are expensive, large, and need a lot of electrical connections. Because of certain inherent advantages over other optical fiber methods, optical fiber sensors based on fiber Bragg gratings (FBG) have been widely utilized for strain sensing. Much research has been conducted on FBG-based strain sensors; nevertheless, there is still a need to develop sensors that gives high sensitivity and a wide range of strain measurement, possibly at a low cost.

In this thesis, Strain sensing in bridge structures using fiber Bragg grating sensors is presented in four phases.

In the first phase, Two FBG rosettes (Three elements) are fixed at two different longitudinal girders of a prototype bridge along the line of motion at different orientations (0^o, 45^o, and 90^o). Micron Optics Interrogator (SM130) is used to acquire the data corresponding to the wavelength shift of FBGs when a loaded vehicle moves over it. This temporal response of the FBG has been analyzed to evaluate the parameters of investigation like the strain developed in the proximity of FBG's and the speed of the vehicle.

In the second phase of the work, a low cost and real time load measurement system employing FBG as a strain sensor on a prototype bridge was developed. The sensor monitors the data and transfers the sensed data to a remote location via mobile application. A simple Pigtailed Photodiode (PPD) and Trans-Impedance Amplifier (TIA) were used in the background electronics. The changes in the optical power are converted to voltage. The voltages corresponding to varying loads is fed to an Arduino Uno and the same is transmitted via Bluetooth to a mobile for continuous monitoring of the load on the bridge beam from a remote location. This set-up was found to measure the loads applied on the structure accurately up to a simulated 3,000 g with an error of ±1.67% (+50 g), thus confirming the ability of the proposed system in the field applications.

In the third phase of the work, Digital Image Correlation (DIC) method and FBG contact sensor system is used for finding the displacement and strains developed on the surface of a modeled Accelerating Pavement Track (APT) for Structural Health Monitoring (SHM) applications. A random speckle pattern on the APT is used as a non-contact sensor for the DIC measurements, while, the FBGs are attached in the tension part of the track to measure the strain. It has been observed that though the strain sensitivity from the FBG measurements is high compared to DIC values, there is a good agreement between the normalized principal strain values obtained from both the methods.

In fourth phase of the work, An FBG based Weigh-In-Motion system is proposed for the study of health condition of damaged structures. Artificial damage is created in the simulated WIM bridge system, and the results are compared with those in the undamaged condition. The experiment was carried out for different loads and

for different magnitudes of damage at different distances from the FBG.

A study using accelerometers to sense the damage in concrete beams and to identify the damage based on frequency response experiments by creating damage and undertaking repair and measuring the response again is taken up. Damage was created in the laboratory cast specimens by cutting a portion of the specimen giving a saw cut and the influence of this damage was observed for charge in dynamic properties. It was found that there is a similarity in the results obtained between the theoretical and experimental investigations. In the third stage a numerical modeling of the beams was carried out based on ABAQUS and it was noticed after comparison that the response obtained from experimental, numerical and theoretical values of the dynamic properties were close.

CHAPTER-1
INTRODUCTION

1.1 Structural Health Monitoring

Structural Health Monitoring (SHM) has been an emerging area of research for the past few years due to the various reasons including aging infrastructure and requirements for rehabilitation among others [1]. SHM is the process of determining a structure's condition by assessing the structure's response to loading while taking the severity of the damage and its location into account [2]. The process of identifying damage is divided into four stages. The first stage involves occurrence of a damage in structure, the second stage involves determination of geometric location of damage, the third stage is the determining quantification of severity of the damage in the structure and the fourth stage includes the prediction the structure's remaining service life [3].

SHM is the process of developing a damage detection method for engineering structures. Components of a SHM process are Operational Evaluation, Data Acquisition, Fusion and Cleansing, Feature Extraction and Information Condensation, Statistical-Model Development for Feature Discrimination. Operational Evaluation deals with Economic and/or Life-Safety issues, Definition of Damage, Environmental and/or Operational Constraints, Data Management. Data Acquisition, Fusion, and Cleansing consider Sensing and collection issues: Extraction Methods-Forced Excitation, Ambient Excitation, and Local Excitation. Feature Extraction and Information Condensation contains parameters and methods like Resonant Frequencies, Frequency Response Functions, Mode Shapes, Mode Shape Curvatures, Modal Strain Energy, Dynamic Flexibility, Damping, Nonlinear Features and Time-Frequency Analysis [4].

A sensor and micro processing unit, a data transmission and collection system, and damage diagnosis techniques are all included in structural damage monitoring systems. Current advancements in wireless communication, micro-machined sensors, global positioning systems, and increasing processing power give the tools for potential new solutions to many of the problems that such systems bring. The sensor unit's data is sent to a data processor. Most sensors now give raw data that has not been processed at the structural site. Site master units are generally used as data collectors but are not always used as processors. The central monitoring facility is designed to receive and process damage data from all monitoring system structures [5,6].

1.2 Data Acquisition

The data collection component of the structural health monitoring process entails deciding on the types of sensors to be used, deciding where the sensors should be located, choosing the number of sensors to be used and specifying the data acquisition/storage/transmittal hardware. These decisions are heavily influenced by economic factors. Another factor to consider is that how frequently the data should be gathered. In certain situations, collecting data shortly before and at regular intervals following a severe occurrence is sufficient. If, on the other hand, fatigue crack development is the failure mode of concern, practical data must be collected continuously at relatively small time intervals [7].

1.3 Feature Selection

The feature selection method involves data extraction. Data extraction is desirable and necessary, especially if one expects comparisons of several data sets over the lifetime of the structure. Furthermore, since data can be collected from the structure over time and in the operating environment, effective data reduction algorithms should be sensitive to selected features for structural changes in the setting of environmental noise [8].

Statistical model design to enhance damage detection is part of a systematic health monitoring procedure that has received little attention in the technical literature. The characteristics chosen to identify faulty systems are statistically significant. However, there have been several published research for rotating equipment damage detection applications in which statistical models have been utilized to improve the damage detection process [9].

Every structure is built to last a specific amount of time, and it is thought that it will continue to serve its purpose throughout that time. Continuous observation and the appropriate maintenance of structure may help to improve the life of the structure and its performance. SHM assists in determining the current condition of the structure or if there is any structural damage, and then determining the type of maintenance. With careful management, it is possible to extend the life of the construction and therefore save money [2].

Most of the country's economy is dependent on transportation infrastructure such as bridges, railways, and roads. Any structural failure of this infrastructure will have a negative impact on the economy of the country. In terms of Indian scenario, many bridges in India have been rebuilt and are still in use. These bridges are now carrying heavier

loads. A sudden failure of any infrastructure could result in a catastrophic accident, resulting in a loss of serviceability or access. Failure of these infrastructures may affect the Gross Domestic Product of the nation. As a result, it is critical to constantly monitor these bridges using appropriate health monitoring methods in order to improve the architectural design. The use of proper SHM can reduce the number of catastrophic events and, as a result, the country's economy [10]. If damage is discovered before the structure fails, appropriate measures can be taken to prevent it from failing.

Assessment of various loads on the bridge and their consequences can be used to monitor the health of major bridges. It usually entails keeping an eye on the wind, weather, and corrosion apart from traffic. Traffic is an important factor to check the status of the bridge. Number of vehicles cross a particular bridge under a certain amount of time, the stresses and strains produced is important for evaluating the health of the bridge. Every bridge structure has a maximum limit or capability of withstanding strains. If this strain variation is increasing beyond the structure’s limit due to any of the reasons like increase in loading, aging of a structure, recurring traffic loads, change in environmental conditions, and increase in fatigue, then it may lead to damage of the structure. This deterioration affects the performance of bridge structure [11].

When it comes to the data gathering from various elements based on structural health monitoring, cost considerations become critical while choosing the excitation methods, sensor types, number of sensors, sensor position and as well as data acquisition/storage or transmittal hardware. Although data might be measured under a variety of situations, data normalization is crucial to the damaged identification process. In structural health monitoring, data normalization is the process of distinguishing variations in sensor readings caused by deterioration from those caused by changing operating and ambient circumstances. However, one has to keep in mind that the selection of sensors and placing the sensors at the right location is a challenge.

In Bridge weigh in motion systems, a number of sensors are to be used for monitoring the health condition of the bridges. Several maintenance and cost optimization strategies have been performed in recent years to keep the infrastructure in well performing condition. Most of the maintenance approach is based on traditional methods to detect the damages in bridge structures like visual observation and use of Non Destructive Testing (NDT) methods employing a wide variety of sensing elements/transducers and are briefly explained in the sections that follow.

1.4 Non Destructive Testing methods

1.4.1 Visual inspection

Visual inspection is a common method for determining the structural integrity of bridges. It is the most popular and oldest damage inspection approach used in bridge monitoring and is the most prevalent way for finding damage by unaided eye (without the use of microscopy) is very limited in scope. Microscopy can provide detailed information on alloy delamination and micro cracks in metallic elements, but only suitable in the laboratory. Large regions should be scanned quickly, with as little disruption to structural operation as possible and individual components should be removed. Recent advancements in this technology include various illumination techniques that enable greater inspection efficiency [12,13].

1.4.2 Ultrasonic inspection

The varied features of the ultrasonic waves propagating in the monitored structures provide the basis for ultrasonic inspection. Wave attenuation, reflection, scattering, wave mode conversion and a number of other physical processes are used in this assessment. Ultrasonic testing is a popular and powerful method for detecting internal flaws in fiber reinforced metals. When a change in sound impedance of the material occurs, the ultrasonic pulses that are transmitted into the sample via a probe with a piezoelectric crystal get reflected back from the structural discontinuity. There are several techniques to display this information with appropriate instrumentation with single point measurements, along single line measurements, and collection of single line forming a surface contour plot. The surface contour plots have become common practice in industry. Immersion testing, which involves mixing the transduced material with water, is a common approach. The probe can also be put on the sample with a viscous gel couplant between the probe and the sample for contact testing. Ultrasonic testing can detect minute cracks, flaws, gaps, or inclusions in aircraft components that could compromise mission performance. New ultrasonic technologies are improving the precision, speed, and cost effectiveness of this method's nondestructive testing. Surface contour tests are a very successful NDT tool for composite structures because they use sophisticated transducers to permit better data collecting and digital signal processing using several signal gates. In general, however, this approach is particularly sensitive to tiny surface and deep material flaws. Combining and scanning requirements have a number of drawbacks. Furthermore, for a surface contour, scanning duration is critical. However, the size and cost of the entire equipment and

inaccessibility due to various reasons are some of the limitations of this technology [14,15].

1.4.3 Strain gauge methods

Resistance strain gauges have been the most important tools in experimental stress analysis since 1940. They're used to detect material faults both inside and externally in a range of applications. Strain gauge method is one of the most employed approaches for monitoring damage in composite materials in a service truck. The strain is measured by the voltage delivered to the foil gauge as the resistor changes owing to deformation. Strain gauges provide extremely precise strain readings with easy-to-understand data. They are low-cost and lightweight. Strain gauges can detect time-history of overloads and deformities by monitoring local stress. They're usually installed on the surface in most applications. When it comes to gauge selection and protective coating, the strain gauge's physical surroundings is a critical factor to consider. Electrical resistance strain gauges are not frequently accepted for embedding in laminated composite materials due to their relatively high surface area and the need for protective coatings. The fundamental problem of this method is that a single gauge can only precisely cover a small part of the surface, requiring a large number of them to monitor the entire vehicle, resulting in a complex system with many wires. Gauges can only be placed on certain issue areas to avoid this situation [16–20]. The arrangement of gauges in the form of rosettes can help identify the principal stresses and strains in structural members.

There are other methods including vibration based methods using accelerometers, image correlation of undeformed and deformed images and fiber optic sensors (Fiber Bragg Grating sensors) used for detecting strain on the bridges as well as identifying damages.

1.4.4 Vibration based monitoring

The vibration response of a structure is affected by structural parameters such as mass, stiffness, and damping, according to vibration-based structural health monitoring [21]. Consequently, by evaluating changes in recorded structural vibration behavior and solving the inverse problem, undiscovered changes in structural characteristics can be found. Vibration-Based Damage Identification (VBDI) or Vibration-Based Damage Detection (VBDD) is a method of identifying changes in structural properties that have a negative impact on a structure's performance. When VBDI is combined with appropriate damage analysis technology, the determination of the impact of damage on structural response can be made. Feature extraction and damage detection are the two major

components of VBDI [22]. A structure's vibration response can be classified using a variety of parameters [23]. As an example, a direct characteristic can be derived from the acceleration time history recorded by accelerometers mounted on a structure during vibration. Natural frequency, damping, mode shape, and its derivatives are examples of structural modal parameters that can be used as a feature. In the construction of motion equations, the parameters of the response time history, system frequency response functions, and autoregressive moving average (ARMA) models are assigned to transfer functions and residual model forces, attraction-generated stability and magnitude state space, and so on can be employed in the characterization of the extent of damage in the structures. There has been a lot of effort put into identifying vibration- related properties that are sensitive to changes in structural qualities, as well as experimental methods to extract them. Comparing characteristics in two different states is a pretty straightforward procedure. It is a common practice to designate one of the structured states as the 'baseline' or 'undamaged' state and use it as a comparison point for all subsequent states. If data about several damage states is available, the change in the features can disclose information regarding the occurrence, location if the characteristic includes spatial information, such as mode shape and relative severity of the damage [24,25].

Thus, this technique of damage detection is based on changes in mass, stiffness, and damping matrix indices that have been correlated with observed dynamic characteristics of intact and damaged structures [26]. The comparison of matrix indices connected with modal characteristics from an undamaged structure to the original correlated matrix indices provides detection of damage, which may be utilized to measure the amount and extent of damage.

1.4.4.1 Natural frequency

Every physical structure has natural frequencies. A structure's natural frequency is the frequency at which it would oscillate if it were disturbed from rest and then permitted to freely vibrate. It is mass and stiffness dependent, decreasing as mass increases for a given stiffness and increasing as stiffness increases [27].

The applied force or base excitation frequency corresponds with a structural natural frequency, resulting in resonance. The response displacement may grow during resonant vibration until the structure undergoes buckling, yielding, fatigue, or another failure mechanism.

1.4.4.2 Resonance

Resonance is a phenomenon that happens when the driving frequency aligns with the system's natural frequency. In this state, the system provides no resistance to the force, resulting in infinite displacement of the system. In fact, the system does not vibrate infinitely but is restricted by the damping inherent in the system [28].

1.4.4.3 Mode shapes

A vibrating structure's intrinsic characteristics are modes. A natural frequency, modal damping, and mode shape characterize each mode. Modes are used to characterize resonant vibration in a quick and easy way. The vast majority of structures are capable of resonating. A vibrating structure naturally deforms into specific patterns at the structure's inherent frequencies. The deformation patterns and their natural frequency are determined only by the structure's properties, not by the input forces. These deformation patterns correspond to the structure's mode forms [24].

1.4.4.4 Damping

Damping is a characteristic of any mechanical system that transfers vibration energy to heat energy. Damping can be caused by a variety of reasons. Damping is considered to be viscous in classic analytical vibration analysis, even if it is not in reality. In a vibratory system, damping force is proportional to vibration velocity [29].

The damping ratio for the flexural beam vibration caused by an impact was calculated using standard logarithmic decrement experiments. The values of acceleration amplitude recorded with an accelerometer might be utilised to compute logarithmic decrement using the Eq. (1.1)[30].

$$\zeta = \frac{1}{2\pi n} \ln \frac{A_0}{A_n} \qquad Eq.(1.1)$$

Where A_0 is an initial amplitude and A_n is an amplitude after n cycles.

1.4.4.5 Half power Bandwidth

The half-power bandwidth technique was initially created in the field of mechanical and structural dynamics to calculate a structure's modal damping ratio ς from the width of its frequency response function peaks. The breadth of the peak when the magnitude of the frequency response function $\frac{1}{\sqrt{2}}$ times the peak value is known as the half-power bandwidth. For a weakly damped single degree of freedom system, the damping ratio ς is then obtained from Eq. (1.2) [30].

$$\zeta = \frac{\omega_b - \omega_a}{2\omega n} = \frac{f_b - f_a}{2\,fn} \qquad Eq.(1.2)$$

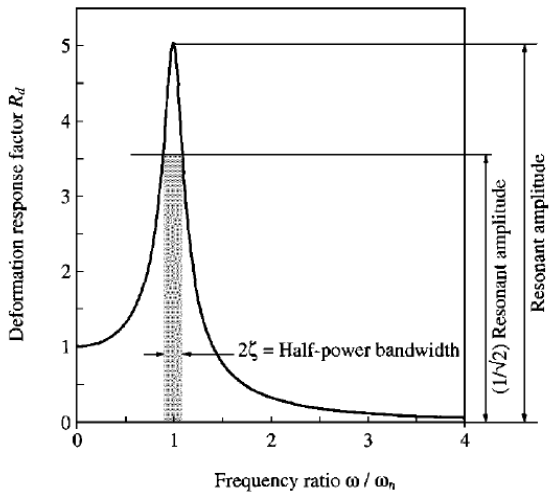

Fig. 1.1 Half power Bandwidth

This important result enables us to evaluate the damping ratio in forced vibration tests without knowing the applied force.

1.4.4.6 Free vibration

Free vibrations are due to momentary excitation (application of force) to a system, which in turn sets the system in to vibration. This is called free because after the instance of excitation, the force levels are zero but vibration persists.

When considering free vibration, the structure is not exposed to any external excitation (force or support motion) and its motion is regulated only by the starting circumstances. The study of the structure in free motion reveals the most essential dynamic characteristics of the structure, which are the natural frequencies and related modal shapes. For free vibration, the frequency of oscillation (which is 1/Time Period) is determined by stiffness (k) and mass (m) and may be calculated using Eq. (1.3) [31].

$$\omega_n = \sqrt{\frac{k}{m}} Radians/\sec \; or \; f_n = \frac{1}{2\pi}\sqrt{\frac{k}{m}} Hertz\,(Hz) \qquad Eq.(1.3)$$

Natural frequency is dependent of spring stiffness and mass. Natural frequency reduces if mass increases for a given stiffness and increases if stiffness increases for a given mass. In reality it is not possible to vary mass or stiffness alone.

In above case we have assumed that there is no damping in the system. But in reality material will have damping property. Resonant frequency decreases if damping is also taken into consideration.

1.4.5 Image correlation

Digital Image Correlation (DIC) Technique is a non-contact based non-destructive evaluation technique for condition monitoring of bridges, dams, nuclear containment structures, defense and aerospace structures. DIC technology is an adaptable tool for surface distortion measurement in experimental solid mechanics. This method involves the correlation of digital images of a random speckle pattern associated with an object before and after deformation [32,33]. The pattern must be random, isotropic and highly contrasting in order to establish an effective correlation. In addition to this, speckles should neither be too small nor too large. A consistent speckle size has to be maintained and this is ideally 3-5 pixels. Correlation may fail with extremely large or small speckle pattern and strain resolution increases with increase in speckle density [34,35]. The pattern must be either bright white dots on a dark black background or dark black dots on a bright white background.

In order to assist a non-contact strain measurement system, an open source DIC software "Ncorr V1.2.2" [36] is being widely used as a tool to visualize deformation history from the initial unloading stage to failure. This method makes it very easy to set up a cost-effective simple optical digital camera, such as a digital single-lens reflex camera (DSLR) or a smartphone camera for capturing the images for analysis [37]. Several researchers have used DSLR camera for DIC measurement and the results have shown that DIC is an effective method for strain measurement with high accuracy at low cost [34,38–41].

1.4.6 Fiber optic sensors

Optical fiber based sensors are of recent origin which can be employed to detect structural problems in bridges and dams [42]. This is an emerging field of sensor technology and a lot of work need to be done. Fiber sensors have the advantage that they are continuously distributed along the whole length of the fiber, so that they cover large area of structure and are also very sensitive to temperature and strain change. Recent researches in this area has led to the development of a structural health monitoring system consisting of 1 million sensing points which can sense the structural change very fast than any other technology present [43,44]. Sensors placed at several locations can be avoided

by a single fiber placed along the length of the fiber with million sensing points to identify any issues in the structural elements [45]. The concept involves light travelling across the optical fiber. Optical fiber can withstand bad weather and corrosion. These fiber sensors can be used in remote areas. The data acquisition time can be reduced by increasing the sensor intensity, so that monitoring can be done precisely. Optical fibers are used for measuring strains, stresses and temperature because of its advantage compared to the other sensors. These factors are crucial in SHM.

Fiber Bragg grating (FBG) and Long Period Grating (LPG) are good sensors for the measurement of parameters like strains and stresses and temperature changes [46–49]. Wireless sensors have the advantage of collecting information based on data acquisition system where data is processed and to monitor the health of the structure. Data can be collected periodically or continuously, and once the critical stage is reached, structure cannot be taken to its initial strength. The passes of the vehicle on the bridge produces stresses and strains on the bridge and when data is collected using data acquisitions system involving various sensors. The stresses and strains on the bridge can be monitored.

Summary

This chapter briefly explained the introduction about the Structural Health Monitoring (SHM) and Nondestructive damage detection methods and also introduced latest methods like Vibration based monitoring, Digital Image correlation and Fiber optic sensing methods.

A detailed explanation about the fiber Bragg grating sensors and their applications is done in the Chapter-2, literature review and motivation and thesis organization are explained.

References

[1] J.M.W. Brownjohn, Structural health monitoring of civil infrastructure, Philos. Trans. R. Soc. A Math. Phys. Eng. Sci. (2007) 589–622. https://doi.org/10.1098/rsta.2006.1925.

[2] P. Cawley, Structural health monitoring : Closing the gap between research and industrial deployment, Struct. Heal. Monit. 17 (2018) 1225–1244. https://doi.org/10.1177/1475921717750047.

[3] S.J. Patil, R.B. Satpute, S.S. Magdum, C. Engineering, D.Y.P. College, Need of Structural Health Monitoring, Int. Res. J. Eng. Technol. 07 (2020) 3812–3814.

[4] G. Lu, Y.J. Yang, Structural health monitoring- An Overview, in: Struct. Heal. Monit. with Appl. to Offshore Struct., 2017: pp. 1–50. https://doi.org/10.1002/9781119173601.ch40.

[5] Raksha M, D. Neethu, a Review on-Structural Health Monitoring and Image Processing, Int. J. Sci. Res. Eng. Dev. X (2018) 1–7. www.ijsred.com.

[6] H. Sohn, C.R. Farrar, F. Hemez, J. Czarnecki, A Review of Structural Health Monitoring Literature 1996 – 2001, 2004th ed., United States of America, 2001.

[7] R.A. Swartz, A. Zimmerman, J.P. Lynch, Structural health monitoring system with the latest information technologies, in: Proc. 5th Infrastruct. Environ. Manag. Symp. Yamaguchi, Japan, 2007: pp. 1–28.

[8] F. Ansari, Sensing Issues in Civil Structural Health Monitoring, Springer Netherlands, Chicago, USA, 2005.

[9] C.R. Farrar, T.A. Duffey, S.W. Doebling, D.A. Nix, A Statistical Pattern Recognition Paradigm for Vibration-Based Structural Health Monitoring Charles R. Farrar, Thomas A. Duffey, Scott W. Doebling, David A. Nix, in: 2nd Int. Work. Struct. Heal. Monit. Stanford,CA, CA,USA, n.d.

[10] A. Dangra, The Missing Piece in India ' s Economic Growth Story : Robust Infrastructure, (2016) 1–12. https://www.spglobal.com/en/research-insights/articles/the-missing-piece-in-indias-economic-growth-story-robust-infrastructure.

[11] J. Mao, H. Wang, Y. Xu, H. Li, Deformation monitoring and analysis of a long-span cable-stayed bridge during strong typhoons, Adv. Bridg. Eng. 1 (2020) 1–19. https://doi.org/10.1186/s43251-020-00008-5.

[12] L. Quirk, J. Matos, J. Murphy, V. Pakrashi, Visual inspection and bridge

management, Struct. Infrastruct. Eng. 14 (2018) 320–332. https://doi.org/10.1080/15732479.2017.1352000.

[13] D. Tenžera, G. Puž, J. Radiæ, Visual inspection in evaluation of bridge condition, Gradjevinar. 64 (2012) 717–726. https://doi.org/10.14256/jce.718.2012.

[14] B.A. Graybeal, R.A. Walther, G.A. Washer, Ultrasonic inspection of bridge hanger pins, Transp. Res. Rec. (2000) 19–23. https://doi.org/10.3141/1697-04.

[15] K.A. Tiwari, R. Raisutis, Comparative Analysis of Non-Contact Ultrasonic Methods for Defect Estimation of Composites in Remote Areas, CBU Int. Conf. Proc. 4 (2016) 846–851. https://doi.org/10.12955/cbup.v4.863.

[16] A.G. Piersol, Thomas L. Paez, Harri's Shock and Viration Handbook, 6th ed., Mc.Graw hill Company Inc., United States, 2002.

[17] E. Cheilakou, N. Tsopelas, A. Anastasopoulos, D. Kourousis, D. Rychkov, R. Gerhard, B. Frankenstein, A. Amditis, Y. Damigos, C. Bouklas, Strain monitoring system for steel and concrete structures, Procedia Struct. Integr. 10 (2018) 25–32. https://doi.org/10.1016/j.prostr.2018.09.005.

[18] S. Laflamme, M. Kollosche, V.D. Kollipara, H.S. Saleem, G. Kofod, Large-scale surface strain gauge for health monitoring of civil structures, Nondestruct. Charact. Compos. Mater. Aerosp. Eng. Civ. Infrastructure, Homel. Secur. 2012. 8347 (2012) 83471P. https://doi.org/10.1117/12.913187.

[19] J.B. Begueret, M.R. Benbrahim, Z. Li, F. Rodes, J.P. Dom, Converters dedicated to long-term monitoring of strain gauge transducers, IEEE J. Solid-State Circuits. 32 (1997) 349–355. https://doi.org/10.1109/4.557633.

[20] J. dos Reis, C. Oliveira Costa, J. Sá da Costa, Strain gauges debonding fault detection for structural health monitoring, Struct. Control Heal. Monit. 25 (2018) 1–14. https://doi.org/10.1002/stc.2264.

[21] F. Magalhães, A. Cunha, E. Caetano, Vibration based structural health monitoring of an arch bridge: From automated OMA to damage detection, Mech. Syst. Signal Process. 28 (2012) 212–228. https://doi.org/10.1016/j.ymssp.2011.06.011.

[22] J.M.W. Brownjohn, A. de Stefano, Y.L. Xu, H. Wenzel, A.E. Aktan, Vibration-based monitoring of civil infrastructure: Challenges and successes, J. Civ. Struct. Heal. Monit. 1 (2011) 79–95. https://doi.org/10.1007/s13349-011-0009-5.

[23] A. Zarafshan, A. Iranmanesh, F. Ansari, Vibration-Based Method and Sensor for Monitoring of Bridge Scour, J. Bridg. Eng. 17 (2012) 829–838. https://doi.org/10.1061/(asce)be.1943-5592.0000362.

[24] W. Fan, P. Qiao, Vibration-based Damage Identification Methods: A Review and Comparative Study, Struct. Heal. Monit. 10 (2011) 83–111. https://doi.org/10.1177/1475921710365419.

[25] S.W. Doebling, C.R. Farrar, M.B. Prime, A summary review of vibration-based damage identification methods, Shock Vib. Dig. 30 (1998) 91–105. https://doi.org/10.1177/058310249803000201.

[26] C.R. Farrar, S.W. Doebling, D.A. Nix, Vibration-based structural damage identification, Philos. Trans. R. Soc. A Math. Phys. Eng. Sci. 359 (2001) 131–149. https://doi.org/10.1098/rsta.2000.0717.

[27] L.J. Prendergast, D. Hester, K. Gavin, J.J. O'Sullivan, An investigation of the changes in the natural frequency of a pile affected by scour, J. Sound Vib. 332 (2013) 6685–6702. https://doi.org/10.1016/j.jsv.2013.08.020.

[28] W.H. Hu, S. Thöns, R.G. Rohrmann, S. Said, W. Rücker, Vibration-based structural health monitoring of a wind turbine system. Part I: Resonance phenomenon, Eng. Struct. 89 (2015) 260–272. https://doi.org/10.1016/j.engstruct.2014.12.034.

[29] M. Cesnik, J. Slavic, M. Boltezar, Uninterrupted and accelerated vibrational fatigue testing with simultaneous monitoring of the natural frequency and damping, J. Sound Vib. 331 (2012) 5370–5382. https://doi.org/10.1016/j.jsv.2012.06.022.

[30] G. Gutenbrunner, K. Savov, H. Wenzel, Sensitivity Studies on Damping Estimation, Proc. Second Int. Conf. Exp. Vib. Anal. Civ. Eng. Struct. (2007). http://www.vce.at/pdf/downloads/Publications/Damping Estimation.pdf.

[31] W.B. Rowe, Vibration Problem-Solving in Grinding, Princ. Mod. Grind. Technol. (2014) 241–262. https://doi.org/10.1016/b978-0-323-24271-4.00012-9.

[32] M.A. Sutton, J. Orteu, H.W. Schreier, Image Correlation for Shape, Motion and Deformation Measurements: Basic concepts, Theory and applications, Springer Science, New york, USA, 2009. https://doi.org/10.1007/978-0-387-78747-3.

[33] B. Murali Krishna, T.P. Tezeswi, P. Rathish Kumar, K. Gopikrishna, M.V.N. Sivakumar, M. Shashi, QR code as speckle pattern for reinforced concrete beams using digital image correlation, Struct. Monit. Maint. 6 (2019) 67–84. https://doi.org/10.12989/smm.2019.6.1.067.

[34] A.H. Salmanpour, N. Mojsilovi, Application of Digital Image Correlation for strain measurements of large masonry walls, in: APCOM ISCM, Singapore, 2013: pp. 1–7.

[35] D. Lecompte, A. Smits, S. Bossuyt, H. Sol, J. Vantomme, D. Van Hemelrijck, A.M.

Habraken, Quality assessment of speckle patterns for digital image correlation, 44 (2006) 1132–1145. https://doi.org/10.1016/j.optlaseng.2005.10.004.

[36] J. Blaber, B. Adair, A. Antoniou, Ncorr : Open-Source 2D Digital Image Correlation Matlab Software, (2015) 1105–1122. https://doi.org/10.1007/s11340-015-0009-1.

[37] B. Suryanto, A. Tambusay, P. Suprobo, Crack Mapping on Shear-critical Reinforced Concrete Beams using an Open Source Digital Image Correlation Software, (2017). https://doi.org/10.9744/ced.19.2.93-98.

[38] B. Pan, K. Qian, H. Xie, A. Asundi, Two-dimensional digital image correlation for in-plane displacement and strain measurement : a review, 062001 (2009). https://doi.org/10.1088/0957-0233/20/6/062001.

[39] N.A. Hoult, W.A. Take, C. Lee, M. Dutton, Experimental accuracy of two dimensional strain measurements using Digital Image Correlation, Eng. Struct. 46 (2013) 718–726. https://doi.org/10.1016/j.engstruct.2012.08.018.

[40] T.M. Fayyad, J.M. Lees, Application of Digital Image Correlation to reinforced concrete fracture, Procedia Mater. Sci. 3 (2014) 1585–1590. https://doi.org/10.1016/j.mspro.2014.06.256.

[41] A. Kumar, S. Vishnuvardhan, A.R. Murthy, G. Raghava, Tensile and fracture characterization using a simplified digital image correlation test set - up, 4 (2019) 467–477.

[42] J.R. Casas, P.J.S. Cruz, M. Asce, Fiber Optic Sensors for Bridge Monitoring, J. Bridg. Eng. 8 (2003) 362–373. https://doi.org/10.1061/(asce)1084-0702(2003)8:6(362).

[43] D. Betz, Application of Optical Fibre Sensors for Structural Health and Usage Monitoring, University of Sheffield, 2004.

[44] P. Aikaterini, Methodology for innovative health monitoring of aerospace structures using dynamic response measurements and advanced signal processing techniques, University of Patras, 2012. http://nemertes.lis.upatras.gr/jspui/handle/10889/5436.

[45] C.K.Y. Leung, Fiber optic sensors in concrete: the future?, NDT&E Int. 34 (2001) 85–94.

[46] D. Li, Strain transferring analysis of fiber Bragg grating sensors, Opt. Eng. 45 (2006) 024402. https://doi.org/10.1117/1.2173659.

[47] P. Moyo, J.M.W. Brownjohn, R. Suresh, S.C. Tjin, Development of fiber Bragg grating sensors for monitoring civil infrastructure, Eng. Struct. 27 (2005) 1828–

1834. https://doi.org/10.1016/j.engstruct.2005.04.023.

[48] M. Kreuzer, Strain Measurement with Fiber Bragg Grating Sensors, HBM, Darmstadt, S2338-1.0 E,. (2006) 1–9. http://micronoptics.ru/uploads/library/documents/FBGS_StrainMeasurement_mo.pdf (accessed September 4, 2021).

[49] G. Durana, J. Gómez, G. Aldabaldetreku, J. Zubia, A. Montero, I.S. De Ocáriz, Assessment of an LPG mPOF for strain sensing, IEEE Sens. J. 12 (2012) 2668–2673. https://doi.org/10.1109/JSEN.2012.2199105.

CHAPTER-2
LITERATURE REVIEW

This chapter presents a brief outline on fiber Bragg grating sensors, different techniques used to draw fiber Bragg gratings in the core of an optical fiber. It also includes a brief overview of long period gratings and their fabrication methods. The effect of temperature and strain on fiber Bragg gratings and long period gratings together with simultaneous measurement of measurands and discrimination has also been discussed.

2.1 Fiber Bragg grating sensors-Principle

A Bragg grating is a periodic arrangement of the refractive index in an optical fiber. When there is a change in the refractive index, a fraction of the light gets reflected from the perturbed region. Once the mode coupling becomes stronger, the reflected portion of the light combines to form a large reflected wave at a specific wavelength which is referred as Bragg wavelength (λ_B) or central wavelength. The phenomenon is known as the Bragg condition or Bragg reflection condition. The Bragg grating is essentially transparent for all the wavelengths other than Bragg wavelength [1].

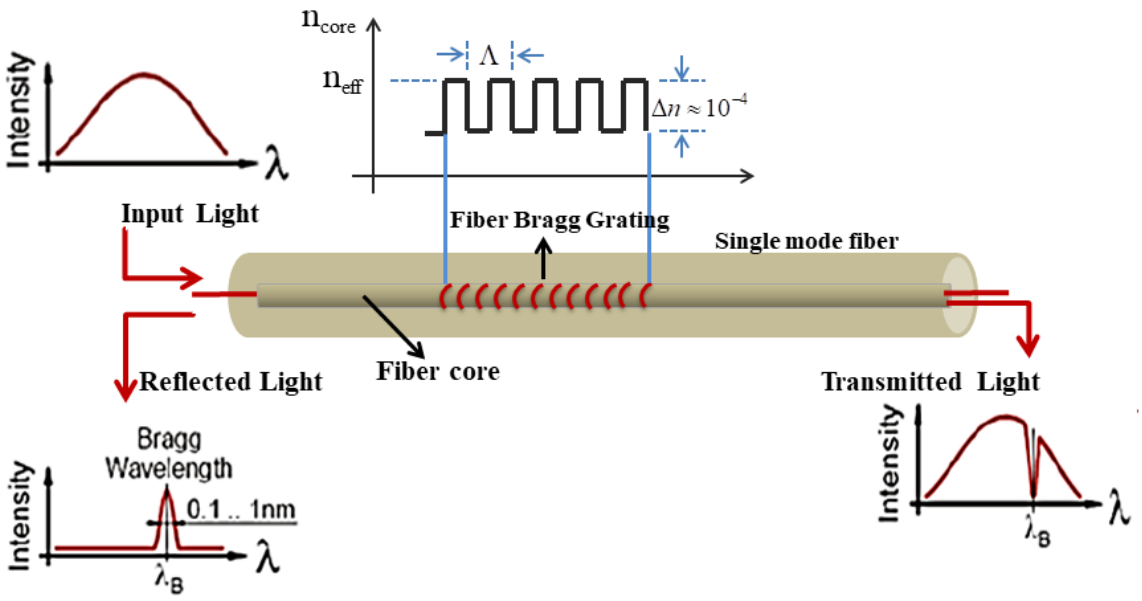

Fig. 2.1 Structure of fiber Bragg grating

The Bragg condition is an essential form that both energy and momentum conservation are satisfied. The incident frequency must match with reflected radiation's frequency in order to observe the energy conservation. To observe the momentum conservation, the sum of grating vector K, and incident wave vector k_i must be equal to the scattered radiation wave vector k_f as shown in Eq. (2.1).

$$k_i + K = k_f \qquad Eq.\ (2.1)$$

Where the grating wave vector, K, has a magnitude and a direction normal to the grating planes, and the diffracted wave vector is equal in magnitude but opposite in direction to the incident wave vector. As a result, the momentum conservation condition is as shown in Eq. (2.2) [2].

$$2\left(\frac{2\pi n}{\lambda_B}\right) = \frac{2\pi}{\Lambda} \qquad Eq.(2.2)$$

This Eq. (2.2) reduces to the first order Bragg condition as shown in Eq. (2.3).

$$\lambda_B = 2n_{eff}\Lambda \qquad Eq.\ (2.3)$$

Where the Bragg wavelength "λ_B" is the free-space central wavelength of the launched radiation that needs to be reflected from the grating, "n_{eff}" is the fiber core's effective refractive index at the free-space-center wavelength, and "Λ" is the grating period.

2.2 Fabrication of fiber Bragg gratings

Exposure to ultra violet (UV) light can cause refractive index modulation in an optical fiber. The UV sensitivity of standard optical fiber is very low, but it can be significantly increased by adding different dopants such as germanium, fluorine, and boron during the fabrication process, as well as by post processing techniques such as hydrogen loading. Depths of refractive index modulation order $\Delta n \approx 10^{-2}$ can thus be attained. Some of the most common methods for fabricating FBGs are described below.

2.2.1 Point-by-Point Technique

In this method, the refractive index variations along the core are introduced as one step at a time. All the planes of the grating are generated independently by a single focused and intensive excimer laser [3]. In this process, the UV pulse enters through a

pin-hole slit and is focused onto the core of the fiber using an imaging lens as shown in Fig. 2.2.

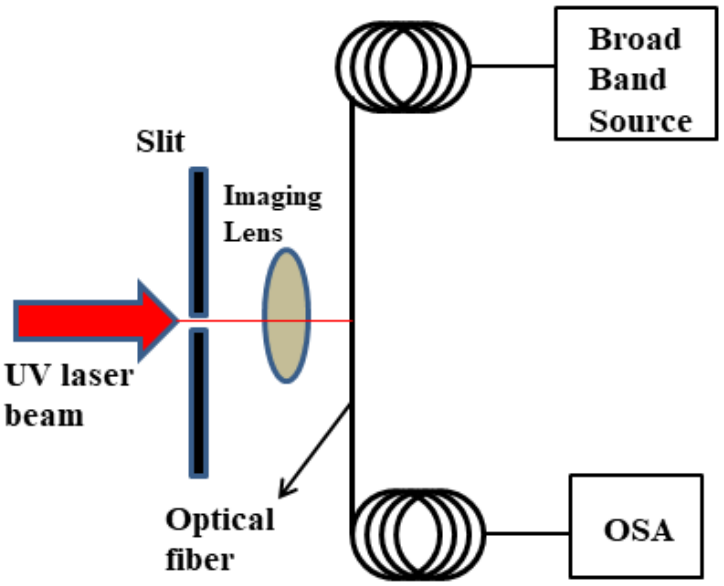

Fig. 2.2 Fabrication of the FBG by point-to-point technique

In this method, as a result of the irradiation process, the refractive index changes locally. Once a step is created, the fiber is then moved by a distance equal to the desired grating pitch Λ . The procedure is reiterated until the desired grating length is achieved in the core. The index profile can be tailored to any desired apodisation and chirp by varying the UV pulse energy and the amount of translation Λ can be varied between points of induced refractive index change using precision translating stages. This technique is not suitable for first-order grating due to the submicron translation and stringent focusing requirements.

2.2.2 Holographic method

This method of producing FBGs is based on the introduction of a periodic modulation of the refractive index in the core of the fiber. This is made feasible by the nonlinear phenomenon known as photosensitivity, which occurs in germanium doped optical fibers and was originally discovered in Hill gratings [4]. This novel approach created FBGs with limited applications since the FBGs could only operate at the wavelength of the laser used to create them. This new method produced FBGs of restricted use, as the FBGs were limited to operation at the wavelength of the laser used to fabricate them.

Meltz, et. al [3], developed a side exposure holographic method in which the optical fiber is side exposed to a spatially structured illumination pattern generated by two interfering UV laser beams at about 240 nm, which spurred current interest in FBGs. The photosensitivity is determined by the absorption peak of the fiber, which is centred at 220 nm and is induced by Germania-related defects. At these wavelengths, the refractive index change is a single photon process, making this method more efficient.

The geometry of the interfering beams determines the Bragg wavelength of FBGs created using this approach, allowing for flexibility in the FBG's properties and the production of a wide variety of Bragg wavelengths. This method enables the creation of FBGs with properties appropriate for telecom and sensor applications. The interferometric setup for the side exposure approach is depicted in Fig.2.3.

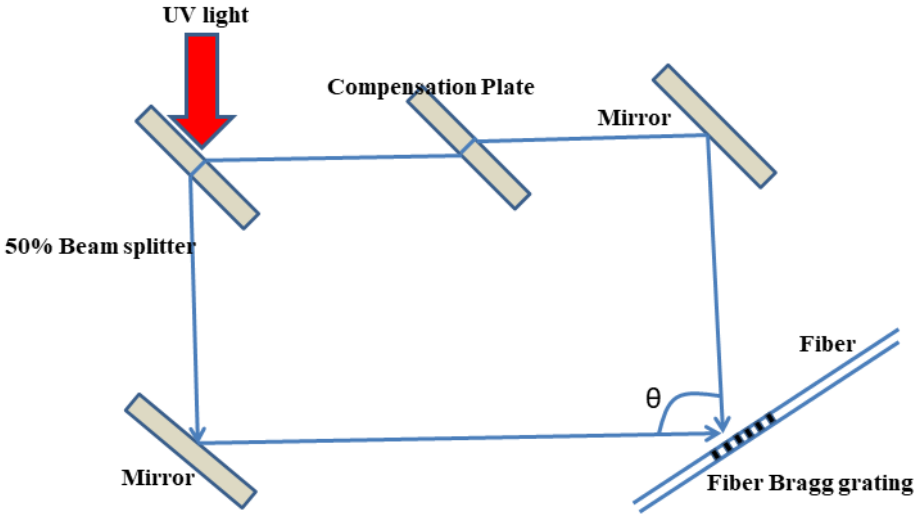

Fig. 2.3 Two beam transverse interferometer

The UV beam is divided into two beams of equal intensity at the 50/50 beam splitter as shown in Fig. 2.3. Using mirrors, the two beams are brought together to cause interference at the fiber's position, enabling control over the mutual angle of the intercepting beams. The Bragg wavelength of the FBG formed by side exposure is given by Eq. (2.4) [4].

$$\lambda_{Bragg} = \frac{n_{eff}\lambda_{uv}}{n_{uv}\sin\left(\frac{\theta}{2}\right)} \qquad Eq.(2.4)$$

Where "λ_{Bragg}" is the Bragg wavelength, "n_{eff}" is the effective refractive index of the fiber, "n_{uv}" is the refractive index of the silica when exposed to the UV light at "λ_{uv}" and "θ" is the mutual angle as seen in the Fig.2.3. Variation of "θ", or of the writing "λ_{uv}", allows a wide range of Bragg wavelengths to be written. The interference pattern created by the two beams intersection deposits a regular pattern of index modulation into the optical fiber. The path difference between the two beams must be matched to produce a high visibility fringe pattern with a low coherence UV source. Vibration and temperature variations that occur during fiber exposure, which may be as high as $\pm$1°C, may also impact the path length difference and, as a result, decreases the interfererogram's quality. This effect will be minimized by using a writing light source with a short exposure period like Femtosecond Laser.

Precision fiber placement is critical when writing FBGs to avoid the formation of slanted FBGs that can link light into other modes. While the holographic side exposure method, by changing the mutual angle between the converging beams, may create Bragg wavelengths of any value, the phase mask-based method is more commonly used.

2.2.3 Phase mask technique

This method is one of the most successful ways for inscribing gratings in the core of a light sensitive optical fibers [5,6]. Initially lithography methods are used to create phase masks. The phase mask itself is a grating engraved on a silica substrate with an etching depth sufficient to diffract the majority of the light in the +1 and -1 orders [7,8]. The interference pattern is generated by these diffraction orders. The diffraction is reduced to minimum or even to zero-order by adjusting the depth of the phase mask's corrugations. In reality, the quantity of light in the zero order may be decreased to less than 5%, with around 40% of total light intensity is distributed evenly between the +1st and -1st orders.

As illustrated in Fig. 2.4, the fiber is positioned exactly behind the phase mask and is exposed to either a beam with a width equal to the desired grating length or a smaller beam that is moved back and forth along the mask. The latter technique is preferable because it separates the grating form from the beam shape or width and allows the grating strength to be adjusted at will along the grating to produce a specific profile. If the phase mask grating has a period of 'Λ_{mask}', the UV induced grating has a

period of '$\frac{\Lambda_{mask}}{2}$'. This period is unaffected by the UV source that is illuminating the fiber [9].

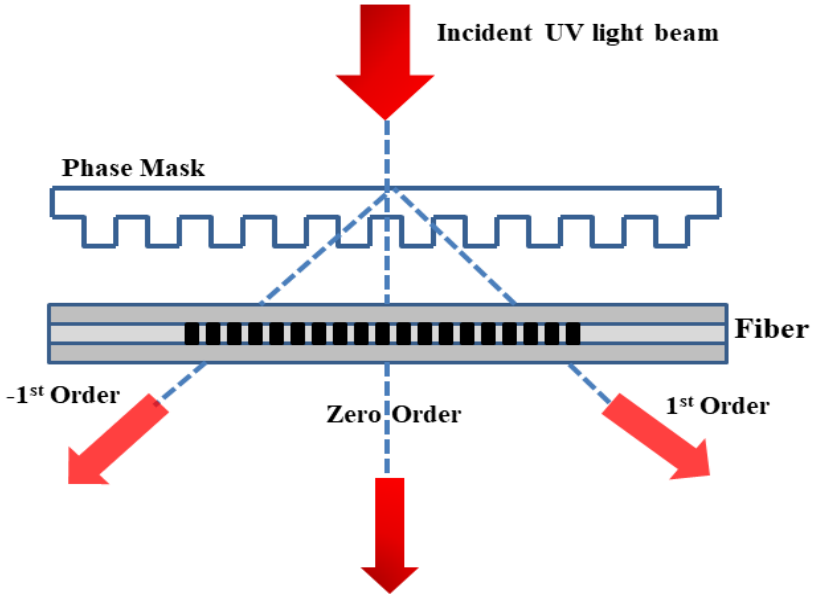

Fig. 2.4 Illustration of the fabrication of FBGs using a phase mask

Advantages of the method:

The technique is similar to the preceding methods in that it allows for better fiber alignment for photo imprinting, with lower photo imprinting apparatus stability requirements, and lower UV-laser source power and coherence requirements. The fiber grating manufacturing system is considerably simplified owing to the phase mask. Robust and inherently stable gratings are produced in this method as only one optical element is present in the replication of the grating. The impact of mechanical vibrations and hence the stability issues are decreased since the fiber is generally positioned right below the mask in the diffracting near field UV beams. Due to the geometry of the problem, low temporal coherence has no effect on the drawing capabilities which are present mostly in the interferometry based methods.

Drawbacks of the method:

Though the method is simple, the method can be implemented at the expense of flexibility. For drawing gratings of different pitch, and Bragg wavelength, a separate phase mask is required. However, employing lenses and stretching the fiber before exposure, it is possible to alter the grating's period as illustrated in Fig. 2.5 (a).

The phase mask can be utilized similarly to a beam splitter. The usage of phase mask in this manner facilitates the manufacturing system's alignment. The Bragg wavelength in Fig. 2.5 (a) can be changed by tuning the mutual angle or changing the UV writing wavelength, but the prism in Fig. 2.5 (b) can only be changed by changing the UV writing wavelength.

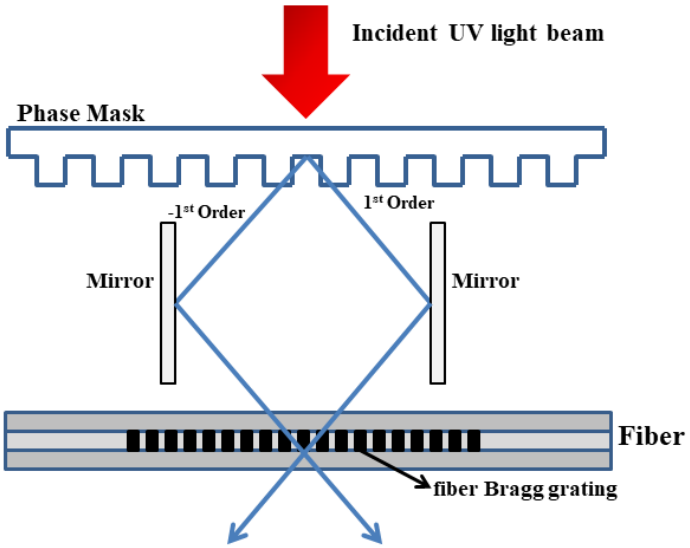

(a)

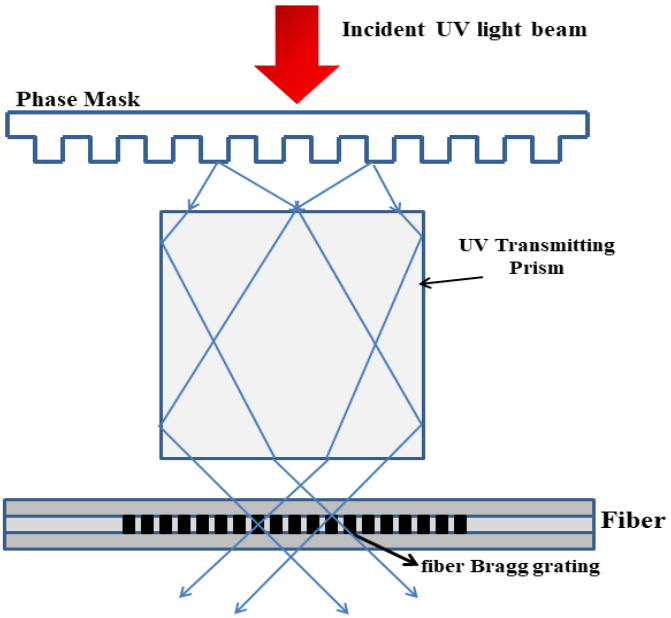

(b)

Fig. 2.5 Holographic writing techniques using a phase mask as a beam splitter (a) Using Mirror and (b) Using a prism to vary the angle between the two interfacing beams

2.3 Sensing Principle

FBG sensors have been used to detect strain, temperature, pressure, dynamic magnetic field, current, and many other physical parameters. The center wavelength of FBG will get shifted when these parameters bring a change in the fiber.

2.3.1 Effect of strain and temperature on fiber Bragg gratings

A variety of measurements, including acceleration, strain, temperature, pressure, and force, can be made using mechanical-sensitive conversion devices using FBGs. As the Bragg wavelength shift is sensitive to both temperature and strain, in practical applications the corresponding relative shift of wavelength can be written as shown in Eq. (2.5) [2,3,10–15].

$$\Delta\lambda_B = 2\left(\Lambda\frac{\partial n_{eff}}{\partial l} + n_{eff}\frac{\partial\Lambda}{\partial l}\right)\Delta l + 2\left(\Lambda\frac{\partial n_{eff}}{\partial T} + n_{eff}\frac{\partial\Lambda}{\partial T}\right)\Delta T \qquad Eq.(2.5)$$

The strain impact on an optical fiber is represented by the first term in the above equation. The period of grating and the strain-optic induced refractive index will be affected by a change in grating length generated by a strain on the fiber. This indicates that the shift in resonant wavelength caused by these effects is attributable to either a shift in effective refractive index or a shift in grating period or both. The strain effect term could also be expressed by Eq. (2.6).

$$\Delta\lambda_{B(s)} = \lambda_B(1-p_e)\varepsilon_z \qquad Eq.(2.6)$$

Where "ε_z" is the applied strain on the fiber grating along the longitudinal axis, and "p_e" is an effective strain optic constant defined by Eq. (2.7).

$$p_e = \frac{n_{eff}^2}{2}\left[p_{12} - \nu(p_{11}+p_{12})\right] \qquad Eq.(2.7)$$

Where "p_{11}" and "p_{12}" are components of the strain-optic tensor, "n_{eff}" is the index of core, and "ν" is Poisson's ratio. For a typical optical fiber these parameters take values as $p_{11}=0.113$, $p_{12}=0.252$, $\nu=0.16$, $n_{eff}=0.482$.

2.3.2 Temperature sensitivity

The impact of temperature on an optical fiber is represented by the second component in Eq. (2.5). Due to thermal expansion, the period of the grating and the

refractive index varies. The central wavelength of the fiber Bragg grating shifts accordingly. For a temperature change (T), this fractional wavelength shift might be expressed as shown in Eq. (2.8).

$$\Delta\lambda_{B(t)} = \lambda_B(\alpha + \zeta)\Delta T \qquad Eq.(2.8)$$

Where $\alpha = \left(\frac{1}{\Lambda}\right)\left(\frac{\partial\Lambda}{\partial T}\right)$ is the coefficient of thermal expansion of the fiber material (approximately 0.55×10^{-6} for silica) and $\zeta = \left(\frac{1}{n_{eff}}\right)\left(\frac{\partial n_{eff}}{\partial T}\right)$, represents the thermo-optic coefficient and is 8.6×10^{-6} for the Germania-doped silica core fiber.

2.4 Simultaneous Measurement of Strain and Temperature and Discrimination

The reflected wavelength of a fiber Bragg grating is sensitive to both temperature and strain [16]. Therefore, it almost results inaccurately sensed data of the measurands based on single Bragg wavelength shift. And it is nearly impossible to distinguish simultaneously the effects of strain and temperature variations. A few methods are discussed below to differentiate strain and temperature in simultaneous measurements using FBG sensors.

2.4.1 Reference FBG method

Separating the temperature impact from a reference FBG is a straightforward approach [14]. The simplest method is to utilize an identical, isolated, strain-free FBG as the temperature sensor to directly measure the temperature of the strain sensor. The strain sensor and the reference FBG are both placed in the same temperature environment. The temperature-induced strain error can be corrected to first order by subtracting the temperature-induced wavelength shift from the overall wavelength shift recorded with the strain sensor. The simplicity of the construction and the inexpensive cost of the sensor probe are the advantages of this technique [17].

2.4.2 Dual-wavelength superimposed FBGs method

Even though the above standard FBG technique is modest and affordable, it may lead to a bigger sensor probe. The dual-wavelength super-imposed FBGs technique employs twofold sets of wavelength shift data [18]. The Bragg wavelength-shift, λ_B in owing to a strain change, $\Delta\varepsilon$; and a temperature change, ΔT; is obtained by supposing

that the shifts in wavelength due to strain and temperature are linear as shown in Eq. (2.9).

$$\Delta\lambda_B = \aleph\Delta\varepsilon + \Re\Delta T \qquad Eq.(2.9)$$

Where $\aleph$, $\Re$ are the sensitivity of FBG due to strain and temperature respectively. The strain and temperature can be determined by monitoring the wavelength changes with strain and temperature independently. The strain and temperature of dual-wavelength superimposed FBGs may be calculated concurrently using the following matrix Eq. (2.10):

$$\begin{pmatrix}\Delta\lambda_{B1}\\ \Delta\lambda_{B2}\end{pmatrix} = \begin{pmatrix}\aleph_1 & \Re_1\\ \aleph_2 & \Re_1\end{pmatrix}\begin{pmatrix}\Delta\varepsilon\\ \Delta T\end{pmatrix} \qquad Eq.(2.10)$$

The two wavelengths are denoted as 1 and 2. The matrix's elements can be determined experimentally by finding the shifts in wavelength with strain and temperature separately. $\Delta\varepsilon$ and ΔT are easily determined as long as the matrix elements are known. A dual-wavelength overlaid FBG using an optical fiber is simple to make. However, its high cost restricts the industry's practical applicability [19].

In addition to these approaches, there are several other methods for simultaneous measurements. These are including hybrid FBG method, in which a long-period grating (LPG) is employed along with two FBGs [20], and fiber Fabry–Perot (FFP) cavity method that uses two FBGs with differing reflectivity values [21]. In this technique the optical path difference (OPD) gives the dynamic strain while the reflected wavelength gives the temperature. This design is bulk in size because the cavity length must be substantial in order to match the route length. The physical size of this sensor limits its usage in several applications [22–27].

2.5 Long Period Grating Theory

The fiber Bragg grating couples light from the optical fiber's forward propagating mode to its backward propagating mode. The long-period fiber grating couples light from the basic guided core mode to co-propagating cladding modes. This is comparable to FBG, except the grating periods in LPFG can significantly surpass the wavelength of light travelling through the fiber. Long-period fiber grating (LPFG) is a fiber component with wavelength dependent loss. As a result, LPFGs are easier to design than FBGs.

A long-period fiber grating (LPFG) is a fiber component with wavelength-dependent loss. All light in a narrow spectral portion is rejected by it like a band rejection filter without affecting the phase and amplitude of neighbouring wavelengths. The LPFGs are extremely sensitive to changes in the refractive index of the medium in which they exist. Because of these characteristics, it is a promising light wave component for linear and nonlinear photonic applications like band-rejection filters [28].

2.5.1 Principle of Operation of Long-Period Fiber Grating

Long-period fiber gratings is a special type of optical fiber grating in which the index modulation period meets the phase matching criterion between the basic core mode and the forward propagating cladding mode of an optical fiber. The radiation modes trapped by the cladding-air interface give rise to cladding modes. These modes get rapidly attenuated during propagation due to absorption by the cladding material and bends in the optical fiber. Resonant wavelength of LPFG is the phase-matched wavelength that causes light at the phase-matched conditions to be vanished from the optical fiber.

For standard optical fibers, the differential refractive index between the guided and cladding modes is from 10^{-3} to 10^{-2}. Thus if the coupling wavelengths is selected in the optical communication window (1200 nm to 1600 nm), then for this grating the periodic variation of the index of refraction in the fiber core has a period in hundreds of micrometer (characteristically in the range of 100 μm to 1,000 μm).

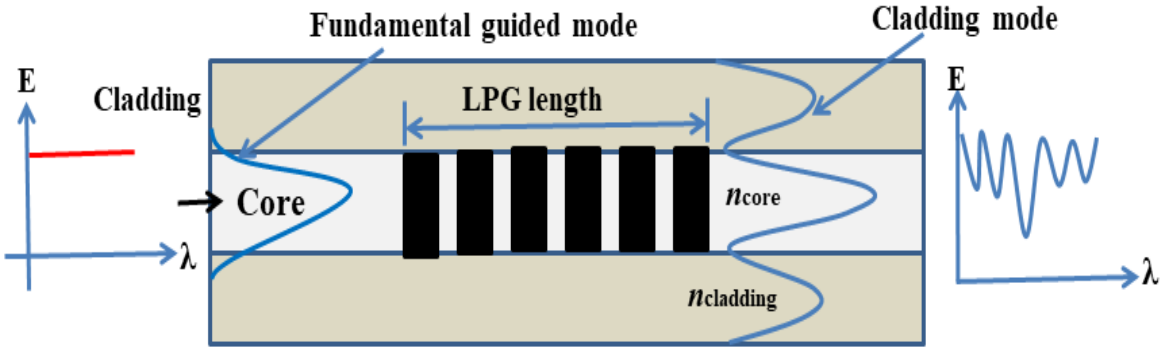

Fig. 2.6 Schematic illustration of Long period Grating (LPG)

In the conventional long-period grating, at various wavelengths, there may be more than one cladding mode those might meet the phase matching criterion. As illustrated in Fig. 2.6, this result in a sequence of attenuation of bands centered at

distinct wavelengths in the transmission spectrum. The light lost at these wavelengths is not reflected back to the source, but rather is lost to the cladding modes. This implies that, unlike fiber Bragg gratings, the reflection spectrum of a grating do not contain reflected light at the resonant wavelength. Because of the spectrum dependence of the propagation constants of the core and cladding modes, the LPFG has a very wavelength selective response.

2.5.2 LPG fabrication techniques

Long-period fiber gratings (LPFG) are generated by introducing periodic variation into the optical characteristics of the fiber core. Most typically, this modulation is accomplished by physical perturbation of the fiber or change of the refractive index of the optical fiber's core. The photo-elastic effect may be used to physically bend the fiber using mechanical pressure or acoustic vibrations to acquire the temporal modulation index, whilst irradiation or heating can be used to produce the permanent modulation index. Fiber gratings are made using a variety of processes [1]. Aside from ultraviolet (UV) irradiation [7,29], other techniques include exposing the fiber core to ion implantation [30], CO_2 laser irradiation [31–34], diffusion of dopants into the core [35,36], with femtosecond pulses in the infrared region [37–40], electrical discharges [41,42], and mechanical stress relaxation [43] are a few innovative and intriguing approaches employed in the production of LPFG. Mechanical distortion of the fiber has also resulted in the development of a grating [44,45]. Tapering the fiber [46], deformation of the core [47,48] or cladding [49] have been observed for LPG manufacturing. Deformation methods are less often employed in the production of LPFG.

2.6 Athermalization of LPG

The LPG must have a distinct response to the wavelength signal even in the presence of environmental variations, particularly temperature fluctuations [50]. It has been observed that the dip in the LPG spectrum is sensitive to temperature variations. As the LPG is also employed as an optical edge filter for FBG sensor interrogation for converting wavelength information into equivalent intensity information, this shift of the LPG dip affects the measurements and hence must be made insensitive to ambient temperature fluctuations. Encapsulating LPG with materials like Teflon to compensate for the thermal expansion has been employed for athermalization. The use of

athermalized LPG in the FBG-based sensor makes the system small, low-cost, high-resolution, and simple to connect with a PC without sacrificing accuracy [51].

2.7 Motivation

Construction of express high-ways and transportation of goods and commodities is getting increased prominence in recent times, resulting in increase in the heavy vehicular traffic on the roads and bridges. Health monitoring of bridge type of infrastructure in civil structures is becoming imperative to detect the stresses and strains thus developed on the bridges, and assess the consequent damages caused due to loads and others to this critical infrastructures.

Rapid progress in monitoring damages is being reported using various types of sensors for acquiring the data to access the condition of civil infrastructure. However, the information on optical fiber-based monitoring, employing FBGs as sensors for detection and health monitoring of engineering structures is not widely done. The motivation of this work is hence doing SHM with FBGs as sensing elements for measuring strains in prototype bridge structures. Also damage detection and remote transfer of sensed data was undertaken in the study. In addition to the FBG sensing, another novel technique which works on the principle of non-contact data acquisition viz., Digital Image Correlation (DIC) is also employed and a critical comparison is made with FBG sensing technique for health monitoring of modeled bridge like structures.

2.8 Literature

Here we gave the literature on Bridge weigh in motion structures using Fiber optic sensors, low cost monitoring of structures, digital image correlation (DIC) method for strain monitoring, and vibration based monitoring on different mixing of concrete beams with embedding steel and glass fibers.

2.8.1 Literature on Bridge type structures using Fiber optic sensors

M. Lydon et.al, (2014) [52]**,** a research was conducted to examine the detection of real-time strain for bridge load in motion in reinforced concrete structures using optical fiber sensor devices. The authors compared sensor types such as electric strain gauges and vibrating wire with FBG sensors and found them to be the most suited. Because it is critical in a field setting that the system be quickly and precisely installed, the challenges connected with the technique of attachment of the ERS sensors were deemed inappropriate for the proposed system.

Guemes, (2010) [53]**,** For large structural testing, the distributed sensing approach is quite beneficial. This may be avoided by bonding one or more plain fibers in the areas of interest, resulting in substantial time and cost savings. Optical fibers provide a one-of-a-kind capacity for obtaining strain or temperature data all the way down the fibers, which span the whole length of the bridge.

K. Wang, et.al, (2005) [54]**,** presented a new WIM system design based on fiber Bragg grating (FBG) technologies The weigh scale was an in-service bridge. The weights of cars passing across the bridge can be tracked using strain gauges mounted on the bridge abutments. They then replaced the bridge beam with a steel plate that sustains the weight of the driving car. As bridge abutments, four steel tubes are firmly connected at the plate's corners. Finally, all weights will be placed into tubes containing four FBGs that can record weight-induced stresses by altering their Bragg wavelengths. With the suggested method, they were able to obtain a resolution of 10 kilogram.

T.H.T. Chan et.al, (2006) [55]**,** Sensors designed for structural health monitoring were placed on Hong Kong's Tsing Ma bridge (TMB), the world's longest (1377 m) suspension bridge that handled both train and ordinary vehicle traffic. FBG sensors outperformed typical resistive strain gauges in terms of remote sensing, ease of installation, non-corrosive properties, and low maintenance costs. This demonstrates that FBG sensor technology is a viable option for monitoring civil and structural dynamic strains.

K. Soga et.al,(2018) [56]**,** The distributed fiber optics sensors for civil engineering infrastructure sensing, as well as measurement methods and their state-of-the-art capabilities, were examined. The major benefit of this approach is its great sensitivity over long distances and capacity to interact with a diverse variety of measurand in a dispersed way. The technologies deploy thousands of "strain gauges," "thermocouples," or "accelerometers" over a single fiber optic cable linked to or implanted in structures, which may then function as a civil infrastructure nervous system.

2.8.2 Literature on Low cost Interrogation Technique

Diaz et.al, (2017) [57]**,** presented a economic interrogation method based on an in-line micro-cavity built by recycling optical fiber that had been damaged by the catastrophic fuse effect The use of an in-line Fabry–Perot interferometer-based edge filter in the interrogation of fiber Bragg grating dynamic data up to 5 kHz is

investigated. Two devices were interrogated: an accelerometer and an arterial pulse wave probe.

Dos Santos et.al, (2019) [58]**,** A low-cost, low-power interrogation platform was described, with data-logging capabilities that may be used in remote sensing. Three thermally modulated fiber-coupled laser diodes were demonstrated to be capable of predicting the spectral shape of long-period fiber gratings by sweeping a few nanometers about their center wavelength locations and combining them with a single photo detector. The sensor transmission spectrum is rebuilt using curve-fitting techniques. It was discovered that intrinsic grating asymmetries contributed significantly to the difference between the true spectrum and that produced by fitting techniques. This technique was capable of tracking LPFG shapes while monitoring different parameters in the range from 1530 nm to 1570 nm within 1.12 nm.

Gautam et.al, (2020) [59]**,** A low-cost interrogation approach for an optical weighing system is described, which employs a single FBG with a small line width laser source. The FBG-based interrogation approach is characterised in order to determine the linear region where the laser source can be adjusted. The change in power due to applied load is estimated after investigating the approximate operating zone of FBG placed on load cell. In addition, strain produced at FBG is computed. A photo detector (FPD 610-FC-NIR, Menlo Systems) with an integrated low noise fixed gain trans-impedance amplifier detects variations in optical power. After converting the optical signal to an electrical signal using a photo detector, the voltage variation is transformed to a digital signal with an ADC. This digital data is transmitted to the Raspberry Pi for processing before being sent to the IoT cloud through the MQTT protocol (Message Queuing Telemetry Transport (MQTT)).

2.8.3 Digital Image Correlation (DIC) method

Peters and Ranson (1982) and Sutton et al. (1983) [60,61]**,** demonstrated that using white light illumination of a random, black and white pattern allowed strain measurements to be obtained using optical methods in combination with a digital computer. They devised sophisticated mathematical and practical methods for cross-correlating a reference picture with a stored image for use in experimental mechanics.

Neil A. Hoult et.al (2013) [62]**,** Digital Image Correlation (DIC) is an alternative approach for measuring strain using digital pictures that enables for the measurement of 2-D strain fields. The degree of precision that may be obtained in physical tests in which

causes of inaccuracy such as lighting and camera quality have been examined. A series of stress tests on steel plates are performed, allowing DIC data to be compared to readings from traditional foil strain gauges. The impact of out-of-plane movement was investigated, and the strain error was discovered to be a function of both the distance between the plate and the camera and the out-of-plane movement. Five potential compensatory techniques for strain faults were considered. Three of these approaches were utilized to enhance the accuracy of the plate test measurements (raising the effective distance between the camera and the specimen, an adjustment based on the material's Poisson's ratio, and a correction based on utilizing cameras to observe both sides of the loaded specimen).

Po-Chih Hung et.al, (2003) [63]**,** presented a “fast and simple” (FAS) surface deformation detection method for planar objects. The technique only employs fine search at pixel level resolution and surface fitting at the sub-pixel level. To examine the viability of this suggested method, two distinct specimens are explored. The displacements estimated by the FAS algorithm are compared to those calculated by the Newton-Raphson technique (N-R) and the Enhanced Sequential Similarity Detection Algorithm (ESSDA) (ESSDA). The findings demonstrate that the experimental data correspond well with the theoretical expectations. In the situations of uniaxial tension and disc under diametrical compression testing, the suggested approach is proven to be significantly quicker than the Newton-Raphson technique with inferior, but respectable, accuracy for displacement and strain measurement.

2.8.4 Vibration based Monitoring on concrete beams

2.8.4.1 Self-Compacting concrete

Nan Su et.al (2001) [64]**,** a new self-compacting concrete (SCC) mix design approach was proposed in a research. The quantity of aggregates, binders, and mixing water are the most significant factors in defining the properties of SCC. The packing factor (PF) of aggregate is defined in this study as the ratio of the mass of tightly packed aggregate in SCC to that of loosely packed aggregate. A higher PF value would imply a greater use of coarse and fine aggregates for SCC, decreasing the binder content. SCC designed and manufactured following the recommended mix design approach has more sand but less coarse stones, improving passage through reinforcing gaps. The amount of binders used in the recommended methodology may be less than that required by prior mix design techniques due to the greater sand content. Binder (the powder concentration

should not be too low in order to give appropriate flow ability and segregation resistance.

Bertil Persson (2001) [65]**,** a research compared the mechanical characteristics of self-compacting concrete (SCC) to those of conventional compacting concrete (NC). This involves examining characteristics including strength, elastic modulus, creep, and shrinkage. This investigation used eight mix proportions of sealed or air-cured specimens with water/binder ratios (w/b) ranging from 0.24 to 0.80. When the strength is held constant, the creep, shrinkage, and elastic modulus of SCC coincide very well with those of NC. When the concrete was loaded at a low age, the creep coefficient of young SCC rose significantly, just as it did for mature SCC and NC. Strength (fc) and relative humidity (RH) are both studied in parallel.

C Parra et.al (2011) [66]**,** a group of researchers investigated the splitting tensile strength and modulus of elasticity of self-compacting concretes of various ages. At 7 days, the difference between self-compacting NVCs and normally-vibrated SCCs is minor, and even disappears when the fines content of the SCC is large. Differences get larger at older ages, 28 and 90 days, with the average being 15.5 %. The modulus of elasticity of cement paste is higher in SCCs than in NVCs. This is due to the paste's significantly higher deformability than that of the particles, with a higher paste concentration resulting in less stiffness in the concrete. Pore volume drops and pore structure becomes finer as the w/c ratio or cement strength is raised.

2.8.4.2 Roles of fibers in concrete

P.S.Song et.al (2004) [67]**,** the inclusion of steel fibers can overcome high-strength concrete's (HSC) brittleness with poor tensile strength and strain capacity. Compressive and splitting tensile strengths, modulus of rupture, and toughness index were among the characteristics measured. The strength was at its peak at 1.5 percent fraction but decreased somewhat at 2 percent fraction compared to 0.5 percent, staying 12.9 percent greater before the fiber addition. With increasing fibre volume percentage, the splitting tensile strength and modulus of rupture of HSFRC both improved. The splitting tensile strength ranged from 19.0 to 98.3 percent greater for fractions ranging from 0.5 to 2.0 percent. Furthermore, the modulus of rupture ranged from 28.1 percent to 126.6 percent greater for the portion 0.5 percent to 2.0 percent. The modulus of rupture was shown to be the most effective for each volume fraction, followed by splitting tensile strength and compressive strength. The compressive and splitting tensile

strengths, as well as the modulus of rupture, are precisely predicted by the strength models established for HSFRC.

Job Thomas et.al (2007) [68]**,** presents the results of an experimental investigation as well as an analytical assessment of the influence of fiber addition on the mechanical properties of concrete. Based on regression analysis of 60 test data, models for various mechanical properties of steel fiber-reinforced concrete have been produced. Cube and cylinder compressive strength, split tensile strength, modulus of rupture and post cracking performance, Poisson's ratio, and strain corresponding to peak compressive stress are among the strength features examined. In various classes of concrete, the highest increase in tensile strength produced by the presence of steel fibers was determined to be about 40%. Fiber dosages significantly enhance the post-cracking response in all concrete grades. The parameters investigated include concrete grade (35 MPa), fairly high strength (65 MPa), and high-strength concrete (85 MPa).

M. L. V. Prasad et.al (2009) [69]**,** Glass fibres in SCC bridge fractures and improve concrete performance by not only preventing crack development but also contributing to improved energy absorption as compared to plain concrete. Based on the experimental data, an analytical stress-strain model was constructed. The goal was to create GFRSCC with the highest possible GF content based on fresh and hardened characteristics. SCC that satisfies EFNARC requirements might be created for non-fibrous and fibrous concretes. Fresh SCC must have essential qualities such as filling capacity, passage ability, and segregation resistance at the appropriate level. With the inclusion of glass fibers, the compressive strength of self-compacting concrete increases slightly. The addition of glass fiber to Self Compacting Concrete increased the peak strain and strain at 85 % of the ultimate strength in the descending part.

S. Mebarkia et.al (1992) [70]**,** At room temperature, the influence of polymer content and glass-fiber content on the compressive behavior of polyester polymer concrete is studied. Fibers, in general, restrict the material and delay fracture propagation, enhancing the failure strain and post peak ductility. To forecast the entire compressive stress-structure curves, a stress-strain model is presented.

2.8.4.3 Vibration analysis and damage detection in structures

Assessing the structural health state of urban infrastructure is crucial in terms of infrastructure sustainability.

Rathish P. Kumar et.al (2012) [71] An algorithm was developed based on changes in the power spectral density (PSD) to detect damage, predict the location and assess the extent of damage in the reinforced concrete beam. The method was based on the measured data on the beam after introducing some damage at salient locations. The algorithm may be a useful tool for continuous health monitoring of structures using ambient vibration as an excitation force.

The PSD technique identified the presence, could locate and monitor the damage growth based solely on measured data, and did not require any modal identification. Furthermore, the proposed approach may anticipate damage at several sites rather than just one. The damage indications 0, 1, and 2 were used to localize the harm. In both the experimental and numerical studies, damage indicator 2 was shown to be effective in precisely localizing the damage.

P. Rathish Kumar et.al (2010) [72] A novel approach for detecting and locating deterioration in reinforced concrete structures has been presented, which involves monitoring the vibration response of the structure. The approach takes the recorded phase angle between two measuring channels from the healthy structure as reference data, then analyses vibration measurements during the structure's life. The test constructions were subjected to a variety of damage scenarios. The suggested approach accurately recognized and localized the damage. Without having to choose the optimal frequency range, the phase angle might be utilized in the whole observed frequency range. The suggested approach outperformed the others in distinguishing phase angle changes associated with damage from noise or measurement mistakes. The experimental and numerical values are in pretty good agreement.

D Ravi Prasad et.al (2008) [73]**,** presents results of an experimental modal analysis of beams made with different materials such as Steel, Brass, Copper and Aluminum. Modal analysis is a process of describing a structure in terms of its natural characteristics which are the frequency, damping and mode shapes - its dynamic properties. The change of modal characteristics directly provides an indication of structural condition based on changes in frequencies and mode shapes of vibration. All the test specimens were tested under free-free condition. A completely free dynamic test setup is only aimed to eliminate the support influence to the dynamic characteristics. The excitation points were marked on the top surface of the beams along the length. The number of excitation points was selected such that they represent the vibration modes of interest. In this case, an accelerometer had a fixed position (at midpoint), whilst an

instrumented impact hammer was roved along the excitation points. The dynamic parameters such as the natural frequency and inherent damping value of their components are very important in compliant structures. In this paper, the application of experimental modal testing to various beams based on the impact hammer excitation is attempted to assess the natural frequency, damping constant and associated mode shapes of these examples. The modal testing has proven to be an effective and non-destructive test method for estimation of dynamic characteristics of beams.

Zhongdong Duan et al (2004) [74] made an effort to extend the flexibility based damage localization methods, especially the damage locating vector (DLV) method, to the case of ambient vibration with incomplete measured degree of freedom, where flexibility matrices are not available. First, the method to assemble a proportional flexibility matrix (PFM) with arbitrarily scaled modal shapes of full measured degrees of freedom (DOF) is introduced. Assuming that the modal masses do not change significantly before and after being damaged, the PFMs for pre-and post-damage at sensor locations. Finally an example of multi-damage sites localization for a 14 days planar truss is given. Five damaged members in the structure are successfully identified by the proposed approach with only outputs and measurements at partial DOFs.

V. Srinivas (2013) [75]**,** Modal analysis was performed on a reinforced concrete beam and a slab-strip using various forms of excitations and forces. The effect of different parameters such as support conditions, excitation sources, excitation level, and so on the modal features has been investigated. Because of non-homogeneity and micro fractures in concrete, the vibrational response (in terms of frequency) received from a tiny hammer differs from that of a huge hammer, and its influence is more pronounced at greater damage levels.

D. Huynh et.al (2005) [76]**,** A technique for detecting structural damage using frequency response functions (FRF) derived from non-destructive vibration tests. It looks into the issue of early structural damage where there is no discernible change in mass or damping. The resultant change in the structural stiffness matrix is represented in FRF data changes. Preliminary results indicate that this Damage Location Vector technique can overcome the issues of coordinate incompatibility and noise.

Tomoo Saito et.al (2005) [77]**,** the technique is used to analyze vibration data from shaking table experiments on a five-story steel frame experimental model. Even damaged floors with stiffness decrease ratios of 1 or 2 percent are detected. The dependability of the calculated values is quantified and represented in the harm

likelihood. This is extremely useful for the application to health monitoring, which necessitates the right judgment on the damage states.

2.8.4.4 Repairing of structure with epoxy based material

2.8.4.4 Repairing of structure with epoxy based material

Moetaz El-Hawary et.al (2000) [78], it has been examined the efficacy of epoxy-repaired concrete in a marine environment. Specimens were cast in normal and sulphate-resistant Portland cement, then damaged and repaired with three different epoxide resins. They were subjected to soaking and drying cycles that may last up to 18 months. The specimens were then divided and slant shear tested to determine their tensile and bond strength. The results revealed that the accumulation of seashells resulted in an improvement in strength at all ages.

Vaziri et.al (2006) [79], the dynamic behavior of repaired composite beams under a harmonic peeling stress was theoretically and empirically investigated. The repair procedure involved removing the damaged area and using glue to attach a composite patch into the gap. Theoretical equations of motion in the axial and transverse directions were developed in the theoretical section, assuming that the viscoelastic adhesive layer resists both peeling and shear forces. According to the findings of the comparison research, the elastic modulus of the adhesive layer dominates the mechanism of deformation of the repaired beam.

2.9 Summary of Literature and Gaps identified

Thousands of "strain gauges," "thermocouples," or "accelerometers" are dispersed across a single fiber optic cable connected to or implanted in structures, which may then operate as a civil infrastructure nervous system. The major benefit of this technique is its high sensitivity over long distances and ability to interact with a wide range of measurement equipment in a scattered manner. Because of its data-logging capabilities, a low-cost and low-power interrogation platform may be used in remote sensing. Digital Image Correlation (DIC) is an alternative approach for measuring strain using digital images that enables for the measurement of 2-D strain fields. A "fast and simple" (FAS) detection algorithm for surface deformation of planar objects. In the situations of uniaxial tension and disc under diametrical compression testing, the suggested approach is significantly quicker than the Newton-Raphson technique with inferior, but acceptable, accuracy for displacement and strain measurement. The packing factor (PF) of aggregate is defined as the ratio of the mass of tightly packed aggregate in SCC to

that of loosely packed aggregate. A higher PF value would suggest a greater number of coarse and fine aggregates utilized, lowering the binder content. SCC's performance was evaluated using V-funnel, L-flow, U-box, and compressive strength tests. Self-Compacting Mortars have higher natural frequencies as compared to Recycled–Natural aggregate based panels. Modal analysis was performed on a reinforced concrete beam and a slab-strip using various forms of excitations and forces. The vibrational response (in terms of frequency) obtained with a tiny hammer is different from that produced by a huge hammer. Because of non-homogeneity and micro fractures in concrete, accurate modeling of adhesive action is critical to model assessments of repaired composites. A theoretical model has been developed for the study of how an adhesive layer deforms under shear forces. For very low values of adhesive elastic modulus, the model replicated the results of the finite element analysis. The results obtained by using the classical composite beam theory were in good agreement with those of a classical analysis.

From the literature, few gaps are identified and those are given in detail.

1. FBG's can be used for real time monitoring of structures- Work on BWIM based on this system is limited.
2. Development of low cost interrogators for strain measurement for bridge health monitoring.
3. Work on developing automated damage detection system for remote monitoring and attending to the repair or rehabilitation precisely is limited.
4. DIC application on damage detection based on strain measurement is not prevalent.
5. Damage detection and localisation using vibration based monitoring and its application for repair structures to test the efficacy of repair is limited.

2.10 Scope and objectives of the Research work

Based on the deficiencies discovered, the study effort is divided into four phases.

1. Study the Bridge Weigh In Motion using FBG sensors keeping them at different angles to the vehicle motion.

2. Develop a Low-Cost Strain Measurement System using Fiber Bragg Grating Sensors for automated bridge monitoring using Bluetooth devices.

3. Monitor dynamic strains on a APT using FBG sensors and compare the same with Digital Image Correlation (DIC) method and numerical model based on finite element method (ABAQUS).

4. Damage Detection using Fiber Bragg Grating Sensors and studies on changes in the dynamic characteristics of concrete beams before & after damage and repair.

2.11 Research methodology

To achieve the defined objectives the work is done in four phases.

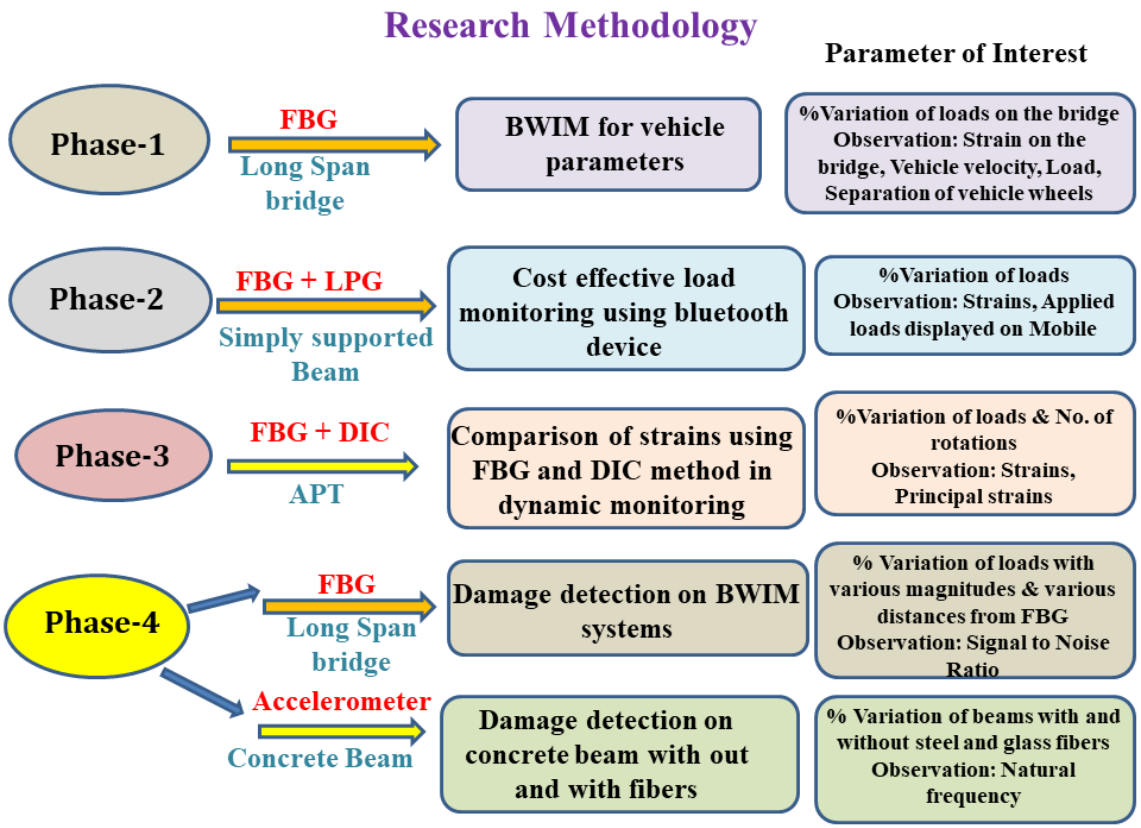

2.12 Organization of Thesis

The thesis is organized in Seven Chapters. A brief description of the content and the work carried out is presented below.

Chapter-1

This chapter gives a brief introduction about Structural Health Monitoring (SHM) in civil engineering structures, and presents a consolidated review of literature pertaining to various conventional and advanced methods of health monitoring of critical infrastructure.

Chapter-2

This chapter thoroughly discusses the characteristics and features of Fiber Bragg Gratings (FBG), techniques to inscribe Fiber Gratings in the core of an optical fiber, and their properties. A brief explanation on the optical fiber sensors used in the strain sensing, and a thorough review on measuring the strain in structural members using FBG sensors and cost effectiveness of interrogation methods for acquiring the sensed data is being presented.

At the end of the chapter, the aim and motivation of the research work i.e.; to detect the damage of a structure by measuring the strain parameters using FBG sensors is being presented. The work involves developing interrogation methods to measure and acquire the sensed data to a control room based on inexpensive methods.

The primary objectives of the work are defined after identify suitable gaps in the literature.

Chapter-3

In this Chapter the details of a prototype Bridge Weigh in Motion (BWIM) system with minimum configuration of Two FBG rosettes (Three elements) is presented to evaluate the principal strain at a point on the proposed structure due to a moving vehicle. The FBG rosettes (Three elements) are fixed at two different longitudinal girders of the prototype bridge along the line of motion at different orientations (0^o, 45^o, and 90^o). Micron Optics Interrogator (SM130) is used to acquire the data corresponding to the wavelength shift of FBGs when a loaded vehicle moves over it. This temporal response of the FBG has been analysed to evaluate the parameters of investigation, like the strain developed in the proximity of FBG's , the speed of the vehicle and the separation between its front and rear wheels.

From these studies, the ideal arrangement of the FBG's was found to be corresponding to that oriented along the bridge axis, as the sensitivity was found high with 0.32 με/gram, with a good linearity of 0.985 compared to other orientations. It was deduced from the results that the suggested BWIM structure could efficiently monitor variations in the load and speed of advancing vehicles over the bridge.

Chapter-4

This chapter discusses a Bluetooth based low-cost real time load measurement system employing FBG as a strain sensor on a prototype bridge for monitoring the data and for remote transfer of sensed data via mobile application. A long-period grating

(LPG) is used as an edge filter to convert the shift in Bragg wavelength due to applied load into a change in Optical power. Further, a simple Pigtailed Photodiode (PPD) and a Trans-Impedance Amplifier (TIA) were used in the background electronics and this change in the optical power is converted to voltage. The corresponding voltage for varying loads is fed to an Arduino Uno and the same is transmitted via Bluetooth to a mobile for continuous monitoring of the load on the bridge beam from a remote location. This set-up was found to accurately measure the load applied on the structure up to a simulated 3000 g with an error of ±1.67% (+50 g), thus confirming the ability of the proposed system in field applications.

Chapter-5

This chapter deals with the use of Digital Image Correlation (DIC) method which is a proved and widely used non-contact optical measurement method and a Fiber Bragg Grating (FBG) contact sensor system for finding the displacement and strains developed on the surface of a modeled Accelerating Pavement Track (APT) for Structural Health Monitoring (SHM) applications. A comparative study has been made between these two methods by assessing dynamic monitoring parameters of a prototype bridge. A random speckle pattern on the APT is used as a non-contact sensor for DIC measurements, while, FBGs are attached in the tension part of the track, where speckle patterns are drawn as contact sensors for measurements and for comparison of the results. A reference image was taken before applying the loads on the pavement, and the sequence of images were captured while applying the loads and varying the number of rotations on the APT. To evaluate the strain parameters, these images are processed in 2D-DIC method in MATLAB software. FBG array is connected to the interrogator (Enlight sm130-Micron Optics) for monitoring the temporal response data from the FBG to calculate the strains developed for comparison.

It has been observed from the experimental results that though the strain sensitivity from the FBG measurements is high compared to DIC values; it was found that there is a very good agreement between the normalized principal strain values obtained from both the methods.

Chapter-6

In this chapter, an FBG based Weigh-In-Motion system is proposed for the study of health condition of damaged structures. Artificial damage is created in the simulated

WIM bridge system, and the results were compared with those in the undamaged condition.

For studying the health condition of a bridge, a bridge prototype is designed by creating different magnitude of damages at different locations. The prototype is 2500 mm long and 300 mm wide along the straight path with five longitudinal bridge beams each of 500 mm length, 4.0 mm thickness of poly-acrylate sheet as bridge beam, and supported with six pairs of piers having 120 mm height. The FBG is fixed exactly at center position of the maximum tension region on the bridge beam, and fixed parallelly, with respect to the line of central axis of the Bridge. This FBG is connected to the interrogator and using software Enlight sm130 (Micron Optics), the data is obtained through the DAQ system. The acquired remote data of BWIM system is saved for further analysis.

An artificial Damage is created in the compression part of the bridge beam, at 0 cm, 1cm, 2cm and 3cm distance from the FBG. The width of the damage is 2.0 mm and the depth of damage is increased in steps of 0.5 mm from 0.5 mm to 2.0 mm. Owing to the live load of the vehicle, the FBG gets strained and causes change in Bragg wavelength. The temporal response of the FBG has been analysed to obtain the information about signal strength and Signal to Noise Ratio (SNR). The experiment was carried out for different loads and for different magnitudes of damage at different distances from the FBG to study the structural health of the BWIM.

A similar type of study using accelerometers was employed to sense the damage in concrete beams and identify the damage based on frequency response experiments by creating damage and under taking repair and measuring the response again. This work is taken up in three stages.

In the first stage, the parameters which influence the concrete viz., effect of compaction type, and fibers, on the vibration characteristics of Self-compacting concrete beams were observed without and with steel fibers/Glass fibers. Damage was created in these laboratory cast specimens by cutting a portion of the specimen giving a saw cut and the influence of this damage was observed for charge in dynamic properties.

OROS ANALYSER along with NV Solutions Smart Office software package was employed to analyze the specimens. Based on the vibration characteristics, the changes in the natural frequency and damping ratios were compared to estimate the influence of fibers and the method of compaction of these concrete specimens. The detection and localization of experimentally simulated damage is estimated. The

theoretical calculation was based on the physical change in the natural frequency due to the damage created by cutting the portion of the specimen say with a saw cut. It was found that there is a similarity in the results obtained between the theoretical and experimental investigations.

In the second stage, the damaged beams were tested after repairing with epoxy-based repair materials and the changes in vibration characteristics were observed to match the dynamic characteristics with the original beams. Significant improvement in dynamic properties was observed. However, it was observed that they could not exactly match with the equivalent natural frequency of undamaged beams.

In the third stage a numerical modeling of the beams was carried out based on ABAQUS and it was noticed after comparison that the response obtained from experimental, numerical and theoretical values of the dynamic properties were close.

Chapter-7

This chapter summarizes the results obtained from the research work, the conclusions and the scope for future work.

Summary

This chapter presented the details of the varying damage detection techniques with more focus on sensing using FBGs, techniques of monitoring BWIM system for measuring dynamic parameters and automated damage detection. Then, the details of works on vibration based damage detection using OROS analyser and DIC methods has been brought out. Based on the literature research gaps identified and objectives and organization of thesis is described.

Chapter-3 explains the first phase of the work, Bridge Weigh In Motion (BWIM) systems for measuring vehicle parameters using fiber Bragg grating sensors.

References

[1] R. Kashyap, Fiber Bragg Gratings, 1965. https://doi.org/10.1192/bjp.111.479.1009-a.

[2] K.O. Hill, Y. Fujii, D.C. Johnson, B.S. Kawasaki, Photosensitivity in optical fiber waveguides: Application to reflection filter fabrication, Appl. Phys. Lett. 32 (1978) 647–649. https://doi.org/10.1063/1.89881.

[3] G. Meltz, W.W. Morey, W.H. Glenn, Formation of Bragg gratings in optical fibers by a transverse holographic method, Opt. Lett. 14 (1989) 823. https://doi.org/10.1364/OL.14.000823.

[4] RamanKashyap, Fiber Bragg gratings, Academic Press, United States of America, 1999. https://doi.org/10.1016/C2009-0-16830-7.

[5] D.Z. Anderson, V. Mizrahi, T. Erdogan, A.E. White, Production of in-fibre gratings using a diffractive optical element, Electron. Lett. 29 (1993) 566–568. https://doi.org/10.1049/el:19930379.

[6] K.O. Hill, B. Malo, F. Bilodeau, D.C. Johnson, J. Albert, Bragg gratings fabricated in monomode photosensitive optical fiber by UV exposure through a phase mask, Appl. Phys. Lett. 62 (1993) 1035–1037. https://doi.org/10.1063/1.108786.

[7] I. Bennion, J.A.R. Williams, L. Zhang, K. Sugden, N.J. Doran, UV-written in-fibre Bragg gratings, Opt. Quantum Electron. 28 (1996) 93–135. https://doi.org/10.1007/BF00278281.

[8] K.-C. Hsu, L.-G. Sheu, K.-P. Chuang, S.-H. Chang, Y. Lai, Fiber Bragg grating sequential UV-writing method with real-time interferometric side-diffraction position monitoring, Opt. Express. 13 (2005) 3795. https://doi.org/10.1364/opex.13.003795.

[9] Kenneth O. Hill and Gerald Meltz, Fiber Bragg Grating Technology Fundamentals and Overview, J. Light. Technol. 15 (1997) 1263–1276. https://doi.org/10.1109/50.618320.

[10] D.K.W. Lam, B.K. Garside, Characterization of single-mode optical fiber filters, Appl. Opt. 20 (1981) 440–445.

[11] J. Stone, Photorefractivity in GeO2-doped silica fibers, J. Appl. Phys. 62 (1987) 4371–4374. https://doi.org/10.1063/1.339070.

[12] G. Meltz, R. Dunphy, H. Glenn, S. Lane, Fiber Optic temparature and strain

sensors, SPIE,Fiber Opt. Sensors II. 798 (1987).

[13] D. Taverner, D.. Richardson, S. Barcelos, M.. Zervas, Dispersion compansestion of 16ps pulses over 100km of step-index fiber using cascaded chirped fiber gratings, Electron. Lett. 31 (1995) 1004–1006.

[14] S.R. Parne, S. R L N, S.G. D, S.S. M, S. K, U. Tiwari, V. Mishra, A Simple FBG sensor for strain-Temparature discrimination, Microw. Opt. Technol. Lett. 53 (2011) 1021–1024. https://doi.org/10.1002/mop.25901.

[15] Y.J. Rao, Recent progress in applications of in-fibre Bragg grating sensors, Opt. Lasers Eng. 31 (1999) 297–324. https://doi.org/10.1016/S0143-8166(99)00025-1.

[16] S. Sarkar, M. Tarhani, M. Khosravi Eghbal, M. Shadaram, Discrimination between strain and temperature effects of a single fiber Bragg grating sensor using sidelobe power, J. Appl. Phys. 127 (2020). https://doi.org/10.1063/1.5139041.

[17] T.C. Haber, S. Ferguson, D. Guthrie, T.W. Graver, B.J. Soller, A. Mendez, Analysis, compensation, and correction of temperature effects on FBG strain sensors, Fiber Opt. Sensors Appl. X. 8722 (2013) 872206. https://doi.org/10.1117/12.2018772.

[18] M.G. Xu, J.L. Archambault, L. Reekie, J.P. Dakin, Discrimination between strain and temperature effects using dual-wavelength fibre grating sensors, Electron. Lett. 30 (1994) 1085–1087. https://doi.org/10.1049/el:19940746.

[19] Y. Zhao, Y. Liao, Discrimination methods and demodulation techniques for fiber Bragg grating sensors, Opt. Lasers Eng. 41 (2004) 1–18. https://doi.org/10.1016/S0143-8166(02)00117-3.

[20] H.J. Patrick, G.M. Williams, A.D. Kersey, J.R. Pedrazzani, A.M. Vengsarkar, Hybrid fiber Bragg grating/long period fiber grating sensor for strain/temperature discrimination, IEEE Photonics Technol. Lett. 8 (1996) 1223–1225. https://doi.org/10.1109/68.531843.

[21] D. Wei-Chong, X. Tao, H.-Y. Tam, Fibre Bragg Grating Cavity sensor for simultaneous measurement of strain and temperature, J. IIEEE Photonics Technol. Lett. 11 (1999) 105–107. https://doi.org/10.1177/1528083704046609.

[22] S.C. Her, W.N. Lin, Simultaneous measurement of temperature and mechanical strain using a fiber bragg grating sensor, Sensors (Switzerland). 20 (2020) 1–12. https://doi.org/10.3390/s20154223.

[23] M. Song, S.B. Lee, S.S. Choi, B. Lee, Simultaneous strain and temperature

sensing using two fiber Bragg gratings embedded in a glass tube, Conf. Proc. - Lasers Electro-Optics Soc. Annu. Meet. 11 (1997) 392. https://doi.org/10.1109/cleo.1997.603321.

[24] O. Frazão, L.A. Ferreira, F.M. Araújo, J.L. Santos, Simultaneous measurement of strain and temperature using fibre Bragg gratings in a twisted configuration, J. Opt. A Pure Appl. Opt. 7 (2005) 427–430. https://doi.org/10.1088/1464-4258/7/8/014.

[25] J. Jung, H. Nam, J.H. Lee, N. Park, B. Lee, Simultaneous measurement of strain and temperature using a single fiber Bragg grating with erbium-doped fiber amplifier, Conf. Proc. - Lasers Electro-Optics Soc. Annu. Meet. 1 (1998) 403–404. https://doi.org/10.1109/leos.1998.737900.

[26] F. Farahi, Simultaneous measurement of strain and temperature using fiber grating sensors, Proc. Eng. Mech. 1 (1996) 351–354. https://doi.org/10.1117/12.185036.

[27] B.O. Guan, H.Y. Tam, X.M. Tao, X.Y. Dong, Simultaneous strain and temperature measurement using a superstructure fiber Bragg grating, IEEE Photonics Technol. Lett. 12 (2000) 675–677. https://doi.org/10.1109/68.849081.

[28] A.M. Vengsarkar, P.J. Lemaire, J.B. Judkins, V. Bhatia, T. Erdogan, J.E. Sipe, Long-period Fiber Gratings as Band-Rejection Filters, J. Light. Technol. 14 (1996) 58–65.

[29] K.P. Chen, P.R. Herman, R. Tam, J. Zhang, Rapid long-period grating formation in hydrogen-loaded fibre with 157 nm F2-laser radiation, Electron. Lett. 36 (2000) 2000–2001. https://doi.org/10.1049/el:20001418.

[30] M. Fujimaki, Y. Ohki, J.L. Brebner, S. Roorda, Fabrication of long-period optical fiber gratings by use of ion implantation, Opt. Lett. 25 (2000) 88–89.

[31] T. Zhu, Y.J. Rao, Y. Song, K.S. Chiang, M. Liu, Highly sensitive temperature-independent strain sensor based on a long-period fiber grating with a CO2-laser engraved rotary structure, IEEE Photonics Technol. Lett. 21 (2009) 543–545. https://doi.org/10.1109/LPT.2009.2014566.

[32] D.. Davis, T.. Gaylord, E.. Glyysis, S.. Kosinski, S.C. Mettler, A.M. Vengsarkar, Long-period fibre grating fabrication with focused CO2 laser pulses, Electron. Lett. 34 (1998) 302–303.

[33] L. Drozin, P.-Y.F. And, L. Stensland, Long-period fibre gratings written by CO 2 exposure of H 2 -loaded, standard fibres, Electron. Lett. 41 (2005) 40–41.

https://doi.org/10.1049/el.

[34] J.M.P. Coelho, M. Nespereira, M. Abreu, J. Rebordão, 3D finite element model for writing long-period fiber gratings by CO2laser radiation, Sensors (Switzerland). 13 (2013) 10333–10347. https://doi.org/10.3390/s130810333.

[35] E.M. Dianov, V.I. Karpov, M. V. Grekov, K.M. Golant, S.A. Vasiliev, O.I. Medvedkov, R.R. Khrapko, Thermo-induced long-period fibre gratings, in: IEE Conf. Publ., 1997: pp. 53–56. https://doi.org/10.1049/cp:19971415.

[36] E.M. Dianov, V.I. Karpov, A.S. Kurkov, M. V Grekov, LONG-PERIOD FIBER GRATINGS AND MODE-Fl LD CONVERTERS FABRICATED BY THERMODIFFUSION IN PHOSPHOSILICATE FIBERS, in: 24th ECOC, 20-24th, Madrid: Telefonica Espana, 1998: pp. 395–396.

[37] Y. Kondo, K. Nouchi, T. Mitsuyu, M. Watanabe, P.G. Kazansky, K. Hirao, Fabrication of long-period fiber gratings by focused irradiation of infrared femtosecond laser pulses, Opt. Lett. 24 (1999) 646. https://doi.org/10.1364/ol.24.000646.

[38] E. Fertein, C. Przygodzki, H. Delbarre, A. Hidayat, M. Douay, P. Niay, Refractive-index changes of standard telecommunication fiber through exposure to femtosecond laser pulses at 810 cm, Appl. Opt. 40 (2001) 3506. https://doi.org/10.1364/ao.40.003506.

[39] B. Li, L. Jiang, S. Wang, H.L. Tsai, H. Xiao, Femtosecond laser fabrication of long period fiber gratings and applications in refractive index sensing, Opt. Laser Technol. 43 (2011) 1420–1423. https://doi.org/10.1016/j.optlastec.2011.04.011.

[40] A. Saad, Y. Cho, F. Ahmed, M.B.G. Jun, Numerical approach to modeling and characterization of refractive index changes for a long-period fiber grating fabricated by femtosecond laser, Materials (Basel). 9 (2016). https://doi.org/10.3390/ma9110941.

[41] G. Rego, O. Okhotnikov, E. Dianov, V. Sulimov, High-temperature stability of long-period fiber gratings produced using an electric arc, J. Light. Technol. 19 (2001) 1574–1579. https://doi.org/10.1109/50.956145.

[42] P. Palai, M.N. Satyanarayan, M. Das, K. Thyagarajan, B.P. Pal, Characterization and simulation of long period gratings fabricated using electric discharge, Opt. Commun. 193 (2001) 181–185. https://doi.org/10.1016/S0030-4018(01)01231-7.

[43] C.S. Kim, Y. Han, B.H. Lee, W.T. Han, U.C. Paek, Y. Chung, Induction of the refractive index change in B-doped optical fibers through relaxation of the

mechanical stress, Opt. Commun. 185 (2000) 337–342. https://doi.org/10.1016/S0030-4018(00)01045-2.

[44] S. Savin, M.J.F. Digonnet, G.S. Kino, H.J. Shaw, Tunable mechanically induced long-period fiber gratings, Opt. Lett. 25 (2000) 710. https://doi.org/10.1364/ol.25.000710.

[45] Y. Jiang, Q. Li, C.H. Lin, E. Lyons, I. Tomov, H.P. Lee, A novel strain-induced thermally tuned long-period fiber grating fabricated on a periodic corrugated silicon fixture, IEEE Photonics Technol. Lett. 14 (2002) 941–943. https://doi.org/10.1109/LPT.2002.1012392.

[46] G. Kakarantzas, T.E. Dimmick, T.A. Birks, R. Le Roux, P.S.J. Russell, Miniature all-fiber devices based on CO_2 laser microstructuring of tapered fibers, Opt. Lett. 26 (2001) 1137. https://doi.org/10.1364/ol.26.001137.

[47] C.D. Poole, J.P. Meester, H.M. Presby, Two-mode fibre spatial-mode converter using periodic core deformation, Electron. Lett. 30 (1994) 1437–1438. https://doi.org/10.1049/el:19940948.

[48] C. Narayanan, H.M. Presby, A.M. Vengsarkar, Band-rejection fibre filter using periodic core deformation, Electron. Lett. 33 (1997) 280–281. https://doi.org/10.1049/el:19970227.

[49] C.Y. Lin, G.W. Chern, L.A. Wang, Periodical corrugated structure for forming sampled fiber Bragg grating and long-period fiber grating with tunable coupling strength, J. Light. Technol. 19 (2001) 1212–1221. https://doi.org/10.1109/50.939803.

[50] S.W. James, R.P. Tatam, A. Twin, R. Bateman, P. Noonan, Cryogenic temperature response of fibre optic long period gratings, Meas. Sci. Technol. 14 (2003) 1409–1411. https://doi.org/10.1088/0957-0233/14/8/329.

[51] V.R. Mamidi, S. Kamineni, L.N. Sai Prasad Ravinuthala, V. Thumu, V.R. Pachava, Method to athermalize a long-period fiber grating for interrogation of fiber Bragg grating–based sensors, Opt. Eng. 53 (2014) 096111. https://doi.org/10.1117/1.oe.53.9.096111.

[52] M. Lydon, S. Taylor, D. Robinson, P. Callender, C. Doherty, S. Grattan, E. O'Brien, Development of a Bridge Weigh-in-Motion Sensor: performancecomparison using fibre optic and electric resistance strain sensor systems, IEEE Sens. J. 14 (2014) 4284–4296. https://doi.org/10.1109/JSEN.2014.2332874.

[53] A. Guemes, B. Soller, Optical fiber distributed sensing: Physical principles and applications, Struct. Heal. Monit. 2009 From Syst. Integr. to Auton. Syst. - Proc. 7th Int. Work. Struct. Heal. Monit. IWSHM 2009. 1 (2009) 14–20.

[54] K. Wang, Z. Wei, B. Chen, H.C.-F.O. Sensor, U. 2005, A Fiber-Optic Weigh-In-Motion Sensor Using Fiber Bragg Gratings, in: J.P.D. Michael A. Marcus, Brian Culshaw (Ed.), Fiber Opt. Sens. Technol. Appl. IV, Spiedigitallibrary, 2005: pp. 1–6. https://doi.org/10.1117/12.629372.

[55] T.H.T. Chan, L. Yu, H.Y. Tam, Y.Q. Ni, S.Y. Liu, W.H. Chung, L.K. Cheng, Fiber Bragg grating sensors for structural health monitoring of Tsing Ma bridge: Background and experimental observation, Eng. Struct. 28 (2006) 648–659. https://doi.org/10.1016/j.engstruct.2005.09.018.

[56] K. Soga, L. Luo, Distributed fiber optics sensors for civil engineering infrastructure sensing, J. Struct. Integr. Maint. 3 (2018) 1–21. https://doi.org/10.1080/24705314.2018.1426138.

[57] C.A.R. Díaz, C. Leitão, C.A. Marques, M.F. Domingues, N. Alberto, M.J. Pontes, A. Frizera, M.R.N. Ribeiro, P.S.B. André, P.F.C. Antunes, Low-cost interrogation technique for dynamic measurements with FBG-based devices, Sensors (Switzerland). 17 (2017) 1–10. https://doi.org/10.3390/s17102414.

[58] P.S.S. Dos Santos, P.A.S. Jorge, J.M.M.M. De Almeida, L. Coelho, Low-cost interrogation system for long-period fiber gratings applied to remote sensing, Sensors (Switzerland). 19 (2019) 1–14. https://doi.org/10.3390/s19071500.

[59] A. Gautam, A. Kumar, K. Kinjalk, J. Thangaraj, V. Priye, A Low Cost FBG Based Online Weight Monitoring System, IEEE Sens. J. 20 (2020) 4207–4214. https://doi.org/10.1109/JSEN.2019.2961688.

[60] W. Peters, W. Ranson, Digital imaging techniques in experimental stress analysis, Opt. Eng. 21 (1982) 427–431.

[61] M. Sutton, W. Wolters, W. Peters, W. Ranson, S. McNeill, Determination of displacements using an improved digital correlation method, Image Vis. Comput. 1 (1983) 133–139. https://doi.org/10.1016/0262-8856(83)90064-1.

[62] N.A. Hoult, W.A. Take, C. Lee, M. Dutton, Experimental accuracy of two dimensional strain measurements using Digital Image Correlation, Eng. Struct. 46 (2013) 718–726. https://doi.org/10.1016/j.engstruct.2012.08.018.

[63] P. Hung, A.S. Voloshin, In-plane Strain Measurement by Digital Image Correlation, J. Brazil Soc. Mech. Sci. Eng. XXV (2003) 215–221.

[64] N. Su, K. Hsu, H. Chai, A simple mix design method for self-compacting concrete, Cem. Concr. Res. 31 (2001) 1799–1807.

[65] B. Persson, A comparison between mechanical properties of self-compacting concrete and the corresponding properties of normal concrete, Cem. Concr. Res. 31 (2001) 193–198.

[66] C. Parra, M. Valcuende, F. Gómez, Splitting tensile strength and modulus of elasticity of self-compacting concrete, Constr. Build. Mater. 25 (2011) 201–207. https://doi.org/10.1016/j.conbuildmat.2010.06.037.

[67] P.S. Song, S. Hwang, Mechanical properties of high-strength steel fiber-reinforced concrete, Constr. Build. Mater. 18 (2004) 669–673. https://doi.org/10.1016/j.conbuildmat.2004.04.027.

[68] J. Thomas, A. Ramaswamy, Mechanical Properties of Steel Fiber-Reinforced Concrete, J. Mater. Civ. Eng. 19 (2007) 385–392. https://doi.org/10.1061/(ASCE)0899-1561(2007)19.

[69] M. Prasad, P. Rathish Kumar, T. Oshima, Development of Analytical Stress-Strain Model for, Int. J. Mech. Solids. 4 (2009) 25–37.

[70] S. Mebarkia, C. Vipulanandan, Compressive behavior o f glass-fiber-reinforced polymer concrete, J. Mater. Civ. Eng. 4 (1992) 91–105.

[71] P. Rathish Kumar, T. Oshima, S. Mikami, Y. Miyamori, T. Yamazaki, Damage identification in a lightly reinforced concrete beam based on changes in the power spectral density, Struct. Infrastruct. Eng. 8 (2012) 715–727. https://doi.org/10.1080/15732471003730674.

[72] P.R. Kumar, T. Oshima, Detection and localization of small damages in a real bridge by local excitation using piezoelectric actuators, J. Civ. Struct. Heal. Monit. 2 (2012) 97–108. https://doi.org/10.1007/s13349-012-0020-5.

[73] D. Ravi Prasad, D. R Seshu, A STUDY ON DYNAMIC CHARACTERISTICS OF STRUCTURAL MATERIALS USING MODAL ANALYSIS, Asian J. Civ. Eng. (Building Housing). 9 (2008) 141–152.

[74] Z. Duan, G. Yan, J. Ou, B.F. Spencer, Damage detection in ambient vibration using proportional flexibility matrix with incomplete measured DOFs, Struct. Control Heal. Monit. 14 (2007) 186–196. https://doi.org/10.1002/stc.149.

[75] V. Srinivas, S. Sasmal, K. Ramanjaneyulu, C.A. Jeyasehar, In fl uence of test conditions on modal characteristics of reinforced concrete structures under different damage scenarios, Arch. Civ. Mech. Eng. 13 (2013) 491–505.

https://doi.org/10.1016/j.acme.2013.04.006.

[76] D. Huynh, J. He, D. Tran, Damage location vector : A non-destructive structural damage detection technique, Comput. Struct. 83 (2005) 2353–2367. https://doi.org/10.1016/j.compstruc.2005.03.029.

[77] T. Saito, S. Mase, K. Morita, A probabilistic approach to structural damage estimation, Struct. Control Heal. Monit. 12 (2005) 283–299. https://doi.org/10.1002/stc.71.

[78] M. El-hawary, H. Al-khaiat, S. Fereig, Performance of epoxy-repaired concrete in a marine environment, Cem. Concr. Res. 30 (2000) 259–266.

[79] A. Vaziri, H. Nayeb-Hashemi, Dynamic response of a repaired composite beam with an adhesively bonded patch under a harmonic peeling load, Int. J. Adhes. Adhes. 26 (2006) 314–324. https://doi.org/10.1016/j.ijadhadh.2005.05.003.

CHAPTER – 3
BRIDGE WEIGH IN MOTION (BWIM) SYSTEM FOR MEASURING THE VEHICLE PARAMETERS

This chapter presents the details of experiments conducted on a Bridge Weigh in Motion (BWIM) system employing two FBGs for understanding the strains developed at a point in an engineering structure suiting various SHM applications. A prototype bridge was constructed for this purpose with poly-acrylic material sheet; and experiment is conducted to measure the strains developed while a simulated vehicle passes over the bridge. The orientations of the FBGs were kept at; 0^o, 45^o and 90^o with respect to the bridge axis. The response of the system has been analysed by considering the FBG orientations as a three-element rosette and the vehicle parameters such as load, speed of vehicle, axle detection, axle weight and the separation of front and rear wheels are determined and are found to be in close agreement. The prototype bridge is assumed as a simply supported beam with varying positions of the concentrated load and simulation study has been performed using MATLAB software.

3.1. Introduction

Although a variety of technologies can be employed for health monitoring, Bridge Weigh in Motion (BWIM) system is considered as one of the prominent SHM methods, as it overcomes the drawbacks of static weighing and acquires moving vehicle's information which is of prime importance in highways. BWIM is not only capable of estimating weight of the vehicle, velocity, separation of front and rear wheels, but also, the recurrence of vehicles across the bridge without interfering their movement [1,2]. Previously health monitoring methods included visual inspection, Non-Destructive Evaluation (NDE) using eddy currents, Acoustic emission, and Ultrasonic tests [3–5]. These methods, which require a high degree of expertise, are time consuming and works only in accessible regions of the structure. BWIM systems based on electrical resistance strain gauges also have limitations in achieving data for long term monitoring of bridges [6].

Fiber optic sensors (FOS) are finding applications in the area of SHM in recent times, as they possess inherent advantages as light weight, high resistance to corrosion, better immunity to electrical interference, accuracy and stability. They are capable of measuring various physical quantities, either by distributed network or by multiplexing techniques. In addition, these are easy to fix and can be easily embedded in a variety of structures compared

to other sensors as explained. Among the family of FOS, the combination of FBG with Long Period Grating (LPG) has produced a surface mounted Non-Destructive Evaluation (NDE) based fiber sensor system, capable of continuously monitoring the integrity of smart structures or their components with a high level of confidence and reliability [7–10]. A series of fiber optic sensors can be used to determine the accuracy of the system by systematic calibration [6], and using optical devices for monitoring bridge deflections, and curvature, under live traffic loading at the bridge sites and further use this information to predict axle loads, wheel count, strains, and displacement [11–17].

3.2. Experimental setup

For the experimental study of BWIM system, a prototype bridge deck is constructed with beam of poly-acrylic material sheet having length and breadth of 0.5 m and 0.3 m respectively. A total of five such longitudinal beams are used for modelling the bridge of length 2.5 m. Six pairs of piers, each of height 0.12 m, have been placed on either side of the deck to support the beams. Two FBG's; used as strain sensors; are pasted between the Piers 2-3 and 4-5 of the simulated bridge deck as shown in Fig. 3.1 (a). The spacing between the two FBG's is maintained as 10 m. The experimental setup is shown in Fig. 3.1 (b).

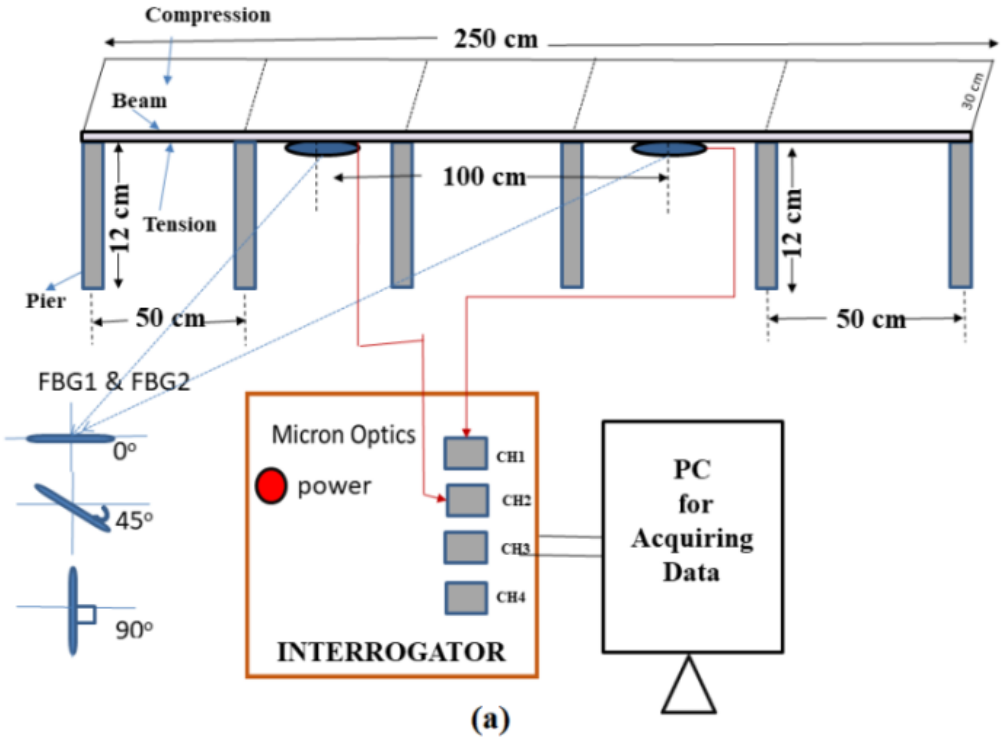

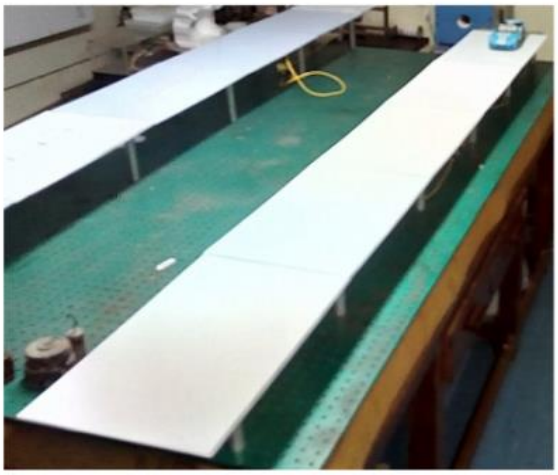

(b)

(c)

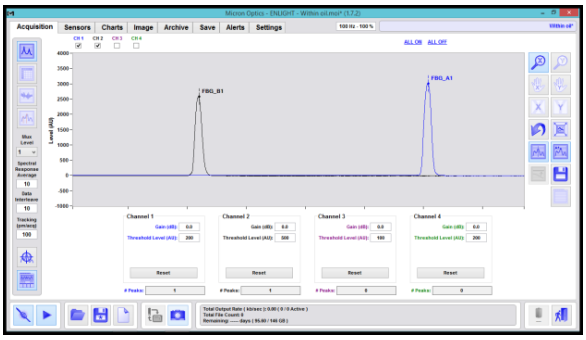

(d)

Fig. 3.1 (a).Schematic Diagram, (b) Experimental set up, (c) Interrogator with PC (d) Reflection spectrum of FBG's

The FBG's employed in the present investigation have Bragg wavelengths of 1552.004 nm and 1543.880 nm and are connected to the two input channels of an interrogator (Micron optics). The experimental data is recorded using interfacing software Enlight SM 130 as shown in Fig. 3.1(c). The recorded information of Bridge Weigh in Motion (BWIM) system has been saved for further analysis.

In the present work, the experiment is conducted with orientation of the FBG in different directions; 0^o, 45^o and 90^o with respect to the bridge axis and the results are analyzed considering it as a three-element rosette. The experimental results are verified with the results of strain equations simulated using MATLAB for simply supported beam with a concentrated load at any section.

3.3. Calibration of sensor

To study the response of the proposed system and evaluate the linearity and sensitivity, static load test is performed on the experimental set up, by keeping FBG sensor at 0^o and 45^o orientations to the axis of the bridge with increasing and decreasing loads in the range of 0-1,500 grams., in steps of 100grams and the results of Bragg Wavelength shift and the corresponding strains developed in the beam deck have been recorded. Fig.3.2 shows the details of the wavelength shift and strain for different loading conditions on the simulated bridge.

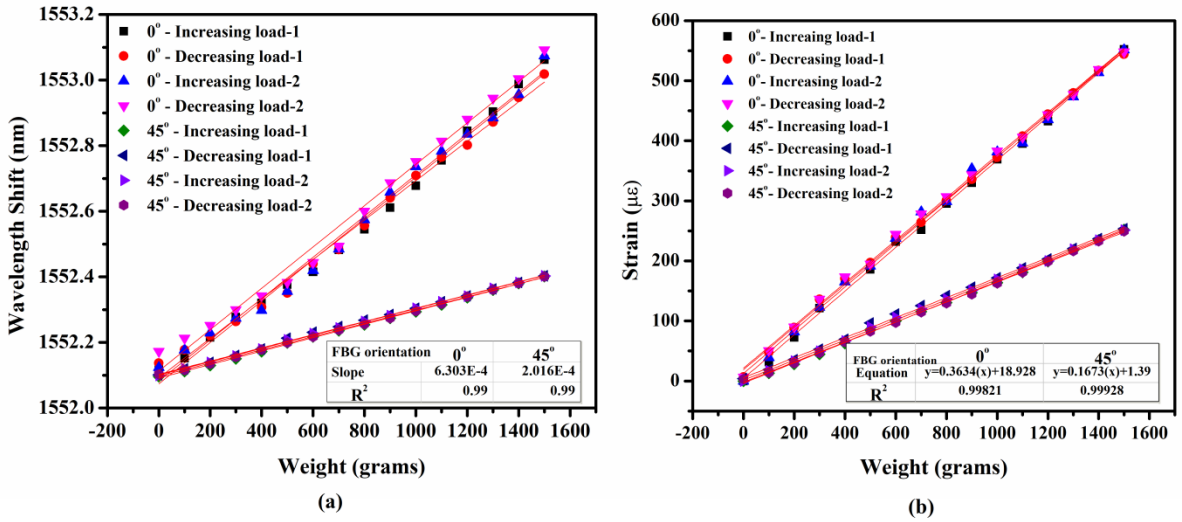

Fig. 3.2 Static load test for calibration, (a) Wavelength shift (b) Strain

Fig. 3.2(a) shows the results of the wavelength shift of FBG sensor placed at 0^o and 45^o orientation to the line of motion with increasing and decreasing loads, while Fig. 3.2(b) represents the corresponding strain response under static load condition calculated by using Eq. (3.1).

$$\Delta\lambda_B / \lambda_B = (1-P_e)\varepsilon \qquad Eq.(3.1)$$

where ($\Delta\lambda_B/\lambda_B$) is the relative Bragg wavelength shift of FBG at constant temperature, 'ε' is the strain applied to the grating and 'P_e' is the effective photo-elastic coefficient of the optical fiber respectively. Typically, for a fused silica fiber P_e= 0.22.

From these results, it can be observed that the sensor response in terms of wavelength shift as well as the strain developed for an applied load is found to be linear with a linearity coefficient more than 0.99. This shows consistency in measurements with negligible hysteresis. A negligible repeatability error of ± 0.92% over full scale is observed. It was also found that the FBG placed at 0^o orientation to the line of motion had more sensitivity; i.e.

0.363 με/gram; than the FBG oriented at 45^o where the sensitivity is measured as 0.167 με/gram.

3.4 Experimental Procedure

For evaluating the vehicle parameters while a loaded vehicle moves on the simulated bridge deck; the experiment has been conducted in three phases; keeping FBG's at different angular orientations; parallel, at an angle of 45^o and perpendicular to the line of motion.

In Phase-I, FBG's are attached parallel to the line of motion to the bridge beams 2 and 4, at a distance of 1,000 mm. A remotely controlled simulated vehicle is used to move on the bridge deck model. As the vehicle moves, the FBGs, experience strain and causes a shift in their Bragg wavelength ($\Delta\lambda_B$) with respect to time. These shifts in wavelength are recorded using the Interrogator to produce the temporal response curve which is processed for determining the vehicle parameters. The temporal response of the designed system is studied by repeating the experiment with increasing and decreasing loads and with varying speeds of the vehicle.

In Phase-II and Phase –III, the experiment is repeated by fixing FBG's, at an angle of 45^o and perpendicular to the line of motion respectively, and the same method as explained earlier for Phase-I is adopted.

Vehicle parameters such as velocity of the vehicle is estimated by keeping the distance 'd' between the two FBG's constant and noting the corresponding time difference (Δt) between observed Bragg wavelength shifts of the two FBGs which is recorded by the interrogator ($V=d/\Delta t$). The load information has been extracted from the observed shift in wavelength of individual FBGs.

3.5. Results and Discussions

The experiment is performed in three phases. In each phase, the load on the vehicle is altered and is operated at various speeds. When the vehicle passes over the simulated bridge; based on the strains developed in the attached FBG sensors; a shift in wavelength occurs and this data is acquired by a micron optics interrogator interfaced with PC. In the first phase, the two FBGs are fixed parallel to the line of motion (0^o) at a constant distance of 1000mm, while in the second and third phases of the experiment; the FBG's are oriented at 45^o and 90^o respectively. From the acquired data, typical temporal response plots between the time and wavelength shift are drawn as shown in Fig. 3.3.

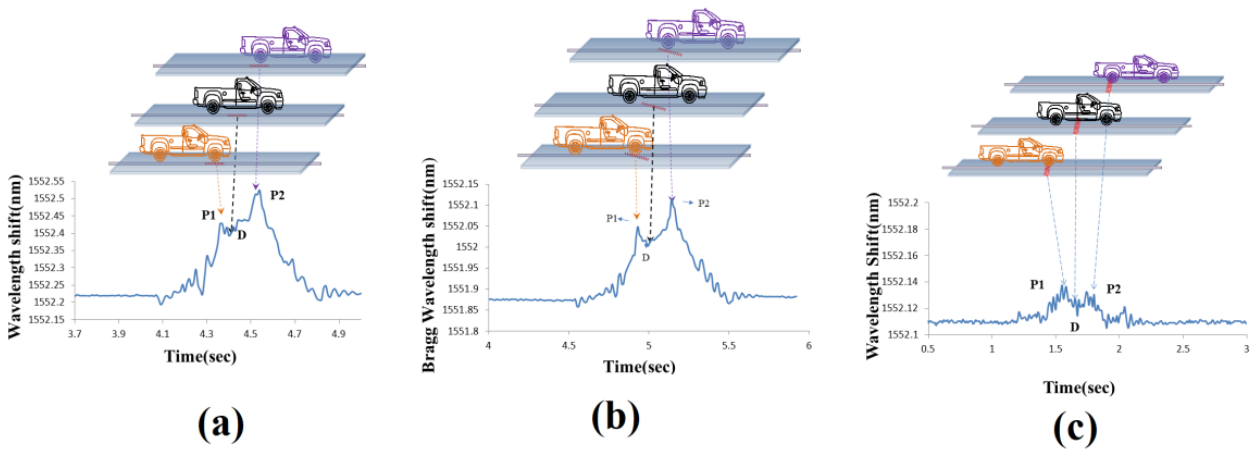

Fig.3.3 Temporal Response of the Bragg Wavelength Shift (a) FBG at 0^o (b) FBG at 45^o (c) FBG at 90^o to the line of motion

Two crests and one trough like shape appear in the temporal response corresponding to the positions of the wheels of the vehicles with reference to the FBG. When the front and rear wheels of the vehicle lie completely on the FBG, a larger shift in the wavelength is recorded in the response, termed as 'P_1' and 'P_2' respectively. When the FBG is in between the wheels, a smaller shift is recorded which is less than 'P_1' and 'P_2' and is forming a trough like shape termed as 'D' in the response as shown in Fig. 3.3(a). Similar types of plots are obtained for second and third phases of the experiment i.e. for 45^o and 90^o orientations of the FBGs as shown in Fig. 3.3(b) and 3.3(c) respectively.

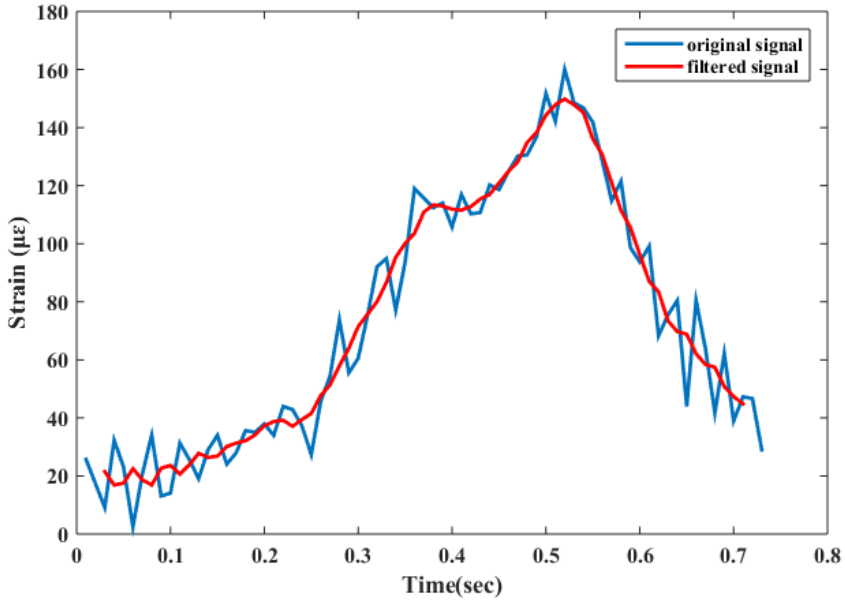

Fig.3.4 Typical temporal response of strain curve of a moving vehicle at FBG_1

Fig. 3.4 shows a typical temporal response of strain developed in a bridge beam for a load of 250grams on the moving vehicle, and influence line of a bending strain [18][19]. A Savitzky-Golay filter provided by MATLAB was used to remove the random noise contained in the measured strain response by convolving the signal with the centre row. Such filtered temporal response curves have been obtained while keeping the FBGs at the three orientations and varying the loads on the vehicle. The results are presented in Fig.3.5 and Fig.3.6.

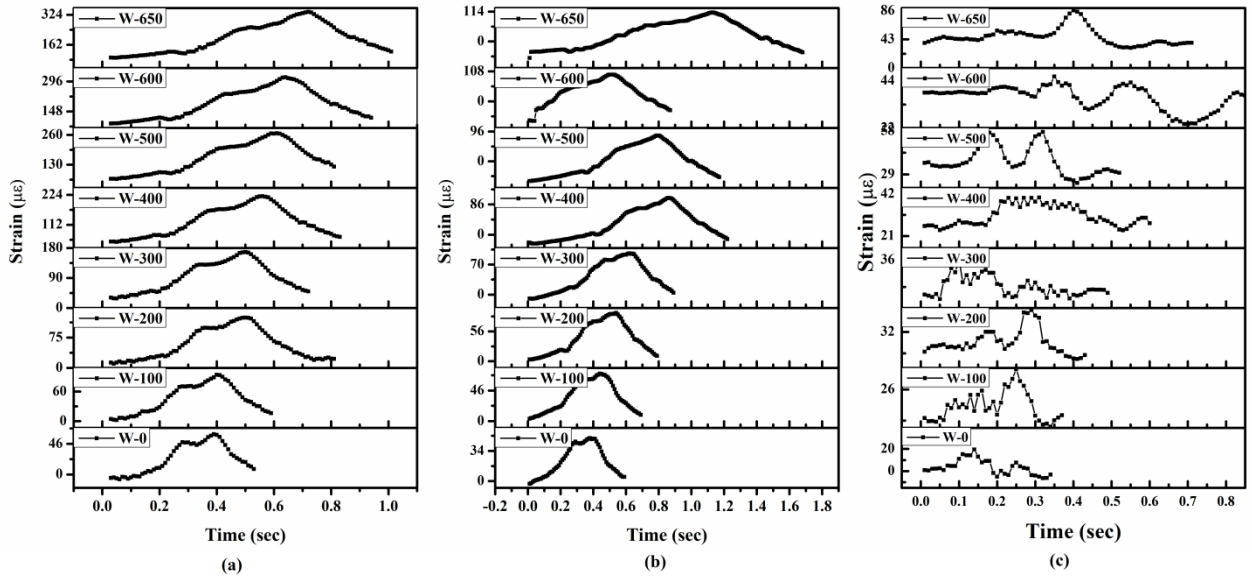

Fig.3.5 Temporal response of FBG_1 at (a) 0^o, (b) 45^o, (c) 90^o to the line of motion

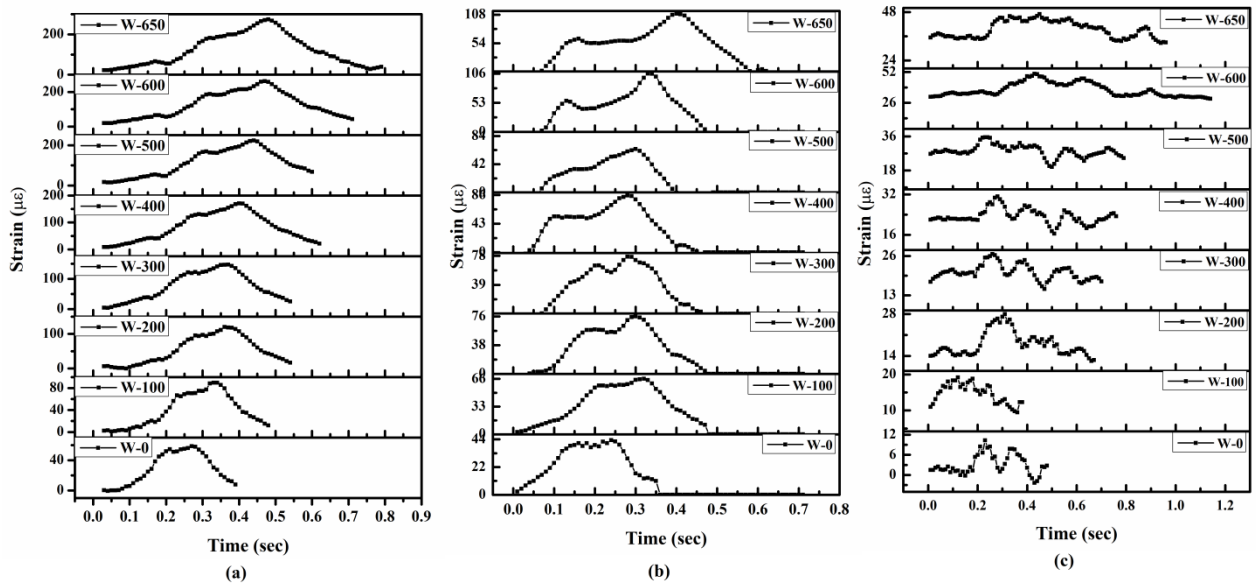

Fig.3.6 Temporal response of FBG_2 at (a) 0^o, (b) 45^o, (c) 90^o to the line of motion

Fig.3.5(a), 3.5(b), 3.5(c) shows the temporal response of strain produced in the bridge beam by varying loads corresponding to FBG_1 placed at different orientation to the line of motion by varying loads on the vehicle. In the parallel and 45^o orientation of the FBG_1 with respect to the line of motion of the vehicle (Axis of the Bridge deck), two peaks 'P_1' and 'P_2' appear indicating the position of the wheels of the vehicle while crossing the FBG_1. However, in case of 90^o orientation of FBG_1 to the line of motion, it was found difficult to distinguish the peaks, indicating that the strain is not experienced by the FBG oriented at an angle 90^o to the line of motion, and is not useful in weigh in motion systems; and further study in this orientation to the line of motion is ignored. Similar results have been obtained event at location of FBG_2, while it is arranged in three orientations to the line of motion and is shown in Fig. 3.6(a), 3.6(b), and 3.6(c).

3.5.1. Strain response of FBG at two peaks

The strains developed on the Bridge deck at the sight of the FBGs while a loaded vehicle moves on the track have been estimated by noting the corresponding Bragg Wavelength shift experienced from the temporal response curves for different loads. The results are presented in Fig 3.7.

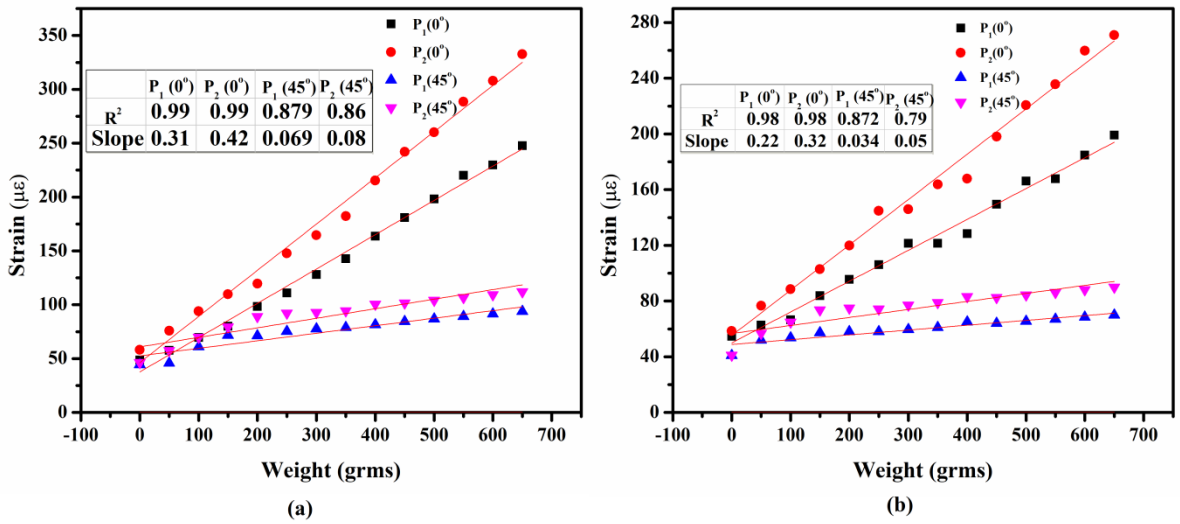

Fig. 3.7 Strain response with applied load at peaks P_1, P_2 (a) FBG_1, (b) FBG_2

Figs. 3.7(a) and 3.7(b) shows the strain response of the FBG_1 and FBG_2 with orientations at 0^o, 45^oat points 'P_1' and 'P_2' with reference to the applied load on the moving vehicle. It has been found that the plots corresponding to 0^o orientation are linear with a good coefficient of correlation of about 0.99 and with an average sensitivity of 0.36με/gram for FBG_1, while with 45^o angular orientation of the FBG_1 the R^2 value was 0.87 and sensitivity 0.07με/gram. Similarly, FBG_2 has shown an average sensitivity of 0.27με/ gram and linear

coefficient correlation is 0.98 along 0^o orientation, while along 45^o angular orientation of the FBG_2, R^2 was 0.87 and average sensitivity 0.06 με/gram.

3.5.2 Vehicle velocity

As the distance between the two FBGs is kept constant at 1000 mm throughout the experiment, the time difference between corresponding peaks 'P_1'and 'P_2'in the temporal responses of the FBGs has been taken to determine the velocity of the moving vehicle. The velocity of the vehicle is estimated at points 'P_1'and 'P_2', when the FBGs are oriented at angles 0^o and 45^o with respect to the line of motion and with varying loads in steps of 50 grams and the results are presented in Fig. 3.8.

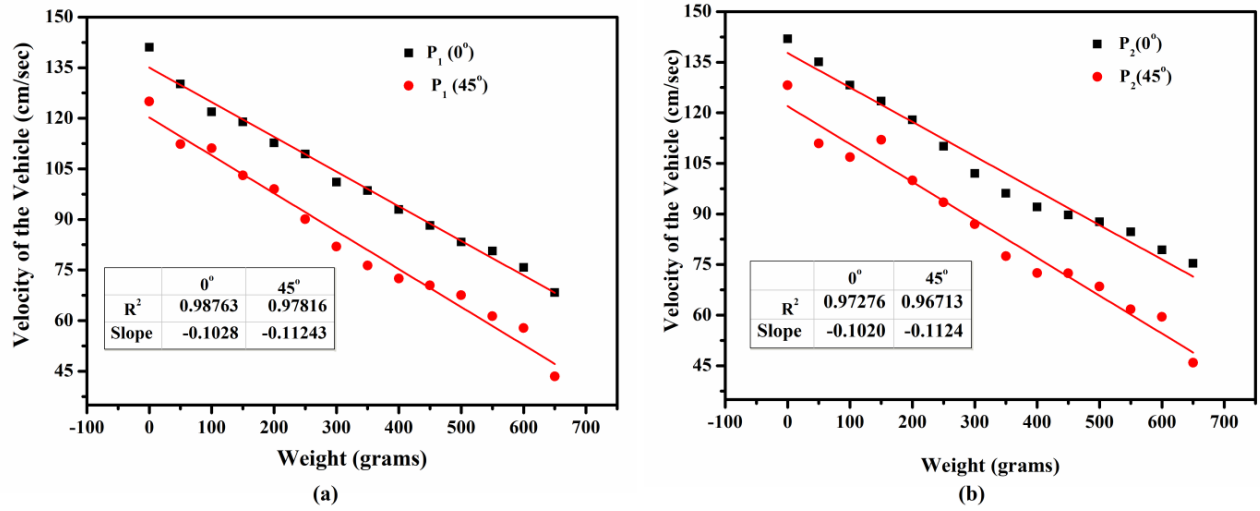

Fig. 3.8 Velocity of the vehicle (a) at Peak P_1, (b) at Peak P_2

From Figs. 3.8(a) and 3.8(b), it is found that, while the vehicle is moving over the bridge, the velocity of it evaluated at peak responses 'P_1' and 'P_2' when FBGs are placed at 0^o orientation to the line of motion has good linearity compared to FBG placed at 45^o to the line of motion. From these observations, the average speed of the vehicle is calculated with varying loads and the same is plotted in Fig. 3.9. These plots showed linear response with a coefficient of linearity 0.98 for parallel orientation of the FBG's (0^o) and 0.97 for FBG's fixed at 45^o angle with respect to the line of motion of the moving vehicle.

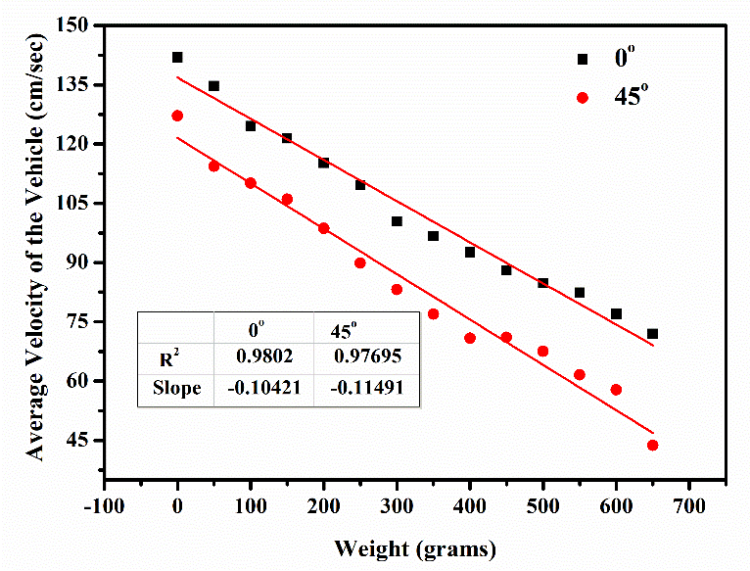

Fig. 3.9 Average velocity of the Vehicle

3.5.3. Weight of the vehicle

The load of the moving vehicle has been found by averaging the strains experienced by FBG at peaks, 'P_1' and 'P_2' of the temporal strain response curves and the results are presented in Fig. 3.10.

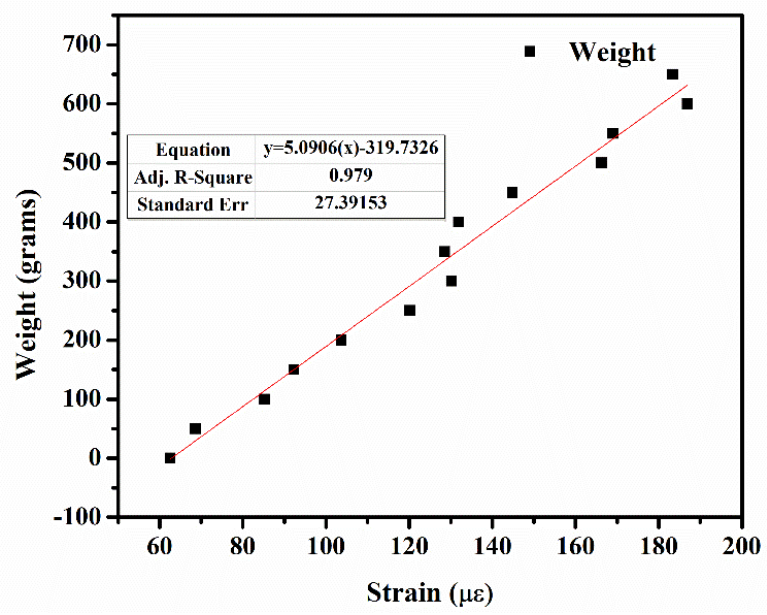

Fig. 3.10 Weight of the vehicle in terms of peak strain

From Fig. 3.10, it can be observed that the calculated weight of the vehicle using average strain experienced by FBG peaks 'P_1' and 'P_2' follows the relation as shown in Eq. (3.2).

$$\text{Weight of vehicle} = 5.09(\text{Strain}) - 319.73 \qquad Eq.(3.2)$$

The coefficient of correlation is high indicates that the designed system is able to estimate vehicle's load and velocity, while the vehicle is moving over the bridge.

3.5.4. Distance between the wheels of the vehicle

From the velocity calculations and considering the time difference between the points 'P_1' and 'P_2' of the FBGs, the separation between front and rear wheels of the vehicle (d_w=V*Δt) has been estimated to be 134.3 mm against the true value of 135 mm showing close agreement, as shown in the Fig.3.11.

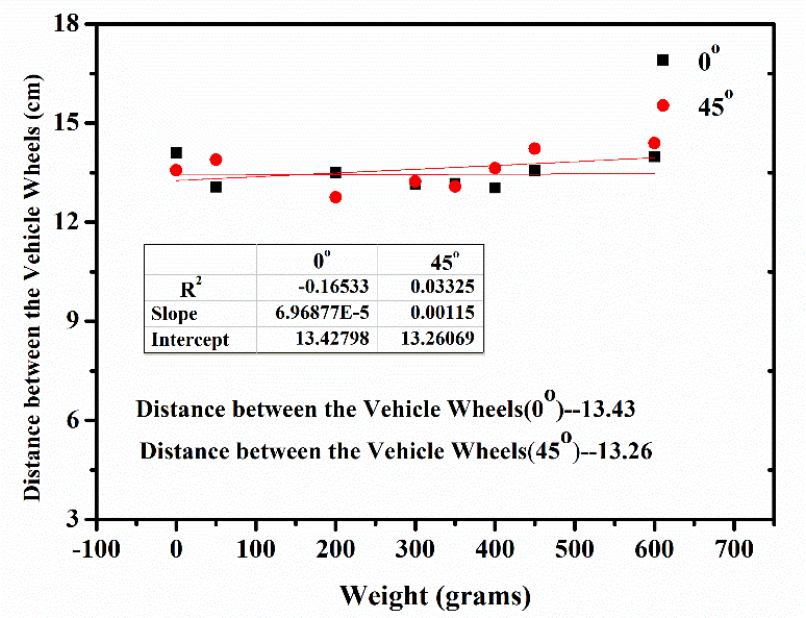

Fig. 3.11 Distance between the vehicle wheels

Thus, it can be concluded from the above experimental observations that, for a WIM system, with FBGs oriented at 90° to the line of motion of the vehicle is not helpful in monitoring the sructural health of a bridge, as their is almsot no response. It is also clear that the FBG placed parallel to line of motion is well suited due to uniform strain translation in the direction of the axis. This arrangement could hence estimate the strains,vehicle velocity, the distance between vehicle wheels and the weight of the vehicle with a high accuracy and so WIM system with FBG's oriented at 0° to the line of motion is an effective arragement.

3.6 Maximum Principal Strain of FBG

Considering the FBG's arrangement in the 0° and 45° orientations as a two element rosette as shown in Fig.3.12, and using the equations for the strains given by Eqs. (3.3)- (3.6) and Eq. (3.1) [20,21], the principal strains have been evaluated substituting the experimental

strain values for FBGs placed at orientations 0^o and 45^o to the line of motion (while avoiding strains along FBGs placed at 90^0 orientation, as the values are insignificant) and the results are shown in Fig. 3.13.

$$\varepsilon_{\phi} = (\varepsilon_x + \varepsilon_y)/2 + \cos 2\phi(\varepsilon_x - \varepsilon_y)/2 + \sin 2\phi\,(\gamma_{xy})/2 \qquad Eq.\,(3.3)$$

Where $\phi=0^o$, 45^o, 90^o as shown in Fig. 3.12,

$$\varepsilon_a = \varepsilon_x \qquad (0^0) \qquad Eq.\,(3.4)$$

$$\varepsilon_b = \frac{\varepsilon_x + \gamma_{xy}}{2} \qquad (45^0) \qquad Eq.\,(3.5)$$

$$\varepsilon_{1,2} = \frac{\varepsilon_x}{2} \pm \sqrt{\left(\frac{\varepsilon_x}{2}\right)^2 + \left(\frac{\gamma_{xy}}{2}\right)^2} \qquad Eq.\,(3.6)$$

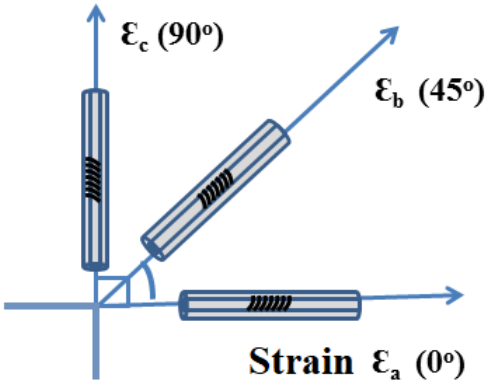

Fig.3.12 Strain at different angles of FBG

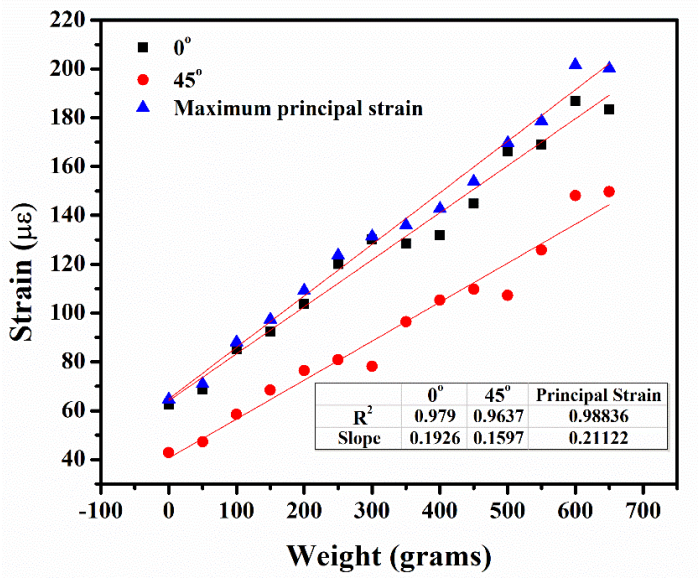

Fig.3.13 Maximum Principal Strain from Experimental Values

From Fig.3.13, it is observed that the maximum principal strains are nearly equal to the FBG placed along 0^o to the line of motion.

3.7 Numerical Analysis using MATLAB software

Owing to its small dimension, FBG can be considered as a point sensor in BWIM systems; which produce a change in wavelength shift corresponding to the strain experienced by it because of the applied load at the location where exactly FBG is situated. To determine the strain produced at a point in a beam employing FBG based strain sensor system, a simply supported beam with concentrated point load under static loading model has been employed. This is extended to dynamic situations as the strain experienced at a point and at a given instant can be interpreted from the dynamic response plot of the FBG.

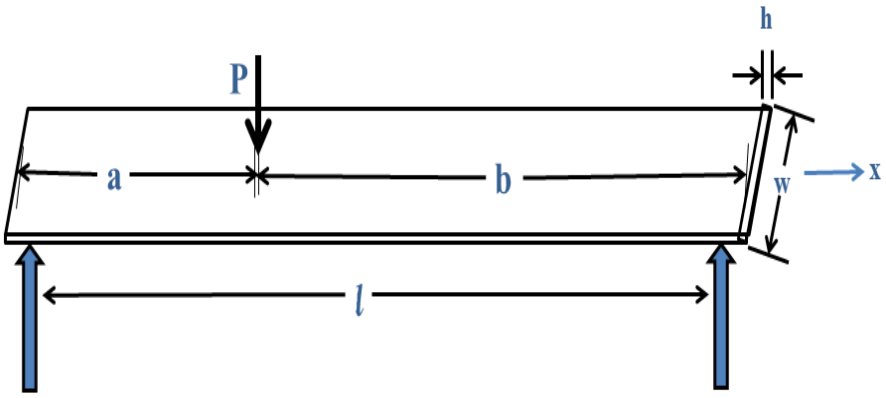

Fig.3.14 Simply supported beam with concentrated load

Considering, a beam of length ‘l’, width ‘w’ and depth ‘h’, supported by two firm supports as shown in Fig. 3.14, and assuming the thickness of the beam assumed is small compared to the length of the beam, the effects of shearing and rotatory deformation can be ignored. If load is applied at a point on the beam, the lateral displacement can be calculated using Euler-Bernoulli Equations (3.7) and (3.8) [22].

$$y = (Pbx / 6EIl)(l^2 - b^2 - x^2) \qquad (0 < x < a) \qquad Eq.(3.7)$$

$$y = (Pa(l - x) / 6EIl)(2lx - x^2 - a^2) \qquad (a < x < b) \qquad Eq.(3.8)$$

where, ‘E’ is the Modulus of Elasticity, ‘I’ is the Moment of Inertia and ‘P’ is the Load applied on the beam at a certain instant of time. In the present study, the material of the simulated beam is made of acrylic sheet with E=1.92 x 10^{14}gm. /cm^{2}sec^2, and Moment of Inertia I=0.3125 cm^4 ($I = bh^3/12$).

By using Equations (3.7) & (3.8) for the simply supported beam (bridge girder) mentioned above, the maximum deflection for varying loads at the centre of the beam where the FBG is attached is evaluated using MATLAB software and the results are presented as shown in Fig. 3.15 and the corresponding strain produced in the beam is calculated using Eq. (3.9).

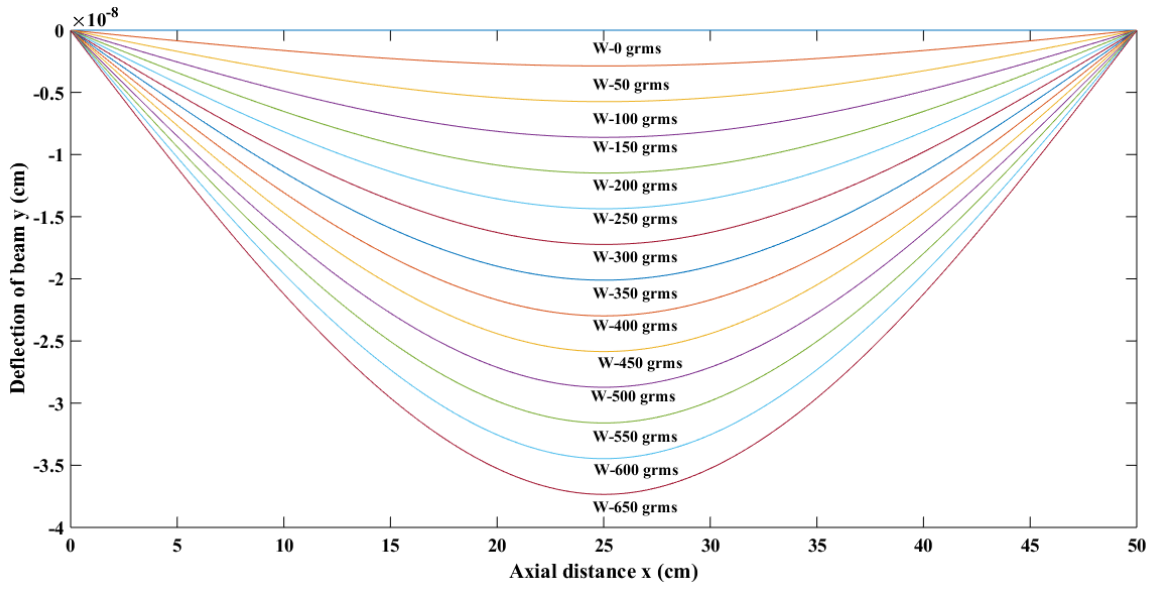

Fig.3.15 Beam deflection by varying loads

$$\text{Strain} = \frac{\Delta y_{max}}{(h/2)} \qquad Eq.(3.9)$$

Where 'Δy_{max}' is the maximum deflection obtained from the simulation. Half of the beam depth is used as a reference along vertical direction in calculating the strain under static load conditions.

3.7.1 Comparing experimental results with simulation results

Using equations (3.1) and (3.9), the strains induced at the central portions of the beam, where FBG_1 is attached have been evaluated and plotted as shown in Fig 3.16. Based on the simulation results for strains based on MATLAB, it can be observed that the plots are following a similar type of response. However, there is a small deviation between the simulated results of strain based on deflection from MATLAB and the experimental data from the FBGs oriented parallel to the axis. The error percentage is found to be less than 5%. The 45^o orientation of FBG details in the same plot is presented for information.

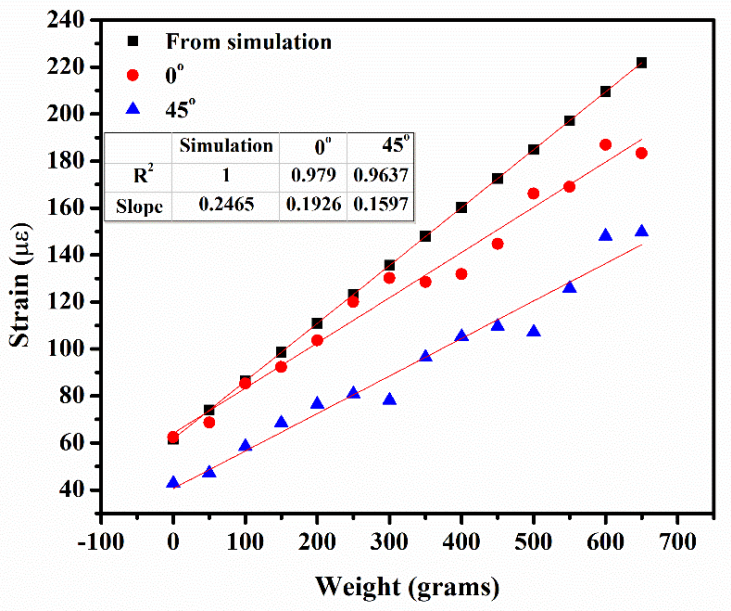

Fig.3.16 Comparison of simulation results with experimental results

Summary of Phase 1 work

1. A BWIM system is proposed using FBG based sensors to study the strain developed in the bridge deck and also to find the vehicle's parameters while it a loaded vehicle is passing over the bridge. Two FBGs have been employed in the present investigation, as a minimum configuration, at angular orientations of (0^o, 45^o, and 90^o) to the bridge axis, and an interrogator is used to acquire the data corresponding to the wavelength shift of FBGs.

2. The vehicle parameters like Load, Velocity and the separation between the front and rear wheels have been estimated from the temporal response curves of the FBGs and are found to be in close agreement.
3. The response of the proposed system is found linear with a good coefficient of average correlation of about 0.985 and an average sensitivity of 0.32με/gram along 0^o orientation of FBG to the line of motion of the bridge beam. The corresponding values for 45^o are 0.85 and 0.06με/gram respectively.
4. The experimental strain values are also observed to be in very close agreement with value simulated based on MATLAB.
5. It is hoped that use of more FBGs can improve the accuracy, however makes the measurements more involved, and increasing the cost of the system as well. Hence, numerical model analysis based on MATLAB is very useful in handling situations involving more experimentation and different conditions.

It is felt that a cost effective load measurement system which can automatically detect the changes from remote locations is needed for continuous monitoring the health of bridges. Chapter 4 deals with this idea.

References

[1] S. Kim, J. Lee, M.S. Park, B.W. Jo, Vehicle signal analysis using artificial neural networks for a Bridge Weigh-in-Motion system, Sensors. (2009). https://doi.org/10.3390/s91007943.

[2] A. Žnidarič, J. Kalin, Using bridge weigh-in-motion systems to monitor single-span bridge influence lines, J. Civ. Struct. Heal. Monit. (2020). https://doi.org/10.1007/s13349-020-00407-2.

[3] V. Gattulli, L. Chiaramonte, Condition assesment by visual inspection for a bridge management system, Comput. Civ. Infrastruct. Eng. 20 (2005) 95–107. https://doi.org/10.1111/j.1467-8667.2005.00379.x.

[4] D. Li, X. Li, Damage Detection with Symplectic Geometry Spectrum, 2 (2016) 116023. https://doi.org/10.1007/978-3-319-29751-4.

[5] J.M.W. Brownjohn, Structural health monitoring of civil infrastructure, Philos. Trans. R. Soc. A Math. Phys. Eng. Sci. (2007) 589–622. https://doi.org/10.1098/rsta.2006.1925.

[6] M. Lydon, S.E.S.E. Taylor, C. Doherty, D. Robinson, E.J.E.J. O'Brien, A. Žnidarič, Bridge weigh-in-motion using fibre optic sensors, Proc. Inst. Civ. Eng. Bridg. Eng. 170 (2017). https://doi.org/10.1680/jbren.15.00033.

[7] J. Wang, J. Tang, Feasibility of Fiber Bragg Grating and Long-Period Fiber Grating Sensors under Different Environmental Conditions, (2010) 10105–10127. https://doi.org/10.3390/s101110105.

[8] A. Sravanthi, R. Sai Prasad, P. RathishKumar, Cost-effective load measurement system for health monitoring using long- period grating as an edge filter, Opt. Fiber Technol. 59 (2020). https://doi.org/10.1016/j.yofte.2020.102328.

[9] C.A.R. Díaz, C. Leitão, C.A. Marques, M.F. Domingues, N. Alberto, M.J. Pontes, A. Frizera, M.R.N. Ribeiro, P.S.B. André, P.F.C. Antunes, Low-cost interrogation technique for dynamic measurements with FBG-based devices, Sensors (Switzerland). 17 (2017) 1–10. https://doi.org/10.3390/s17102414.

[10] P.S.S. Dos Santos, P.A.S. Jorge, J.M.M.M. De Almeida, L. Coelho, Low-cost interrogation system for long-period fiber gratings applied to remote sensing, Sensors (Switzerland). 19 (2019) 1–14. https://doi.org/10.3390/s19071500.

[11] R.K. Ramalingam, M. Klaser, T. Schneider, H. Neumann, Fiber bragg grating sensors for strain measurement at multiple points in an NbTi superconducting sample coil, IEEE Sens. J. 14 (2014) 873–881. https://doi.org/10.1109/JSEN.2013.2290153.

[12] A. Zrelli, T. Ezzeddine, Measurement of Temperature, Humidity and Strain Variation Using Bragg Sensor, Int. J. Math. Comput. Phys. Electr. Comput. Eng. 11 (2017) 167–170. https://doi.org/https://waset.org/Publications/measurement-of-temperature-humidity-and-strain-variation-using-bragg-sensor/10007063.

[13] G.P. Brady, S. Hope, A.B. Lobo Ribeiro, D.J. Webb, L. Reekie, J.-L. Archambault, D.A. Jackson, Bragg grating temperature and strain sensors, Tenth Int. Conf. Opt. Fibre Sensors. 2360 (1994) 510. https://doi.org/10.1117/12.184975.

[14] A. Sravanthi, P. Kishore, R.L.N. Sai Prasad, P. Rathish Kumar, Study of bridge weigh-in-motion using FBG sensors, in: Opt. InfoBase Conf. Pap., 2014: pp. 4–6. https://doi.org/10.1364/PHOTONICS.2016.Tu3G.3.

[15] H. lin Liu, Z. wei Zhu, Y. Zheng, B. Liu, F. Xiao, Experimental study on an FBG strain sensor, Opt. Fiber Technol. 40 (2018) 144–151. https://doi.org/10.1016/j.yofte.2017.09.003.

[16] A. Zninidari, J. Kalin, M. Kreslin, P. Favai, P. Kolakowski, Railway Bridge Weigh-in-Motion System, Transp. Res. Procedia. 14 (2016) 4010–4019. https://doi.org/10.1016/j.trpro.2016.05.498.

[17] C. Du, S. Dutta, P. Kurup, T. Yu, X. Wang, A Review of Railway Infrastructure Monitoring using Fiber Optic Sensors, Sensors Actuators A. Phys. (2019) 111728. https://doi.org/10.1016/j.sna.2019.111728.

[18] E.J. Obrien, M.J. Quilligan, R. Karoumi, Calculating an influence line from direct measurements, (2006) 31–34.

[19] W. He, T. Ling, E.J. Obrien, L. Deng, D. Ph, M. Asce, Virtual Axle Method for Bridge Weigh-in-Motion Systems Requiring No Axle Virtual Axle Method for Bridge Weigh-in-Motion Systems Requiring No Axle Detector, (2019). https://doi.org/10.1061/(ASCE)BE.1943-5592.0001474.

[20] James W.Dally, W. F.Riley, Experimental Stress Analysis, 3rd ed., Mc.Graw hill Inc., n.d.

[21] K. Helmi, T. Taylor, F. Ansari, Shear force – based method and application for real-time monitoring of moving vehicle weights on bridges, 26 (2015) 505–516. https://doi.org/10.1177/1045389X14529612.

[22] AWC, National Design Specification ® for Wood Construction Beam Design Formulas With Shear and Moment, (2007). http://www.awc.org/pdf/codes-standards/publications/design-aids/AWC-DA6-BeamFormulas-0710.pdf.

CHAPTER-4

COST-EFFECTIVE LOAD MEASUREMENT SYSTEM FOR HEALTH MONITORING

This chapter deals with developing a low-cost real time load measurement system employing Fiber Bragg Grating as a strain sensor and Long-Period Grating as an edge filter for structural health monitoring applications. Further for automatic detection, the sensed load has been transmitted via Bluetooth to a mobile, which can be employed for continuous monitoring of load on bridges to monitor the changes in the various elements like bridge girders (beams) from a remote location without the need for intervention of a bridge inspector.

4.1. Introduction

Most of the optical fiber based load measurements reported in literature employ cantilever based spring type load cell structures to which FBG's are glued; like Bimetallic cantilever [1], Fiber optic load cell [2], matched filter [3]; which have a very limited range of less than 1 kg. Online measurement of load for industrial applications, making use of binocular cantilever based load cell embedded with FBG; has very recently been reported and can go up to 8 kg of load [4]. This method has employed the transmitted spectrum of the FBG as edge filter for interrogation of the sensed data.

Even though FBG sensors offer great advantages in SHM, most of these systems involve expensive data logging devices like fiber interrogator and optical spectrum analyzer (OSA) which are bulky, expensive and interconnected through long fiber cables, and hence are not suitable for field applications; thereby; preventing their widespread usage in SHM. Also, wired architecture is generally not advisable in consumer-grade applications because of the deployment costs [5,6]. Therefore, widespread public use of SHM systems requires the use of inexpensive interrogation systems based on reliable wireless communications. To address this necessity, low-cost and wireless methods are being investigated [4,7].

Using edge-filter methods for signal acquisition and interrogation looks economical and effortless to implement in the field applications [4,7–9]. To reduce the cost of sensing, various interrogation techniques have been employed in the schematics of the FBG based sensors for signal extraction; the most popular being the conversion of wavelength shift into corresponding intensity variation; usually referred to as edge filtering, which is implemented

by convolving FBG spectra with that of edge filter spectra [10][11]. Many such schemes of edge filtering have been reported and some of which include; using FBG itself, Long period Grating (LPG), unbalanced interferometers, Fabry-Perot cavity filters etc. [12][13][14]. Out of these, LPG has been employed as an edge filter in the sensing circuit in the present study to replace OSA, because of low fabrication cost, compact size, ease of installation and good dynamic range together with sensitivity [7,8,15].

4.2. Brief theory about Components used in Experiment

4.2.1 Optical Circulator

An Optical Circulator consists of three ports. Light entering in to the one of the ports of the circulator is transmitted into the second port but not light reflected or exit from the third port. Fiber optic circulators are used to separate optical signals that travel in opposite directions in an optical fiber as shown in Fig. 4.1. Optical circulators are non-reciprocal optics, meaning that changes in the characteristics of light passing through the device are not reversed when light travels in the opposite direction. This only happens when the symmetry of the system is broken, for example by an external magnetic field.

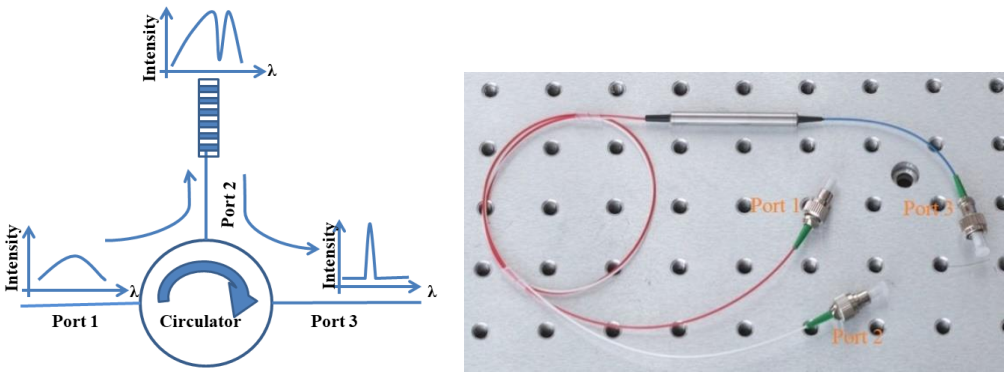

Fig. 4.1 Optical Circulator

4.2.2 LPG as an edge filter

LPG is similar to FBG with a relatively longer grating period which has characteristic light attenuation bands at certain wavelengths, where, the transmission of light becomes a minimum value, referred to as the central wavelength of LPG. On either side of it, the light transmission rises linearly and this region can be used as an edge filter in the optical sensors to convert the wavelength shift into corresponding intensity [16]. The typical transmission spectrum of LPG used in the present investigation; obtained by OSA; is presented in Fig. 4.2.

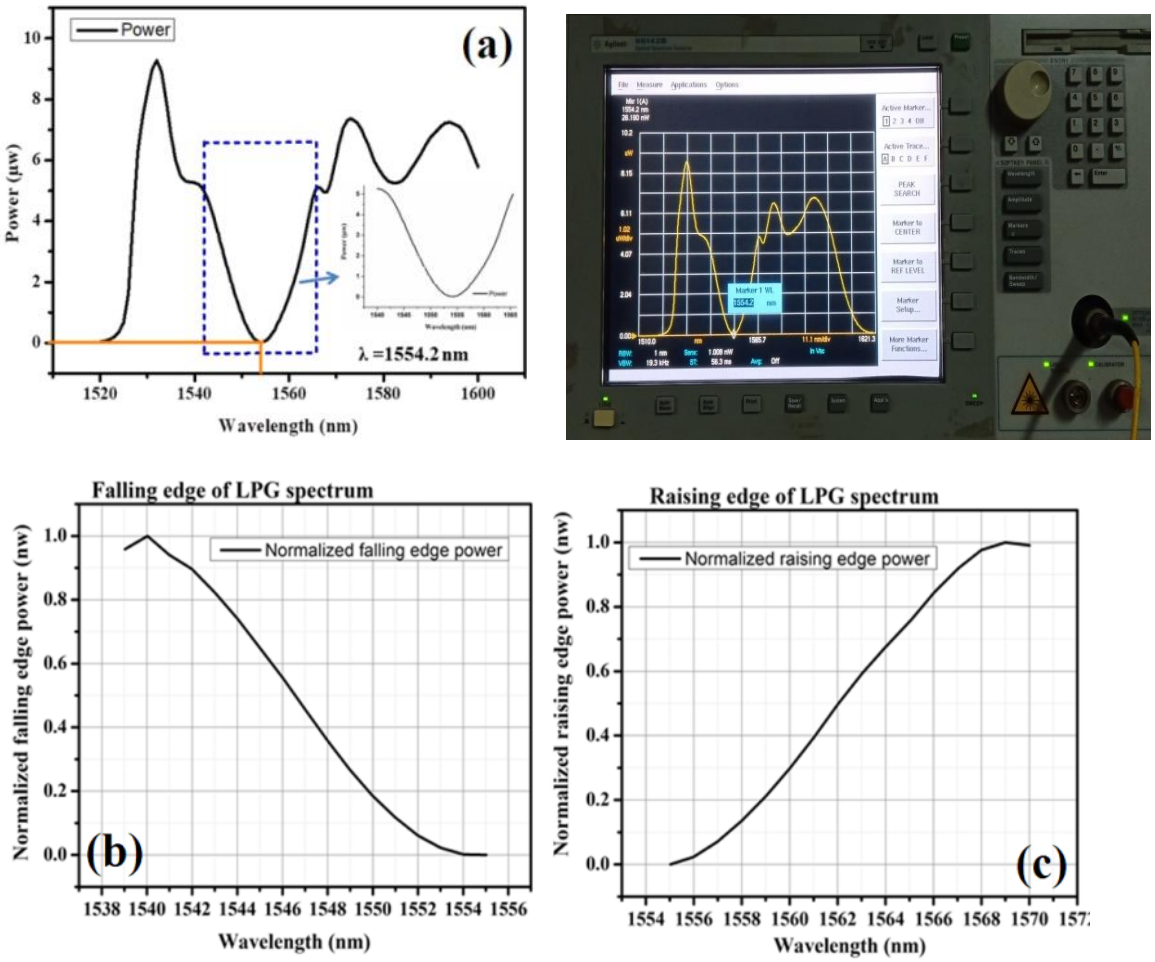

Fig. 4.2 LPG transmission spectrum. (a): Band rejection nature (b): The falling edge of LPG spectrum (c): The raising edge of LPG spectrum

From Fig.4.2 (a) it can be noticed that there is a sudden fall in the optical power of light at a particular characteristic wavelength of LPG due to resonance with several cladding modes (in a single-mode fiber) and the band rejection nature of LPG [17]; with its fallen and raised edges of the spectrum shown in Figs 4.2 (b) & 4.2 (c) respectively. The central wavelength of LPG employed in the present study is 1554.2 nm with 450μm grating length. The Bragg wavelength of FBG must be selected either in the rising edge or in the falling edge of the LPG spectrum, to use it as an edge filter. The optical power emerging out from the LPG will then be intensity-modulated in proportion to the shift in Bragg wavelength peak. In the present study; wavelength of the FBG is selected to lie in the falling edge of the LPG spectrum; with central wavelength 1546.5nm and giving 3μw optical power at this wavelength; as shown in Fig. 4.3.

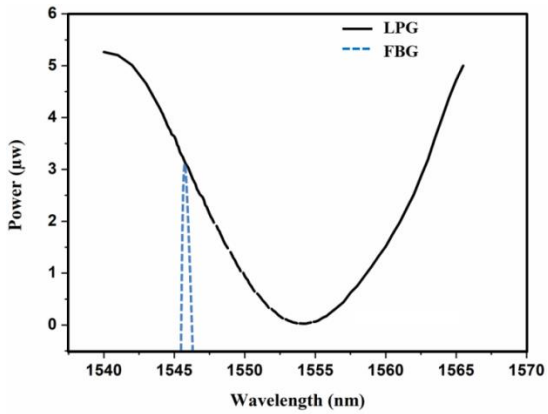

Fig 4.3 Selecting the FBG wavelength from LPG spectrum

4.2.3 Trans-Impedance Amplifier (TIA) as Signal Conditioning Circuit

A pigtailed photodiode followed by a multifunctional Trans-Impedance Amplifier (TIA) board (TWLUX TW30-series) has been employed for signal conditioning and to convert the detected light from LPG to current and subsequently to corresponding voltage signal [15,18] as shown in Fig. 4.4. This board has two amplifier channels with an adjustable gain range of $10^4 - 10^7$ V⁄A.

Fig. 4.4 Trans-impedance Amplifier circuit

4.2.4. Arduino Uno circuit with Bluetooth HC-05 module

Arduino Uno and HC-05 Bluetooth module have been employed for remote transfer of the sensed data. Arduino Uno is a 14 digital input/output pin compact microcontroller-based device programmed to accept the analog input from TIA at its pin (A0). The transmitter (Tx), and receiver (Rx) pins of the Arduino are connected to the HC-05 Bluetooth module of receiver (Rx), and transmitter (Tx) respectively to transfer the data to a mobile/ PC using software application as shown in Fig.4.5. The baud rate of the Arduino Uno is 9,600 Bd.

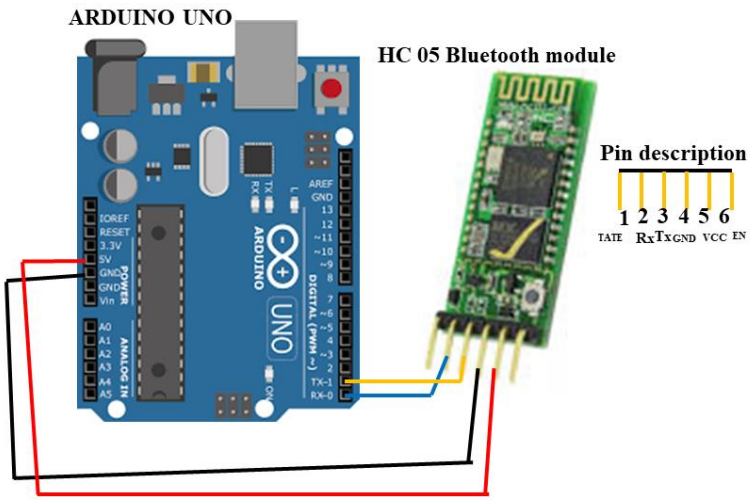

Fig. 4.5 Arduino Uno circuit with Bluetooth HC-05 module

4.3 Experiment and Results

In the present investigation, a prototype bridge girder made up of polyacrylic material, having young's modulus (E) 1.92×10^4 gram/mm^2, the moment of inertia (I) 3125 mm^4, and the material mass density (ρ) 1.19 gram/cc, with geometric measurements: length l=500 mm, width b=300 mm, and thickness h=5 mm has been employed. This is supported on two pairs of piers (supports), which are made up of aluminum material with a 30 mm diameter and 150 mm height. An FBG with a Bragg wavelength of 1546.5 nm at room temperature is attached at the center of the bridge beam for the measurement of load and for subsequent remote transfer of the same via Bluetooth. The flow chart is shown in Fig. 4.6.

Ambient temperature variations do have significant effect on the FBGs central wavelength λ_B and $\Delta \lambda_B$, We have not implemented the strain-Temperature discrimination as the experiments are carried out at room temperature. In real field situation, this compensation is necessary, and we need to employ a reference FBG on the specimen for this purpose.

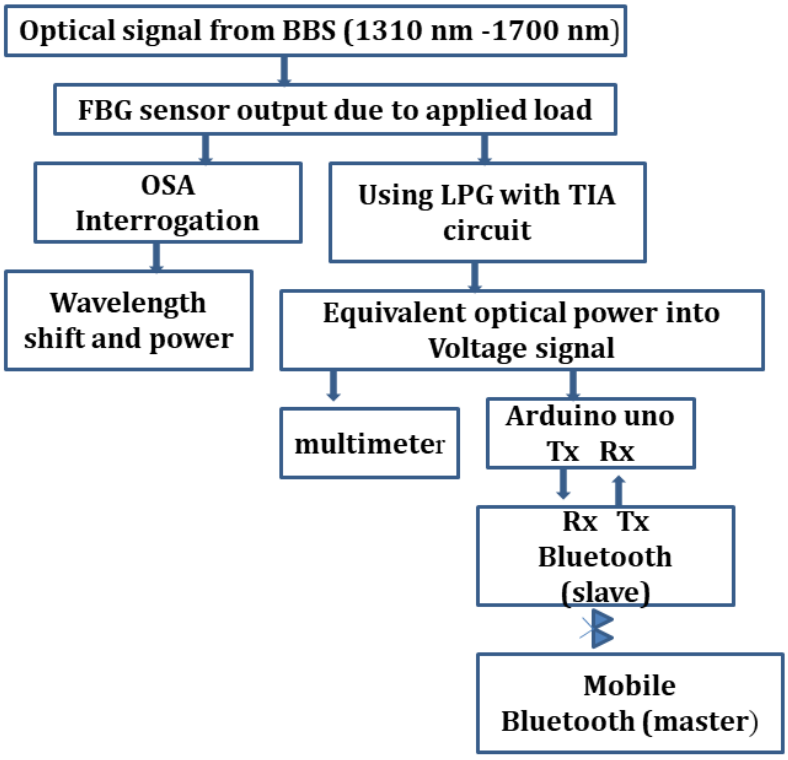

Fig. 4.6 Flow chart for work flow

4.3.1. Strain measurement using OSA

A schematic experimental setup for the strain measurement for an applied load on the bridge girder is shown in Fig 4.7. It consists of a broadband source of light (BBS-having a wavelength range of 1310 nm-1700 nm), a circulator and the prototype bridge. In Fig. 4.7 OSA based interrogation is represented. The BBS is connected to Port 1 of a three-port optical circulator which in turn couples the light to FBG that is connected to the Port 2. The reflected light from the FBG appears at the Port 3 of the circulator which in turn is connected to the OSA through LPG. OSA now gives the reflected Bragg wavelength for a particular load and the corresponding reflected power of light at that wavelength after edge filtering by the LPG.

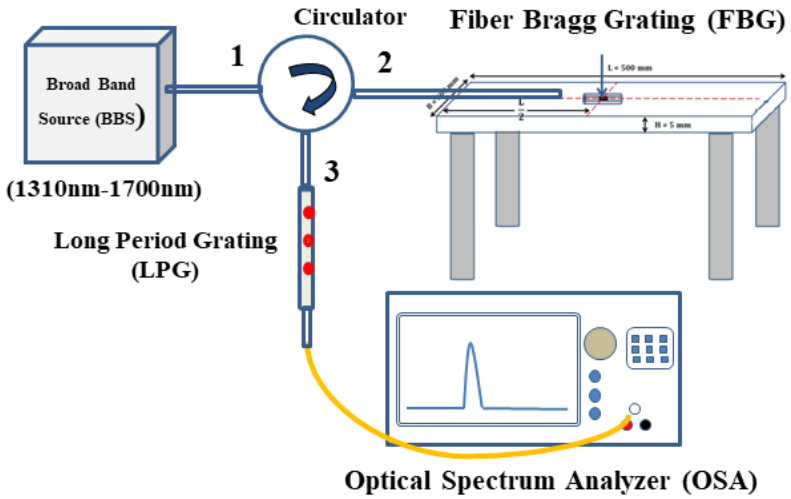

Fig. 4.7 Schematic experimental setup using OSA

The reflected Bragg wavelength and the reflected optical power are measured using OSA and are plotted against the applied load as shown in Fig. 4.8. The maximum load applied on the beam is 3,000 grams, with an increment of 100 grams, in each step. The downward displacement of the bridge beam causes an increase in the grating period of the FBG and this result in increase in the reflected Bragg wavelength.

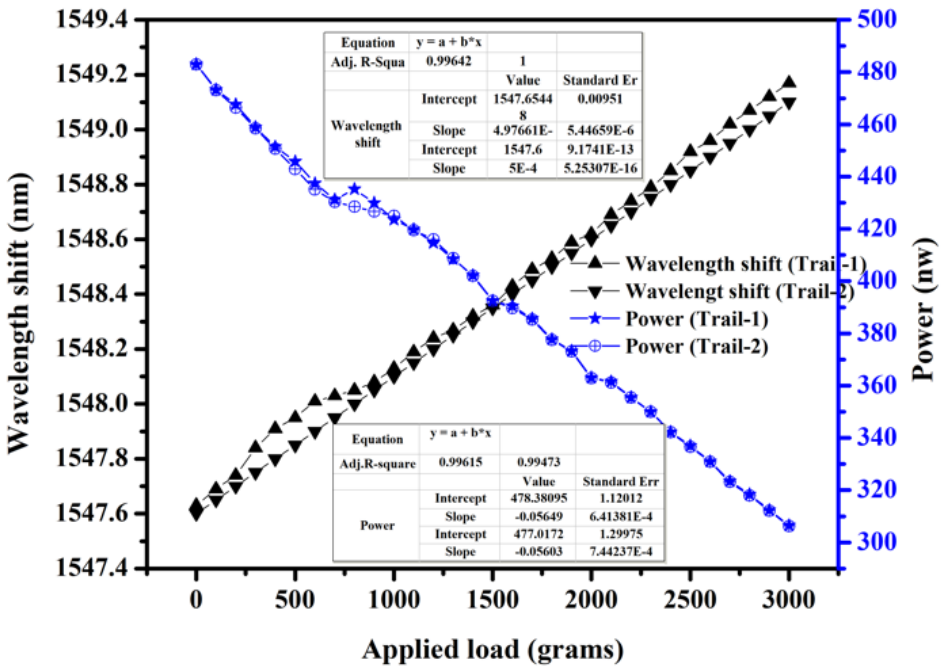

Fig. 4.8 Interrogation using OSA, measured shift in Bragg wavelength and optical power

As the trailing edge of the LPG spectrum is used in this investigation, the reflected optical power is decreased with increase in load as shown in Fig 4.8, which is indicative of the edge filtering characteristic of the LPG, since the power is measured after the LPG. There is a linear response with the applied load in terms of the reflected wavelength shift. The coefficient of correlation has been found to be 0.996. This indicates the consistency of sensor to the applied load.

The strain (ε) experienced by the bridge beam with load increments is calculated using Eq. (4.1).

$$\varepsilon = \frac{\Delta\lambda_B}{0.78(\lambda_B)} \qquad Eq.(4.1)$$

Where λ_B is Bragg wavelength of FBG and the results of the plot between strains vs. load increments is plotted in Fig. 4.9. The response of the FBG based system has been found linear and therefore can effectively be used to evaluate the strain in the bridge beams. The experiment is repeated twice to verify the repeatability and to check the performance of the designed system. The strain sensitivity of the FBG is found to be 0.41με/gram, which confirms that the system is highly sensitive and reliable.

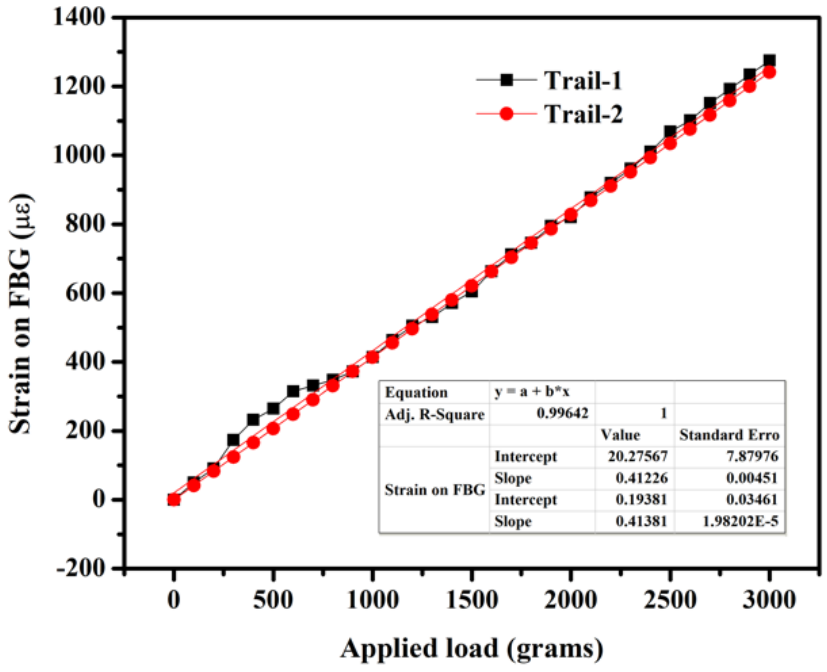

Fig. 4.9 Interrogation using OSA Corresponding strain

4.3.2 Measurement of applied load in terms of voltage

4.3.2.1 Voltage after TIA circuit With Multimeter

The most popular technique employed to extract the signal is to employ an Optical Spectrum Analyzer (OSA) or a commercial Interrogator; which are bulky and expensive and hence are not suitable for field applications. To overcome this difficulty and to reduce the cost of sensing, an LPG based interrogation technique has been designed for replacing the OSA as shown in Fig. 4.10.

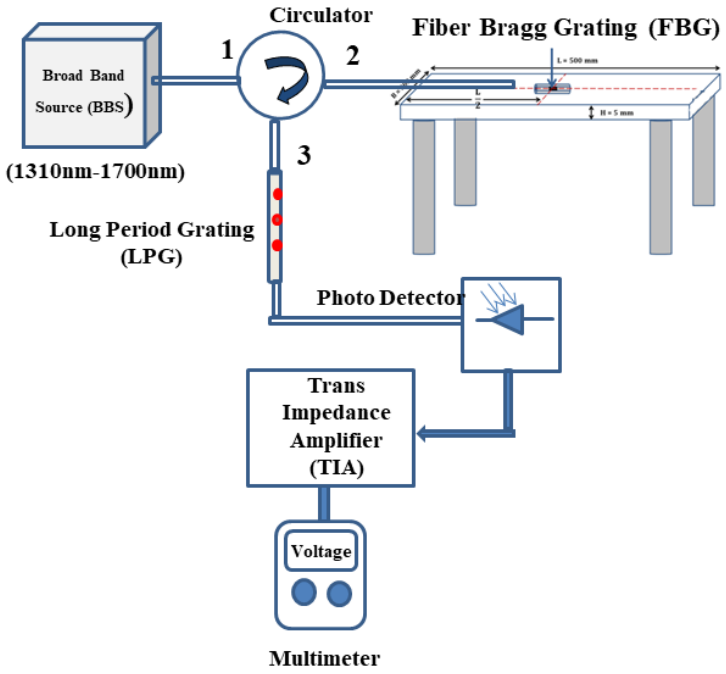

Fig. 4.10 Schematic **e**xperimental setup with multimeter

When a load is applied, the reflected wavelength from FBG at Port 2 of the circulator goes to Port 3, where, LPG is connected. This LPG acts as an edge filter and converts the wavelength shift into corresponding optical power. The other end of the LPG is connected to a pigtailed photo diode, followed by a Trans impedance amplifier circuit to convert this optical power into an equivalent voltage signal. The output voltage of TIA is then connected to a multimeter.

The response of the sensor is studied by varying the load at the center of the bridge girder where FBG is attached. Since FBG acts as an elastic element, the load applied must be limited to be within the elastic strain it can withstand, which is approximately 1% ($10^4 \mu\varepsilon$). This also depends on the elastic properties of the material on which the FBG is glued. Further, the Bragg Wavelength shift should be within the linear dynamic range of the chosen

edge filter characteristic. In view of this, the load applied in the present experiment is restricted to 3 kg. The shift in Bragg wavelength with applied load and the corresponding output voltage of TIA from the multimeter is noted and is shown in Fig. 4.11.

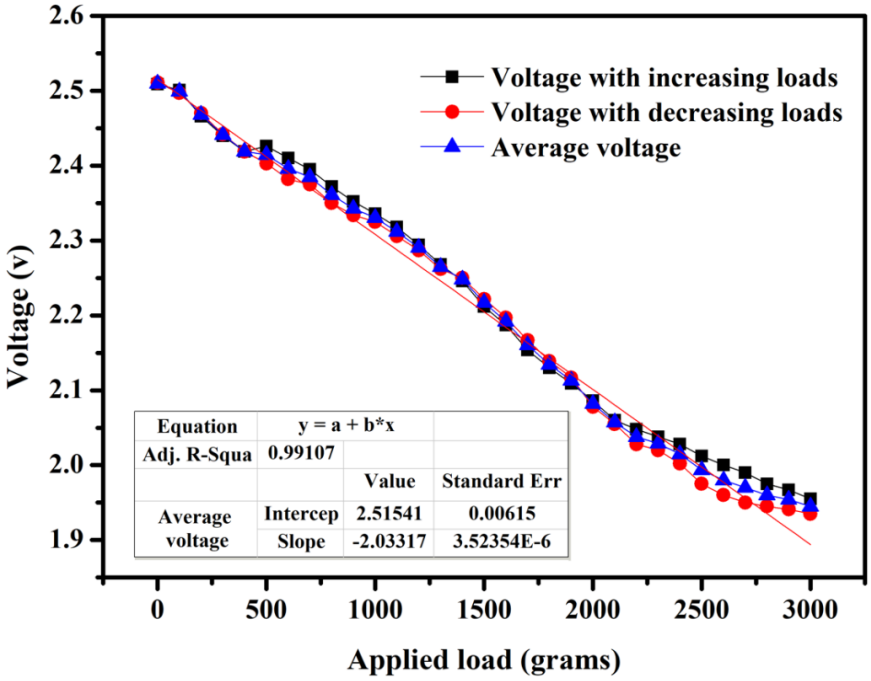

Fig. 4.11 Voltage response of the sensor using multimeter

Fig. 4.11 shows the measured voltages after TIA with multimeter. The experiment is repeated with increasing and decreasing loads varying between 0 grams and 3,000 grams with 100 grams interval. The average voltage has also been plotted. It can noted that with increase in the load, the voltage decreases linearly as the trailing slope of the LPG is used, and there is a good correlation (R^2 =0.99) with a standard error of 0.00615.

4.3.2.2 Voltage after TIA circuit with Bluetooth

For implementing the remote transfer of the sensed load data using the above experimental setup, the multimeter has been replaced with an Arduino Uno and Bluetooth module. The output of TIA is now connected to Arduino and the output of Arduino is connected to HC 05 Bluetooth module, enabling the data transmission to a mobile/ PC via Bluetooth as shown in Fig.4.12, and the photograph of the experimental setup is presented in Fig.4.13. The response of the sensor is studied by varying the load at the center of the bridge girder, where, the FBG is attached. The shift in Bragg wavelength with applied load, the corresponding output of TIA and the voltage received via Bluetooth have been recorded with change in the load in intervals of 100 grams up to 3Kg.

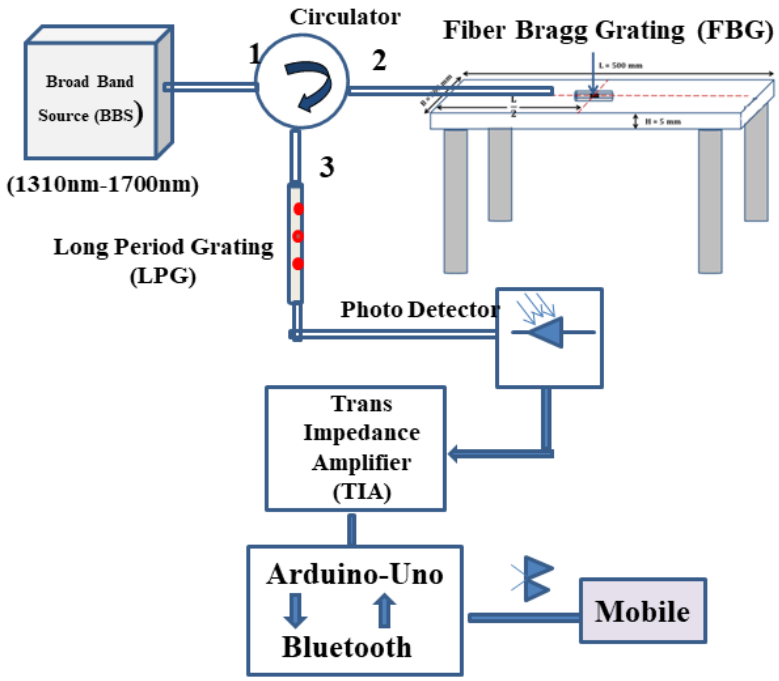

Fig. 4.12 Interrogation using proposed method

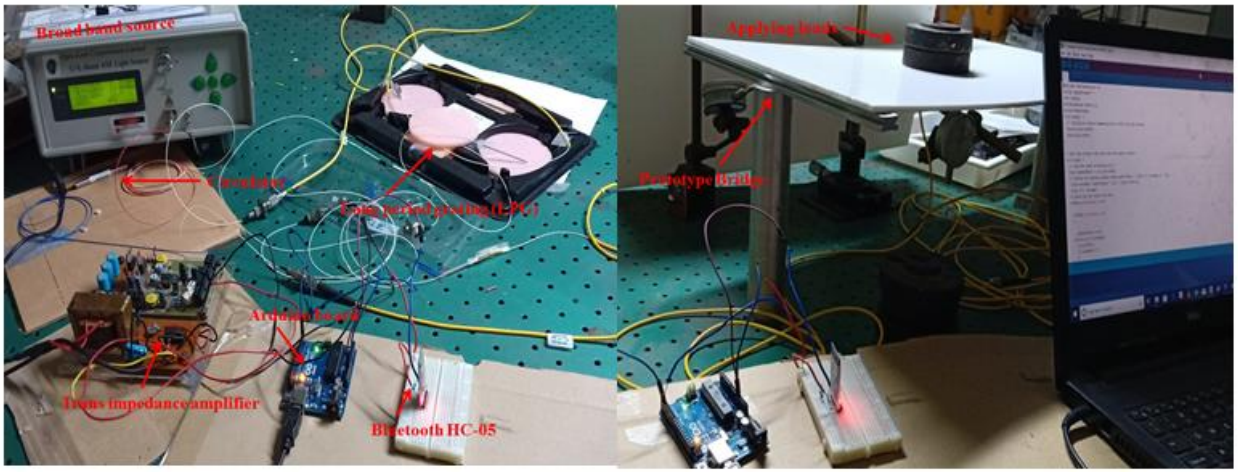

Fig. 4.13 Photograph if the Experimental setup

The output of TIA is coupled to the Arduino Uno board which is programmed to transmit the voltage signals over short distances via Bluetooth. The flowchart for programming the Arduino Uno is shown in Fig.4.14. With a command from the mobile through software application, the voltage can be displayed on the mobile. The baud rate of the Arduino Uno is 9,600 Bd.

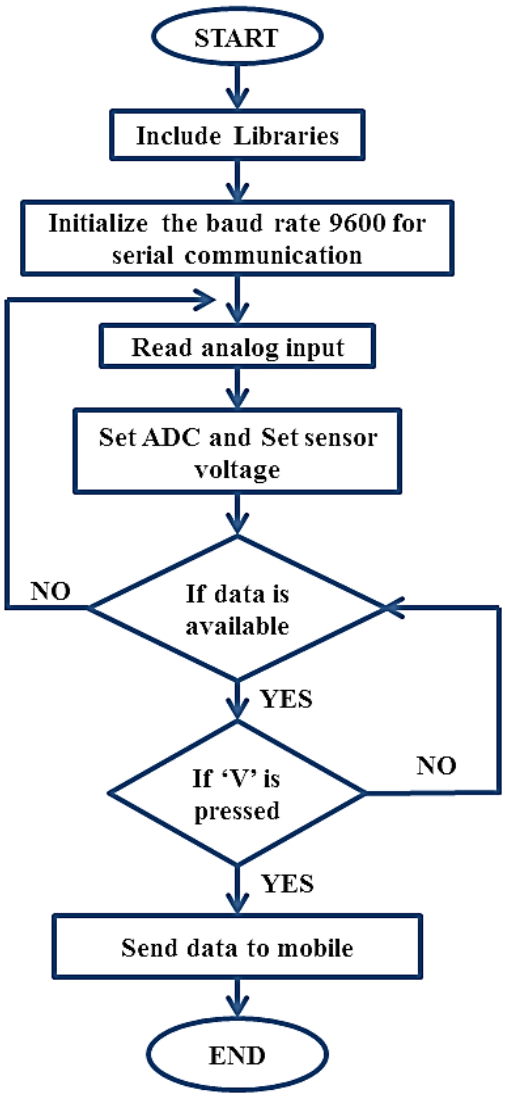

Fig. 4.14 Flowchart for programming Arduino Uno

This measurement system consists of an LPG, a PPD and a TIA to capture the sensor output. A commercially available PPD is used after the LPG for converting optical power into its equivalent current. TIA circuit acts as a current controlled voltage source and produces corresponding voltage signal. After applying load on the beam, the reflected wavelength from the FBG and the corresponding optical power edge filtered through LPG is rendered into a voltage signal using the PPD and TIA circuit. This voltage is transmitted via Bluetooth module to a mobile.

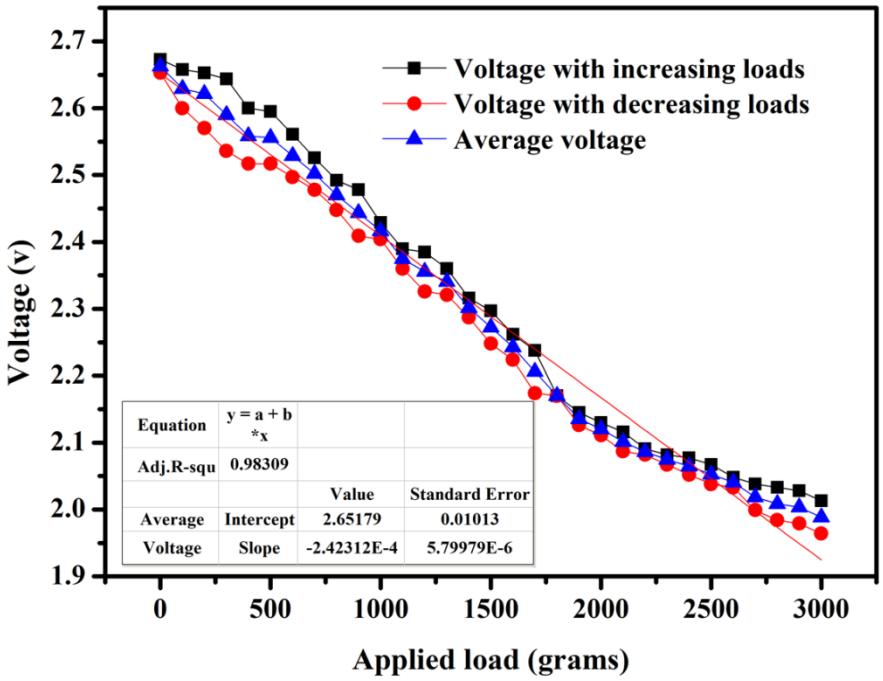

Fig. 4.15 Voltage response of the sensor after Bluetooth module

Fig. 4.15 shows the voltage received on the mobile for the applied loads. It is found that the average transmission voltage via Bluetooth is found linear with a correlation of 0.98 with a standard error of 0.010. To ensure the results and to check the repeatability, the experiment is repeated twice with increasing and decreasing loads and it is noticed that the voltage response after TIA from the multimeter and from the Bluetooth are well comparable.

4.3.3 Comparing voltages after TIA with multimeter and Bluetooth

The voltages measured at TIA and the voltages received on mobile were compared to evaluate the performance of the proposed system. Fig. 4.16 shows the response of the FBG sensor as the voltage signal is measured after TIA using a multimeter and voltage received on the mobile via Bluetooth module. In both cases, the response was found to be linear with a coefficient of linearity 0.987 and 0.983 respectively and with sensitivity – 0.002 mV/gr and – 0.0024 mV/gr respectively.

The main aim of conversion of wavelength shift to voltage has been to eliminate the presence of bulky and costly OSA. The linearity of this conversion mainly depends on the slope of the LPG response. The center wavelength of the FBG and LPG are to be properly selected such that the wavelength shift to voltage conversion should be in the linear region of the slope of the LPG characteristic. Athermalisation of LPG and FBG also is required in the

real field applications. We agree that the sensor is to be periodically recalibrated for obtaining accurate results.

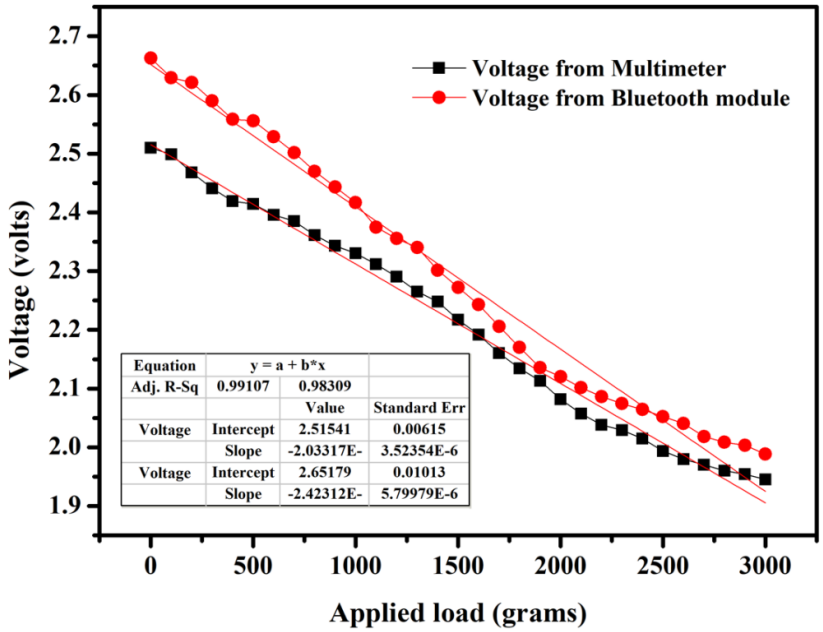

Fig. 4.16 Applied load vs. voltages observed at TIA using multimeter and Bluetooth module

From Fig, 4.16, it is observed that the multimeter voltage (TIA) recorded is lesser than the Bluetooth voltage data at the lower load regime. This is probably due to the fact that while performing with Bluetooth set up, the connections are firmly attached to the Arduino board whereas the multimeter voltage is measured manually. Manual measurement error may be the probable reason for this small discrepancy.

4.3.4 Performance of the sensor and load measurement

After analyzing the voltage response from Bluetooth, the circuit is calibrated using load and voltage relation, and the system is programmed to directly transmit the applied load to be displayed on the mobile via Bluetooth. The plot in the Fig. 4.17 shows the relation between applied load and displayed load. The graph has a linearity of 0.983 up to 3,000 grams weight (or equivalent force of 29.4 N) and a standard error of $\pm$50 grams which confirms the ability of the proposed system in field applications.

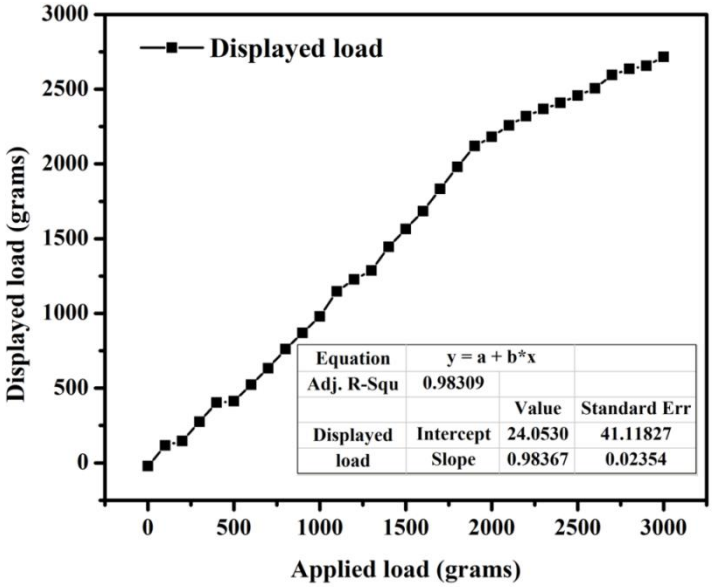

Fig.4.17 Displayed load on mobile corresponding to applied load

From Fig. 4.17, it is observed that the load displayed at the mobile device follows a different slope at 2000 gms. This may be due to the response being nonlinear.

Since the experiment is conducted on a prototype bridge beam which is made up of acrylic material of 5 mm thickness, the applied load is limited to 3000grams, taking into consideration that the maximum strain on the FBG is not greater than 1με.This can be up scaled to the actual field requirements taking into consideration the elastic modulus of the material used for the actual Bridges. This is also in accordance with the Airy's stress equation which is not dependent on the elastic properties ($\Delta^4\phi=0$) for a plane stress problem.

Summary of Phase 2 work

In the present work, an FBG based sensor for load measurement accompanied by a low-cost detection and remote transmission system employing Bluetooth has been designed and tested. The following are some of the broad conclusions:

1. A cost-effective measurement system has been adopted by employing an LPG as an edge filter to replace OSA with a simple PPD and TIA circuit.
2. The sensor output transmitted via Bluetooth to a mobile has been observed to accurately measure the load applied on the structure up to 3,000 grams with an error of ±1.67% (±50 grams).
3. The proposed system could measure the applied load on the structure and can be monitored from a distance of about 10 meters. This wireless and inexpensive method has

potential applications for remote load monitoring and can further be extended for online monitoring for higher transmission ranges by uploading this data to a cloud.

4. FBG sensor can be replaced with an etched FBG, POFBG to further improve the sensitivity of the proposed system.

This chapter presented a low cost load measurement system for remote monitoring of structure. Chapter 5 deals with the comparative study of strain measurements between FBG sensors and existing method Digital Image Correlation (DIC) with random speckle pattern distribution for dynamic monitoring on Accelerated Pavement Testing Track (APT).

References

[1] K. Tian, Y. Liu, Q. Wang, Temperature-independent fiber Bragg grating strain sensor using bimetal cantilever, Opt. Fiber Technol. 11 (2005) 370–377. https://doi.org/10.1016/j.yofte.2005.03.001.

[2] K. Nakamura, T. Matsumura, S. Ueha, A load cell using a fiber Bragg grating with inherent mechanical temperature compensation, Struct. Control Heal. Monit. 12 (2005) 345–355. https://doi.org/10.1002/stc.74.

[3] B. Varghese P, K.N. Madhusoodanan, P. Vinod, P. Radhakrishnan, A novel fiber Bragg grating sensor for measuring weight, Proc. - 2011 Annu. IEEE India Conf. Eng. Sustain.Solut.INDICON-2011.(2011)0–2. https://doi.org/10.1109/INDCON.2011.6139568.

[4] A. Gautam, A. Kumar, K. Kinjalk, J. Thangaraj, V. Priye, A Low Cost FBG Based Online Weight Monitoring System, IEEE Sens. J. 20 (2020) 4207–4214. https://doi.org/10.1109/JSEN.2019.2961688.

[5] C. Ayyildiz, H.E. Erdem, T. Dirikgil, O. Dugenci, T. Kocak, F. Altun, V.C. Gungor, Structure health monitoring using wireless sensor networks on structural elements, Ad Hoc Networks. 82 (2019) 68–76. https://doi.org/10.1016/j.adhoc.2018.06.011.

[6] J.P. Lynch, A Summary Review of Wireless Sensors and Sensor Networks for Structural Health Monitoring, Shock Vib. Dig. 38 (2006) 91–128. https://doi.org/10.1177/0583102406061499.

[7] P.S.S. Dos Santos, P.A.S. Jorge, J.M.M.M. De Almeida, L. Coelho, Low-cost interrogation system for long-period fiber gratings applied to remote sensing, Sensors (Switzerland). 19 (2019) 1–14. https://doi.org/10.3390/s19071500.

[8] S.C. Her, S.C. Chung, Dynamic responses measured by optical fiber sensor for structural health monitoring, Appl. Sci. 9 (2019). https://doi.org/10.3390/app9152956.

[9] C.A.R. Díaz, C.A.F. Marques, M.F.F. Domingues, M.R.N. Ribeiro, A. Frizera-Neto, M.J. Pontes, P.S. André, P.F.C. Antunes, A cost-effective edge-filter based FBG interrogator using catastrophic fuse effect micro-cavity interferometers, Meas. J. Int. Meas.Confed.124 2018) 486–493. https://doi.org/10.1016/j.measurement.2018.03.067.

[10] Y. Zhao, Y. Liao, Discrimination methods and demodulation techniques for fiber Bragg grating sensors, Opt. Lasers Eng. 41 (2004) 1–18. https://doi.org/10.1016/S0143-8166(02)00117-3.

[11] J.E. Alfonso, L.G. Cardenas, C.A. Triana, M.V. Duran, Design of an optical sensing interrogator using an edge filter scheme, SBMO/IEEE MTT-S Int. Microw. Optoelectron. Conf. Proc. (2013). https://doi.org/10.1109/IMOC.2013.6646509.

[12] A.D. Kersey, Interrogation and Multiplexing Techniques for Fiber Bragg Grating Strain-Sensors, in: Spiedigitallibrary.Org, n.d.: pp. 30–48.

[13] J. Cui, Y. Hu, K. Feng, J. Li, J. Tan, FBG interrogation method with high resolution and response speed based on a reflective-matched FBG scheme, Sensors (Switzerland). 15 (2015) 16516–16535. https://doi.org/10.3390/s150716516.

[14] C.A.R. Díaz, C. Leitão, C.A. Marques, M.F. Domingues, N. Alberto, M.J. Pontes, A. Frizera, M.R.N. Ribeiro, P.S.B. André, P.F.C. Antunes, Low-cost interrogation technique for dynamic measurements with FBG-based devices, Sensors (Switzerland). 17 (2017) 1–10. https://doi.org/10.3390/s17102414.

[15] V.R. Mamidi, S. Kamineni, L.N.S.P. Ravinuthala, M. Martha, S.S. Madhuvarasu, V.R. Thumu, High-temperature measurement using fiber Bragg grating sensor accompanied by a low-cost detection system, J. Appl. Remote Sens. 9 (2015) 094098. https://doi.org/10.1117/1.jrs.9.094098.

[16] R.P. Tatam, S.W. James, Optical fibre long-period grating sensors: characteristics and application, Meas. Sci. Technol. 14 (2003) R49–R61.

[17] C.Y. Lin, L.A. Wang, L.A. Wang, Corrugated long period fiber gratings as band-rejection filters, Conf. Opt. Fiber Commun. Tech. Dig. Ser. 1 (2000) 20–22.

[18] A.B. For, T. Sia, a By, V. For, Application Note Multifunctional 2-Channel Amplifier Board Application Note Multifunctional 2-Channel Amplifier Board, Comp. A J. Comp. Educ. (n.d.) 1–5.

CHAPTER-5
COMPARATIVE STUDY BETWEEN DIGITAL IMAGE CORRELATION AND FIBER BRAGG GRATING SENSORS

Digital Image Correlation (DIC) techniques is a popular tool that involves measurement of displacements, strains making use of a random speckle pattern drawn on the specimen under study: A comparison is made between the deformed and undeformed images which is useful in SHM applications. FBG based sensing and analysis of strains in engineering structures has been a growing area of research in SHM applications. The present chapter deals with a comparative study between DIC and FBG methods of analysis. The study has been carried out in two phases: In the first phase experimental study on the dynamic monitoring of an Accelerated Pavement Track (APT) using FBG and DIC techniques is undertaken, while in the second phase, numerical analysis using Finite Element Method (ABAQUS software) is carried out on APT. The results are compared with the values obtained from experimental results on FBG based method.

5.1. Theory

5.1.1. Digital Image Correlation (DIC)

DIC gives the details of displacements and strains developed in the selected Region of Interest (ROI) by correlating results between the undeformed and deformed states of an object. Speckle's criterion is mandatory for this correlation. In DIC method, a reference image is drawn on the specimen, in the form of random speckle pattern. This image is captured initially, and following this, the deformed images are captured subsequently as loads are applied on the specimen [1]. The main concept of DIC method is a one to one correspondence between reference and deformed images as shown in Fig.5.1. Initially, the speckles present at the reference point (x, y) in the undeformed state will now be considered at $(x^{'}, y^{'})$ in the deformed state. The DIC finds a selected subset of the reference image and a corresponding position in the deformed image. Once the location of the subset is matched in deformed images with the reference image, correlation criteria is established between the two images by using Eq.(5.1).Then, each subset of the deformed image is matched with the subset of reference image, with each deformed image having its individual deformations. The results will be Lagrangian displacements and strains developed in the deformed state of the specimen with respect to the reference image.

If F(x,y) and G(x',y') are the grey scale intensity functions of the images at reference and deformed states of the specimen respectively, the correlation represented as 'C' in Eq.(5.1) shows the similarity between the reference and deformed state images. The Correlation value varies between -1 to +1 depending on the similarity between the two images [2–4].

$$C = \frac{\int_{M} \left(F(x,y)\right)\left(G(x'+U, y'+V)\right)dA}{\left[\int_{M} [F(x,y)]^2 dA \int_{M} [G(x'+U, y'+V)]^2 dA\right]^{1/2}} \qquad Eq.(5.1)$$

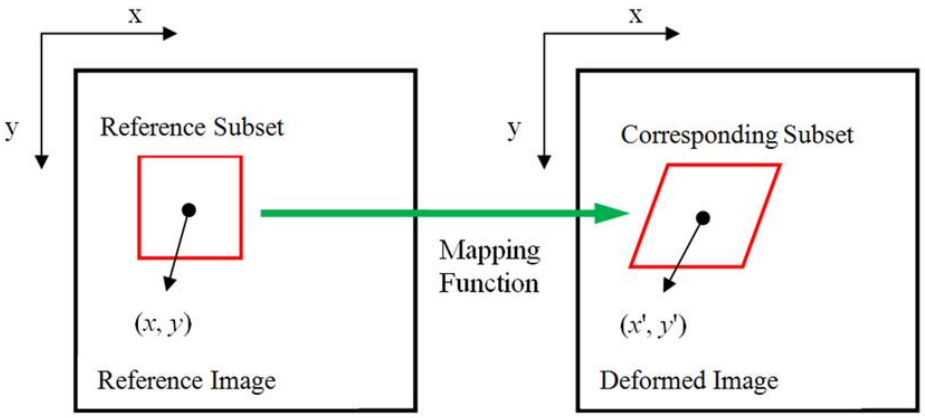

Fig. 5.1 Reference and deformed images

5.1.2 Computation of strain measurement

The measured displacement fields (u, v) have been converted into Cartesian coordinate system (x, y) and the strain matrices are calculated using Eq. (5.2) to Eq. (5.4). Displacement gradients are determined in order to get the strain at any point in a body. Four displacement gradients have been used to find the Lagrangian strains, as follows [5]:

$$\varepsilon_{xx} = \frac{1}{2}\left[2\frac{\partial u}{\partial x} + \left(\frac{\partial u}{\partial x}\right)^2 + \left(\frac{\partial v}{\partial x}\right)^2\right] \qquad Eq.(5.2)$$

$$\varepsilon_{xy} = \frac{1}{2}\left[\frac{\partial u}{\partial y} + \frac{\partial u}{\partial x}\frac{\partial u}{\partial y} + \frac{\partial v}{\partial x}\frac{\partial v}{\partial y} + \frac{\partial v}{\partial x}\right] \qquad Eq.(5.3)$$

$$\varepsilon_{yy} = \frac{1}{2}\left[2\frac{\partial v}{\partial y} + \left(\frac{\partial u}{\partial y}\right)^2 + \left(\frac{\partial v}{\partial y}\right)^2\right] \qquad Eq.(5.4)$$

5.1.3 Methodology

Two dimensional DIC technique involves three consecutive steps: (1) Spraying speckle pattern on the specimen surface in order to obtain random grey scale intensity distribution, (2) Capturing the digital images of both undeformed and deformed specimen surfaces using DSLR camera and (3) Post processing the images with Ncorr V1.2.2 DIC software for obtaining full-field displacements and strains. This method gives the image information in the form of pixels, as well as strain and displacement of a specimen. The minimum deflection/strain expected is in the order of 0.01 mm/micro strains [6].

5.1.4 Specimen preparation

Preparation of the specimen plays a vital role in DIC method. The specimen should be clean and dry and any dust particles or moisture is to be removed on the surface of the specimen. Randomness in the speckles on the surface of the specimen is also very important in specimen preparation in order to obtain good results. A good speckle means the size of the speckle is three times the size of pixel from the captured image. The material used for the simulated pavement model of the study is an acrylic sheet white in colour. The surface was thoroughly cleaned with acetone and then black speckles were painted taking enough care to maintain the randomness and the size of the speckles [7].

5.1.5 Capturing of images

DIC is mainly influenced by the image quality for providing accurate values of deformations and strains. If the images are poor, the algorithm does not give good results. The quality of the image depends on the illumination condition on the specimen, capturing of the image and the camera settings. Uniform brightness is very important and the lighting should not change during the experiment. It is preferable to use LED lights for illuminating the specimen in DIC. While capturing the images, the camera has to be kept in stable position to avoid vibrations. The legs of the camera tripod should be stable. Even the manual triggering for capturing the images can make some movement and to avoid this, use of wireless triggers is highly recommended to click the camera for capturing the images. ISO setting in the camera should be appropriate based on the lighting for excellent resolution and quality of the images. In the present study, images were captured using Nikon DSLR Camera D5200, with a width of 6000 pixels and height of 4000 pixels, ISO-400, focal length of 18mm, focal speed f/3.5, and shutter speed of 1/125 s. The DC regulated power supplied LED was used for producing uniform illumination without fluctuations, while, wireless remote-control triggering was used for capturing images to avoid vibrations [8–10].

5.1.6 Strain computation process in Ncorr V1.2.2 software

In DIC, several steps are involved in the calculation of strains and displacements. The step by step procedure involved in the calculation of strains and displacements in DIC is represented in the flow chart shown in Fig. 5.2.

It is required to import the reference image first, followed by the import of the sequence of deformed images. After that, subset selection divides the reference image into small sections and is then compared with the deformed image. To find the similarity between reference and deformed image, cross correlation function is used. At the matching point, the peak correlation is formed. Once the correlation is matched with reference and deformed images, the software will start calculating displacement in the form of pixels, which it then converts into engineering units. Later, it compares this with initial lengths and gives inputs with regard to the strains [11,12].

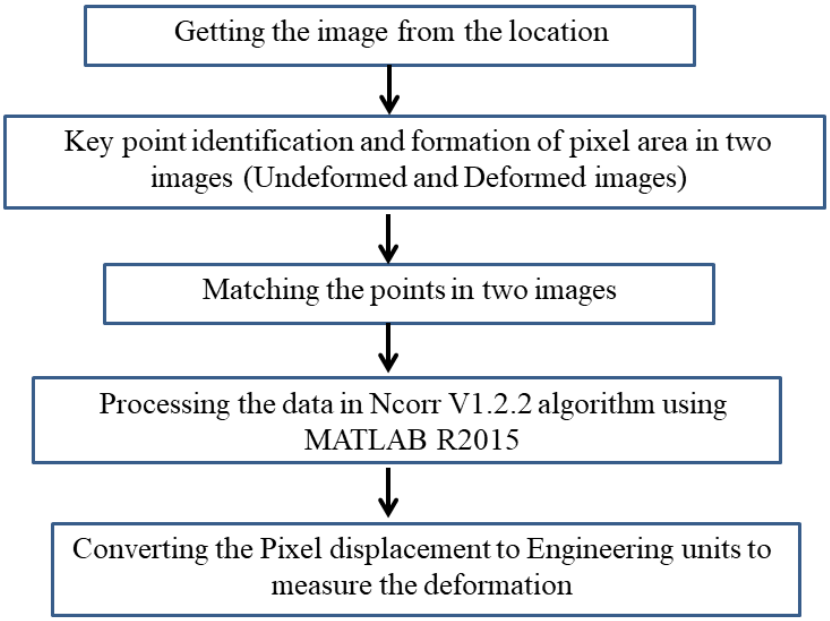

Fig. 5.2 Flow chart of DIC technique

5.2. Experimental setup

Accelerated Pavement Track (APT) is primarily used to understand pavement behavior in SHM for the design and rehabilitation of pavements, which suffer from low priority maintenance and limited pavement care applications. In most parts of the world, road authorities are spending much on pavement maintenance in place of new construction. Hence, studies on the test set up as APT was done for rapid comparison and evaluation, to enable the selection of appropriate treatment [13].

An Accelerated Pavement Track (APT) of 54.5 cm inner diameter and 33 cm width made of poly-acrylic sheet of 5mm thickness was used in the present investigation. Three random speckle patterns were drawn on the pavement surface; each pattern was of 11 x 11 cm^2area, the first one near the inner edge, the second at the outer edge and the third in the middle of the pavement track for DIC recording. A Nikon D5200 DSLR camera with 24.1 Megapixel DX-format CMOS sensor was used to capture the images from the top view of the experimental setup, without interrupting the testing process as shown in Fig. 5.3.

An array of three FBGs, having Bragg wavelengths of 1528.33nm, 1534.55nm, and 1545.96nm respectively, were pasted in the tension part of the pavement along the line of motion (0^o) where speckle patterns are drawn as shown in Fig. 5.4. The FBGs were connected to the Interrogator (Micron Optics SM 130) for scanning FBG data for further analysis with the help of Enlight software. The experiment was repeated with the FBGs at 45^o to the line of motion.

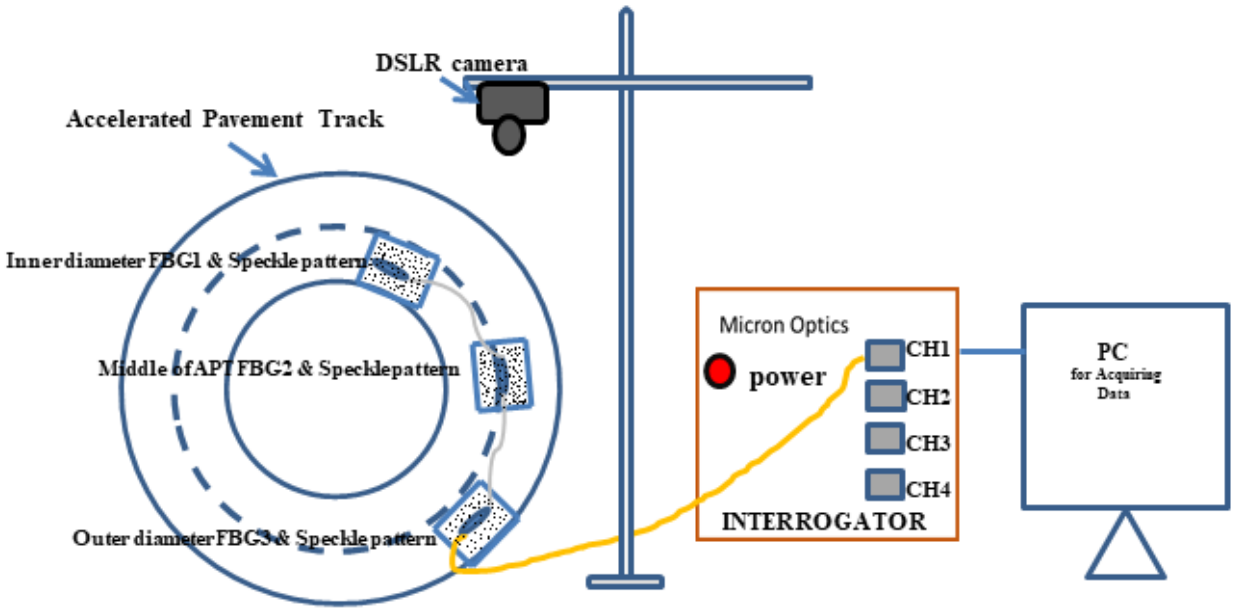

Fig.5.3 Schematic experimental setup

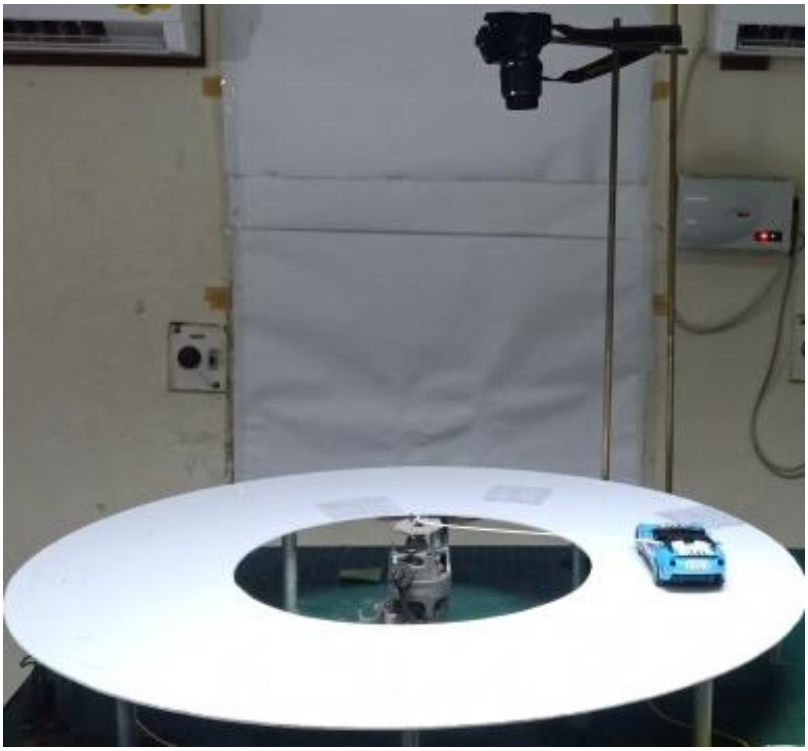

Fig.5.4 Experimental setup

5.2.1 Experimental Procedure

A remote-controlled car has been used to encircle on the pavement surface with varying loads and for required number of rotations on the APT. First, the experiment is conducted with the dead load (200grams) of the vehicle and varying the number of rotations from a minimum value of 10 to a maximum value of 30 with increments in steps of 5 rotations. The experiment is repeated by varying the loads on the vehicle in the range of 0 grams to 300 grams in steps of 50 grams each for acquiring the DIC data. Simultaneously, the temporal response of the FBGs is obtained for the corresponding loads and number of rotations using the Micron Optics Interrogator for comparison.

A reference image has been taken before, without applying loads and rotations of the vehicle on the APT, and a sequence of images were taken with the Nikon D5200 DSLR camera for each desired number of rotations completed and for different loads. After capturing the sequence of images, image processing is done by Ncorr V1.2.2 open source DIC code using MATLAB R2015a software, the flowchart as shown in Fig. 5.5.

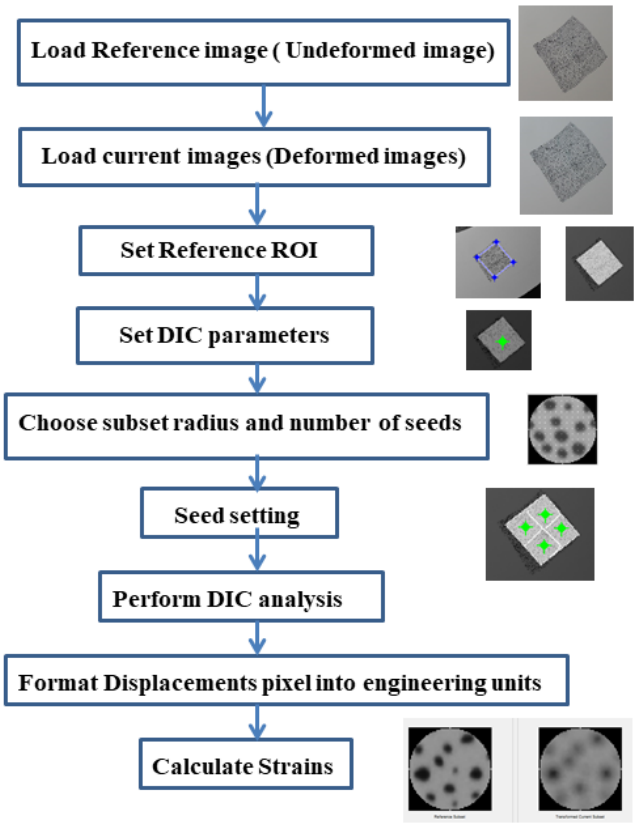

Fig.5.5 Flow chart of DIC Technique in MATLAB Ncorr V.1.2.2

The optimal radius of subset was found to be 15 mm with subset spacing of 1mm for the present investigation. Fig. 5.6 shows the grey scale intensity distribution and histogram of speckle pattern, with Fig. 5.6(a) & 5.6(c) for case without applying loads and rotations while Fig. 5.6(b) & 5.6(d) indicate the condition for maximum load with maximum number of rotations of a vehicle.

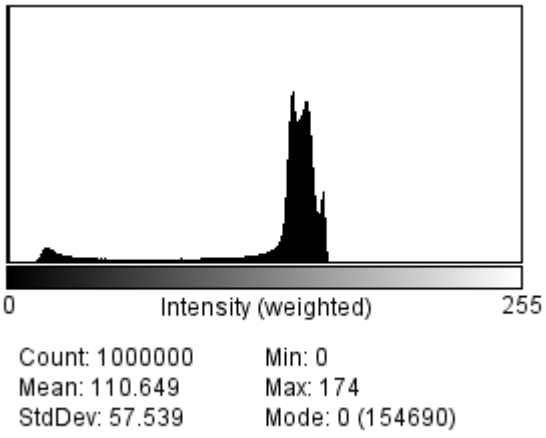

(a)

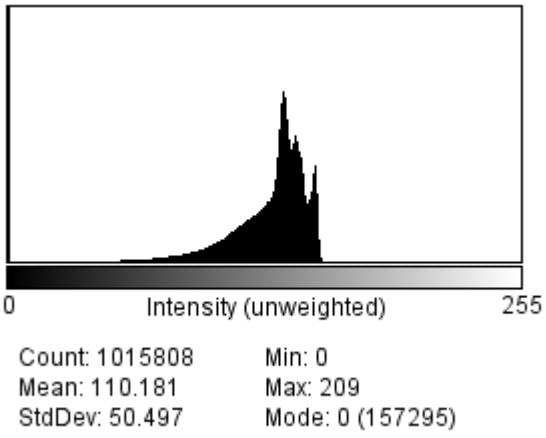

(b)

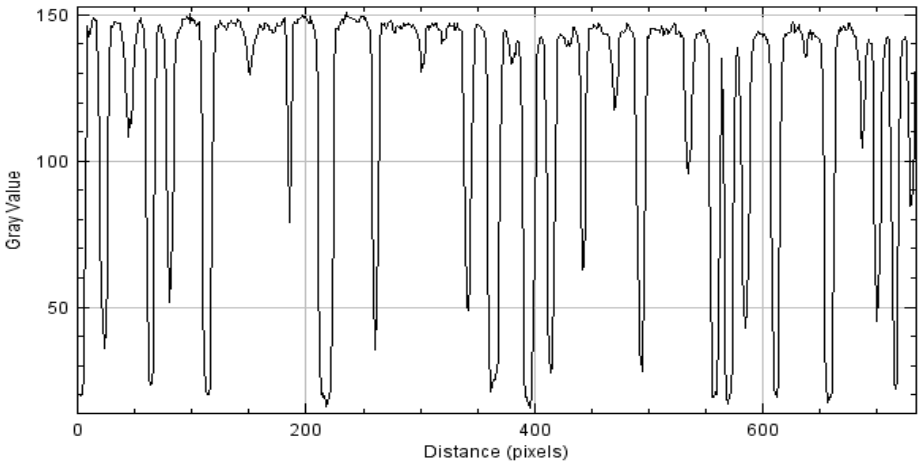

(c)

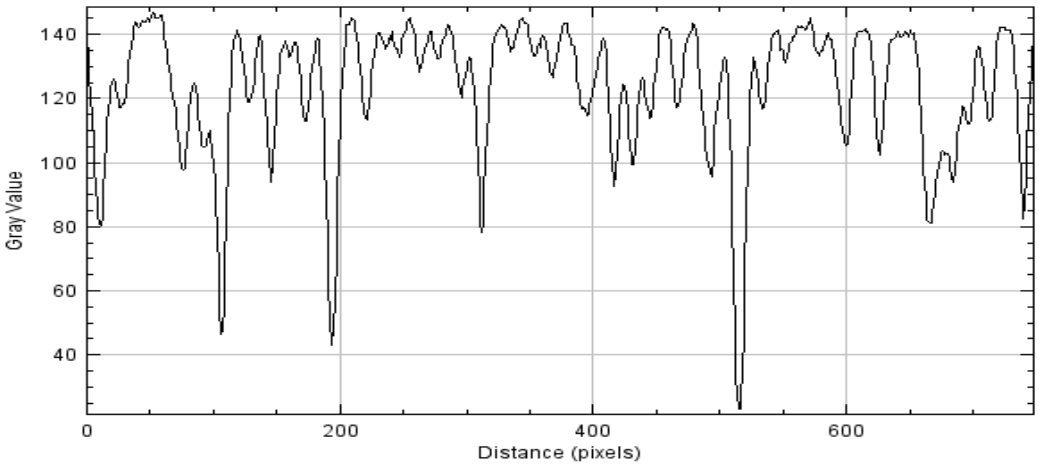

(d)

Fig. 5.6 Histogram and Surface distortion of speckle pattern, (a) & (c) Reference image (b) & (d) after 30 rotations with maximum load

5.3 Results and discussion

5.3.1 DIC Results

The experimental analysis was carried out for three Regions of Interest (ROI); namely the inside, middle and outer diameters of the track, where, the speckle patterns were drawn for evaluation of the type of strains. First, the load on the vehicle was altered for each number of preferred rotations starting with the dead load of the vehicle. Fig. 5.7 (a) shows the speckle pattern in the middle of the APT, which is one of the ROIs for the computation of the strains, and the strain field distribution after computation using DIC (Fig.5.7 (b)). As the vehicle passes over the pavement track; based on the correlation between the images before and after the application of the loads on the vehicle; the strains have been computed using DIC technique along ε_{xx}, ε_{xy} and ε_{yy} directions- with variation of live load on the vehicle (ranging

from 0 grams to 350 grams in steps of 50 grams), and the number of rotations of travel of the vehicle (10 to 30 rotations in steps of 5 rotations) in all three ROIs respectively. The results presented in Fig.5.8, Fig.5.9 and Fig. 5.10 respectively are for the above three ROI's.

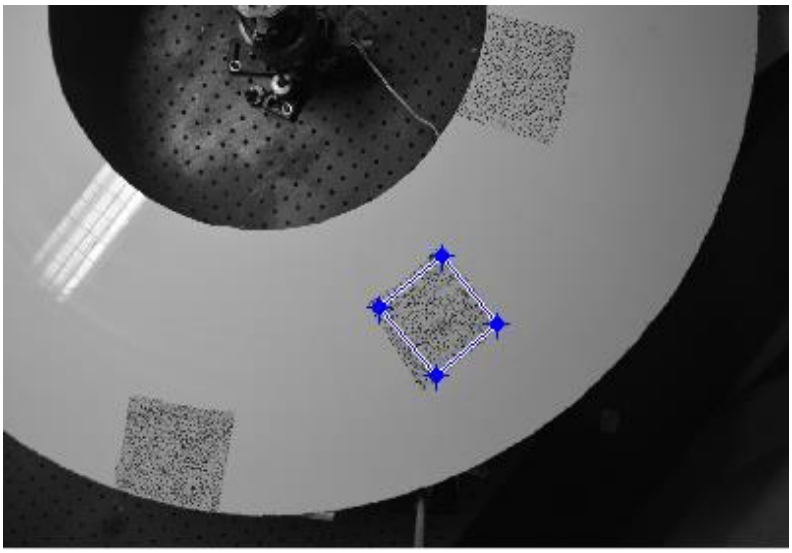

(a)

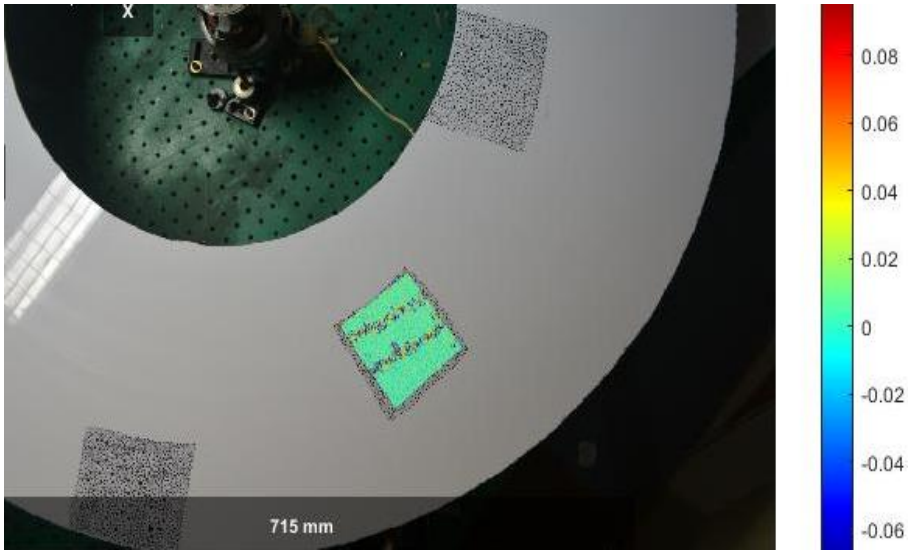

(b)

Fig. 5.7 a) ROI on the specimen b) Strain field on the specimen

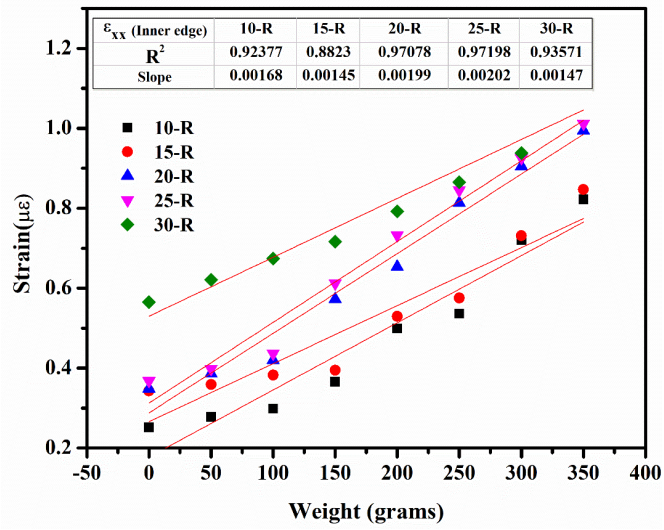

(a)

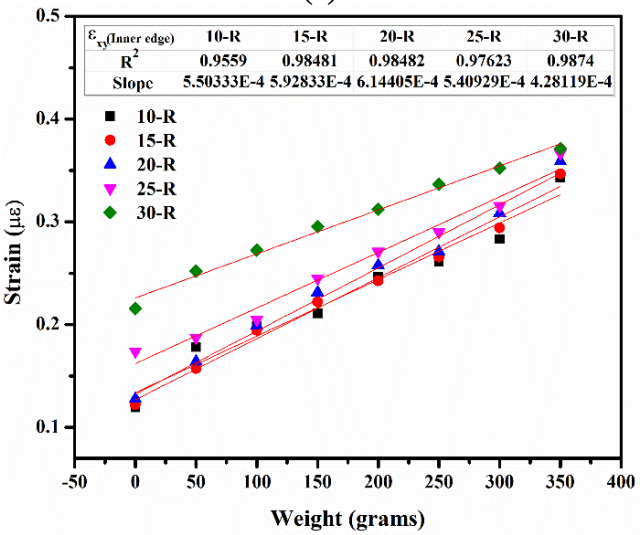

(b)

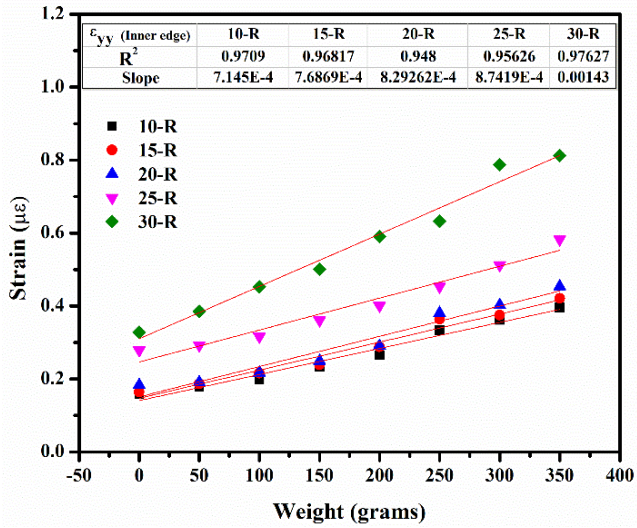

(c)

Fig. 5.8 Strain distribution on Inner edge of pavement (a) ε_{xx} (b) ε_{xy} (c) ε_{yy}

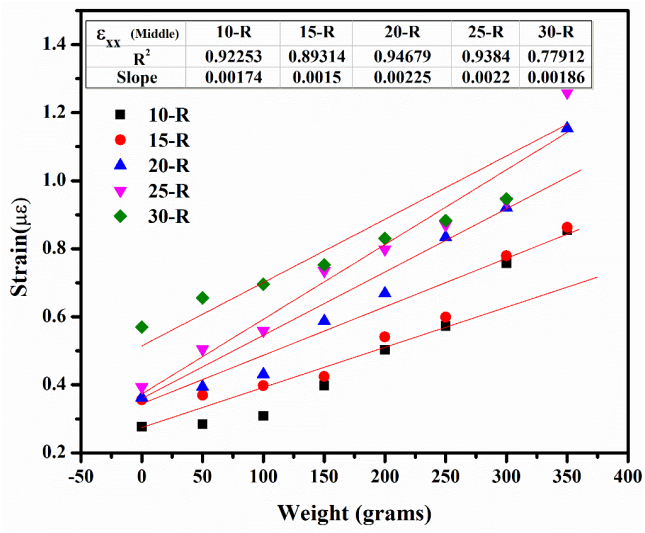

(a)

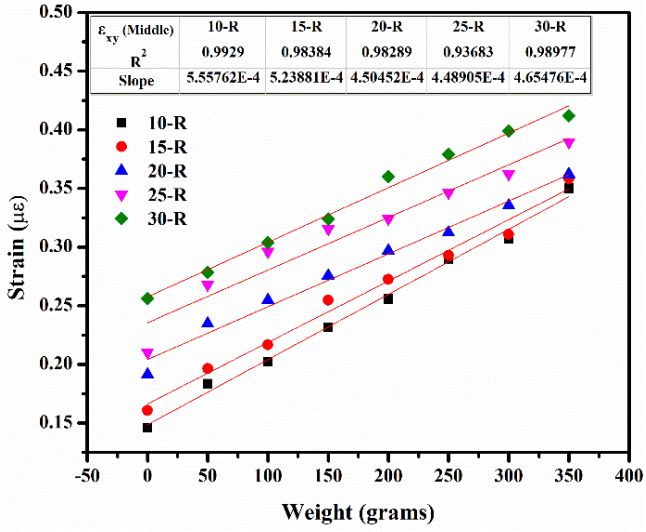

(b)

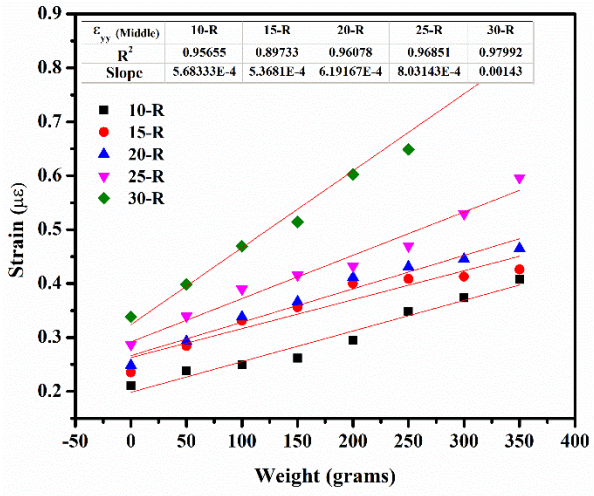

(c)

Fig. 5.9 Strain distribution on Middle of the pavement track (a) ε_{xx} (b) ε_{xy} (c) ε_{yy}

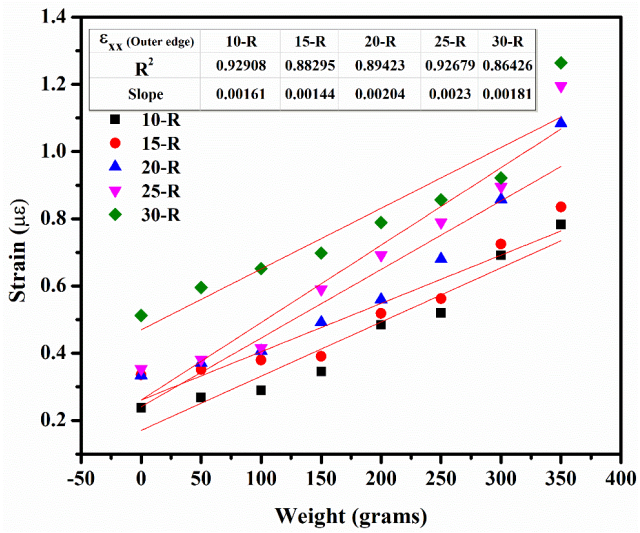

(a)

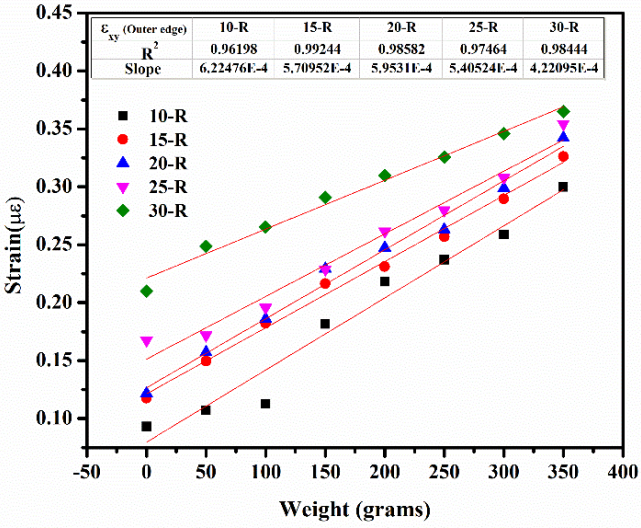

(b)

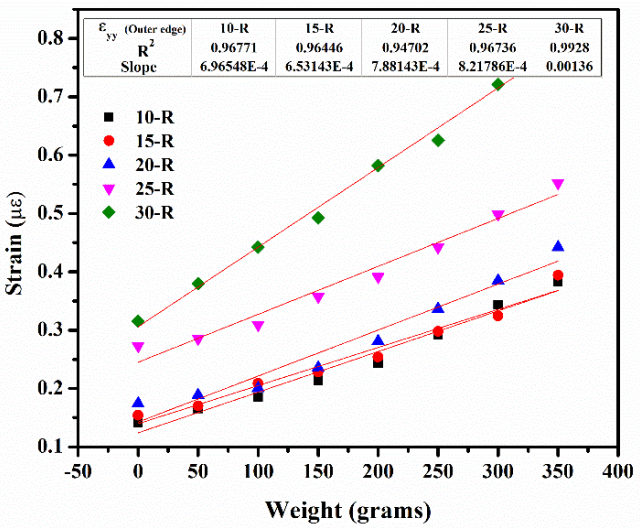

(c)

Fig. 5.10 Strain distribution on the outer edge of pavement (a) ε_{xx} (b) ε_{xy} (c) ε_{yy}

It can be observed that with increase in the number of rotations of the vehicle on APT, there is an increase in the amount of strain developed even with dead load. Further, the strain increased with increasing load. The strain at the middle of the APT was found to be 0.276με in ε_{xx} direction, 0.146με in ε_{xy} direction and 0.21 με in ε_{yy} direction when the vehicle moved with dead load alone. The corresponding maximum strain at 30 rotations with a live load of 350g on the vehicle was found to be 1.387με in ε_{xx} direction, 0.412με in ε_{xy} direction, and 0.821με in ε_{yy} direction.

The strain at the inner edge of the APT was observed to be 0.251με in ε_{xx} direction, 0.119με in ε_{xy} direction and 0.159με in ε_{yy} direction, when the vehicle is rotated with dead load, while the corresponding maximum strain at 30 rotations with added live load of 350g was found to be 1.131με in ε_{xx} direction, 0.371με in ε_{xy} direction, and 0.812με in ε_{yy} direction respectively.

The strain at the outer side of the APT was found to be 0.237με in ε_{xx} direction, 0.093με in ε_{xy} direction and 0.142με in ε_{yy} direction when the vehicle rotated with dead load and the corresponding maximum strain for 30 rotations with added live load of 350g was found to be 1.264με in ε_{xx} direction, 0.3651με in ε_{xy} direction, and 0.798με in ε_{yy} direction. The observations are presented in Table -5.1.

Table-5.1: Details Strain and sensitivity of DIC measurements at Three ROI

	Without live load and for 10 rotations						**With Maximum live load(350gr) and for 30 rotations**					
	Inner edge		**Middle**		**Outer edge**		**Inner edge**		**Middle**		**Outer edge**	
	Strain (με)	**Sensitivity (με/gr)**	**Strain (με)**	**Sensitivity (με/gr)**	**Strain (με)**	**Sensitivity(με/gr)**	**Strain (με)**	**Sensitivity (με/gr)**	**Strain (με)**	**Sensitivity (με/gr)**	**Strain (με)**	**Sensitivity (με/gr)**
ε_{xx}	0.25	0.00168	0.27	0.00174	0.24	0.0016	1.13	0.0014	1.39	0.0018	1.26	0.0018
ε_{xy}	0.12	$5.5*10^{-4}$	0.15	$5.5*10^{-4}$	0.09	$6.2*10^{-4}$	0.37	$4.3*10^{-4}$	0.41	$4.6*10^{-4}$	0.36	$4.2*10^{-4}$
ε_{yy}	0.16	$7.1*10^{-4}$	0.21	$5.7*10^{-4}$	0.14	$7*10^{-4}$	0.81	0.00143	0.82	0.0014	0.8	0.0013

From Table 5.1, it can be observed that along ‘x’ direction, the strain ε_{xx} is higher compared to ε_{xy} and ε_{yy} directions. This is true with regard to the number of rotations and with increase in the load.

The variation of strain along ε_{xx}, ε_{xy}, and ε_{yy} directions at the three ROI after the vehicle passed 10 and 30 number of constant rotations with variation of live loads from 0-350 grams is shown in Fig.5.11.and Fig.5.12 respectively.

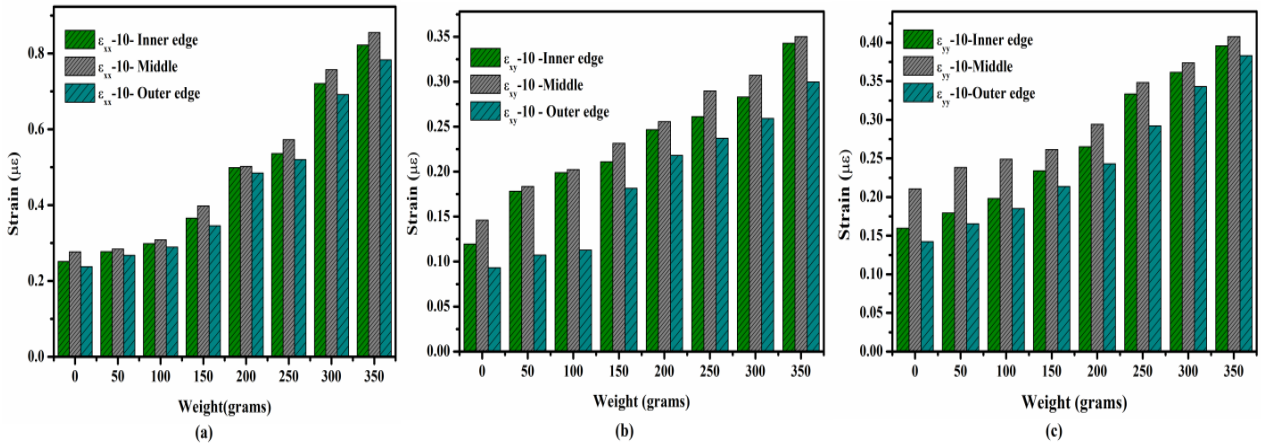

Fig.5.11 Typical Strain response by varying loads at constant 10 rotations of vehicle along (a) ε_{xx} (b) ε_{xy}(c) ε_{yy}

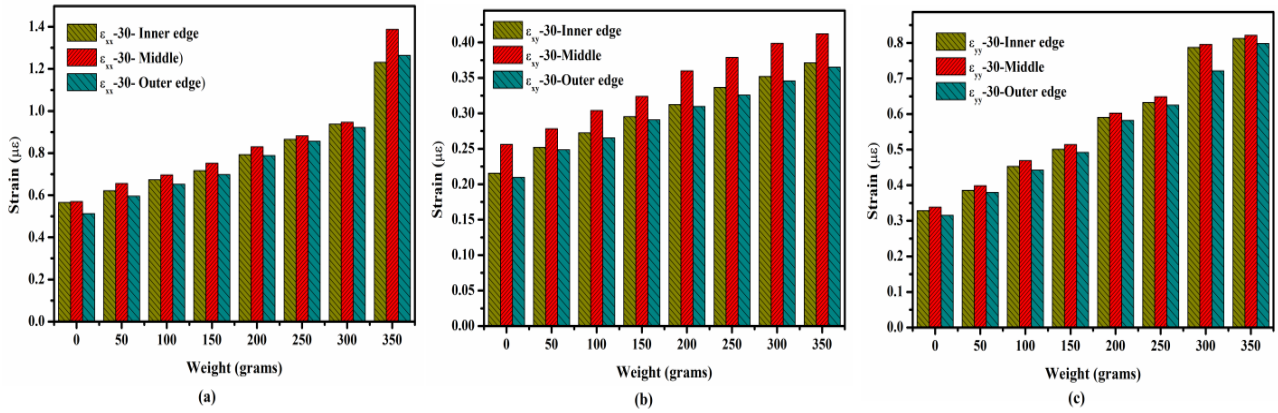

Fig.5.12 Typical Strain response by varying loads at constant 30 rotations of vehicle along (a) ε_{xx} (b) ε_{xy}(c) ε_{yy}

From these figures, it can be observed that with increase in load and the number of rotations of the vehicle, the strains also increased. The middle track of the pavement showed higher strains compared to the other two ROI (Inner and outer edges).

The in-plane strains in Cartesian coordinate system from DIC method have been transformed to strains along the principal strain directions following the method shown in Fig. 5.13 and the Principal strains have been calculated using Equation (5.5) and the results are shown in Fig.5.14,

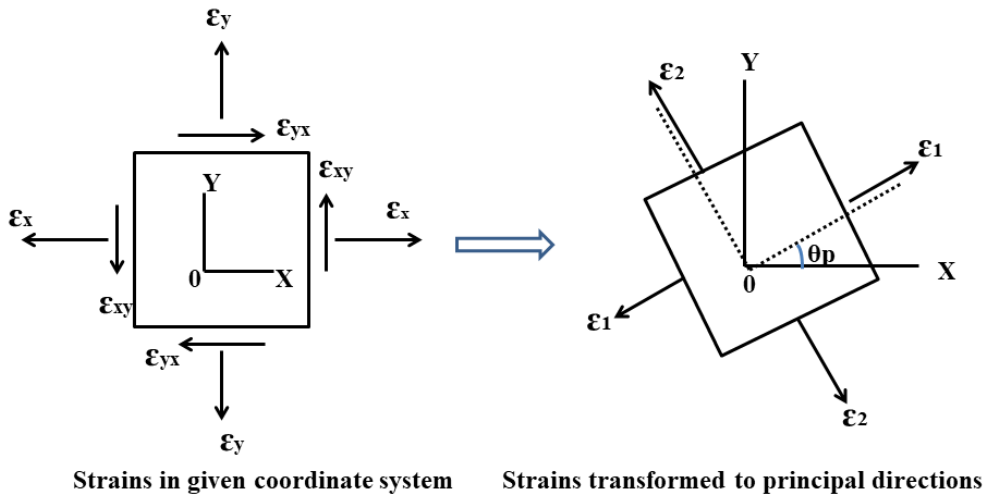

Fig. 5.13 In plane strain transforming to principal directions

$$\varepsilon_{1,2} = \frac{\varepsilon_{xx} + \varepsilon_{yy}}{2} \pm \sqrt{\left(\frac{\varepsilon_{xx} - \varepsilon_{yy}}{2}\right)^2 + \left(\frac{\varepsilon_{xy}}{2}\right)^2} \qquad \textit{Eq.}(5.5)$$

Fig.5.14 shows the typical Principal strain response for varying rotations of the vehicle at three locations of ROI with a constant live load of 350 grams.

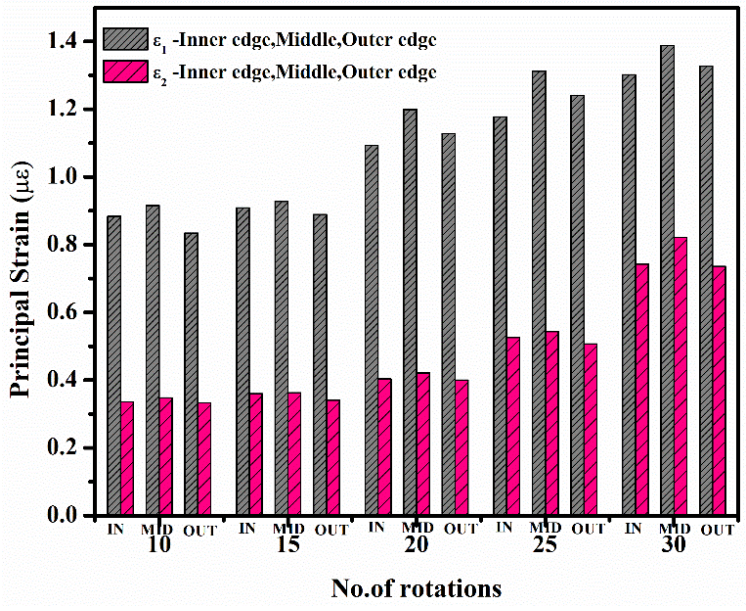

Fig. 5.14 Principal strain response for varying rotations at three locations of ROI at a constant live load of 350 grams

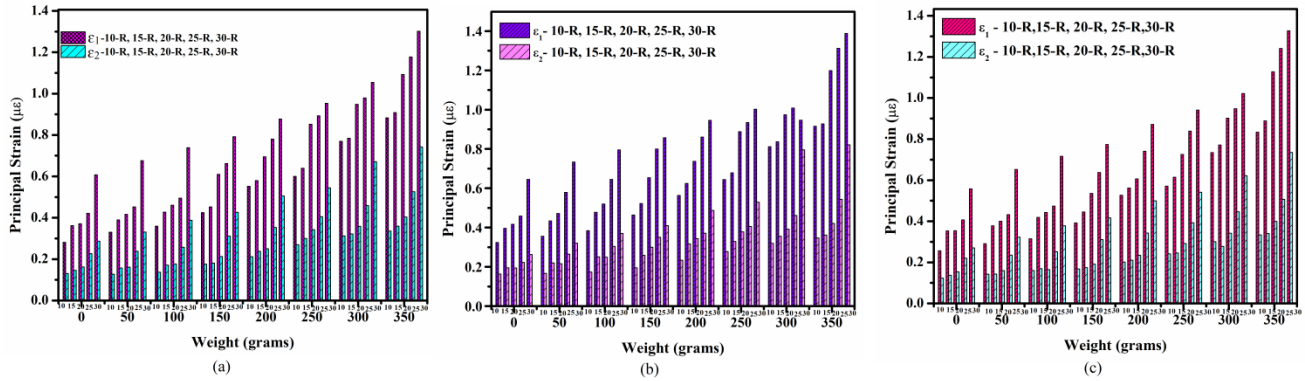

Fig. 5.15 Principal strain response for varying loads and varying rotations at three ROI (a) Inner edge (b) Middle (c) Outer edge

Fig. 5.15 shows the Principal strain response for varying loads and varying number of rotations of the vehicle on the APT. The maximum value of the principal strain developed at the middle of the track for 30 rotations and at 350g of live load on the vehicle was found to be 1.4με, while the corresponding value was 1.3με at the inner and outer sides of the pavement track.

5.3.2 FBG Results

The experimental analysis in the case of the temporal response obtained from the FBGs has been performed in two phases, namely for the FBGs oriented along the direction of motion of the vehicle at (0^o) and at 45^o to the direction of motion. The FBG array (consisting of three FBGs having Bragg wavelengths 1528.33nm, 1534.55nm, and 1545.96nm respectively); is attached in the tension part of the APT track at three ROI of interest (Inner diameter, Outer diameter, Middle of the pavement) under the respective speckle patterns. As the vehicle moves on the APT, each FBG experiences strain which shows up in the form of corresponding wavelength shift, giving rise to a temporal response which is recorded by the Interrogator. The temporal responses have been recorded for various live loads, and for various number of rotations of the vehicle on the APT for both orientations of the FBG with respect to direction of motion of the vehicle.

Fig. 5.16 shows a typical temporal response of the strain developed by the FBG attached at the middle of the APT after completion of 10 rotations of the vehicle for a live load of 250grams on it with FBGs oriented along the direction of motion of the vehicle. The Savitzky-Golay filter provided by MATLAB was used to remove the random noise contained in the measured strain response by convolving the signal with the centre row.

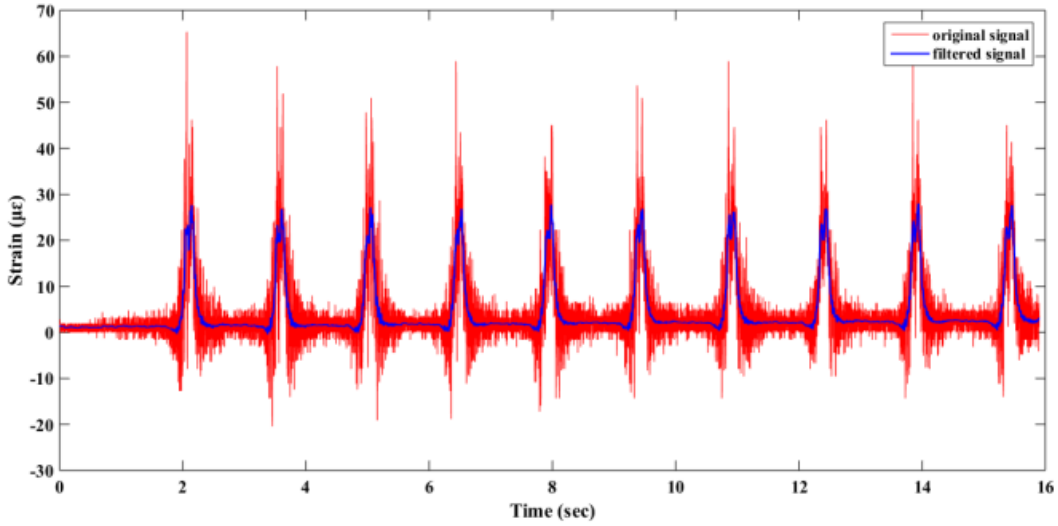

Fig. 5.16 Temporal response of FBG w.r.to strain

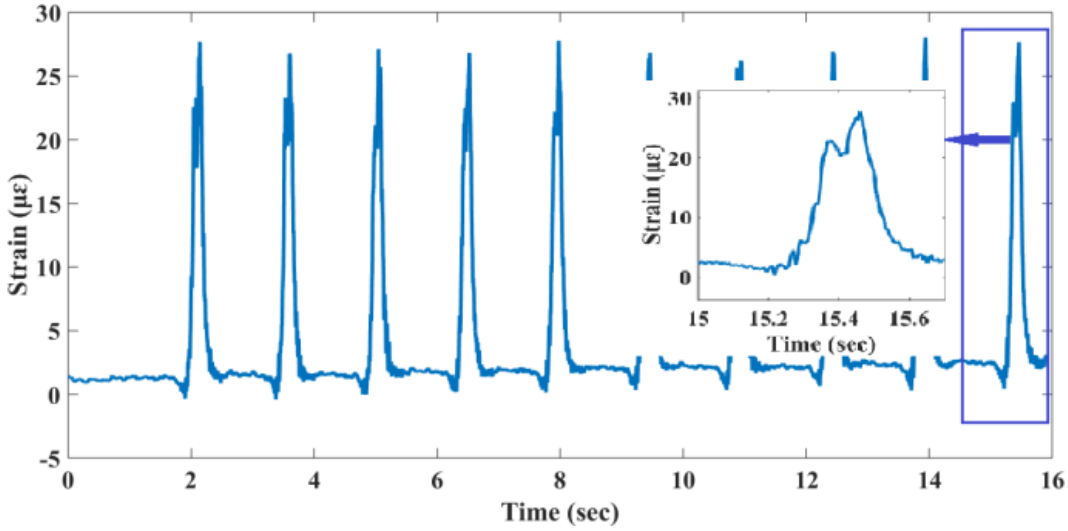

Fig. 5.17 Temporal response of FBG at the middle ROI of APT after filtering

Fig. 5.17 shows the temporal response of FBG pasted in the middle of APT after filtering the response shown in Fig.5.16. It suggests that the two crests and one trough like shape that appear in the response correspond to the positions of the wheels of the vehicle while it passes over FBG. When the front and rear wheels of the vehicle lie completely on the FBG, a larger shift in the wavelength is recorded, while when the FBG is in between the wheels, a smaller shift is recorded in the wavelength forming a trough like shape.

Fig. 5.18 and Fig. 5.19 shows the typical temporal response of the FBGs while the vehicle completed 10 rotations on the APT at the three ROI, with varying loads on the vehicle. The response was carried out after removing random noise using Savitzky-Golay filter for FBG orientation along 0^o and at an angle 45^o respectively, with respect to the

direction of motion of the moving vehicle. The idea of using FBG at different orientations is to evaluate principal strains considering as Rosette.

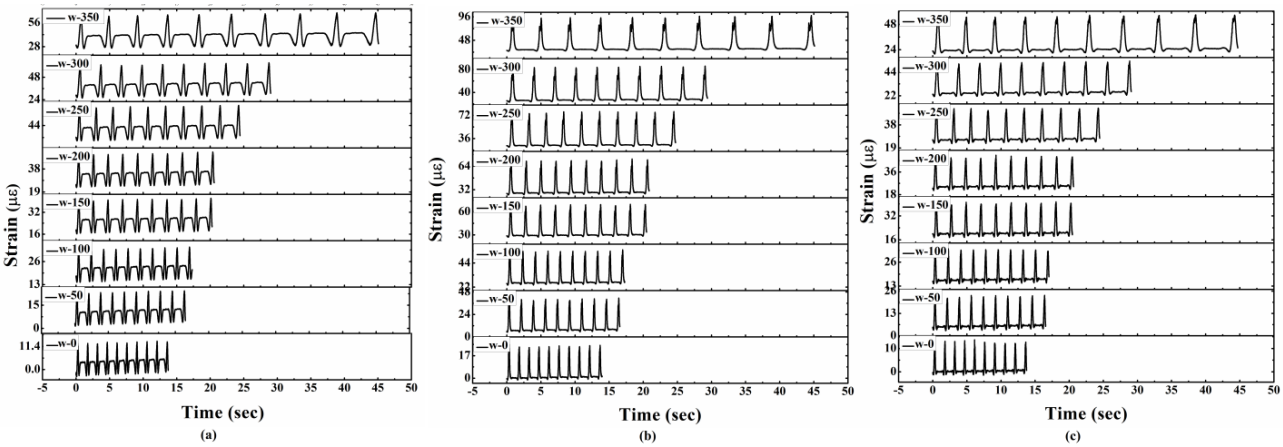

Fig. 5.18 Temporal response of FBGs with varying loads (a) Inner edge (b) Middle (c) Outer edge ROI along the line of the motion of the vehicle

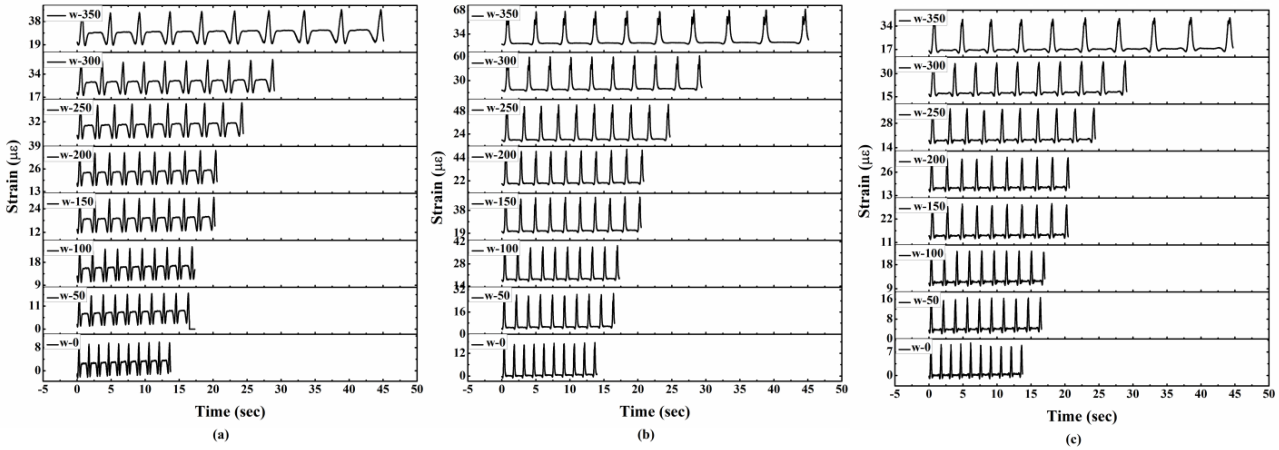

Fig. 5.19 Temporal response of FBGs with varying loads (a) Inner edge (b) Middle (c) Outer edge ROI along 45^{o} to the line of the motion of the vehicle

Such response curves for varying loads and varying number of rotations of the vehicle on the APT at the three ROIs of interest were acquired by using the interrogator, with random noise filtered in each case using Savitzky-Golay filter. From the temporal response curves, the average strains developed along the direction of motion of the vehicle (ε_{xx}) and at an angle 45^{o} to the motion (ε_{xy}) were calculated for different rotations made by the vehicle and for applied live loads at the three ROIs using Eq. (5.6).

$$\varepsilon = \frac{\Delta\lambda_B}{\lambda_B(1-P_e)} \qquad Eq.(5.6)$$

Where ε is strain on the FBG, $\Delta\lambda_B$ is Change in central wavelength of FBG, λ_B is central wavelength of FBG, and P_e is photo elastic coefficient (for silica core P_e~0.22). The results are presented in Fig. 5.20 and Fig. 5.21.

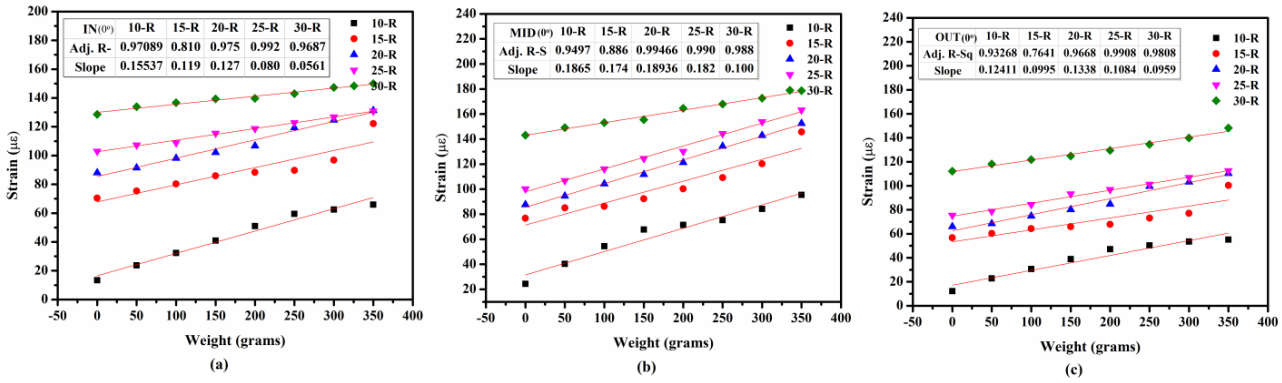

Fig. 5.20 Average Strain response of FBG placed at (a) Inner edge (b) Middle, and (c) Outer edge of Pavement along the line of motion (ε_{xx}) of the vehicle

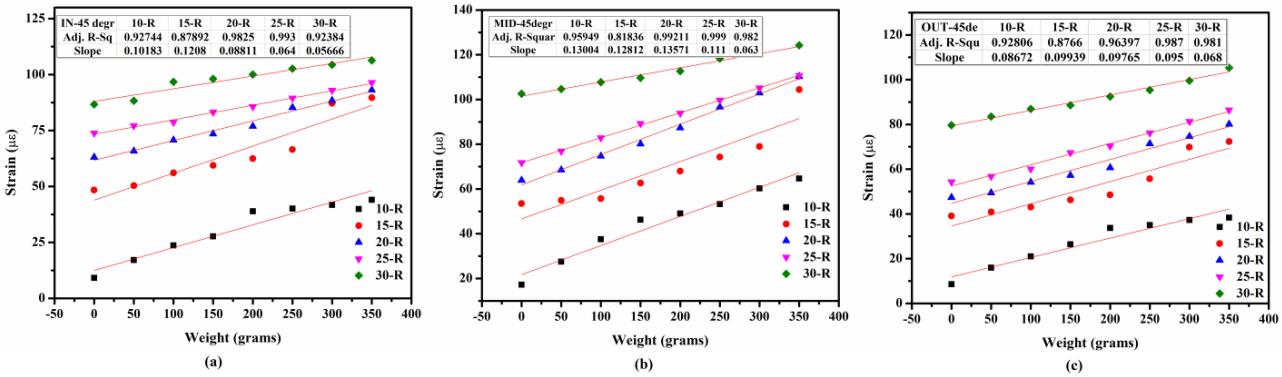

Fig. 5.21 Average Strain response of FBG placed at (a) Inner edge (b) Middle, and (c) Outer edge of Pavement along 45°(ε_{xy})to the line of motion of the vehicle

It can be observed that the strain response of FBG along the middle of the pavement was high and found to be (175.64 με) and (124.18 με) respectively for the FBG oriented at 0° to the direction of motion of the vehicle and at 45° to the direction of motion; and for a maximum of 30 rotations made by the vehicle on the APT and for a maximum live load of 350 grams on the vehicle. The corresponding values recorded for the inner and outer diameter of the pavements were (150.43 με) and (106.35 με); (148.96 με) and (105.31 με) respectively for these two orientations. The average linearity and average sensitivity were found to be 0.96, 0.95 and 0.1663 με/gram, and 0.1135 με/gram respectively for these FBG orientations and the results are presented in Table-5.2.

Table-5.2: Strain and sensitivity of FBGs at three ROI, FBG placed along 0^o and 45^o to the line of motion

	Vehicle load only (10 rotations)						Total live load (350grams) 30 rotations					
	Inner edge		Middle		Outer edge		Inner edge		Middle		Outer edge	
FBG Orientation ε	Strain (με)	Sensitivity (με/gr)	Strain (με)	Sensitivity (με/gr)	Strain (με)	Sensitivity(με/gr)	Strain (με)	Sensitivity (με/gr)	Strain (με)	Sensitivity (με/gr)	Strain (με)	Sensitivity (με/gr)
0^o (ε_{xx})	12.9	0.16	24.33	0.19	12.1	0.12	150.43	0.06	175.65	0.10	148.96	0.10
45^o (ε_{xy})	9.15	0.10	17.20	0.13	8.56	0.09	106.35	0.06	124.18	0.06	105.31	0.07

5.3.2.1 Velocity of the Vehicle

The speed of the vehicle while it is moving on the APT has been calculated from the temporal response of the FBGs. Fig. 5.17 shows the temporal response at the portion of the FBG corresponding to the middle speckle on the APT along 0^o to the line of motion. It can be observed that there are two peaks and one dip shape which are acquired as when front and rear wheels of the vehicle. When the vehicle exactly on the FBG, there is a maximum shift in its wavelength, whereas when FBG is in between the vehicle wheels, lower shift was obtained compared to maximum peak wavelengths as shown dip like shape.

The speed of the vehicle is calculated from the time difference for the distance travelled by the vehicle for completing one rotation; which is taken as the circumference of the circle ($2\pi r$) (where r is the radius of APT 437.5mm) ($V= 2\pi r/\Delta t$); for different applied loads and number of rotations of the vehicle. The average speed the vehicle computed; for a fixed number of rotations and for varying applied loads from 0-350 grams; is shown in Fig. 5.22.

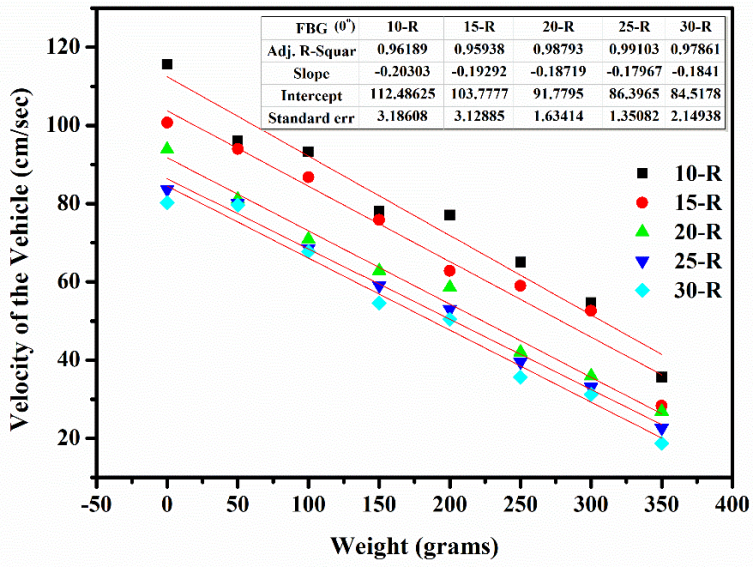

Fig. 5.22 Speed of the vehicle while varying load for different rotations of the vehicle

From Fig. 5.22, it can be observed that as load is varying and number of rotations increases the velocity of the vehicle decreases linearly. The coefficient of correlation is 0.98, for the variation between velocity and weight on the vehicle.

5.3.2.2 Principal Strain response of APT from FBG

Considering the FBG's arrangement at 0^o and 45^o orientations to the direction of motion of the vehicle and considering it as a two element rosette (shown in Fig. 5.23) and using the equations for measuring strain given by Eq. (5.7) and Eq. (5.8) [14],[15], the principal strains have been evaluated substituting the experimental strain values obtained for FBGs placed at orientations 0^o and 45^o to the line of motion[16] and the results are shown in Fig. 5.24.

$$\varepsilon_{\phi} = (\varepsilon_{xx} + \varepsilon_{yy})/2 + \cos 2\phi(\varepsilon_{xx} - \varepsilon_{yy})/2 + \sin 2\phi(\gamma_{xy})/2 \qquad Eq.(5.7)$$

Where $\phi=0^o$, 45^o as shown in Fig. 5.23,

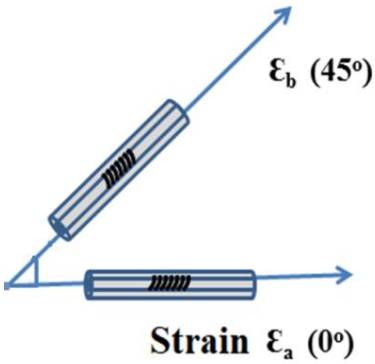

Fig. 5.23 Strain at different angles of FBG

$$\varepsilon_a = \varepsilon_{xx} \qquad (0^o)$$

$$\varepsilon_b = \varepsilon_{xy} = \frac{\varepsilon_{xx} + \gamma_{xy}}{2} \qquad (45^o)$$

$$\varepsilon_{1,2} = \frac{\varepsilon_{xx}}{2} \pm \sqrt{\left(\frac{\varepsilon_{xx}}{2}\right)^2 + \left(\frac{\gamma_{xy}}{2}\right)^2} \qquad Eq.(5.8)$$

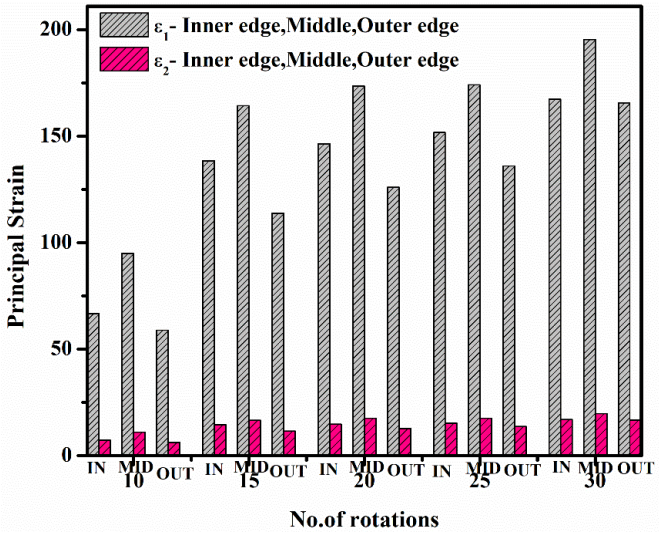

Fig.5.24 Principal strain response for varying rotations at three ROI at a live load of 350 grams

Fig. 5.24 shows the principal strain response for varying rotations made by the vehicle on the APT at three locations of ROI with a constant load of 350 grams.

5.3.3 Comparing DIC results with FBG results

It can be observed from Table-5.1 and Table-5.2 that the strain and the strain sensitivity values obtained from DIC method are very low compared to the corresponding values from FBG technique. Further, the principal strain response for varying rotations of the vehicle on the APT from Fig. 5.14 and Fig. 5.24 also confirms better sensitivity with FBG measurements at three ROI respectively compared to DIC method. This can be attributed to the fact that the strains have been recorded in terms of wavelength shift at the instant at which the vehicle passes over the FBG and also because of the high strain sensitivity of the FBG measurements; whereas the recording was done immediately after the predetermined number of rotations of the vehicle on the APT is completed in case of DIC measurements: DIC measurements are sensitive to pattern distribution, subset radius and seed settings.

DIC yields strain information obtained from speckles over a finite area of the speckle pattern. As the area of the speckle pattern is 11x11 cm^2, and the FBG's is are placed in the middle of the pattern in all the cases in the ROI, the strains experienced by the FBG will be a symbolic representation of the strains developed in that area. The same must be given by DIC method also, and hence these values can be correlated.

As there is a marked variation between the principle strain responses values obtained due to the two methods, the normalised principal strain response (ε_1, and ε_2) was calculated from the experimental observations for 10, 20 and 30 rotations of the vehicle on the APT at three ROI's for varying live loads. The results are presented in Fig.5.25and Fig.5.26, and the corresponding average normalised principal strain values are shown in Table.5.3.

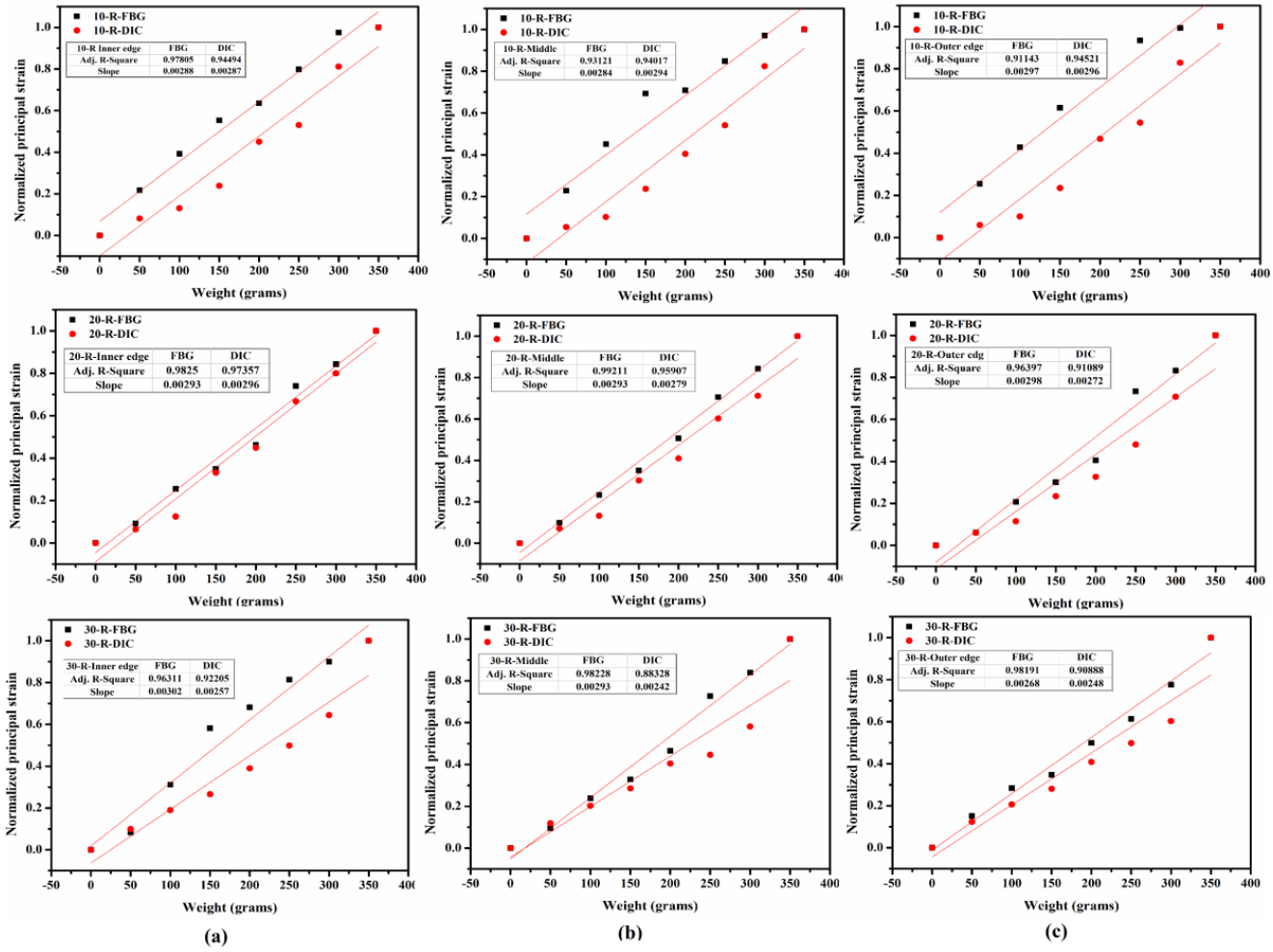

Fig. 5.25 Normalized principal strain (ε_1) response of FBG and DIC for 10, 20 and 30 rotations of vehicle at (a) Inner edge (b) Middle (c) Outer edge ROI

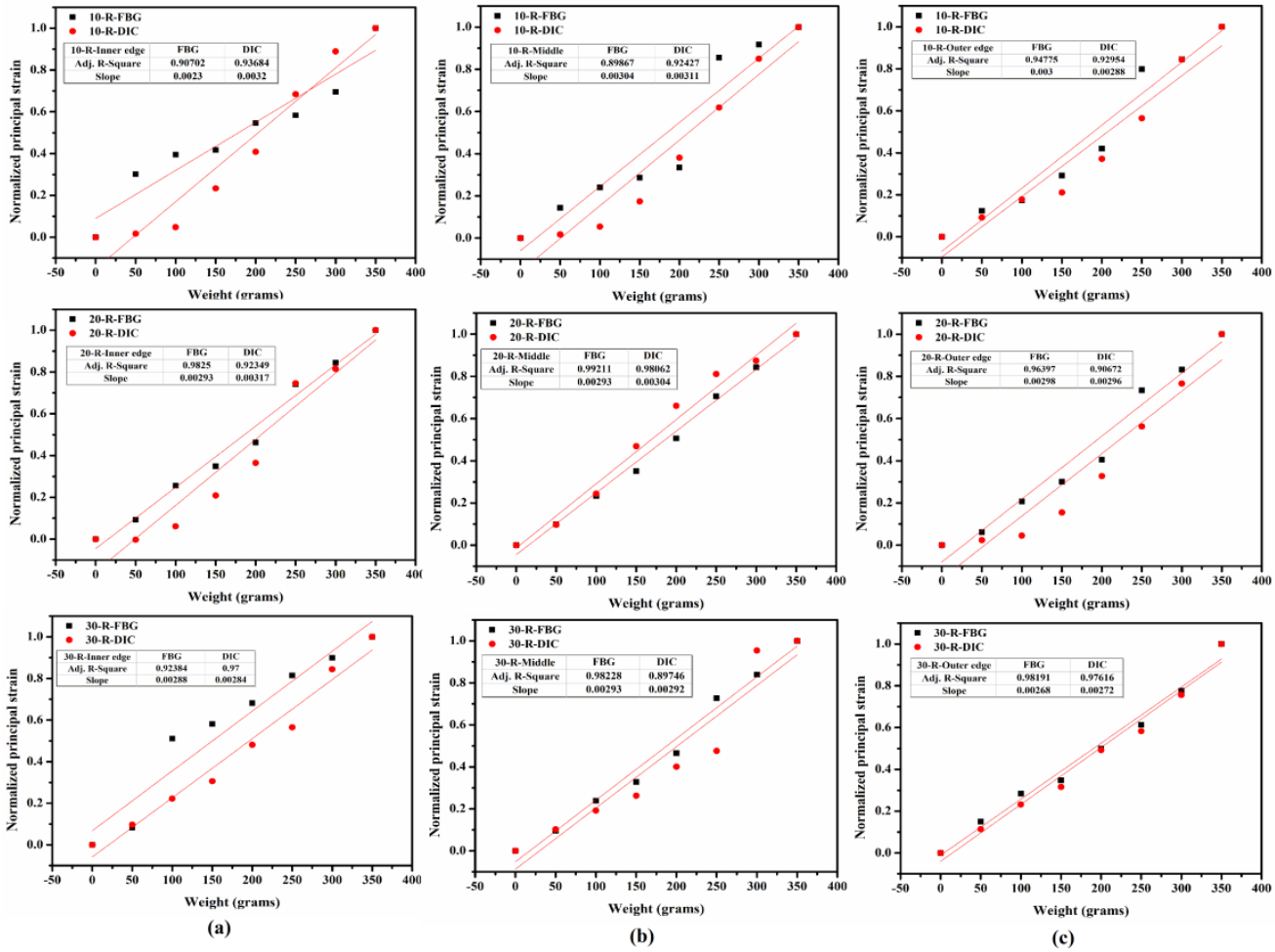

Fig. 5.26 Normalized principal strain (ε_2) response of FBG and DIC for 10, 20 and 30 rotations of vehicle at (a) Inner edge (b) Middle (c) Outer edge ROI

Table-5.3: Average normalized principal strain values of FBG and DIC at three ROI

Location on the Pavement	**Inner edge**				**Middle**				**Outer edge**			
Measurement type	**FBG**		**DIC**		**FBG**		**DIC**		**FBG**		**DIC**	
	ε_1	ε_2	ε_1	ε_2	ε_1	ε_2	ε_1	ε_2	ε_1	ε_2	ε_1	ε_2
R^2	0.97	0.94	0.95	0.94	0.97	0.96	0.93	0.93	0.95	0.96	0.92	0.94
Slope	0.003	0.0027	0.0028	0.003	0.0029	0.003	0.0027	0.003	0.003	0.003	0.0027	0.0028

It can be noted from Fig.5.25, Fig.5.26 and Table.5.3 that there is a very good agreement between normalised principal strain responses due to FBG and DIC methods with the FBG method showing slightly better sensitivity than DIC technique. It can therefore be concluded that both the techniques respond to normalised strain measurements in the same manner, while differing greatly in terms of individual responses.

5.4 Finite Element Analysis of the APT

A three-dimensional model of the APT experiment has been modeled using Finite Element Method and is examined under different moving loads utilizing ABAQUS v6.14/CAE software. It is assumed that the load is concentrated at a point in the present analysis.

The pavement track of 54.5cm inner diameter, 33cm width and 5mm thickness is built in the drawing module. The elastic material model has been chosen with material characteristics of the poly acrylic sheet used in the experiment given as: modulus of elasticity (3.1 GPa) and Poisson's ratio (0.37). Fig 5.27 shows the layout model of APT and the Boundary conditions are incorporated by fixing the pavement at eight symmetrically located points on the inner edge and corresponding eight symmetrical points on the outer edge to simulate the supports on which the pavement rests.

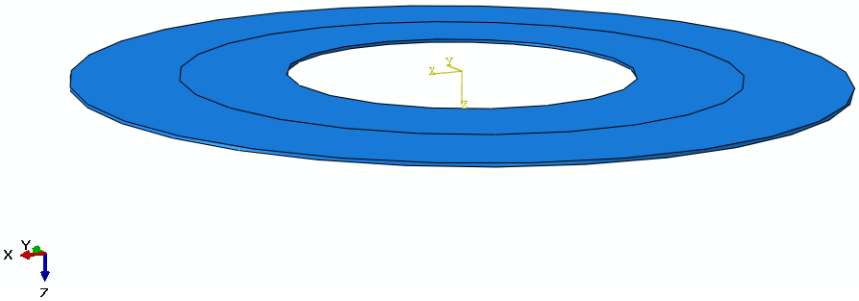

Fig.5.27 Layout of APT

To specify the moving load, the model is meshed with 10-node quadratic tetrahedral elements (C3D10M) as shown in the Fig.5.28.

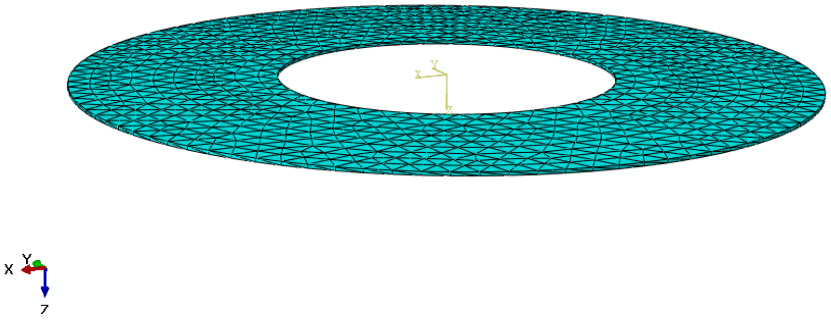

Fig. 5.28 Mesh the model with quadratic tetrahedral elements

To account for the variation of load with time, periodic loads are defined in a systematic manner at each of the nodes on the central path of the pavement by means of 'periodic' option in the amplitude manager so as to replicate actual vehicular load repetitions in real-time as shown in Fig. 5.29.

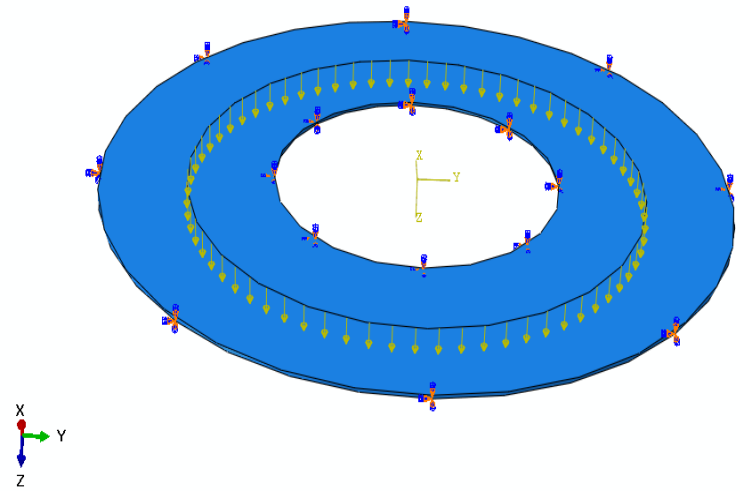

Fig. 5.29 Load applied along the center line lane of the APT with support condtions

To give load as input to the model, load cycle associated with each node is broken down to a Fourier series interpretation as shown in Eq. 5.9.

$$f(t) = a_0 + \sum_{n=1}^{\infty} (a_n \cos n\omega(t - t_0) + b_n \sin n\omega(t - t_0)) \qquad Eq.(5.9)$$

Where, a_0 stands for initial amplitude, n is equal to the number of parametric constants (which is five in the current study), ω represents circular frequency, (a_n, b_n) are different amplitude parameters for different 'n', t_0 stands for starting time and t indicates different time instants.

Simulation has been carried with loads on the vehicle varying between zero (dead load) and 350g with an increment of 50g in each case. For every applied load, the load is made to revolve ten times around the pavement, where, each rotation starts and terminates at the same node indicating one complete rotation. The total simulation time for each applied load is varied according to the velocity of the moving vehicle; which is obtained from the temporal response of middle region of FBG for each load as shown in Table 5.4.

Table-5.4: Velocity of the vehicle obtained from FBG

Applied load (grams)	Average velocity of the Vehicle for 10 rotations (cm/s)
0	185.66
50	149.67
100	154.32
150	125.52
200	123.76
250	104.49
300	87.81
350	57.20

5.4.1 Results and Discussion

Analysis has been carried out in respect of the three ROIs namely, at middle of APT, Inner edge and outer edge of APT where FBG sensors are approximately positioned. As the load is applied on the center line of the APT and is allowed to rotate in the simulation, the strains developed at the three ROI's are extracted. The strains developed due to the applied load and maximum principal strains are obtained from the field output section during post-processing. A typical strain contour plot for the applied load of 300 grams from the simulation is as shown in Fig. 5.30 for two different time instants, and also a typical maximum principal strain contour plot for the applied load 300grams at two different time instants as shown in Fig. 5.31.

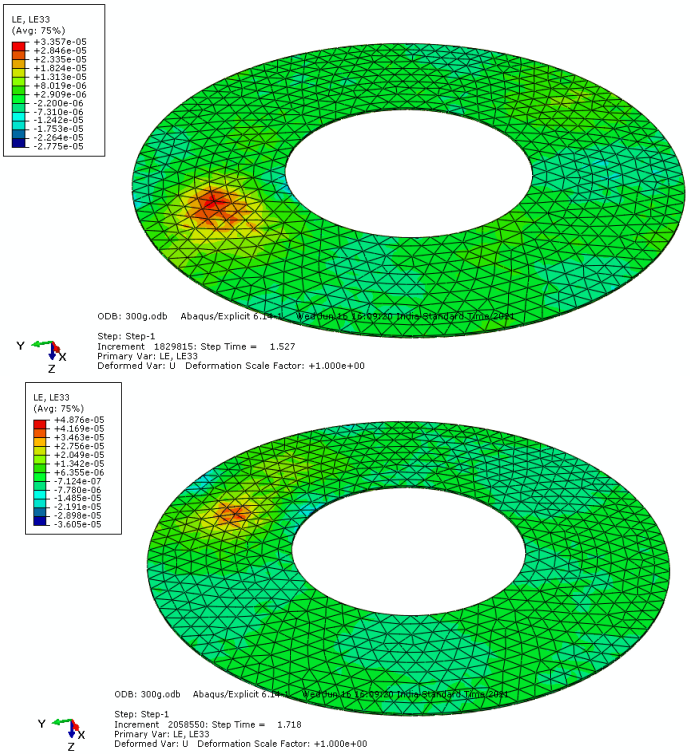

Fig. 5.30 Contour plot of strain at two different time instants

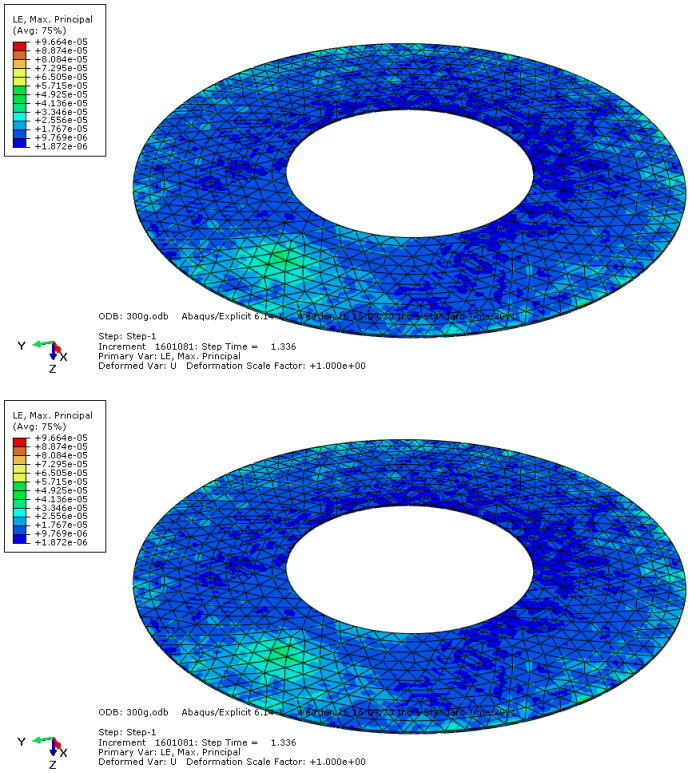

Fig. 5.31 Maximum principal strain contour at two different time instants

5.4.2 Comparison of FBG results with FEM results

The strain values at the three ROI's from the FBG method and finite element analysis simulation for 10 complete rotations of the vehicle with loads varying in the range 0gm to 350gms are as shown in Table. 5.5.

Table-5.5: The Average strain values of FBG and FEM after 10 rotations of a vehicle

Applied load (grams)	Average Strain (με) after 10 rotations of a vehicle					
	Inner edge of the APT		Middle of the APT		Outer edge of the APT	
	FBG	FEM	FBG	FEM	FBG	FEM
0	12.94	12.19	24.33	23.08	12.11	7.81
50	22.80	24.61	38.92	29.72	22.57	10.11
100	30.65	27.50	53.07	37.41	29.69	14.40
150	39.11	30.62	66.90	44.64	37.38	20.27
200	57.85	37.51	69.39	51.83	47.73	27.32
250	58.12	42.55	75.28	57.10	49.52	32.44
300	59.03	50.73	83.87	63.79	52.70	44.06
350	59.42	62.96	91.51	67.35	54.20	53.16

From Table 5.5 it can be observed that the average strain responses from FBG method and FEM analysis are almost similar with an error of $\pm$5% at three ROI's. The strain response in the middle of the APT is the maximum from both the methods compared to other two ROI (i.e. Inner diameter, Outer diameter of the APT).

The maximum principal strains obtained from FBG method (presented in section 5.3.2.2) and the maximum principal strain response obtained from the FEM analysis at the three ROIs, for 10 complete rotations made by the vehicle for different applied loads is as shown in Fig. 5.32.

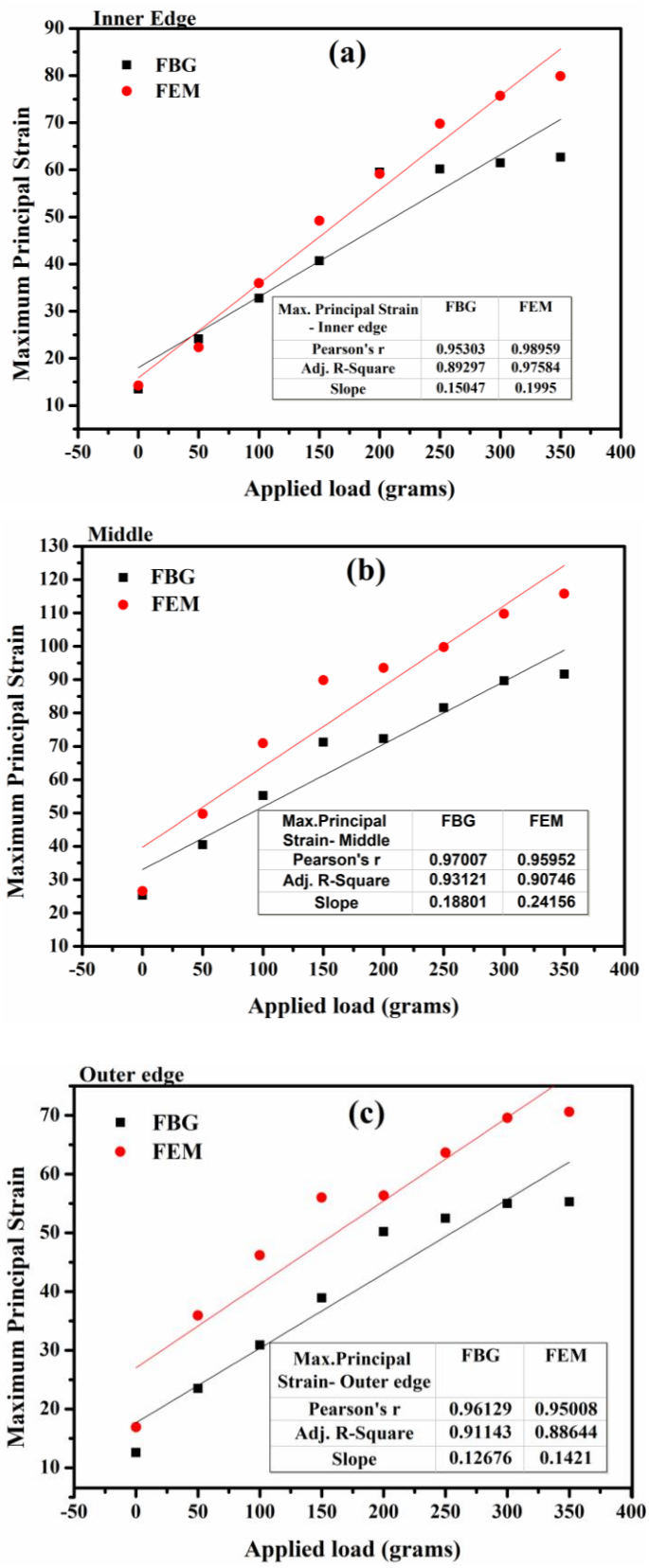

Fig. 5.32 Maximum Principal strain response (a) Inner edge (b) Middle (c) Outer edge of the APT

From Fig. 5.32 it is observed that maximum principal strains for varying applied loads from 0-350 grams for 10 numbers of rotations of a vehicle, obtained from FBG and FEM analysis shows a good correlation along three ROI. However, the maximum principal strains are high at middle ROI due to vehicle moving at middle of the pavement with a good correlation coefficient of FBG experimentally is 0.97 and from numerical model based on FEM is 0.95. The strains at inner edge and outer edge of the pavement has a correlation coefficient of FBG 0.95 and 0.96, while that from numerical model FEM is 0.98and 0.95 respectively.

Summary of Phase 3 work

Image correlation technique is a popular tool to measure displacements for as less as one point and as many as thousands of points for full-field analysis. The random speckle pattern drawn on the object under study serves the purpose of embedding data in the structural component for DIC measurements and analysis, which is helpful for non-contact sensor-based condition monitoring, as well as integration of component level data for SHM. Since FBG based sensing and analysis of strains in engineering structures has been a growing area of research in SHM applications, a comparative study has been made between the results of the two methods. The strain developed while a loaded vehicle rotates on an APT has been employed for making the comparison between these methods. Based on the observations, the following conclusions are drawn:

1. The strain response while a loaded vehicle is moving on APT was evaluated by placing FBG array in the section experiencing tension on the APT as a contact sensor, and by drawing random speckle pattern distribution on the surface of the pavement and capturing the undeformed and deformed images by a DSLR camera which was used as a non-contact sensor (DIC method).
2. The strain response was determined at three Regions of Interest (ROI), namely, the inner, outer and middle regions of the pavement track, where the speckle patterns were drawn using FBG and DIC techniques.
3. The FBG method has been observed to give very high strain response compared to DIC method in all the cases where the load was increasing and the number of revolutions made by the vehicle on the APT. However, the normalised principal strain responses evaluated in both the cases has shown a very good agreement, indicating that even though the individual responses in both methods differ markedly, the results show similar trend where normalised strain responses were concerned.

4. Since the FBG based measurements showed high sensitivity compared to results from DIC method, it is advisable to use FBG method as a better alternative. Further, this method can also provide information about the velocity as well as spacing between the wheels of the vehicle.
5. The results obtained experimentally based on FBG are compared with the finite element analysis method (FEM) using ABAQUS software. The normalised values compared well.
6. The strain measurements obtained from FBG and FEM analysis at three ROIs are having almost similar response with an error of $\pm$5%. The maximum principal strain responses at three ROIs, from both the methods also have a good coefficient of correlation of 0.97.

Chapter 6 deals with studying the dynamic characteristics of concrete beams using vibration based damage detection technique.

References

[1] D. Lecompte, H. Sol, J. Vantomme, A. Habraken, Analysis of speckle patterns for deformation measurements by digital image correlation, SProceedings SPIE. 6341 (2006) 63410E1-6. https://doi.org/10.1117/12.695276.

[2] A. F. Ab Ghani, M. B. Ali, S. Dharmalingam, J. Mahmud, Digital Image Correlation (DIC) Technique in Measuring Strain Using Opensource Platform Ncorr, J. Adv. Res. Appl. Mech. 26 (2016) 10–21.

[3] J. Gorszczyk, K. Malicki, T. Zych, Application of digital image correlation (DIC) method for road material testing, Materials (Basel). 12 (2019). https://doi.org/10.3390/ma12152349.

[4] B. Pan, K. Qian, H. Xie, A. Asundi, Two-dimensional digital image correlation for in-plane displacement and strain measurement : a review, 062001 (2009). https://doi.org/10.1088/0957-0233/20/6/062001.

[5] T.A. Berfield, J.K. Patel, R.G. Shimmin, P. V. Braun, J. Lambros, N.R. Sottos, Micro- and nanoscale deformation measurement of surface and internal planes via digital image correlation, Exp. Mech. 47 (2007) 51–62. https://doi.org/10.1007/s11340-006-0531-2.

[6] N. McCormick, J. Lord, Digital image correlation, Mater. Today. 13 (2010) 52–54. https://doi.org/10.1016/S1369-7021(10)70235-2.

[7] J. Brillaud, F. Lagattu, Limits and possibilities of laser speckle and white-light image-correlation methods: theory and experiments, Appl. Opt. 41 (2002) 6603. https://doi.org/10.1364/ao.41.006603.

[8] M. Luo, Displacement/strain measurements using an optical microscope and digital image correlation, Opt. Eng. 45 (2006) 033605. https://doi.org/10.1117/1.2182108.

[9] Z. Sun, J.S. Lyons, S.R. McNeill, Measuring Microscopic Deformations with Digital Image Correlation, Opt. Lasers Eng. 27 (1997) 409–428. https://doi.org/10.1016/S0143-8166(96)00041-3.

[10] B. Murali Krishna, V. Guru Prathap Reddy, T. Tadepalli, P. Rathish Kumar, Y. Lahir,

Numerical and experimental study on flexural behavior of reinforced concrete beams: Digital image correlation approach, Comput. Concr. 24 (2019) 561–570. https://doi.org/10.12989/cac.2019.24.6.561.

[11] J. Blaber, B. Adair, A. Antoniou, Ncorr : Open-Source 2D Digital Image Correlation Matlab Software, (2015) 1105–1122. https://doi.org/10.1007/s11340-015-0009-1.

[12] B. Murali Krishna, T.P. Tezeswi, P. Rathish Kumar, K. Gopikrishna, M.V.N. Sivakumar, M. Shashi, QR code as speckle pattern for reinforced concrete beams using digital image correlation, Struct. Monit. Maint. 6 (2019) 67–84. https://doi.org/10.12989/smm.2019.6.1.067.

[13] A.H. Alavi, H. Hasni, N. Lajnef, K. Chatti, Continuous health monitoring of pavement systems using smart sensing technology, Constr. Build. Mater. 114 (2016) 719–736. https://doi.org/10.1016/j.conbuildmat.2016.03.128.

[14] James W.Dally, W. F.Riley, Experimental Stress Analysis, 3rd ed., Mc.Graw hill Inc., n.d.

[15] K. Helmi, T. Taylor, F. Ansari, Shear force – based method and application for real-time monitoring of moving vehicle weights on bridges, 26 (2015) 505–516. https://doi.org/10.1177/1045389X14529612.

[16] A. Sravanthi, R.L.N. Sai Prasad, P. Rathish Kumar, V.D.R. Pavan, P. Kishore, Study on bridge weigh in motion (BWIM) system for measuring the vehicle parameters based on strain measurement using FBG sensors, Opt. Fiber Technol. 61 (2021) 102440. https://doi.org/10.1016/j.yofte.2020.102440.

CHAPTER-6

STUDY ON CHANGES IN THE DYNAMIC CHARACTERISTICS OF VIBRATED AND SELF-COMPACTING BEAMS BEFORE DAMAGE AND AFTER REPAIR

This chapter deals with vibration based studies on concrete beams using model studies. The methods deal with inducing damage in prototype structures and studying the response of the specimens under damage conditions. The investigation focussed on two types of prototype structures deals in two stages. The first one is an FBG based bridge weigh in motion (BWIM) system made up of poly acrylic sheet, whereas the second stage deals with the experimental and numerical studies on concrete prisms making use of accelerometers. These two stages of study are conducted in four parts.

Part I focuses on creating artificial damages of different depths and at different locations on the simulated BWIM system and recording the signal to noise ratio in the temporal response of the FBG.

Part II includes vibration analysis of normally vibrated and self-compacting concrete with different types of fibres (steel fibres and glass fibres) and with induced artificial damages.

Part III deals with retrofitting of concrete prisms with epoxy-based material and to compare the dynamic parameters with its original undamaged condition.

Part IV corresponds to the validation of experimentally obtained dynamic parameters through software. The parameters in the study include use of steel and glass fibres and method of vibration i.e. normally vibrated concrete and self-compacting concrete with two types of fibres and without any fibre.

6.1 Introduction

Structural health monitoring (SHM) is developing as a critical tool to assist engineers in reinforcing the safety and maintainability of critical structures. SHM captures, logs, and analyses real-time data by combining a sort of sensing applied sciences with an embedded size controller. The capacity to monitor and detect deterioration to a structure at the earliest possible stage is a crucial maintenance task [1].

Fiber Bragg Grating (FBG) strain sensors have been used in a variety of applications, including load monitoring, impact localization, and damage detection. Many articles have been written that use a structure's change in vibration response to assess how stiff or rigid it

is. FBGs can identify smaller damages than vibration-based approaches, such as high sample rate interrogators, leading to increased study into damage detection [2,3].

Surface measurements of a vibrating structure can offer information on the health of its interior members without requiring the structure to be dismantled, which can be costly (or impossible). Vibration-based structural monitoring has gained popularity in recent years due to its efficacy in the approval and verification of structures. In this study OROS Analyzer was used to study vibration characteristics (Mode shapes, Natural frequencies and Damping) of normally vibrated [4] and self-compacting concrete [5] in presence of steel fiber [6] and glass fiber [7]. Many damage detection algorithms are there to identify different damage level in concrete beam [8–10]. Simplest way to get modal parameters is by curve fitting a set of FRFs. The distinction in the level of modernity or level of precision, among curve fitters is between a single mode and multiple mode strategy. Global methods work much superior to any MDOF methods for cases with local modes.

6.2 Part- I: Damage detection in BWIM systems

6.2.1 Experimental setup

For studying the health condition of a bridge under simulated damage conditions, a bridge prototype is designed by creating different magnitudes of damages at different locations. The Bridge prototype is made with of poly-acrylate sheet having length of 250 cm and 30 cm width with five longitudinal bridge beams each of 50 cm length. It is supported by six pairs of piers having 12 cm height and 4.0mm thickness as shown in Fig.6.1.

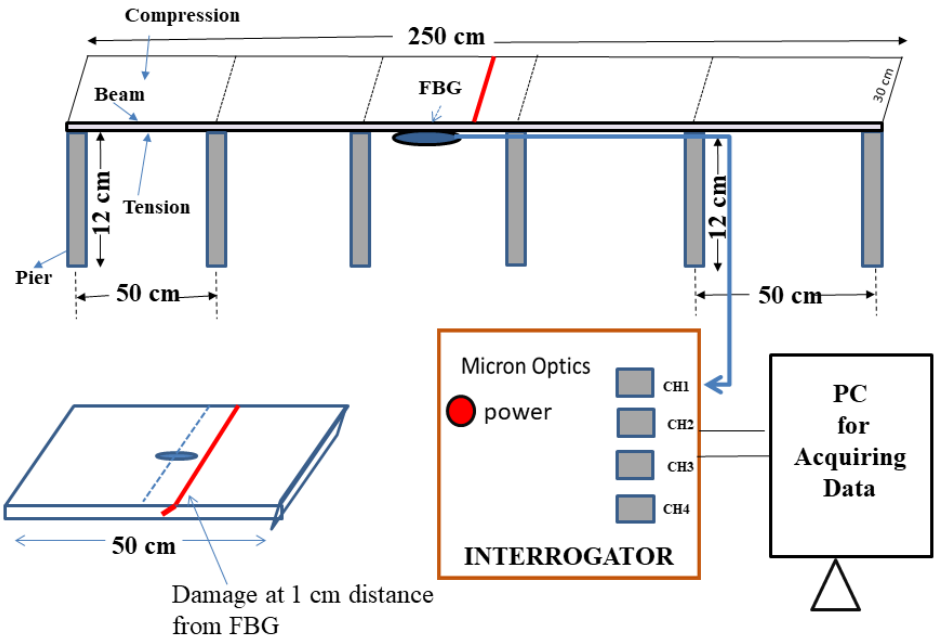

Fig. 6.1 Schematic Experimental setup

A FBG with Bragg wavelength of 1544.300nm at room temperature is used as the sensing element and is placed between the piers 3-4 as shown in Fig.6.1. The FBG is fixed exactly at the center position corresponding to the area of maximum flexural tension part of the bridge beam, and parallel to the line of central axis of the Bridge. This FBG is connected to the interrogator (Micron Optics) and using software (Enlight SM130), the data pertaining to the temporal response of the FBG is obtained through the networked PC. The acquired remote data of BWIM system is saved for further analysis.

Damage is created at the compression part of the bridge beam, at 0 cm, 1cm, 2cm and 3cm distance from the FBG and the depth of damage is increased in steps of 0.5 mm from 0.5 mm to 2.0 mm. with increase in the load on the vehicle, FBG gets strained and causes change in Bragg wavelength with load as the vehicle moves on the bridge deck. This temporal response of the FBG gives information about signal strength (SNR) which is acquired by the interrogator. The experiment was carried out for different loads for different magnitudes of damage at different distances from the FBG to study the structural health of the BWIM system.

6.2.2 Results and Discussion

In this experiment an FBG is fixed with the structure for the WIM studies. When a loaded vehicle passes over the bridge, Bragg wavelength shift i.e., in the form of strain values experienced are recorded with respect to time and from which, the signal to noise ratio is calculated by the ratio of average of the signal to standard deviation of the signal. As the magnitude of damage is increasing, the SNR has been found decreasing for various loads owing to stiffness loss in the material due to damage in the structure. The study has been performed for two different cases.

Case1: Keeping the magnitude of damage constant and varying the damage location from the center (1cm, 2 cm and 3cm from the FBG location). The temporal response of the FBG with a damage depth of 1mm magnitude for varying damage locations from the FBG location is as shown in Fig. 6.2.

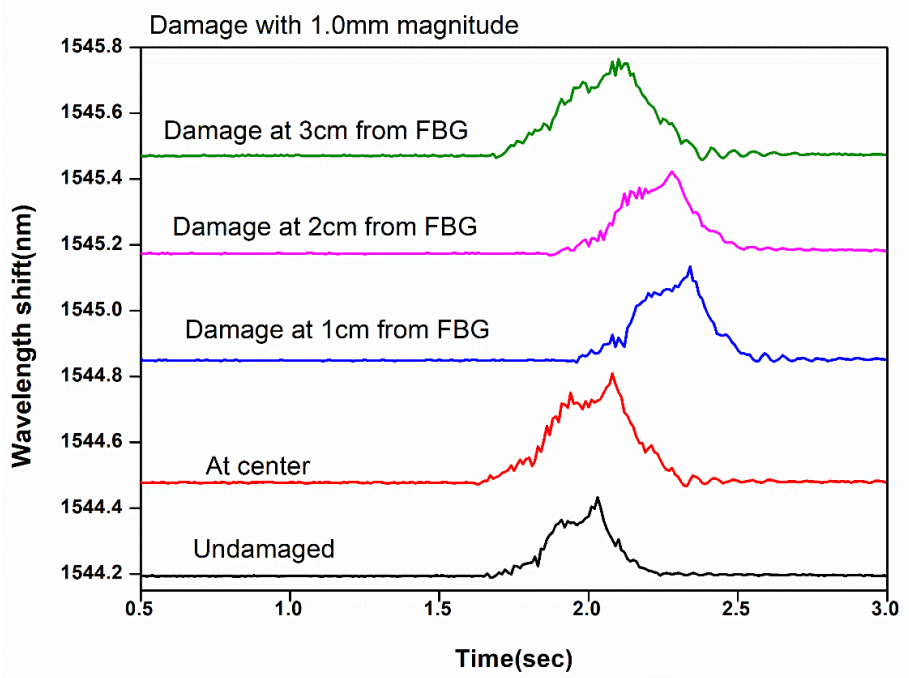

Fig. 6.2 Temporal response of FBG with 1 mm magnitude of damage for varying damage locations from FBG

Fig.6.2 depicts the temporal response of FBG for varying the damage locations (1, 2 and 3cm from the FBG) with constant 1 mm magnitude depth of damage and for 450 grams of applied load. It can be observed that as the distance of damage from the FBG location decreases, FBG's wavelength shift increases with increasing loads.

From the temporal response of FBG, the signal to noise ratio is calculated using Eq. (6.1) and the results are presented in Fig.6.3

$$\text{SNR}=\frac{\text{Average of the Signal}}{\text{Standard deviation of the signal}} \qquad Eq.(6.1)$$

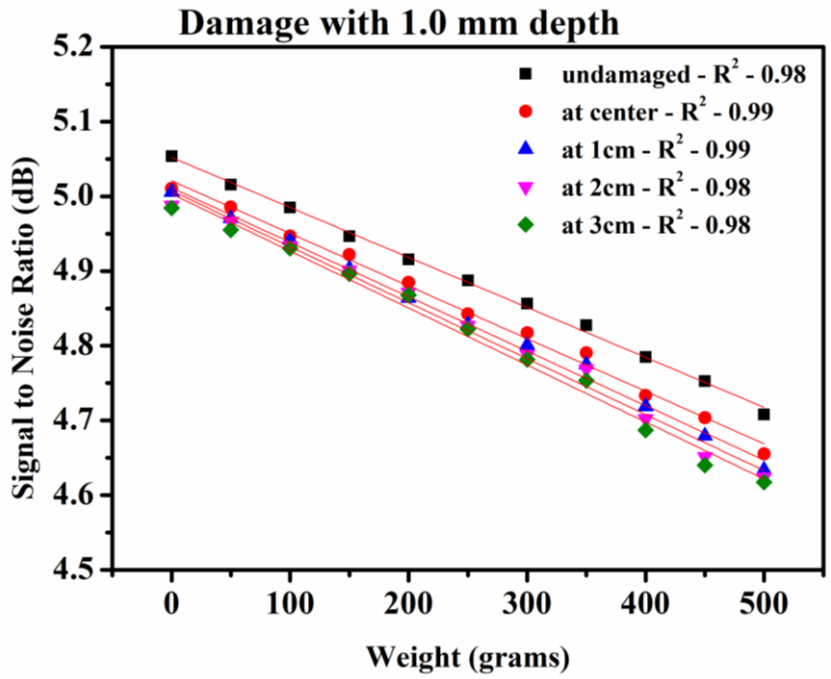

(a)

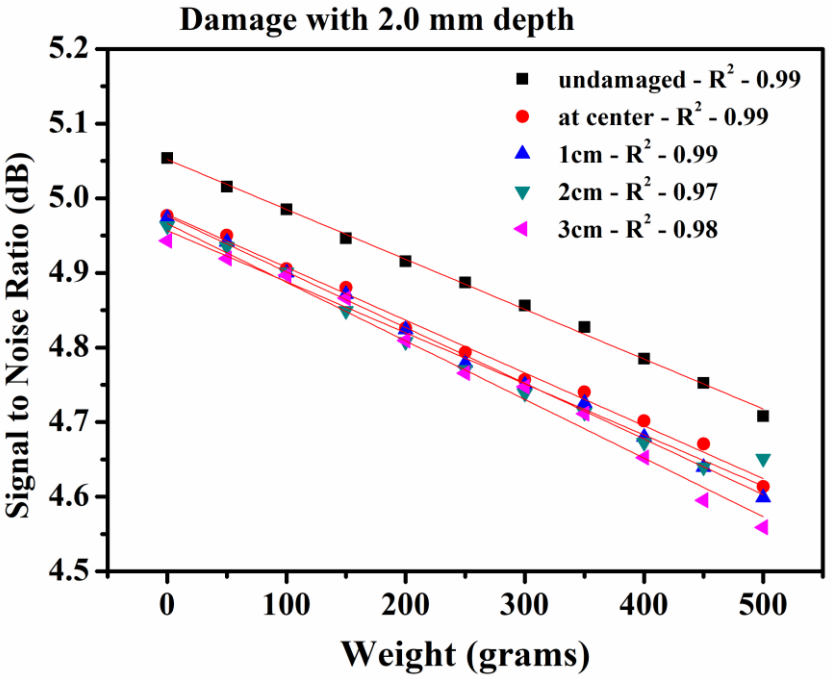

(b)

Fig. 6.3 (a) Damage with 1.0mm depth **(b)** Damage with 2.0mm depth at different distances from FBG Location

Fig. 6.3 illustrates the variation of SNR for fixed damage magnitude at various distances from the location of the FBG, and it is observed that as the location of damage from the FBG increases the SNR is found decreasing for various loads. As the damage distance from FBG location increases the signal strength also decreases. If the damage is exactly at the

point where FBG is attached, the proposed system was able to detect the damage by comparing with the undamaged response of the structure. As the damage distance from the FBG increases beyond some limit, the system did not detect the damage, in which case use of distributing FBG sensors can be employed to identify the damage location.

Case2: Keeping a fixed damage distance of 1 cm from the FBG location as fixed and varying the depth of damage by 0.5 mm, 1.0 mm, 1.5 mm, 2.0 mm and undamaged conditions with varying magnitudes of applied load on the vehicle(between 0 to 500grams), the temporal response of the FBG has been acquired and SNR values are calculated. The typical temporal response curves obtained for the case of damage from 1cm of the FBG location and for an applied load of 450grams on the vehicle are shown in Fig. 6.4.

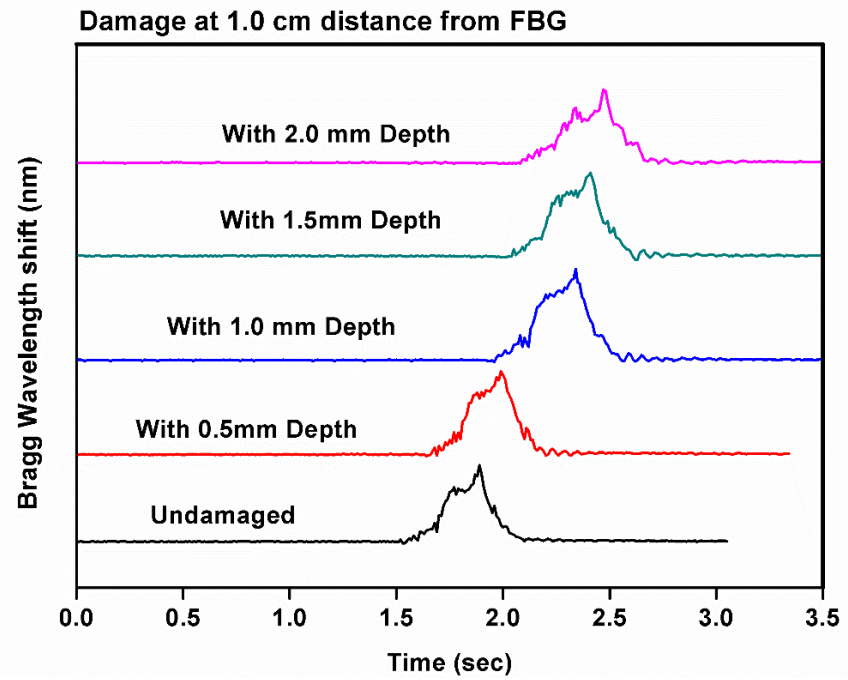

Fig. 6.4 Temporal response of FBG with varying magnitude of damage at constant 1 cm from the FBG location

Fig. 6.4 corresponds to constant distance of damage 1cm from the FBG and with different depths of damages (0.5, 1, 1.5, and 2mm) for a constant load of 450 grams. As the depth of damage increases closer to the FBG, the wavelength shift increases, while the damage magnitude away from the FBG has not that much impact on the FBG characteristics.

From the temporal response of FBG, the SNR values obtained, using Eq. (6.1) for variation of applied loads, the damage depths and for damage locations at 1.0 cm and at 2.0 cm distance from FBG location and are plotted as shown in Fig.6.5.

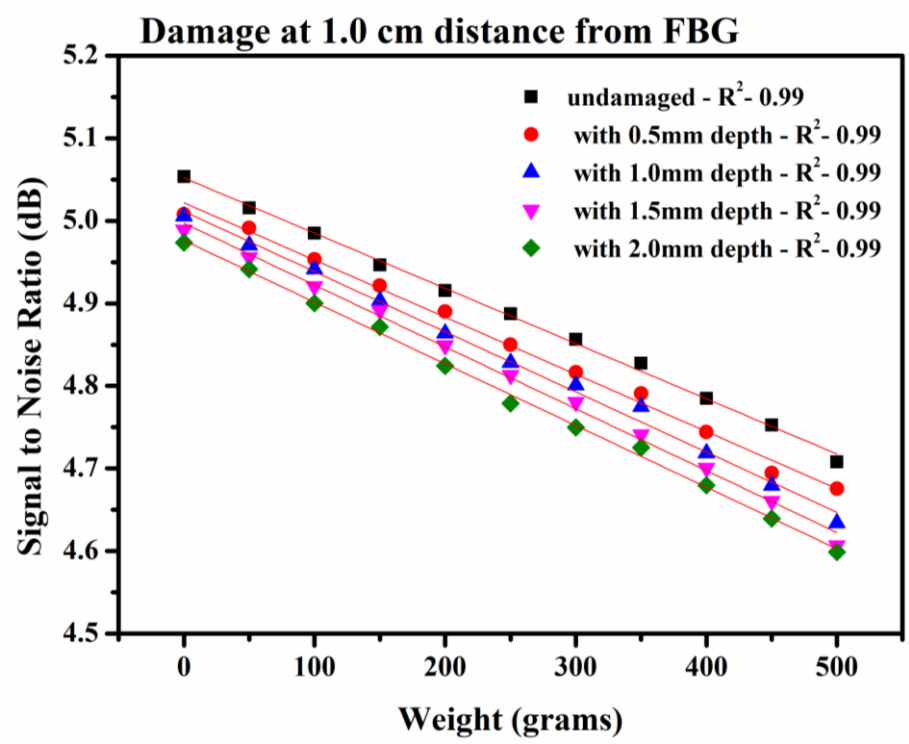

(a)

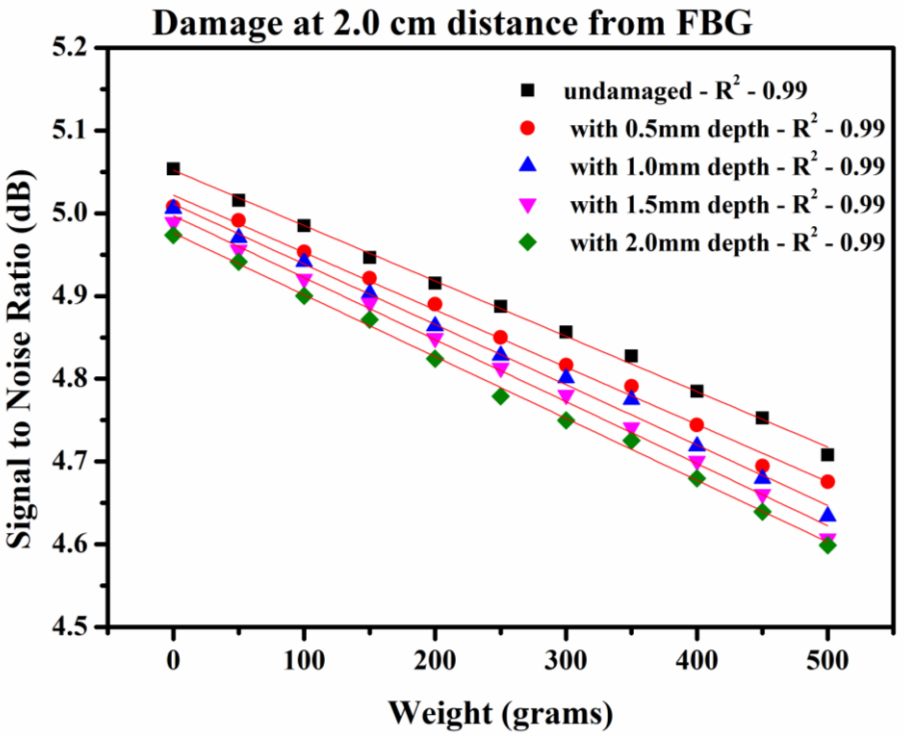

(b)

Fig. 6.5 (a) Damage at 1.0 cm **(b)** Damage at 2.0 cm distance from FBG Location at different magnitudes of damage

From Fig. 6.5, it can be observed that with increase in damage the SNR value is decreases. It means that the signal strength decreases as the magnitude of damage increases,

and hence, by comparing the SNR with the undamaged values, the severity of damage can be identified.

6.3 Part- II: Vibration analysis of Normally Vibrated and Self-compacting Concrete

This part of study deals with studies on vibration based damage detection of different types of beams vize, normal, SCC and without and with two types of fibers steel and glass.

6.3.1 Material preparation

The present study includes casting and testing of concrete samples of different material. The samples are 100x100x500 mm size prism/beam specimens of different types of materials viz., con-central, self-compacting and without and with different types of fibers. The details of the specimens cast and tested for vibration based modal analysis is as below:

1. Vibrated Concrete without fibers (VCNF)
2. Self-Compacting Concrete without fibers (SCCNF)
3. Vibrated Concrete with steel fibers (VCSF)
4. Self-compacting concrete with steel fiber (SCCSF)
5. Vibrated Concrete with glass fiber (VCGF)
6. Self-Compacting Concrete with glass fiber (SCCGF)

6.3.2 Mix proportioning

The mix design adopted in the present study is based on IS-10262-2009 for vibrated concrete while the self-compacting concretes designed based on Nan-su method [11]. Trial mixes have been performed before obtaining the required strength of concrete.

6.3.3 Preparation and Casting

All the dry materials (cement, fine aggregate, coarse aggregate) were initially mixed for about two minutes. Water and super plasticizer were added to the mixture of dry materials, and then thoroughly mixed for a few minutes to get the uniform mixture. Care has been taken to allow all the materials to get mixed up uniformly to ensure materials not to get stuck to the walls of the mixer. There was no segregation and bleeding issues in concrete.

Standard prism moulds were taken and the prepared concrete mix was poured in three layers and compacted with table vibrator. However, in the preparation of self-compacting concrete beams, no vibration was provided. At the end of casting, the top surface was made plane using trowel to ensure a uniform top surface.

6.3.4 Experimental setup

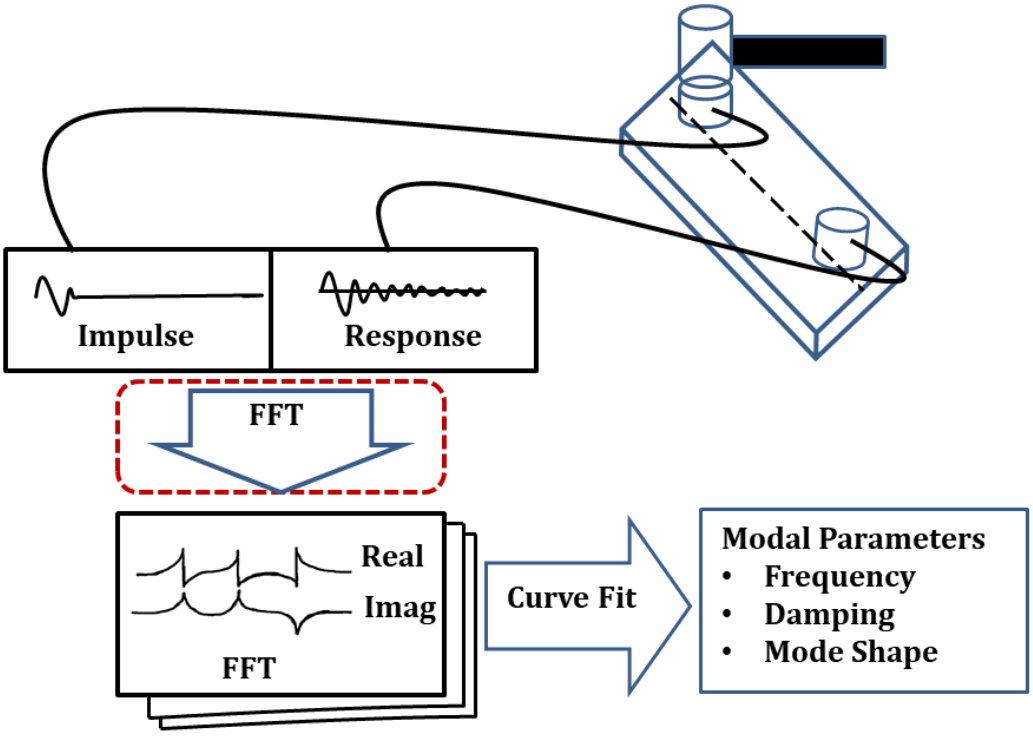

Fig. 6.6 Schematic Representation of Test setup

The measurement set up for the present investigation is as shown in Fig 6.6. Force is applied to the structure by the impulse hammer and the response is measured by a suitable response transducer. After the application of force on the specimen, the response signals picked up by the transducer are allowed to pass through signal conditioning equipment, including amplifiers, and further the signals are digitized. The digitized signals are then Fourier transformed using the appropriate windows and the cross spectrum and the power spectra are computed and averaged. Finally, the frequency response and coherence functions are computed from the averaged power spectrum and cross spectrum.

6.3.5 Testing procedure

The prisms having dimensions 100x100x500 mm were marked with 11 points (Grid points) along longitudinal direction to the beam leaving space for the supports at either ends as shown in Fig.6.7. The prisms to be tested were to be in free-free condition. But creating the free-free condition is not realistic and hence; to simulate this free-free condition experimentally, the prisms were hung using simple thread of negligible mass and stiffness. Accelerometer was attached to the prism at geometric center of the top surface of the panel using wax and was connected to the central unit of the OROS analyser set up through one of the channels as shown in Fig.6.8. The input excitation was given by the impulse hammer and

the readings from the hammer were connected to a particular channel. The response of the accelerometer has been acquired and stored for further analysis.

Fig. 6.7 Grid points on the prism

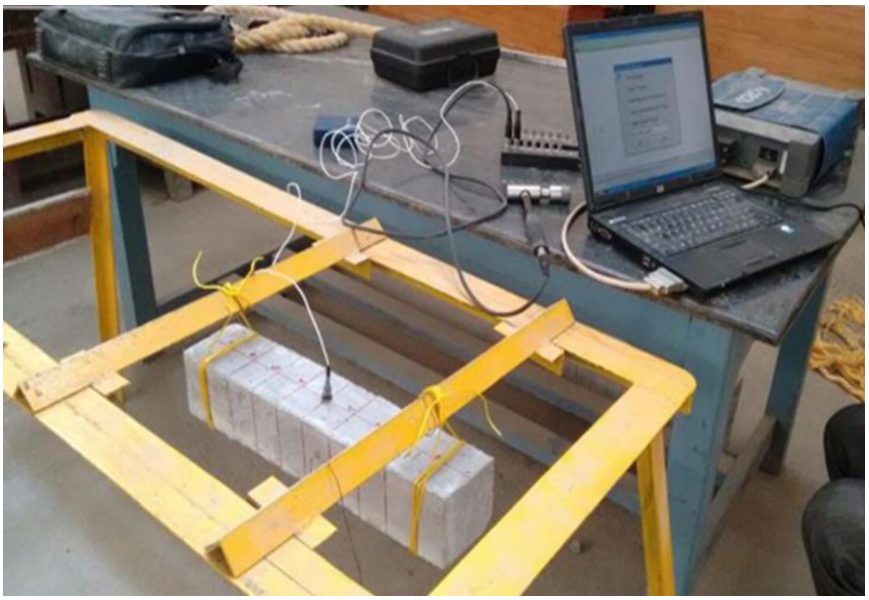

Fig. 6.8 Setup of OROS analyser

Damage was induced on the specimens by making cuts on the beam at different location of different percentages. The cast specimens cut to different damage scenarios is as listed below:

1. **D0**: No damage
2. **D1-1**: 10% damage at centre
3. **D1-2**: 10% damage at centre and at a dist. of 100mm towards right.
4. **D1-3**: 10% damage at centre and at a dist. of 100mm towards right and left.
5. **D2-1**: 25% damage at centre
6. **D2-2**: 25% damage at centre and at a dist. of 100mm towards right.

7. **D2-3**: 25% damage at centre and at a dist. of 100mm towards right and left.
8. **D3-1**: 35% damage at centre
9. **D3-2**: 35% damage at centre and at a dist. of 100mm towards right.
10. **D3-3**: 35% damage at centre and at a dist. of 100mm towards right and left.

(a)

(b)

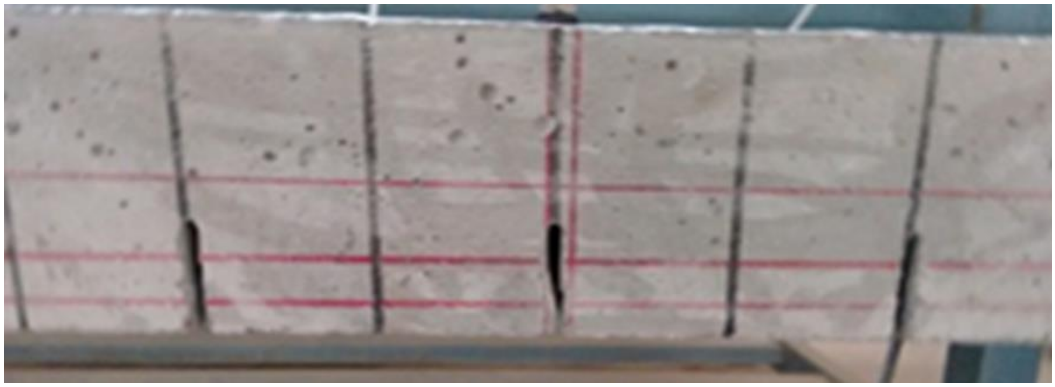

(c)

Fig. 6.9 Different Damage cases (a) damage case D1-3 (b) D2-3 (c) D3-3

Fig. 6.9 shows the different damage cases, i.e, 6.9(a) shows damage 10% damage at centre and at a distance of 100mm towards right and left (D1-3), 6.9 (b) shows 25% damage

at centre and at a distance of 100mm towards right and left (D2-3), 6.9(c) shows 35% damage at centre and at a distance of 100mm towards right and left. Schematic diagrams of the damage cases are shown in Fig. 6.10 (a) to Fig. 6.10 (I).

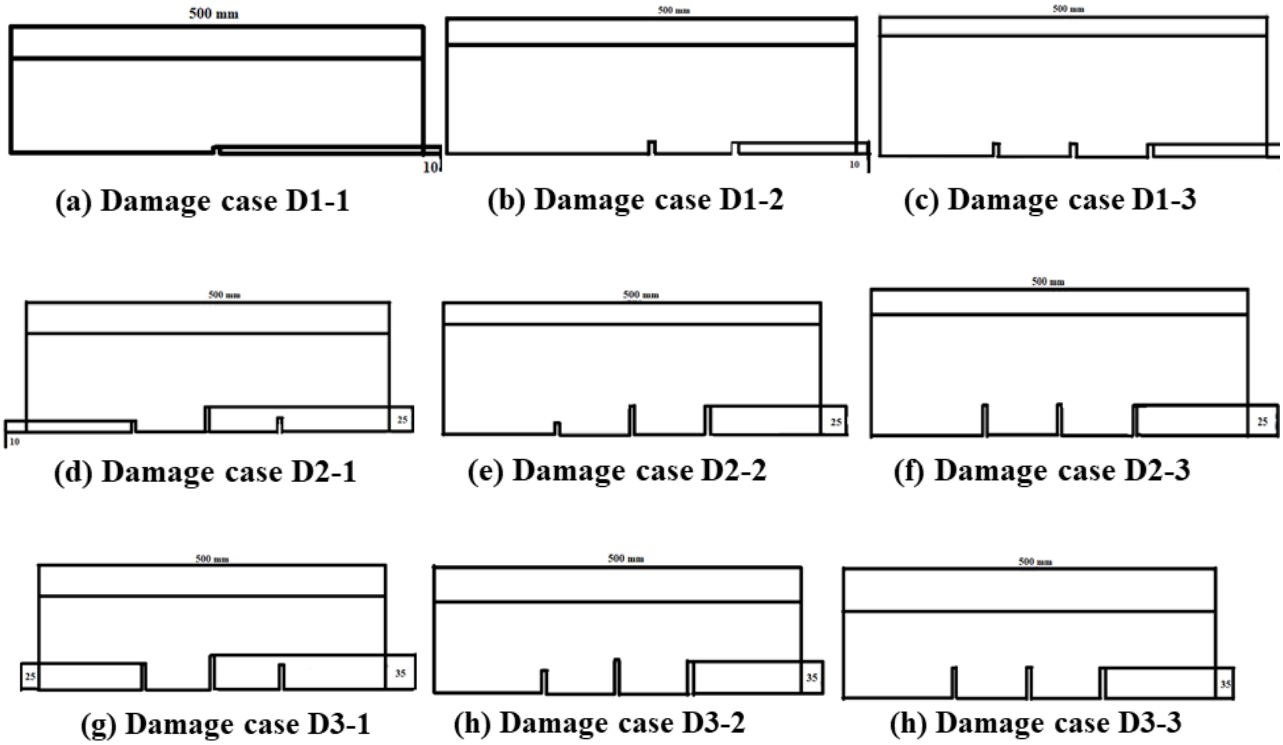

Fig. 6.10 Schematic damage cases

There are two methods of conducting modal analysis – roving impact method and roving accelerometer method.

6.3.5.1 ROVING IMPACT

In this method, the accelerometer is fixed at a particular point of the marked grid and the specimen is excited using an impact hammer at any grid point and the corresponding FRF is recorded at that grid point. This is orderly repeated for all the grid points without moving the accelerometer from the initial point. Since the impact hammer is only moved keeping the accelerometer at a ·constant point, it is called roving impact.

6.3.5.2 ROVING ACCELEROMETER

In this method, instead of moving the impact hammer from one point to another, accelerometer is sequentially moved to each grid point giving the excitation by the impact hammer at any given fixed point.

Here both methods have been adopted and results have been accepted from both the methods as per requirement.

Table 6.1: Input settings

Input Channel	**Range**	**Gain**	**Coupling**	**Unit**	**Transducer**	**Sensitivity**
External			AC			
Ch.1	310mV	20 dB	ICP	N	PCB IMPULSE HAMMER	0.00225 V/N
Ch.2	31mV	40 dB	ICP	m/s^2	PCB	0.00101940V/m/s^2

Table 6.2: Analyzer settings

Frequency	Range	0-2 kHz	Resolution	801	Zoom	Without	Envelope	Off
Analysis	Overlap	0%	Weight W1	Force	W2	Response		
Average	Domain	Spectral	Mode	Linear	Number	3	Refresh	1
Trigger	Mode	Level	Channel	Ch.1	Thresh. %	10%	Delay	-0.02
Tach	Mode	Off	Channel	External	Thresh. %	10%	Tach/rev.	1.00
Arming	Mode	Free Run	Channel					
Generator1	Mode	Stopped	Freq.	0.100 kHz	Level	1 V		
Generator2	Mode	Stopped	Freq.	0.100 kHz	Level	1 V	phase	0^o
Waterfall	Mode	Stopped	Type	off	Number	50		

The frequency response functions are measured and then these FRFs are converted from AE2 format to UFF format. The frequency response functions are analysed to get the Modal Parameters using NV Solutions Smart Office software package.

6.3.6 Results and Discussion

It was observed that there is decrease in the natural frequency with increase in damage from D0 case to D3-3 case. This is attributed to the fact that with increasing levels of damage, the integrity of the material gets disturbed and the wave propagation through the material is seriously affected.

Changes in frequencies for different damage cases for different samples are given in the following tables.

Table 6.3 A: Natural frequencies for the samples for Damage case D0

Specimen	Mass [m] (kg)	Length [L] (m)	Mass/Length [$\overline{m}$] (kg/m)	Breadth [b] (m)	Depth [d] (m)	Moment of Inertia *** [I] (m^4)	Approximate Young's Modulus [E] (MPa)	$\omega_n = \frac{\left\{\left[n+\frac{1}{2}\right]\pi\right\}^2 \sqrt{\frac{EI}{\overline{m}L^4}}}{2\pi}$ (Hz)	Experimental obtained frequencies (Hz)	
									Roving Impact	Roving acceleration
VCNF	11.88	0.5	23.76	0.1	0.1	8.33E-06	3.71E+10	1611.49	1532.63	1532.45
SCCNF	11.76	0.5	23.53	0.1	0.1	8.33E-06	3.65E+10	1606.15	1559.15	1558.89
VCSF	12.2	0.5	24.4	0.1	0.1	8.33E-06	3.74E+10	1596.63	1527.8	1528.67
SCCSF	12.35	0.5	24.7	0.1	0.1	8.33E-06	3.67E+10	1571.99	1526.36	1527.98
VCGF	12.00	0.5	24	0.1	0.1	8.33E-06	3.93E+10	1650.27	1594.55	1592.5
SCCGF	12.00	0.5	24	0.1	0.1	8.33E-06	3.84E+10	1631.5	1544.60	1544.09

Table 6.3 B: Natural frequencies for the samples for Damage case D1-1

Specimen	Mass [m] (kg)	Length [L] (m)	Mass/Length [$\bar{m}$] (kg/m)	Breadth [b] (m)	Depth [d] (m)	Moment of Inertia *** [I] (m^4)	Approximate Young's Modulus [E] (MPa)	$\omega_n = \frac{\left\{\left[n+\frac{1}{2}\right]\pi\right\}^2 \sqrt{\frac{EI}{\bar{m}L^4}}}{2\pi}$ (Hz)	Experimental obtained frequencies (Hz)	
									Roving Impact	Roving acceleration
VCNF	11.88	0.5	23.76	0.1	0.1	6.08E-06	3.71E+10	1376.19	1483.37	1485.24
SCCNF	11.76	0.5	23.53	0.1	0.1	6.08E-06	3.65E+10	1371.67	1513.99	1512.99
VCSF	12.2	0.5	24.4	0.1	0.1	6.08E-06	3.74E+10	1363.5	1491.82	1490
SCCSF	12.35	0.5	24.7	0.1	0.1	6.08E-06	3.67E+10	1342.46	1471.36	1471.4
VCGF	12	0.5	24	0.1	0.1	6.08E-06	3.93E+10	1409.89	1509.75	1509.45
SCCGF	12	0.5	24	0.1	0.1	6.08E-06	3.84E+10	1393.65	1469.83	1469.304

Table 6.3 C: Natural frequencies for the samples for Damage case D1-2

Specimen	Mass [m] (kg)	Length [L] (m)	Mass/Length [$\bar{m}$] (kg/m)	Breadth [b] (m)	Depth [d] (m)	Moment of Inertia *** [I] (m^4)	Approximate Young's Modulus [E] (MPa)	$\omega_n = \frac{\left\{\left[n+\frac{1}{2}\right]\pi\right\}^2 \sqrt{\frac{EI}{\bar{m}L^4}}}{2\pi}$ (Hz)	Experimental obtained frequencies (Hz)	
									Roving Impact	Roving acceleration
VCNF	11.88	0.5	23.76	0.1	0.1	6.06E-06	3.71E+10	1374.49	1463.65	1459.24
SCCNF	11.76	0.5	23.53	0.1	0.1	6.06E-06	3.65E+10	1369.98	1482.79	1481.364
VCSF	12.2	0.5	24.4	0.1	0.1	6.06E-06	3.74E+10	1361.82	1470.33	1466.97
SCCSF	12.35	0.5	24.7	0.1	0.1	6.06E-06	3.67E+10	1340.8	1436.77	1434.54
VCGF	12	0.5	24	0.1	0.1	6.06E-06	3.93E+10	1407.59	1494.73	1495.98
SCCGF	12	0.5	24	0.1	0.1	6.06E-06	3.84E+10	1391.36	1436.92	1437.5

Table 6.3 D: Natural frequencies for the samples for Damage case D1-3

Specimen	Mass [m] (kg)	Length [L] (m)	Mass/Length [$\bar{m}$] (kg/m)	Breadth [b] (m)	Depth [d] (m)	Moment of Inertia *** [I] (m^4)	Approximate Young's Modulus [E] (MPa)	$\omega_n = \frac{\left\{\left[n+\frac{1}{2}\right]\pi\right\}^2 \sqrt{\frac{EI}{\bar{m}L^4}}}{2\pi}$ (Hz)	Experimental obtained frequencies (Hz)	
									Roving Impact	Roving acceleration
VCNF	11.88	0.5	23.76	0.1	0.1	6.05E-06	3.71E+10	1373.35	1435.67	1435.96
SCCNF	11.76	0.5	23.53	0.1	0.1	6.05E-06	3.65E+10	1368.84	1459.09	1455.03
VCSF	12.2	0.5	24.4	0.1	0.1	6.05E-06	3.74E+10	1360.69	1445.63	1444.54
SCCSF	12.35	0.5	24.7	0.1	0.1	6.05E-06	3.67E+10	1339.69	1412.81	1412.55
VCGF	12	0.5	24	0.1	0.1	6.05E-06	3.93E+10	1406.40	1484.31	1483.86
SCCGF	12	0.5	24	0.1	0.1	6.05E-06	3.84E+10	1390.21	1425.34	1425.00

Table 6.3 E: Natural frequencies for the samples for Damage case D2-1

Specimen	Mass [m] (kg)	Length [L] (m)	Mass/Length [$\bar{m}$] (kg/m)	Breadth [b] (m)	Depth [d] (m)	Moment of Inertia *** [I] (m^4)	Approximate Young's Modulus [E] (MPa)	$\omega_n = \frac{\left\{\left[n+\frac{1}{2}\right]\pi\right\}^2 \sqrt{\frac{EI}{\bar{m}L^4}}}{2\pi}$ (Hz)	Experimental obtained frequencies (Hz)	
									Roving Impact	Roving acceleration
VCNF	11.88	0.5	23.76	0.1	0.1	3.50E-06	3.71E+10	1044.42	1317.06	1318.18
SCCNF	11.76	0.5	23.53	0.1	0.1	3.50E-06	3.65E+10	1040.99	1358.18	1356.48
VCSF	12.2	0.5	24.4	0.1	0.1	3.50E-06	3.74E+10	1034.8	1351.37	1354.64
SCCSF	12.35	0.5	24.7	0.1	0.1	3.50E-06	3.67E+10	1018.82	1298.11	1297.77
VCGF	12	0.5	24	0.1	0.1	3.50E-06	3.93E+10	1069.71	1370.455	1369.25
SCCGF	12	0.5	24	0.1	0.1	3.50E-06	3.84E+10	1057.4	1316.95	1317.27

Table 6.3 F: Natural frequencies for the samples for Damage case D2-2

Specimen	Mass [m] (kg)	Length [L] (m)	Mass/Length [$\overline{m}$] (kg/m)	Breadth [b] (m)	Depth [d] (m)	Moment of Inertia *** [I] (m^4)	Approximate Young's Modulus [E] (MPa)	$\omega_n = \frac{\left\{\left[n+\frac{1}{2}\right]\pi\right\}^2 \sqrt{\frac{EI}{\overline{m}L^4}}}{2\pi}$ (Hz)	Experimental obtained frequencies (Hz)	
									Roving Impact	Roving acceleration
VCNF	11.88	0.5	23.76	0.1	0.1	3.36E-06	3.71E+10	1023.42	1261.66	1260.11
SCCNF	11.76	0.5	23.53	0.1	0.1	3.36E-06	3.65E+10	1020.11	1315.47	1315.29
VCSF	12.2	0.5	24.4	0.1	0.1	3.36E-06	3.74E+10	1014.08	1320.00	1320.55
SCCSF	12.35	0.5	24.7	0.1	0.1	3.36E-06	3.67E+10	998.38	1265.77	1265.68
VCGF	12	0.5	24	0.1	0.1	3.36E-06	3.93E+10	1048.1	1307.27	1310.68
SCCGF	12	0.5	24	0.1	0.1	3.36E-06	3.84E+10	1036.03	1269.2	1272.4

Table 6.3 G: Natural frequencies for the samples for Damage case D2-3

Specimen	Mass [m] (kg)	Length [L] (m)	Mass/Length [$\bar{m}$] (kg/m)	Breadth [b] (m)	Depth [d] (m)	Moment of Inertia *** [I] (m^4)	Approximate Young's Modulus [E] (MPa)	$\omega_n = \frac{\left\{\left[n+\frac{1}{2}\right]\pi\right\}^2 \sqrt{\frac{EI}{\bar{m}L^4}}}{2\pi}$ (Hz)	Experimental obtained frequencies (Hz)	
									Roving Impact	Roving acceleration
VCNF	11.88	0.5	23.76	0.1	0.1	3.24E-06	3.71E+10	1004.42	1232.73	1228.64
SCCNF	11.76	0.5	23.53	0.1	0.1	3.24E-06	3.65E+10	1001.41	1270.88	1269.57
VCSF	12.2	0.5	24.4	0.1	0.1	3.24E-06	3.74E+10	995.45	1275.3	1275.30
SCCSF	12.35	0.5	24.7	0.1	0.1	3.24E-06	3.67E+10	980.09	1208.68	1207.73
VCGF	12	0.5	24	0.1	0.1	3.24E-06	3.93E+10	1029.21	1260.59	1262.73
SCCGF	12	0.5	24	0.1	0.1	3.24E-06	3.84E+10	1017.36	1230.62	1235.45

Table 6.3 H: Natural frequencies for the samples for Damage case D3-1

Specimen	Mass [m] (kg)	Length [L] (m)	Mass/Length [$\bar{m}$] (kg/m)	Breadth [b] (m)	Depth [d] (m)	Moment of Inertia *** [I] (m^4)	Approximate Young's Modulus [E] (MPa)	$\omega_n = \frac{\left\{\left[n+\frac{1}{2}\right]\pi\right\}^2 \sqrt{\frac{EI}{\bar{m}L^4}}}{2\pi}$ (Hz)	Experimental obtained frequencies (Hz)	
									Roving Impact	Roving acceleration
VCNF	11.88	0.5	23.76	0.1	0.1	2.02E-06	3.71E+10	793.56	1051.81	1051.37
SCCNF	11.76	0.5	23.53	0.1	0.1	2.02E-06	3.65E+10	790.96	1065.91	1064.37
VCSF	12.2	0.5	24.4	0.1	0.1	2.02E-06	3.74E+10	786.25	1128.41	1126.60
SCCSF	12.35	0.5	24.7	0.1	0.1	2.02E-06	3.67E+10	774.11	1065.23	1063.63
VCGF	12	0.5	24	0.1	0.1	2.02E-06	3.93E+10	812.66	1103.71	1101.71
SCCGF	12	0.5	24	0.1	0.1	2.02E-06	3.84E+10	803.30	1107.05	1102.14

Table 6.3 I: Natural frequencies for the samples for Damage case D3-2

Specimen	Mass [m] (kg)	Length [L] (m)	Mass/Length [$\bar{m}$] (kg/m)	Breadth [b] (m)	Depth [d] (m)	Moment of Inertia *** [I] (m^4)	Approximate Young's Modulus [E] (MPa)	$\omega_n = \frac{\left\{\left[n+\frac{1}{2}\right]\pi\right\}^2 \sqrt{\frac{EI}{\bar{m}L^4}}}{2\pi}$ (Hz)	Experimental obtained frequencies (Hz)	
									Roving Impact	Roving acceleration
VCNF	11.88	0.5	23.76	0.1	0.1	1.66E-06	3.71E+10	719.38	1003.74	1000.26
SCCNF	11.76	0.5	23.53	0.1	0.1	1.66E-06	3.65E+10	717.02	1004.91	1000.91
VCSF	12.2	0.5	24.4	0.1	0.1	1.66E-06	3.74E+10	712.75	1063.56	1059.78
SCCSF	12.35	0.5	24.7	0.1	0.1	1.66E-06	3.67E+10	701.75	1007.4	1005.53
VCGF	12	0.5	24	0.1	0.1	1.66E-06	3.93E+10	736.66	1059.45	1051.64
SCCGF	12	0.5	24	0.1	0.1	1.66E-06	3.84E+10	728.21	1058.71	1056.36

Table 6.3 J: Natural frequencies for the samples for Damage case D3-3

Specimen	Mass [m] (kg)	Length [L] (m)	Mass/Length [$\bar{m}$] (kg/m)	Breadth [b] (m)	Depth [d] (m)	Moment of Inertia *** [I] (m^4)	Approximate Young's Modulus [E] (MPa)	$\omega_n = \frac{\left\{\left[n+\frac{1}{2}\right]\pi\right\}^2 \sqrt{\frac{EI}{\bar{m}L^4}}}{2\pi}$ (Hz)	Experimental obtained frequencies (Hz)	
									Roving Impact	Roving acceleration
VCNF	11.88	0.5	23.76	0.1	0.1	1.30E-06	3.71E+10	636.62	951.77	948.63
SCCNF	11.76	0.5	23.53	0.1	0.1	1.30E-06	3.65E+10	634.53	953.77	949.54
VCSF	12.2	0.5	24.4	0.1	0.1	1.30E-06	3.74E+10	630.74	1021.45	1018.86
SCCSF	12.35	0.5	24.7	0.1	0.1	1.30E-06	3.67E+10	621.00	982.05	978.67
VCGF	12	0.5	24	0.1	0.1	1.30E-06	3.93E+10	651.94	1009.23	1002.95
SCCGF	12	0.5	24	0.1	0.1	1.30E-06	3.84E+10	644.43	1008.77	1007.66

Table 6.4 shows the details of the natural frequency of all the six samples for different damage scenarios

Table 6.4: Natural frequencies of samples for different damage cases

Specimen	Experimental frequencies at Damage Cases									
	D0	**D1-1**	**D1-2**	**D1-3**	**D2-1**	**D2-2**	**D2-3**	**D3-1**	**D3-2**	**D3-3**
VCNF	1532.6	1483.4	1463.7	1435.7	1317.1	1261.7	1232.7	1051.8	1003.7	951.8
SCCNF	1559.2	1514.0	1482.8	1459.1	1358.2	1315.5	1270.9	1065.9	1004.9	953.8
VCSF	1527.8	1491.8	1470.3	1445.6	1351.4	1320.0	1275.3	1128.4	1063.6	1021.5
SCCSF	1526.4	1471.4	1436.8	1412.8	1298.1	1265.8	1208.7	1065.2	1007.4	982.1
VCGF	1594.6	1509.8	1494.7	1484.3	1370.5	1307.3	1260.6	1103.7	1059.5	1009.2
SCCGF	1544.6	1469.8	1436.9	1425.3	1317.0	1269.2	1230.6	1107.1	1058.7	1008.8

It can observed from Table.6.4, that the Natural frequencies of VCNF and SCCNF samples for different damage cases (D0 to D3-3) decreased by 37.89% and 38.82% respectively. In case of steel fiber reinforced concrete, it was observed that this decrease in frequency is 33.14% and 35.66% respectively in case of VCSF and SCCSF samples. In case of glass fiber reinforced concrete samples there is a 36.70% and 34.69% decrease.

6.3.7 Comparison of Natural Frequencies between Normally Vibrated and Self-Compacting Concrete

Comparative studies between normally vibrated concrete and self-compacting concrete with no fiber, with silica fiber and with glass fiber are as shown in Fig.6.11 to Fig. 6.13 respectively.

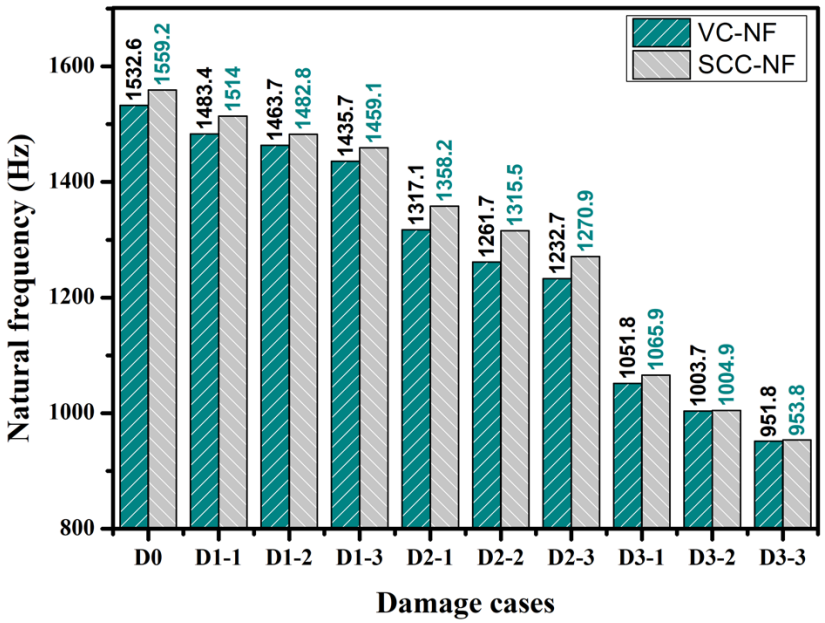

Fig. 6.11 Comparison of Natural freq. between VCNF & SCCNF

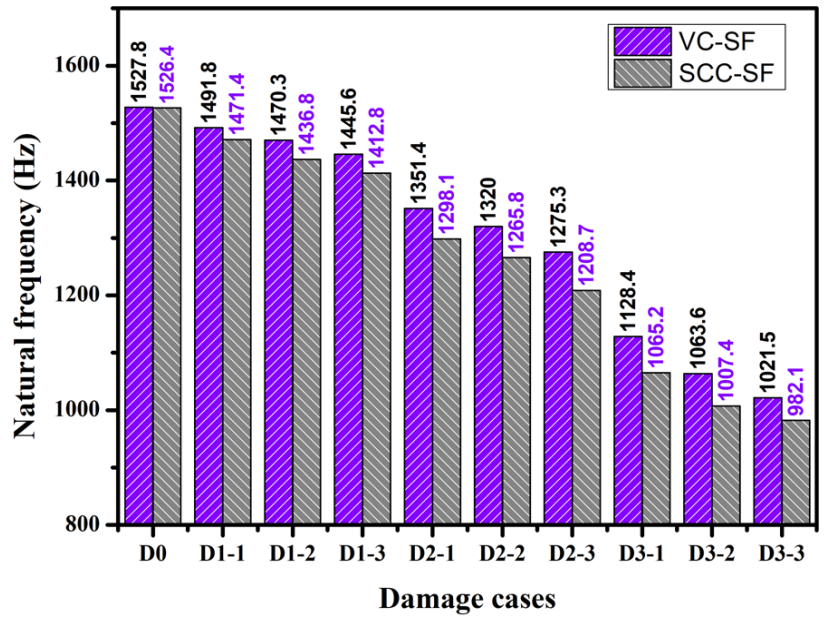

Fig. 6.12 Comparison of Natural freq. between VCSF & SCCSF

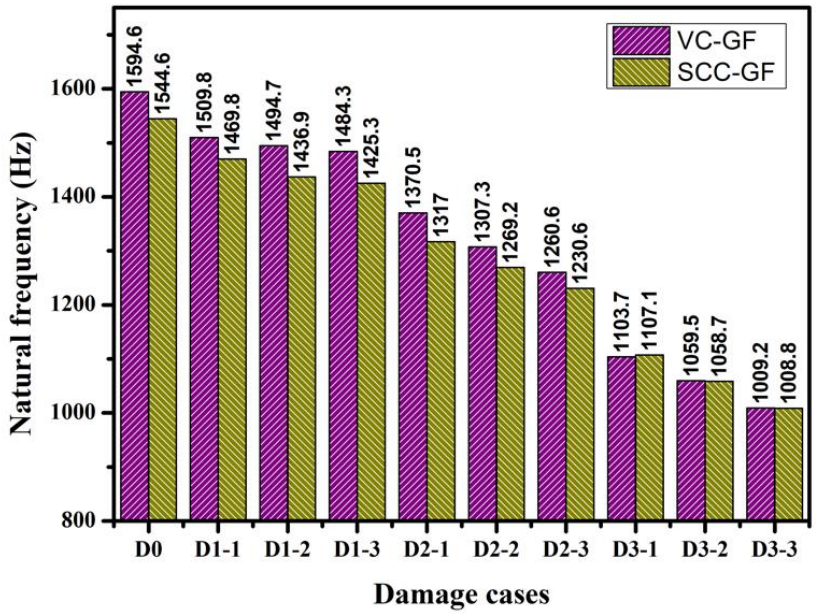

Fig.6.13 Comparison of Natural freq. between VCGF & SCCGF

From these figures it is observed that SCCNF has higher values of natural frequencies as the modulus of elasticity of SCC is more compared to normally vibrated concrete. Hence, the rigidity of SCCNF is more than VCNF. In all the damage scenarios the reluctance difference is more and less uniform.

6.4 Part III: Retrofitting of Concrete Prisms with Epoxy-Based Material

In this part, the damaged specimens were repaired with epoxy resin in the reverse pattern of how the damage is induced. Dynamic parameters were observed after each level of repairing the specimens with both roving accelerometer and roving hammer method.

It was observed that the frequencies at all damage levels are low compared to the original prism.

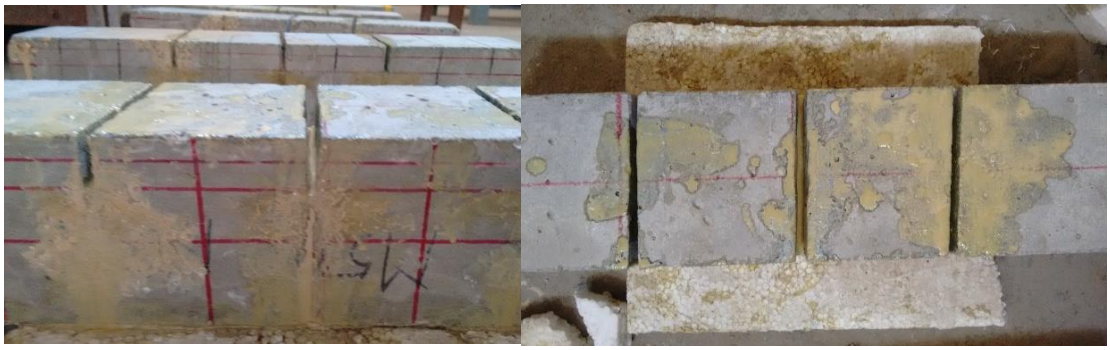

Fig 6.14 Samples after repairing with Epoxy

6.4.1 Results and discussion

Tables 6.5(a) to 6.5(i) shows the natural frequencies of the repaired prisms in Tables

Table 6.5 (a): Natural frequencies for the samples after repair - case D3-2

Specimen	Theoretical Frequency (ω_n)	Experimentally obtained Frequencies (Hz)	
		Before Repair	After Repair
VCNF	719.38	1003.74	961.45
SCCNF	717.02	1004.91	961.23
VCSF	712.75	1063.56	1033.45
SCCSF	701.75	1007.4	982.33
VCGF	736.66	1059.45	1017
SCCGF	728.21	1058.71	1014.78

Table 6.5 (b): Natural frequencies for the samples after repair - case D3-1

Specimen	Theoretical Frequency (ω_n)	Experimentally obtained Frequencies (Hz)	
		Before Repair	After Repair
VCNF	793.56	1051.81	973.01
SCCNF	790.96	1065.91	974.33
VCSF	786.25	1128.41	1066
SCCSF	774.11	1065.23	993.63
VCGF	812.66	1103.71	1045.2
SCCGF	803.30	1107.05	1031.37

Table 6.5 (c): Natural frequencies for the samples after repair - case D2-3

Specimen	Theoretical Frequency (ω_n)	Experimentally obtained Frequencies (Hz)	
		Before Repair	After Repair
VCNF	1004.42	1232.73	1000
SCCNF	1001.41	1270.88	994.09
VCSF	995.45	1275.3	1108.41
SCCSF	980.09	1208.68	1007.95
VCGF	1029.21	1260.59	1064.09
SCCGF	1017.36	1230.62	1057.95

Table 6.5 (d): Natural frequencies for the samples after repair - case D2-2

Specimen	Theoretical Frequency (ω_n)	Experimentally obtained Frequencies (Hz)	
		Before Repair	After Repair
VCNF	1023.42	1261.66	1083.86
SCCNF	1020.11	1315.47	1082.95
VCSF	1014.08	1320.00	1168.18
SCCSF	998.38	1265.77	1058.86
VCGF	1048.1	1307.27	1142.73
SCCGF	1036.03	1269.2	1127.95

Table 6.5 (e): Natural frequencies for the samples after repair - case D2-1

Specimen	Theoretical Frequency (ω_n)	Experimentally obtained Frequencies (Hz)	
		Before Repair	After Repair
VCNF	1044.42	1317.06	1188.18
SCCNF	1040.99	1358.18	1125.23
VCSF	1034.8	1351.37	1253.41
SCCSF	1018.82	1298.11	1155.45
VCGF	1069.71	1370.45	1242.27
SCCGF	1057.4	1316.95	1202.27

Table 6.5 (f): Natural frequencies for the samples after repair - case D1-3

Specimen	Theoretical Frequency (ω_n)	Experimentally obtained Frequencies (Hz)	
		Before Repair	After Repair
VCNF	1373.35	1435.67	1261.32
SCCNF	1368.84	1459.09	1209.54
VCSF	1360.69	1445.63	1327.5
SCCSF	1339.69	1412.81	1252.04
VCGF	1406.40	1484.31	1325
SCCGF	1390.21	1425.34	1270.23

Table 6.5 (g): Natural frequencies for the samples after repair - case D1-2

Specimen	Theoretical Frequency (ω_n)	Experimentally obtained Frequencies (Hz)	
		Before Repair	After Repair
VCNF	1374.49	1463.65	1355
SCCNF	1369.98	1482.79	1294.32
VCSF	1361.82	1470.33	1414.02
SCCSF	1340.8	1436.77	1329.77
VCGF	1407.59	1494.73	1380.91
SCCGF	1391.36	1436.92	1331.10

Table 6.5 (h): Natural frequencies for the samples after repair - case D1-1

Specimen	Theoretical Frequency (ω_n)	Experimentally obtained Frequencies (Hz)	
		Before Repair	After Repair
VCNF	1376.19	1483.37	1372.04
SCCNF	1371.67	1513.99	1317.5
VCSF	1363.5	1491.82	1431.82
SCCSF	1342.46	1471.36	1351.818
VCGF	1409.89	1509.75	1409.77
SCCGF	1393.65	1469.83	1369.77

Table 6.5 (i): Natural frequencies for the samples after repair - case D0

Specimen	Theoretical Frequency (ω_n)	Experimentally obtained Frequencies (Hz)	
		Before Repair	After Repair
VCNF	719.38	1003.74	961.45
SCCNF	717.02	1004.91	961.23
VCSF	712.75	1063.56	1033.45
SCCSF	701.75	1007.4	982.33
VCGF	736.66	1059.45	1017
SCCGF	728.21	1058.71	1014.78

6.4.2 Comparison of Natural frequencies before and after repair

The results obtained after repairing the prisms with epoxy has brought significant changes in the frequency, though it could not match with the frequency of the original prism at any damage levels. A comparison between the frequencies before and after repair of VC and SCC with no fiber, silica fiber and glass fiber are shown in Figs.6.15 to 6.20 respectively.

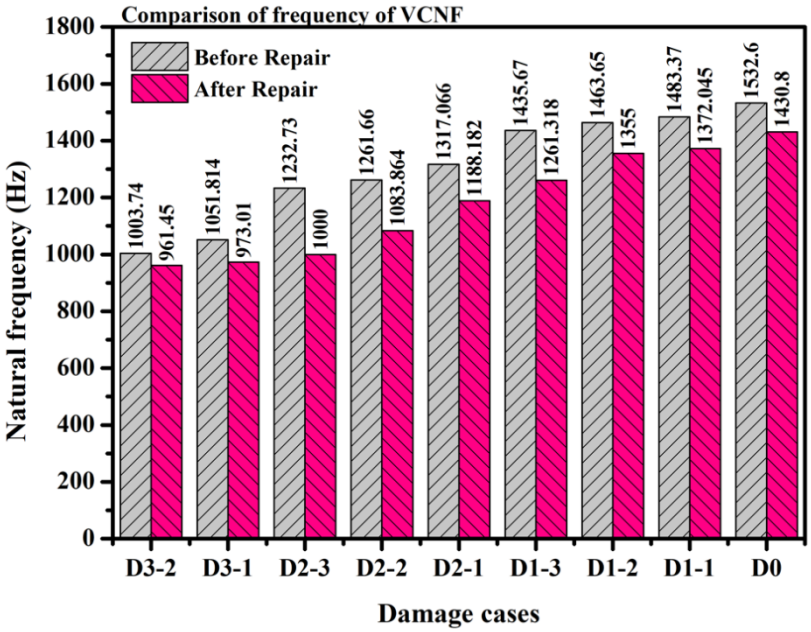

Fig 6.15 Comparison of frequency of VCNF before and after repair

.

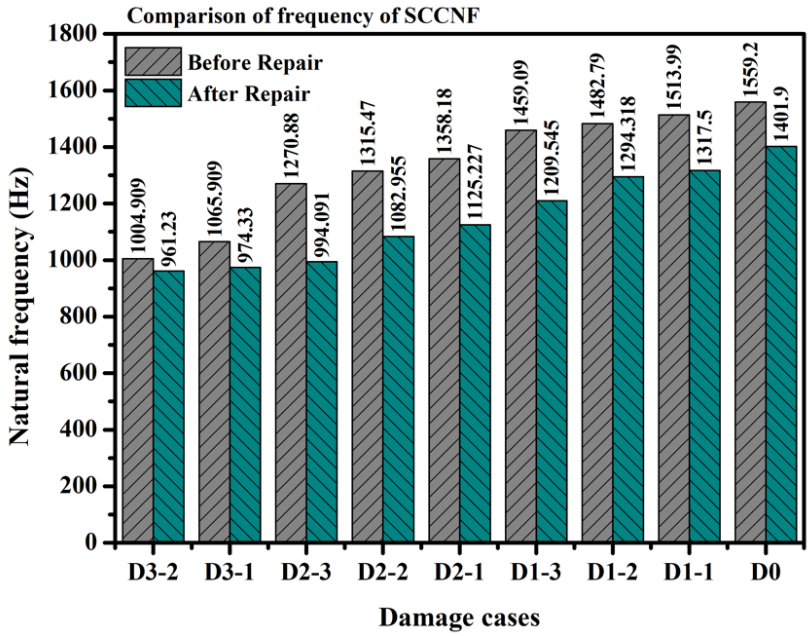

Fig.6.16 Comparison of frequency of SCCNF before and after repair

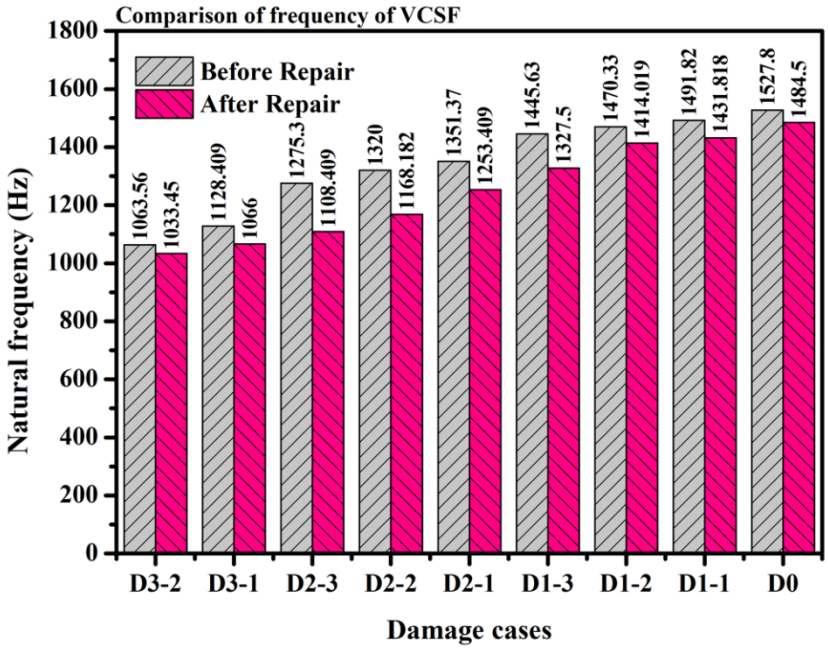

Fig.6.17 Comparison of frequency of VCSF before and after repair

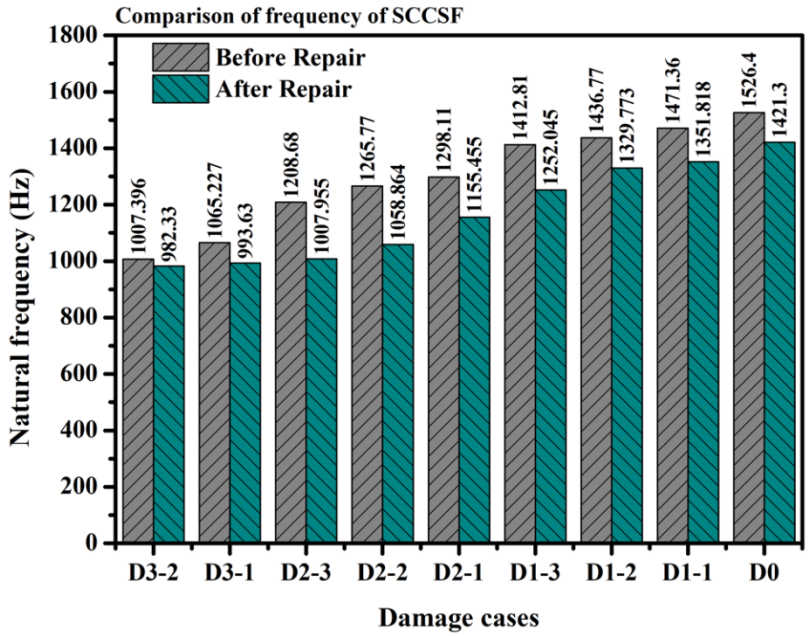

Fig. 6.18 Comparison of frequency of SCCSF before and after repair

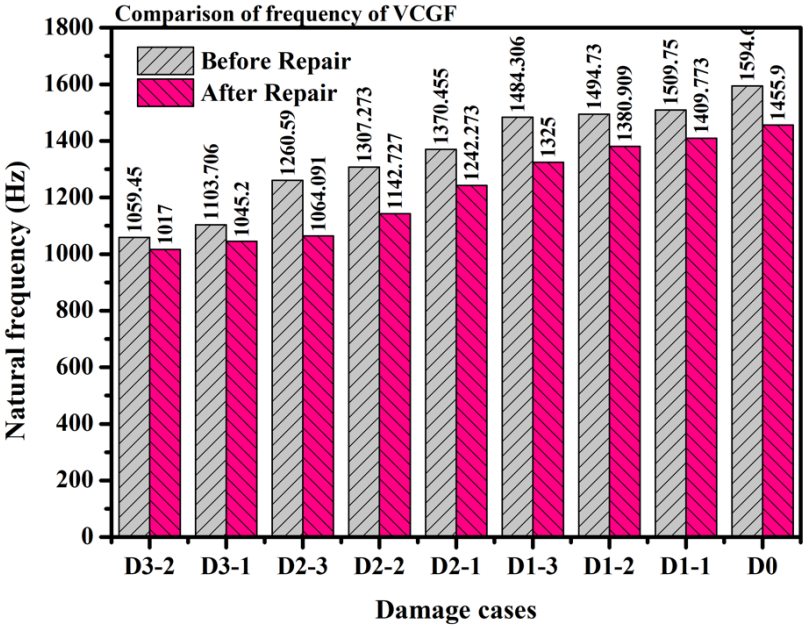

Fig.6.19 Comparison of frequency of VCGF before and after repair

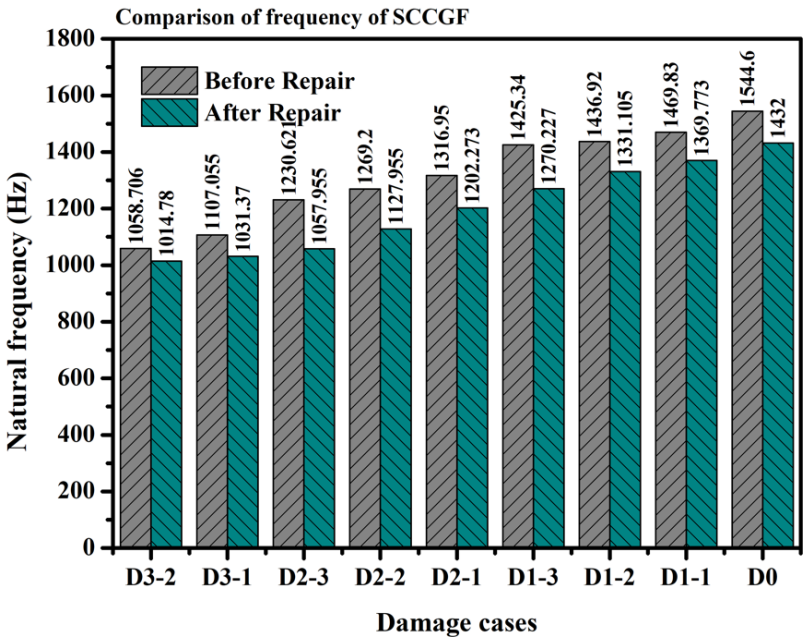

Fig. 6.20 Comparison of frequency of SCCGF before and after repair

From Fig. 6.15, it is evident that for a particular case, let's say D0, the frequency for unrepaired prism is around 6.63% higher than that of the repaired prism. Similar trend was found to be observed for other damage cases also.

6.5 Part-IV: Numerical Modelling of vibrated concrete sample (VCNF)

In this section, a numerical model was prepared for undamaged sample of VCNF and for damage case D3-1 for the same VCNF sample. The dynamic parameters obtained from experiment has been validated through these models. A similar model has been done for repaired beam for the same 2 cases and results are validated with experimental results.

6.5.1 Geometry and Material modeling

The model in ABAQUS consists of a 100x100x500 mm sized VCNF beam with free-free boundary condition.

The beam has been modelled with a 3D beam element. The material properties have been provided as per IS 456-2000. The elastic properties have been taken based on experimental values. The values are E = 35355 MPa and μ= 0.3. Density of concrete has been taken as 24kN/m^3. Hexagonal element shape was used for meshing technique and is shown in Fig 6.21. Eigen value analysis has been performed on the beam to find the natural frequencies and mode shapes.

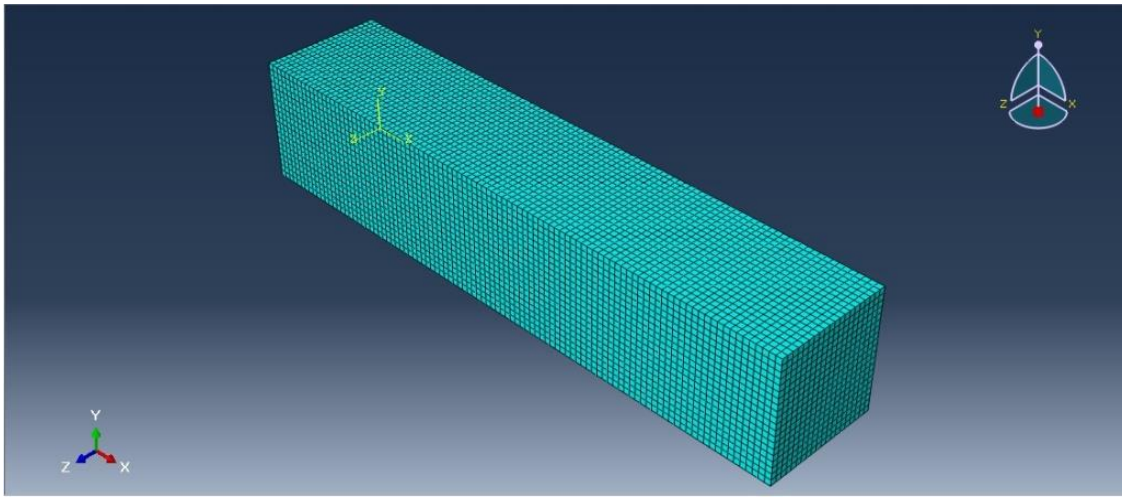

Fig 6.21 Finite element model of VCNF beam without damage (Damage case D0)

The same beam has been modelled for damage case D3-1 i.e. 35% damage at centre and 25% damage at 100mm distance from centre on both right and left sides with the same material properties and boundary conditions. The element shape was hexagonal for meshing and technique is structured. Eigen value analysis has been performed to find natural frequencies and mode shapes after the damage has been induced. The model is shown in Fig. 6.22.

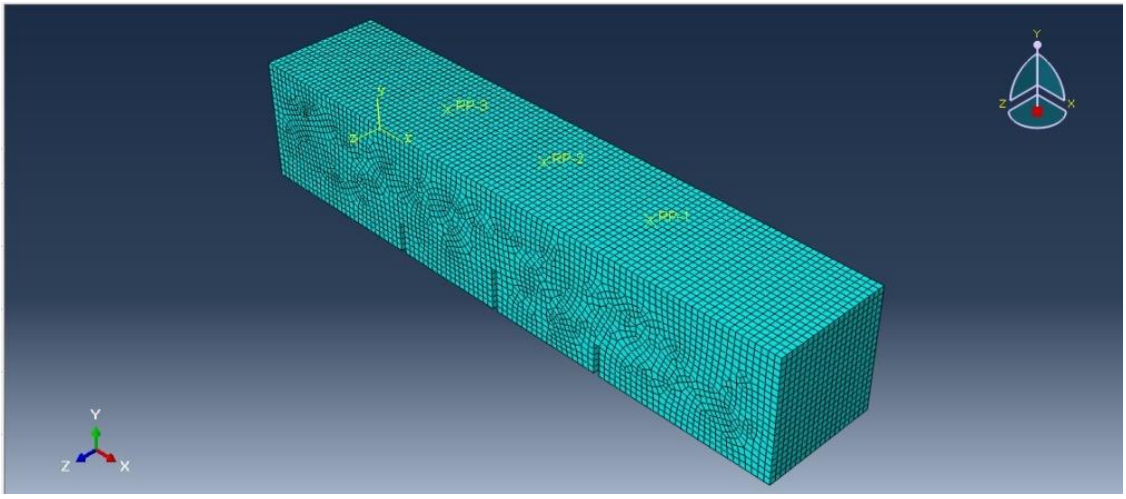

Fig 6.22 Finite element model of the VCNF beam (Damage case D3-1)

6.5.2 Results and discussion

A finite element model of the VCNF sample has been modelled in ABAQUS. Two damage cases D0 & D3-1 have been validated though finite element analysis software. Modal analysis (Eigen value problem) has been run on the model, to get the mode shapes and natural frequencies.

From literature, it has been found that for very rigid body, frequency will be very high and hence for free-free support condition the first few modes of analytical model may not give expected results. Therefore, in this study, higher modes were observed to give proper mode shapes and natural frequency.

In D0 case, 7^{th} mode shape along with the frequency was matching with experimental value and in D3-1 case 6^{th} mode shape and corresponding frequency matches the experimental value. The mode shapes and frequencies are shown in Fig. 6.23 and Fig. 6.24, for damage scenarios D0 and D3-1.

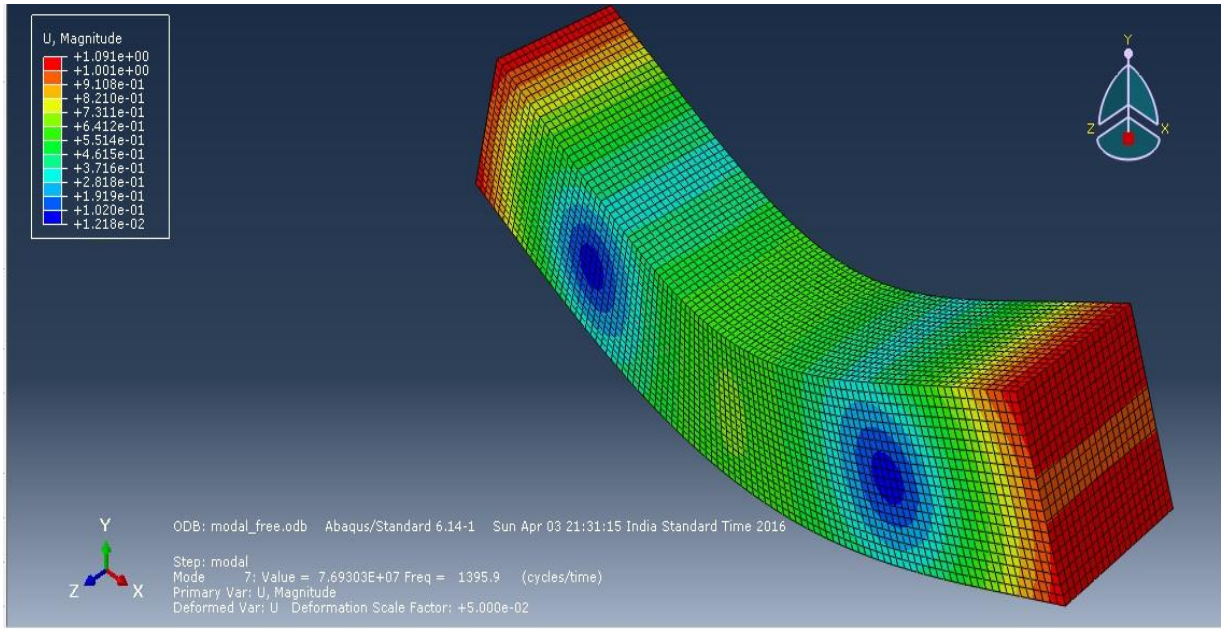

Fig 6.23 Mode shape and Natural frequency for VCNF- damage case- D0

The results obtained from numerical model **for VCNF- damage case- D0** is compared with the theoretical and experimental values of frequencies and are presented in Table 6.6.

Table 6.6 Comparison of Theoretical, Experimental & Analytical frequencies - D0

Theoretical Frequency (Hz)	Experimental Frequency (Hz)	From Numerical Model Frequency (Hz)
1577.91	1532.00	1395.9

It can be observed from the results that the numerically obtained natural frequency is 1395.9 Hz whereas, for the same case, the experimentally obtained natural frequency is 1532.00 Hz. While, that numerically obtained frequency from ABAQUS differs only by 8.81% from experimental frequency and 11% from theoretical frequency.

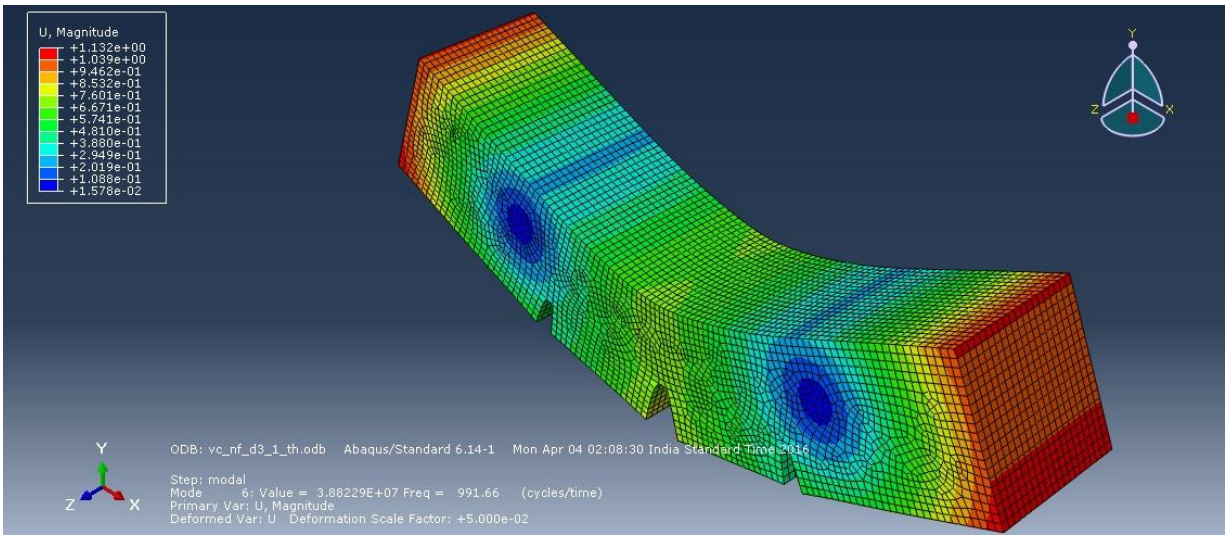

Fig 6.24 Mode shape and Natural frequency for VCNF- damage case- D3-1

The results obtained from analytical model for **VCNF- damage case- D3-1** is compared with theoretical and experimental values of frequencies and are presented in Table 6.7

Table 6.7: Comparison of Theoretical, Experimental & from Numerical model Frequencies – D3-1

Theoretical Frequency (Hz)	Experimental Frequency (Hz)	Analytical Frequency (Hz)
1004.42	1051.84	991.66

It can be observed from the results that the numerically obtained natural frequency is 991.66 Hz whereas, for the same case, the experimentally obtained natural frequency is 1051.84 Hz. and hence the numerically obtained frequency differs only by 6% with experimental frequency and 2% from theoretical frequency.

Summary of Phase 4 work

1. In the first part of this phase, the damage detection in a structure is simulated by designing a weigh-in motion system and detection using FBG sensors.
2. An artificial damage is created at different distances from FBG with various magnitudes, to test the proposed bridge prototype system and its response is studied using a remotely controlled vehicle with varying loads.
3. The monitoring system using WIM works satisfactorily and is also capable of studying the health condition of the bridges.
4. In second part of the study, a vibration analysis of normally vibrated and self-compacting concrete with different types of fibres (steel fibres and glass fibres) and with induced artificial damages was studied. The sensing devices used are accelerometers.
5. Natural frequency decreased with increase in damage.
6. Addition of steel fibres and glass fibres increases the Modulus of Elasticity of the structure and hence increase in the natural frequency.
7. Although with increasing damage, there is a decrease in frequency, it was noted that fibre reinforced concrete performed well.
8. When the damaged beams were repaired with Epoxy there is an improvement in natural frequency, but the values could not reach the natural frequency of the original specimen. Epoxy is not as rigid as concrete. Hence energy dissipation was more.
9. A Numerical model employs FE was prepared in ABAQUS. The results revealed that the experimental frequency of the structure and analytical frequency matches by more than 90%. In D0 case it differed by 8.81% from experimental value and 11% from theoretical value whereas for D3-1 case, the difference was 6% from experimental values and only 2% from theoretical values.
10. Due to rigidity of the structure and support conditions, the first few mode shapes were ignored. However, the results from numerical model matched well with the experimental results in higher modes.

In this chapter damage detection in BWIM systems using FBG sensors, by creating artificial damage on a prototype bridge is discussed and also detecting damage and repairing that damage with epoxy resin in concrete beams with embedding steel and glass fibers is discussed by use of vibration characteristics of a specimen with accelerometers, the same is simulated with FEM (ABAQUS) and results are compared.

References

[1] F.N. Catbas, Structural health monitoring: Applications and data analysis, in: Struct. Heal. Monit. Civ. Infrastruct. Syst., 2009: pp. 1–39. https://doi.org/10.1533/9781845696825.1.

[2] F. Grooteman, Multiple load path damage detection with optical fiber Bragg grating sensors, Struct. Heal. Monit. 20 (2021) 46–57. https://doi.org/10.1177/1475921720919678.

[3] B.W. Jo, R.M.A. Khan, Y.S. Lee, J.H. Jo, N. Saleem, A fiber Bragg grating-based condition monitoring and early damage detection system for the structural safety of underground coal mines using the Internet of things, J. Sensors. 2018 (2018). https://doi.org/10.1155/2018/9301873.

[4] PLAIN AND REINFORCED CONCRETE - CODE OF PRACTISE, Public.Resource.org, INDIA, 2000.

[5] Indian Standard, Coarse and Fine Aggregate for Concrete — Specification, 2016.

[6] J. Thomas, A. Ramaswamy, Mechanical Properties of Steel Fiber-Reinforced Concrete, J. Mater. Civ. Eng. 19 (2007) 385–392. https://doi.org/10.1061/(ASCE)0899-1561(2007)19.

[7] M. Prasad, P. Rathish Kumar, Development of Analytical Stress-Strain Model for Glass Fiber Reinforced Self Compacting Concrete, (2015).

[8] P. Rathish Kumar, T. Oshima, S. Mikami, Y. Miyamori, T. Yamazaki, Damage identification in a lightly reinforced concrete beam based on changes in the power spectral density, Struct. Infrastruct. Eng. 8 (2012) 715–727. https://doi.org/10.1080/15732471003730674.

[9] P.R. Kumar, T. Oshima, Detection and localization of small damages in a real bridge by local excitation using piezoelectric actuators, J. Civ. Struct. Heal. Monit. 2 (2012) 97–108. https://doi.org/10.1007/s13349-012-0020-5.

[10] B. Sherif, M. Shuichi, T. Oshima, Structural damage detection and localization using

changes in phase angle, J. Struct. Eng. 52A (2006) 29–40.

[11] N. Su, K. Hsu, H. Chai, A simple mix design method for self-compacting concrete, Cem. Concr. Res. 31 (2001) 1799–1807.

CHAPTER-7
CONCLUSIONS AND FUTURE SCOPE OF WORK

This chapter summarizes the results obtained from the research work. The detailed conclusions and the scope for further work is also presented. The entire work is divided into four phases to realize the set objectives.

7.1 Conclusions

1. A BWIM system is proposed using FBG based sensors to estimate the strains on the bridge and also to find the vehicle's parameters, while it is passing over the bridge. Two FBG rosettes are employed in the present investigation, oriented at 0^o, 45^o, and 90^o (3 element) to the bridge axis. The vehicle parameters like the Load, Velocity and the separation between the front and rear wheels have been estimated from the temporal response curves of the FBGs and there is a very close agreement.
2. The response of the proposed system is found linear with a good coefficient of average correlation of about 0.985 and an average sensitivity of 0.32 με/gram along 0^o orientation of FBG to the line of motion of the bridge beam. The corresponding values for 45^o are 0.85 and 0.06 με/gram. The experimental strain values are also observed to be in very close agreement with the simulated values based on MATLAB. Inclusion of more FBGs can improve the accuracy, however makes the measurements more involved, increasing the cost of the system as well.
3. A low-cost detection system has been designed and tested for static load conditions using an FBG sensor accompanied by a Long Period Grating (LPG) as an edge filter. The sensor output transmitted via Bluetooth to mobile could accurately measure the increase in the load up to 3000gms with an error of $\pm$1.67%. Hence, damage detection could be done effectively.
4. The proposed system could monitor the strain on the structure remotely in this case from a distance of about 10 meters. This distance can however be increased by adopting other frequency modulation techniques. This is an inexpensive and novel method for automated damage detection. This can further be extended for online monitoring for higher transmission ranges.

5. A novel noncontact strain measurement method based on Digital Image Correlation (DIC) is adopted for dynamic monitoring of pavement structures and the results are compared with the conventional method of sensing using Fiber Bragg gratings (FBG) as contact sensors.
6. A comparison of the FBG method and DIC method has revealed that FBG sensor has very high strain response compared to DIC method and is true with increasing load and number of revolutions made by the vehicle on the pavement with good linearity and sensitivity. However, the normalized principal strain responses evaluated by both the methods are in good agreement.
7. Damage detection simulated using weigh in motion system in a bridge prototype and FBG sensors could effectively monitor the response remotely for different load conditions. This was verified by simulating an artificial damage to the bridge girders.
8. Vibration based damage detection of conventional and self-compacting concrete beams was tested for influence of fibers by simulating damage scenarios. The accelerometer was used to measure the response. OROS analyzer with NV solutions software was adopted.
9. From the vibration based monitoring system, it was evident that with increase or damage there in a drop in natural frequency. Similarly, addition of fibers (Steel& glass) increased the natural frequency compared to no fiber specimens.
10. When conventional/ SCC beams were repaired using Epoxy system, there is an improvement in the natural frequency. However, none of the damaged specimens could reach the natural frequency.
11. The results from the FE model revealed that the experimental and numerical frequencies matched by more than 90%. In D0 case it varied by 8.81% from experimental value and 11% from theoretical value, while for D3-1 case, the difference was 6% from experimental values and only 2% from theoretical values.
12. In all the cases, there is a close comparison of the numerical and experimental values at higher modes.

7.2 Scope for Future Study

a. The Remote monitoring and technique developed can further be extended for higher transmission ranges based on wireless techniques by uploading data to the cloud.
b. FBG sensors can be replaced with etched FBG [1,2], POFBG [3–7] and tapered FBGs to further improve the sensitivity.
c. Embedding FBGs in prototype as well as real structures can be carried out for damage detection and prediction in engineering infrastructure.

References

[1] D. Luo, J. Ma, Z. Ibrahim, Z. Ismail, Etched FBG coated with polyimide for simultaneous detection the salinity and temperature, Opt. Commun. 392 (2017) 218–222. https://doi.org/10.1016/j.optcom.2016.12.068.

[2] K. Putha, D. Dantala, S. Kamineni, V.R. Pachava, Etched optical fiber vibration sensor to monitor health condition of beam like structures, Photonic Sensors. 3 (2013) 124–130. https://doi.org/10.1007/s13320-013-0106-7.

[3] C.A.F. Marques, A. Pospori, G. Demirci, O. Çetinkaya, B. Gawdzik, P. Antunes, O. Bang, P. Mergo, P. André, D.J. Webb, Fast bragg grating inscription in PMMA polymer optical fibres: Impact of thermal pre-treatment of preforms, Sensors (Switzerland). 17 (2017) 1–8. https://doi.org/10.3390/s17040891.

[4] A. Leal-Junior, A. Theodosiou, C. Díaz, C. Marques, M.J. Pontes, K. Kalli, A. Frizera-Neto, Polymer optical fiber Bragg Gratings in CYTOP Fibers for angle measurement with dynamic compensation, Polymers (Basel). 10 (2018). https://doi.org/10.3390/polym10060674.

[5] C.A.F. Marques, R. Min, A.L. Junior, P. Antunes, A. Fasano, G. Woyessa, K. Nielsen, H.K. Rasmussen, B. Ortega, O. Bang, Fast and stable gratings inscription in POFs made of different materials with pulsed 248 nm KrF laser, Opt. Express. 26 (2018) 2013. https://doi.org/10.1364/oe.26.002013.

[6] A.G. Leal-Junior, A. Theodosiou, C. Marques, M.J. Pontes, K. Kalli, A. Frizera, Compensation Method for Temperature Cross-Sensitivity in Transverse Force Applications with FBG Sensors in POFs, J. Light. Technol. 36 (2018) 3660–3665. https://doi.org/10.1109/JLT.2018.2848704.

[7] A. Leal-Junior, A. Frizera, C. Marques, M. José Pontes, Polymer-optical-fiber-based sensor system for simultaneous measurement of angle and temperature, Appl. Opt. 57 (2018) 1717. https://doi.org/10.1364/ao.57.001717.

List of Publications

International Journal Publications

1. **Sravanthi Alamandala**, RLN Saiprasad, P.Rathish Kumar**, "Cost-effective load measurement system for health monitoring using long-period grating as an edge filter**", Journal of Optical Fiber Technology, Volume-59, pp-10228,October 2020. https://doi.org/10.1016/j.yofte.2020.102328.
2. **Sravanthi Alamandala**, RLN Saiprasad, P.Rathish Kumar**,** VDR Pavan, P.Kishore, **"Study on bridge weigh in motion (BWIM) system for measuring the vehicle parameters based on strain measurement using FBG sensors",** Journal of Optical Fiber Technology, Volume- 61, pp-102440, January 2021. https://doi.org/10.1016/j.yofte.2020.102440.
3. **Sravanthi Alamandala**, V. Guruprathap Reddy, RLN Saiprasad, P.Rathish Kumar**, "Investigation of the strain measurement on Accelerated Pavement Track (APT) using Digital Image Correlation and fiber Bragg grating sensors" (**communicated to Journal of Innovative Infrastructure Solutions).

International Conference Proceedings

1. **A Sravanthi**, P Kishore, RLN Sai Prasad, P Rathish Kumar, "**Study of Bridge Weigh-in-Motion using FBG Sensors**", International Conference on Fibre Optics and Photonics, OSA,2016.
2. **Sravanthi Alamandala**, Kishore Putha, RLN Sai Prasad, P Rathish Kumar "**FBG Sensing system to Study the Bridge Weigh-in-Motion for Measuring the Vehicle parameters**", 3rd International Conference on Microwave and Photonics (ICMAP), IEEE, 2018.
3. **Sravanthi Alamandala**, RLN Sai Prasad, P Rathish Kumar, M Ravi Kumar, "**Damage Detection in Bridge-Weigh-In-Motion Structures using Fiber Bragg Grating Sensors**", International Conference "Frontiers in Optics: the 102nd OSA Annual Meeting and Exhibit/Laser Science Conference",OSA, 2018.
4. **Sravanthi Alamandala**, V Durga Rama Pavan, RLN Sai Prasad, P Rathish Kumar ,**"A Low Cost Interrogation Method for Strain Monitoring in Bridge Beams"**, MicroOptics Conference (MOC-2019,IEEE,2019.